

The Hampering Active Wellbore Kit (HAWK) for Rapidly Controlling a Free Flowing Oil Well ARCHIVES

by

Folkers Eduardo Rojas

B.S., Massachusetts Institute of Technology (2009)

M.S., Massachusetts Institute of Technology (2011)

Submitted to the Department of Mechanical Engineering
In partial fulfillment of the requirements for the degree of

Doctor of Philosophy in Mechanical Engineering

at the

MASSACHUSETTS INSTITUTE OF TECHNOLOGY

June 2014

© Folkers Eduardo Rojas. All rights reserved.

The author hereby grants to MIT permission to reproduce and distribute publicly paper and electronic copies of this thesis document in whole or in part.

Author Signature redacted

Department of Mechanical Engineering

15 May, 2014

Certified by Signature redacted

Alexander H. Slocum

Pappalardo Professor of Mechanical Engineering

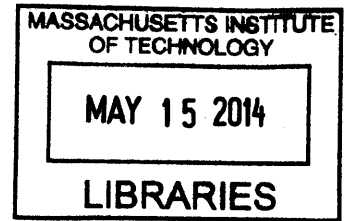
Thesis Supervisor

Accepted by..... Signature redacted

David E. Hardt

Professor of Mechanical Engineering

Chairman, ME Committee for Graduate Students



[Left Blank]

The Hampering Active Wellbore Kit (HAWK) for Rapidly Controlling a Free Flowing Oil Well

by

Folkers Eduardo Rojas

Submitted to the Department of Mechanical Engineering
on 15 May 2014 in partial fulfillment of the
requirements for the degree of
Doctor of Philosophy in Mechanical Engineering

Abstract

To mitigate the impact of a Blowout Preventer (BOP) failure, this work proposes a method and machine that can create a gradual flow reduction to zero in an offshore well by introducing a mechanical plug inside the BOP. The backup safety tool, referred to as the Hampering Active Wellbore Kit (HAWK), is a machine that gradually introduces a continuous medium (e.g. wire) from a spool through the choke/kill lines of a failed BOP to gradually stem the flow through the BOP. The machine can couple to a standard choke/kill line on the BOP and can co-exist with the BOP or be deployed at the time of an accident.

This work presents the design theory for wire feeding in order to form an entanglement, and the mechanism by which to accomplish the reliable feeding of the continuous structure. The efficacy of the entanglement is evaluated by comparing flow rates of a single experimental wellbore before and after the introduction of the mechanical plug.

Thesis Supervisor: Alexander H. Slocum
Title: Pappalardo Professor of Mechanical Engineering

[Left Blank]

*In loving memory of Maria Luisa Rojas Burgos my dear grandmother who has shaped my life and instilled in me many of my core values. She was a strong woman who taught me the value creativity, art, respect, and education.
May she rest in peace.*

[Left Blank]

Acknowledgements

In a quest for answers I have only more questions, but remain determined thanks to outstanding friends and a supportive family.

To my parents Martha and Joaquin, who have allowed me to reach my objective and were supportive of my craziest endeavors. As a baby, my mom would apparently wake me up just to play with me, maybe that is why I don't sleep a great deal now. I don't remember ever getting in trouble for breaking my toys, or taking a car apart in the backyard.

To Alex who for some time has served as a mentor, role model (fashion), and a father figure. The walks through the woods, and the gasps for air during triathlons have served to enrich my PhD experience. To Melissa Martin-Greene for helping me become a better writer over the last 10 years. Thank you Melissa for all of the numerous edit iterations commenting on most of the things I have written at MIT. I believe that Melissa is the person who went through my thesis with a fine-tooth comb for over a year.

As a very good friend said during his PhD defense: "We are born alone, but we don't graduate MIT alone." Thriving at MIT is only done with the help of many. People like Mark Belanger who understand student dynamics, and who has been an incredible friend and instructor since I joined Edgerton Student Shop. Mentors like Ken Stone who have helped me grow as an engineer and a friend.

I would also like to thank the Gates Millennium Scholars Program for ten years of support.

May others be as fortunate to have such a family!

I would also like to thank:

Dean Julie Norman: Julie has been an influential mentor and life friend. From the very first day of my freshmen year I always felt that I had someone looking out for me.

Dean Donna Friedman: Donna has been an outstanding friend that set me on my mechanical engineering journey by choosing my freshmen academic advisor. Little was I to know at the time that it would shape my entire career.

Hector H. Hernandez: As a graduate resident advisor, Hector was not only a role model but an inspiration to take a role in mentoring. He was there to advise me when I wrote a poem freshmen year that had some people running around like bees.

Prof. Maria Zuber: An outstanding mentor who taught me the level of greatness that a scientist and engineer can achieve. Who else can say that they purchased a rocket? Maria instilled in me a desire to reach for the stars and then make a mission plan.

Roberta Allard: Roberta has facilitated many meetings and events for me over the last ten years. The MIT EAPS department is fortunate to have Roberta on board.

Jackie Taylor: Jackie helped me gain access to the resources I needed to get research done as part of the EAPS department during my undergraduate, and also inspired me to take on another hobby.

Prof. Sam Bowring: One great life lesson that I got from Sam was: "Calm Down!" Has a geology professor and mentor he advised to explore another field of science.

Dr. Susan D. Kern: As my astronomy instructor Susan gave me the opportunity to start my engineering career by offering me a research position with the Planetary Astronomy Laboratory (PAL).

Prof. Jim Elliot: There are many lessons that I learned from Jim, not the least how to lead a project. With no existing knowledge on astronomical instruments, Jim offered me a position to gather data at the Wallace Observatory, which eventually lead to my undergraduate thesis designing a camera for the twenty-four inch telescope at Wallace Observatory. With a year into my thesis, Jim put me as the lead engineer in charge MagIC Upgrade, which was another great learning opportunity.

Ken Stone: With my undergrad thesis came my mechanical engineering career. As the director of the Hobby Shop, Ken helped me make my first part: a disk for a vacuum chamber. Ever since I joined the Hobby Shop, Ken has been a valuable mentor and wonderful source of knowledge.

Pat & Dave: With the help of the 2.008 instructors at MIT I learned a great deal about design for manufacturing that otherwise I would not have picked up. Pat and Dave were just an amazing resource to have as part of the class.

Dr. Amanda Gulbis: As a postdoc in the Planetary Astronomy Laboratory (PAL), Amanda gave me the responsibility of making an optics instrument enclosure for the Infrared Telescope Facility (IRTF).

Mark Belanger: With the POETS on IRTF project I got access to the Edgerton Student shop, where Mark would allow me to learn from my mistakes in an effective manner. Throughout a period of 7 years I made various components at the shop. From September to November (2013) I spent more time at the Edgerton shop than I had for the rest of the seven years. Towards the end of November (2013) as I rushed to finish the work for this thesis I ended up using three machines simultaneously. Mark just laughed and asked if I needed help. In truth, my PhD work could not have been completed on time if it wasn't for all the help I received from Mark.

Larry Griffith: As the V.P. of the Hispanic Scholarship Fund and friend, Larry helped me navigate the administrative world of the Gates Millennium Scholars Program. Had it not been for Larry it would have been more difficult to accomplish my work.

Prof. John Brisson: A role model who exemplified the dedication to learning and the need for understanding a system at its simplest level.

Richard Cournoyer: Richard as a division manager at NASA's Jet Propulsion Laboratory (JPL) gave me access to the machine shops at JPL, a luxury unforeseen to any intern, based only on my ability to program CNC machines. He made my experience at JPL worthwhile and further taught me how to get things done.

Dr. Julio Guerrero: As a former boss, Julio became one of my early mentors who contributed greatly to my growth as an engineer.

Prof. Trumper: Prof. Trumper was the person who in the midst of my qualifying exam taught me the difference between a master level student and a PhD student: Look at the trees and the forest.

Prof. Gareth McKinley: As my thermodynamics professor and then member of my thesis committee Prof. McKinley has taught me to pay attention to details and to get inspired by nature.

Prof. Amos Winter: Amos has been a role model demonstrating the impact an engineer can have on the world.

Pierce Hayward: Pierce is an asset to the every mechanical engineering student at MIT. During this research he helped me setting up the testing machines for the preliminary compression tests.

Melissa Martin-Greene: A friend and mentor who has helped me become a better writer and a better person. As I proofread this thesis, I notice how far I have come and how far I must go before I become a great writer. Thank you Melissa.

Dan Chapman: As a confidant and a great friend Dan helped me get through some of the difficult times in college by providing perspective and a place to stash snacks on campus during undergrad.

Chapman Family: Provided a home away from home where I could always crash and touch base with reality.

UAAP: During the last ten years I have also had the support of Michael Bergreen, Leslie Bottari, Stephen Pepper, and Elizabeth Young who have all at one time or another helped me grow or supported my crazy endeavors.

PERG Group: Over the years Precision Engineering Research Group or better known as PERG has helped me with peer reviews to become a better engineer.

Prof. A. Zachary Trimble: As one of the more senior members in PERG, Zach set a high standard for the accomplishments of a PhD candidate in Mechanical engineer.

Deborah Alibrandi: I was able to focus on the engineering because Deborah had our back when it came to logistics planning, scheduling events, financials, etc. Our lab is fortunate to have her.

Candace Royer: Candace has provided me with friendship, support, and guidance in the process of developing my career.

Enrique Shadah: As a member of the MIT Industrial Liaison Program, Enrique has been an advocate for the HAWK technology and connected me with industry partners when possible.

Prof. Anette Hosoi: As a member of my thesis committee, I have had the privilege of receiving guidance from Prof. Hosoi. I have also learned that there can be a balance between sports and research.

Prof. Justus Herder: As a visiting faculty, Justus provided an objective evaluation of the HAWK technology and has been a mentor moving forward with my career.

Eli Carey: Eli was one of the first people outside of my lab group who was happy to help out with this work. One Saturday morning we met for lunch, went over the project and test plan, and within less than a month I had my first data point that showed that the concept might work better than expected.

Tuckertown Fire Department (Rhode Island): This volunteer fire department helped me obtain the preliminary testing required to size the testing prototype.

Josh Dittrich: Josh was the person that decided to lift my head out of the water when I was drowning in work by teaching me how to use the CNC lathe at Edgerton. I initially refused to learn. I naively thought that I could make parts much faster than a CNC lathe, at which point Josh took a part and programmed the machine. This allowed me to increase productivity and to deliver my PhD in a very tight deadline. Sometimes the machines weren't enough, and Josh would keep the shop open a little later to finish up parts.

Ilan Moyer: When it came down to the last second deadlines Ilan was there to let me stay a little later and machine the last couple of passes to finish parts. I'm truly grateful to have friends like Ilan.

High Pressure Testing Lab: A great deal of people helped make this happen, from technicians to machinists. I was very fortunate to have skilled technicians to help me with the final tests.

Dr. Nevan Hanumara: Nevan has been someone who has always had my back through thick and thin. In the midst of a storm, I can count on him to come through and deliver. During the crazy time in my PhD he would make sure that I ate drove me home plenty of times so I could rest. Others would be so lucky to have a friend like Nevan.

Samantha Marquart: I was originally Sam's associate advisor have continued our friendship for over nine years. I can always count on her support and

Eve Carroll: As my second in command, my sister Eve could always take care of family affairs and shield me from distractions when I needed to focus.

Katarina Popovic: Katarina has been a great friend who has supported my crazy endeavors and has shared outstanding long hikes. A great deal of people helped make this happen, from technicians to machinists.

Debie Slocum: A dear friend who has also provided a home away from home and has shared a great deal of wisdom. It was here that I learned to deliver sheep and to extract honey.

Sandy: A man who has shown me how to balance personal life and academic achievement. I enjoyed many great runs through the woods and long talks about life the universe and everything. He has taken my cherries in many ways, and I have taken him new places and made him hurt like no other. We have delivered sheep together and got sick after drinking rotten grape juice. May we continue to share many bottles of grape juice and keep traveling around the world! As a friend and confidant I'm lucky to have found such a friend at MIT.

[Left Blank]

Table of Contents

Chp 1.	Introduction.....	25
1.1.	Background.....	27
1.2.	Existing Response Time	29
1.3.	Motivation	30
1.4.	Thesis Scope	32
1.5.	Functional Requirements.....	34
Chp 2.	Prior Art	35
2.1.	Blowout Control Technology.....	37
2.2.	Mechanical Wire Feeding.....	57
2.3.	Wire Buckling Considerations	62
2.4.	Axially Moving Structure with Fluid Interactions.....	64
2.5.	Spontaneous Knotting.....	67
2.6.	Flow Through Porous Media	68
2.7.	Post Clogging Procedure	72
Chp 3.	Design Parameters	73
3.1.	BOP Environmental Parameters.....	74
3.2.	BOP Geometrical Parameters	77
3.3.	Flow Parameters.....	82
Chp 4.	Bench Level Experiments.....	85
4.1.	Entanglement Generation in Air Stream.....	87
4.2.	Entanglement Generation in Fluid Stream (PI)	101
4.3.	Entanglement Generation in Fluid Stream (PII).....	105
4.4.	Anchoring Entanglement.....	112
4.5.	Sealing by Porous Occlusion 2.5 cm Bore	118
4.6.	Sealing by Porous Occlusion 10.2 cm Bore.....	126
4.7.	Anchoring and Sealing At High Pressure	129
Chp 5.	Entanglement Model.....	139
5.1.	Background.....	140
5.2.	Derivation	141
5.3.	Interaction Loading	154
5.4.	Model Discussion	155
Chp 6.	Machine Design.....	157
6.1.	Prototype Functional Requirements.....	158
6.2.	Design and Analysis.....	159
6.3.	Measurement and Instrumentation.....	170
6.4.	Wire Sizing.....	173

6.5. Preliminary Testing.....	175
6.6. Full Flow Loop Test Setup.....	177
6.7. Data.....	181
6.8. Technology Comparison	184
6.9. Conclusion.....	185
Chp 7. Discussion.....	187
7.1. Future Work	187
7.2. Closing Remarks	187
Bibliography.....	189
Appendix	197
Calculations.....	197
Natural Phenomena	207
PUPs Problems.....	208

List of Figures

FIGURE 1-1: MECHANICAL PLUG GENERATED INSIDE BOP CREATED BY FEEDING A CONTINUOUS MEDIUM VIA THE EXISTING CHOKE/KILL PORTS (THE IMAGE ON THE LEFT SHOWING OIL RIG FROM MILLHEIM – EARLY RESERVOIR APPRAISAL)	26
FIGURE 1-2: HAMPERING ACTIVE WELLBORE KIT (HAWK) SYSTEM INCORPORATED INTO AN ROV AND CONNECTED IN A DIRECT AND MEANDERING PATH TO THE WELL BORE.....	26
FIGURE 1-3: BLOWOUT PREVENTER STACK COMPONENTS ANNULAR AND RAM STYLE (THE IMAGE ON THE LEFT SHOWING OIL RIG FROM MILLHEIM – EARLY RESERVOIR APPRAISAL).....	28
FIGURE 1-4: POSSIBLE RESPONSE TIMES FROM THE INTERNATIONAL ASSOCIATION OF OIL & GAS PRODUCERS – CAPPING AND CONTAINMENT.....	29
FIGURE 1-5: PRELIMINARY EXPERIMENT SUBSECTION: GENERATION, ANCHORING, AND SEALING. PROCESS FOR FINDING THE OPERATING PARAMETERS.....	33
FIGURE 2-1: INSERTION OF WIRE COIL TOWER INTO BASILAR TIP ANEURYSM WHERE IT PROMOTES THE GENERATION OF A THROMBUS (BLOOD CLOT) (U.S. PAT. No. 6,183,495 B1)	35
FIGURE 2-2: PRIOR ART FLOW CHART WHICH DETERMINISTICALLY IDENTIFIES AREAS CONTRIBUTING TO THE DESIGN SPACE.	36
FIGURE 2-3: DEEPWATER HORIZON BOP ASSEMBLY (SOURCE: CHIEF COUNSEL REPORT - TRIAL GRAPHIX) [29]	37
FIGURE 2-4: BOP STACK TESTING UNITS. THE UNIT DESCRIBED BY <i>COUREN ET AL'S</i> PATENT IS THE TOOL THAT IS LOWERED INTO THE BOP WELLBORE WHERE IT IS USED TO SIMULATE A PRESSURE SPIKE INSIDE THE BOP. THE UNIT DESCRIBED BY <i>WINTER ET AL'S</i> PATENT GOES OVER THE INFRASTRUCTURE REQUIRED TO EXECUTE THE FULL SYSTEM TEST.	39
FIGURE 2-5: BONNET LOCK MECHANISM WITH RADIAL LOCK (U.S. PAT. No. 6,554,247)	40
FIGURE 2-6: MAGNETORHEOLOGICAL BLOWOUT PREVENTER (U.S. PAT. No. 2011/0297374 A1)	41
FIGURE 2-7: ANNULAR BOP ELASTOMER SEAL FINITE ELEMENT ANALYSIS.....	42
FIGURE 2-8: STRAIGHT AND V SHAPED SHEAR BLADES	43
FIGURE 2-9: SHEAR BLADE WITH PIECING POINT	43
FIGURE 2-10: A) RAM BLADE ASSORTMENT FOR PUNCTURING TUBULAR MEMBERS (U.S. PAT. No. 7,814,979 B2). B) SHEAR BLADES WHERE ONE BLADE IS USED TO SECURE THE POSITION OF THE TUBULAR AND THE SECOND BLADE PROMOTES PUNCTURING THROUGH THE USE OF PUNCTURING TIPS (U.S. PAT. No. 2012/0193556 A1)	44
FIGURE 2-11: RAM BODIES BLADE-TO-BLADE SEAL ENHANCEMENT (U.S. PAT. No. 2006/0113501 A1).....	45
FIGURE 2-12: TOP KILL OPERATION VESSEL REQUIREMENT (SOURCE BP BRIEFING MAY 2010) [10]	45
FIGURE 2-13: PLUG FORMING USING TWO-PHASE FLUIDS IN WELLBORE AND HARDENABLE PLUG MATERIAL (U.S. PAT. No. 4,275,788)	46
FIGURE 2-14: CHEMICAL MEANS OF PLUGGING A WELLBORE.....	47
FIGURE 2-15: PLUG GENERATED BY INTRODUCING 2-CYANOACRYLATE ESTER MONOMER INTO WELLBORE (U.S. PAT. No. 2012/0285683 A1)	48
FIGURE 2-16: RELIEF WELL PATENTS	49
FIGURE 2-17: ISOLATION ZONES PATENTS	49
FIGURE 2-18: LOCAL CAP BELL SHAPED FOR PRODUCTION AND CEMENTING.....	50
FIGURE 2-19: SAMPLE DIVERTER PATENTS.....	51
FIGURE 2-20: FLEXIBLE DOME STRUCTURES AND RISER WITH COLLECTION BALLOONS.....	52
FIGURE 2-21: OSPRAG CAPPING DEVICE DIMENSIONS AND PORT SYSTEM [76]	53
FIGURE 2-22: MWCC CAPPING DEVICE WITH A SINGLE BLIND RAM TO CONTROL THE FLOW	53
FIGURE 2-23: IMPROVING JUNK SHOT USING CASING CONSTRICTION AND DEPLOYABLE PINS	55
FIGURE 2-24: JAVELIN INSERTS INTO THE WELLBORE TO CONTROL THE WELL (U.S. PAT. No. 8,205,677 B1)	55
FIGURE 2-25: MIG WELDER WIRE FEEDERS (U.S. PAT. No. 2013/0048621 A1) AND MILLER PYTHON PUSH-PULL HEAD FOR WELDING ALUMINUM	57
FIGURE 2-26: SELF-ALIGNING WIRE FEEDER (U.S. PAT. No. 5,934,537)	58
FIGURE 2-27: GRADUAL AND DISCRETE WIRE FEEDERS FOR VARYING WIRE DIAMETER	58
FIGURE 2-28: DYNAMIC VARIABLE DIAMETER SPLIT ROLLER MECHANISM (U.S. PAT. No. 3,447,730)	59
FIGURE 2-29: VARIABLE GRIPPING FORCE MECHANISM	59
FIGURE 2-30: LOCKING MECHANISM (U.S. PAT. No. 6,247,894 B1).....	60
FIGURE 2-31: HOSE FEEDER INTO PRESSURIZED CHAMBER (U.S. PAT. No. 3,946,918)	60
FIGURE 2-32: CONTINUOUS DRIVE SYSTEM WITH GRIPPING BLOCKS THAT PRESS ONTO TUBING	61

FIGURE 2-33: WIRE STORAGE CONFIGURATIONS INCLUDING RADIAL AND AXIAL SPOOLS.....	62
FIGURE 2-34: WELDING WIRE GUIDE RING.....	63
FIGURE 2-35: POTENTIAL PHYSICAL MODELS FOR DETERMINING WIRE INTERACTION THROUGH DIFFERENT AREAS ALONG THE FEEDING PROCESS	64
FIGURE 2-36: HENRY DARCY SAND COLUMN EXPERIMENT SETUP FROM LES FONTAINES DE LA VILLE DE DIJON [119].....	69
FIGURE 2-37: SCHEMATIC DIAGRAM OF DARCY'S EQUATION SHOWING A PERMEABLE PLUG OBSTRUCTING FLOW IN A CHANNEL.....	70
FIGURE 3-1: WELLBORE SCHEMATIC ILLUSTRATED DESIGN PARAMETERS.....	73
FIGURE 3-2: OFFSHORE DRILLING & PRODUCTION DEPTH OVER TIME [134].....	75
FIGURE 3-3: GLOBAL AVERAGE OCEAN TEMPERATURE DEPENDENCE ON DEPTH FROM 1982 TO 2004 (NATIONAL WEATHER SERVICE CLIMATE PREDICTION CENTER [136])	76
FIGURE 3-4: BOP OBSTRUCTION CONFIGURATIONS. THE CLEAR FLOW CONFIGURATION CAN ALSO HAVE AN ANNULAR CONFIGURATION (NOT SHOWN ABOVE).....	79
FIGURE 3-5: RAM BOP FROM T3 ENERGY SERVICES SHOWING LOCATION OF CHOKE/KILL PORTS AND CROSS SECTION OF SYSTEM LEADING INTO THE WELLBORE.....	81
FIGURE 3-6: GULF OF MEXICO CRUDE OIL PRODUCTION (SOURCE EIA).....	82
FIGURE 3-7: ABSOLUTE OIL VISCOSITY AS A FUNCTION OF OIL GRAVITY AND TEMPERATURE FROM 37.7 TO 104.4° C.....	84
FIGURE 4-1: MEAN AIR VELOCITY AS A FUNCTION OF INLET PRESSURES RANGING FROM 0.14 TO 0.48 MPA.....	87
FIGURE 4-2: EXPERIMENTAL LAYOUT AND WIRE SYSTEM. THE DIAMETER OF THE PIPE IS 2.54 CM (1 IN) AND THE LENGTH IS ~ 150 CM.	88
FIGURE 4-3: CROSS SECTION OF WIRE FEEDING MECHANISM. A) IS THE FRONT VIEW SHOWING THE EXTERIOR HOUSING AROUND THE MOUNTING UNIT CONTAINING SIZE ENTRY PORTS. B) WIRE ENTERING THROUGH THE EXTERNAL GUIDE AND BEING PUSHED BY THE DRIVE WHEELS INTO THE FLOW CHAMBER THROUGH AN INTERNAL GUIDE. C) PHOTO OF SYSTEM SHOWING THE SYNCHRONIZING GEARS THAT LINK THE MOTION OF THE FEED DISKS.....	89
FIGURE 4-4: FEEDER DISK CONCEPTS.....	89
FIGURE 4-5: MAX FRICTION FORCE (N) AS A FUNCTION OF INTERIOR DIAMETER OF THE O-RING HOLDER USING THREE STANDARD ORINGS (0.301 IDX0.70W) WITH AN ALUMINUM WIRE (812 UM DIAMETER) AND STRING WIRE (812 UM).LOCKING THE WHEELS AND PULLING TILL SLIPPING MEASURED THE MAXIMUM AMOUNT OF FORCE EXERTED BY WHEELS.....	90
FIGURE 4-6: BRASS KNURLED DRIVE DISKS WITH A CENTER CHANNEL TO PREVENT THE WIRE FROM TRAVELING.....	90
FIGURE 4-7: WIRE DEFLECTION INDUCED BY DRAG LOADING WITH LAMINAR (PURPLE DOTTED LINE) OR TURBULENT (BLUE DASHED LINE) FLOW.....	91
FIGURE 4-8: FOURTH ORDER POLY DEFLECTION FOR LAMINAR CONDITIONS.....	92
FIGURE 4-9: DEFLECTION SHAPE FOR LAMINAR FLOW CONDITIONS. ON THE LEFT IS CHANGING THE NON-DIMENSIONAL STIFFNESS BY CHANGING MATERIALS ($E_{Al} = 70$ GPa, $E_{Mg} = 45$ GPa, $E_{NY} = 2$ GPa) AND KEEPING THE FLOW RATE TO 1GMP. ON THE RIGHT IS CHANGING THE NON-DIMENSIONAL STIFFNESS BY CHANGING THE FLOW RATE (0.32 L/SEC (5 GPM), 0.47 L/SEC (7.5 GPM), AND 0.64 L/SEC (10 GPM)) FOR A WELLBORE DIAMETER OF 2.54 CM, AND WIRE DIAMETER ($E_{LDPE} = 0.5$ GPa) OF 800 UM.....	93
FIGURE 4-10: TURBULENT LOADING SHAPE OVER THE LENGTH OF THE FULL WELLBORE.....	94
FIGURE 4-11: FLEXURE MEMBER ONSET OF BUCKLING MODEL.....	96
FIGURE 4-12: STIFFNESS CHART AS A FUNCTION OF AXIAL LOAD FOR RANGES IN WIRE LENGTH VERSUS AXIAL LOADS, WHERE THE STIFFNESS IS IN UNITS OF [N/M].....	96
FIGURE 4-13: BUCKLING OF CURVED MEMBER.....	97
FIGURE 4-14: PRE-CURVED MEMBER DISPLACEMENT FOR $\Xi = 45$ DEGREE WITH A 25.4 MM DIAMETER FLOW CHANNEL AND ALUMINUM WIRE 400 UM RADIUS.....	98
FIGURE 4-15: PRE-CURVED MEMBER DISPLACEMENT FOR $\Xi = 30$ DEGREE WITH A 25.4 MM DIAMETER FLOW CHANNEL AND ALUMINUM WIRE 400 UM RADIUS.....	98
FIGURE 4-16: PRE-CURVED MEMBER DISPLACEMENT FOR $\Xi = 15$ DEGREE WITH A 25.4 MM DIAMETER FLOW CHANNEL AND ALUMINUM WIRE 400 UM RADIUS.....	98
FIGURE 4-17 CURVED MEMBER BUCKLING WITH DISTRIBUTIVE LOADING.....	99
FIGURE 4-18: WIRE NON-DIMENSIONAL ENTANGLEMENT COEFFICIENT AS A FUNCTION OF THE AVERAGE AIR VELOCITY FOR AN ALUMINUM WIRE WITH A DIAMETER OF 812 UM.....	100
FIGURE 4-19: STRING AND ALUMINUM WIRE IN AIR BUCKLING.....	100
FIGURE 4-20: FLUID EXPERIMENTAL FLOW LAYOUT SHOWING THE WIRE FEEDING MECHANISM INCORPORATED INTO THE TANK AND DRIVEN BY AN EXTERNAL MOTOR.....	101
FIGURE 4-21: ENTANGLEMENT REGIONS.....	102
FIGURE 4-22: CHARACTERIZATION OF ENTANGLEMENT BEHAVIOR.....	103

FIGURE 4-23: REYNOLDS NUMBER VERSUS FEED RATE FOR ALUMINUM WIRE (WITH A 812 UM RADIUS)	103
FIGURE 4-24: REYNOLDS NUMBER VERSUS NON-DIMENSIONAL ENTANGLEMENT COEFFICIENT SHOWING THAT FUTURE WORK MAY NEED TO INCLUDE A CORRECTION FOR THE ENTRY VELOCITY	104
FIGURE 4-25: ON THE LEFT IS A WATER TANK WITH A 2.5 CM (1 INCH) IN DIAMETER PIPE THAT CONNECTS TO THE SUBMERGED WIRE FEEDER. A MOTOR ON TOP OF THE TANK DRIVES THE WIRE FEEDER VIA A BELT SYSTEM.....	105
FIGURE 4-26: KINEMATIC COUPLINGS FOR STAGES AND DRIVE SYSTEM.....	106
FIGURE 4-27: WIRE DRIVE SYSTEM HOUSED IN STAGE TWO	107
FIGURE 4-28: REYNOLDS VERSUS FEED RATE FOR NYLON WIRE WITH A THETA OF 180 DEGREES AND TILT OF 70 DEGREES.....	109
FIGURE 4-29: REYNOLDS NUMBER VERSUS FEED RATE FOR ALUMINUM WIRE (WITH A 812 UM DIAMETER) WITH A THETA OF 180 DEGREES AND TILT OF 70 DEGREES.....	109
FIGURE 4-30: ROTATION ANGLE FOR TILT 30 DEGREES FOR A GIVEN REYNOLDS NUMBER.....	110
FIGURE 4-31: ROTATION ANGLE FOR TILT 70 DEGREES FOR A GIVEN REYNOLDS NUMBER.....	111
FIGURE 4-32: DRAWING PROCESS SCHEMATIC DIAGRAM SHOWING AN EFFECTIVE WORK PIECE THAT WOULD BE THE ENTANGLEMENT NEST PASSING THROUGH THE RESTRICTION.....	113
FIGURE 4-33: DRAWING FORCE IN NEWTONS AS A FUNCTION OF PERCENTAGE COMPACTION AND AREA REDUCTION CALCULATED USING EQUATION 4.21. THE CALCULATION IS FOR A 50 MPA YIELD STRESS MATERIAL WITH A BORE DIAMETER OF 10.2 CM (4 INCHES) WITH VARYING COMPACTION PERCENTAGE.....	113
FIGURE 4-34: MAX OPERATING PRESSURE OF A PARTIALLY COMPACTED MECHANICAL PLUG PRIOR TO SHEAR FAILURE FOR VARYING MATERIAL PROPERTIES WITH THE FOLLOWING GEOMETRY $D_{BORE} = 47.6$ CM (18.75 INCH), EFFECTIVE HEIGHT $H_c \sim 47.6$ CM (18.75 INCH) USING EQUATION 4.23.....	114
FIGURE 4-35: ANCHOR LOADING PRELIMINARY EXPERIMENT	115
FIGURE 4-36: THEORETICAL WIRE DIAMETER FOR THE EXPERIMENTAL TEST SHOWING THE EFFECT OF THE NON-DIMENSIONAL ENTANGLEMENT COEFFICIENT ON THE WIRE DIAMETER FOR GIVEN GEOMETRIC AND MATERIAL PROPERTIES: $D_{BORE} = 10.2$ CM, $E_{ST} = 210$ GPa, $E_{AL} = 70$ GPa, USING WATER.....	116
FIGURE 4-37: MASS ENTANGLEMENT $M_E = 170 \pm 14$ G (3/8 LB), $D_{BORE} = 9.5$ CM (3.75 INCHES), GALVANIZE STEEL WIRE $D_{WIRE} = 1.55$ MM.....	117
FIGURE 4-38: POROUS OCCLUSION EXPERIMENTAL SETUP CONSISTING OF A PUMP, OMEGA FLOW METER (FTB791), AND A PRESSURE METER (MG1-200-A-9V-R). THE INTERIOR DIAMETER OF THE PIPE IS 2.5 CM (1 INCH).....	118
FIGURE 4-39: PERMEABILITY EXPERIMENT SUMMARY FOR ALUMINUM (AL), NITRILE RUBBER (SI), AND RIBBON CORE DESIGN (RC) WITH VARYING LENGTH TO DIAMETER RATIO. DUE TO PUMP LIMITATIONS OF THE EXPERIMENTAL SETUP ADDITIONAL FLOW RATE MEASUREMENTS FOR LOW PERMEABILITY'S CANNOT BE OBTAINED WITH THIS SETUP.	119
FIGURE 4-40: ALUMINUM WIRE 0.8 MM (0.032 INCH) WITH POROSITY OF 73%	120
FIGURE 4-41: PERMEABILITY (DARCY) FOR ALUMINUM WIRE (POROSITY OF 73%) WITH VARYING GEOMETRY CONFIGURATIONS.....	120
FIGURE 4-42: BUNA O-RING WIRE 1.8 MM (0.070 INCH) WITH POROSITY OF 40% TO 15%	121
FIGURE 4-43: PERMEABILITY (DARCY) FOR BUNA O-RING WIRE (POROSITY OF 73%)	121
FIGURE 4-44: SLUG DESIGN FLOW RATE TREND. THE ERROR FOR THE FLOW MEASUREMENT IS 2% OF THE MEASUREMENT; WHEREAS THE PRESSURE MEASUREMENT HAS AN ERROR OF $\pm 1\%$ OF THE FULL SCALE.	122
FIGURE 4-45: SLUG DESIGN CHANGED THE COMPRESSION BY THE FLOW.....	122
FIGURE 4-46: EFFECTIVENESS OF A PLUG WITH AN RANGES OF L_{PLUG}/D_{WELL} , $M_{FLUID} = 0.010$ PA*SEC, WELL PRESSURE $P_{WELL} = 68.9$ MPA (10KSI) PERMEABILITY ($K = 30$ DARCY) EXPERIMENTALLY REASONABLY ACHIEVABLE, INITIAL VOLUMETRIC FLOW RATE $V_i = 15.9 \times 10^3$ M ³ /DAY, WELL PRESSURE $P_{WELL} = 68.9$ MPA (10 KSI)	123
FIGURE 4-47: PERMEABILITY SENSITIVITY FOR AN 47.6 CM (18.75 INCH) BORE DIAMETER WITH AN UNCONTROLLED FLOW RATE OF 100,000 BBL/DAY, VISCOSITY 8.39×10^{-3} PA SEC RANGES OF L_{PLUG}/D_{BORE} , BOP BORE DIAMETER (D_{BORE} (18.75 INCHES)), $M_{FLUID} = 0.010$ PA*SEC. INITIAL VOLUMETRIC FLOW RATE $V_i = 15.9 \times 10^3$ M ³ /DAY (100,000 BBL./DAY), WELL PRESSURE $P_{BORE} = 68.9$ MPA (10KSI).....	124
FIGURE 4-48: PERMEABILITY RESULTS FOR A 2.5 CM DIAMETER CHANNEL WITH AT MOST 38 LITER/MIN FLOW RATE WITH VARYING INITIAL POROSITIES.....	125
FIGURE 4-49: FOUR INCH PERMEABILITY EXPERIMENTAL SETUP.....	126
FIGURE 4-50: PERMEABILITY EXPERIMENTAL RESULTS FOR 10.2 CM WELLBORE SCALE.....	127
FIGURE 4-51: CUSTOM FLOW CHAMBER WITH INTERFACE REGION. THE CHAMBER IS CONNECTED TO THE OUTLET OF A FIRE TRUCK HOSE VIA A 2.5 NH SWIVEL CONNECTOR.	129
FIGURE 4-52: BOLT MINIMUM PRELOAD REQUIRED FOR RANGE INTERNAL PRESSURES CALCULATED USING TWO EQUATIONS IN LITERATURE.....	132
FIGURE 4-53: RAM AND ANNULAR OBSTRUCTION APERTURES.....	133

FIGURE 4-54: INTERFACE REGION AND BOLT REGION	134
FIGURE 4-55: FLANGE FLATNESS MEASUREMENTS FOR FLANGE 3 SHOWING THE O-RING GROOVE FLATNESS PROFILE AND THE OVERALL PLATE FLATNESS.....	136
FIGURE 4-56: FIRE TRUCK PERMEABILITY EXPERIMENTAL SETUP.....	136
FIGURE 4-57: PRESSURE DIFFERENCE ACROSS PLUG VERSUS PERCENT CLOSURE FOR ANNULAR (ANN) AND RAM (RAM) OBSTRUCTIONS WITH VARYING AMOUNT OF PLUGGING MATERIAL. BLUE LABELS ARE FOR 0.412 KG OF HEAT SHRINK PLUGGING MATERIAL. RED LABELS ARE FOR 0.812 KG OF HEAT SHRINK AS PLUGGING MATERIAL. THE ENTANGLEMENT USED IS A GALVANIZED STEEL ($M_E=0.32\text{KG}$) WITH A WAVELENGTH OF ~ 1.5 INCHES (ROUGHLY $1/3$ OF THE WELLBORE DIAMETER).....	137
FIGURE 4-58: MAXIMUM PRESSURE DIFFERENTIAL MEASURED FOR A GIVEN OBSTRUCTION PERCENTAGE OF THE ANNULAR AND RAM GEOMETRY FOR THE DATA PRESENTED IN FIGURE 4-57.....	138
FIGURE 5-1: FLEXIBLE WIRE ENTERING THE WELLBORE.....	139
FIGURE 5-2: COORDINATES ON ANY POINT IN THE ACTIVE REGION AS A FUNCTION OF $\phi(s)$	141
FIGURE 5-3: DEFORMATION POTENTIAL WITH BOUNDARY CONDITIONS.....	142
FIGURE 5-4: CURVATURE DERIVATION.....	143
FIGURE 5-5 ELEMENT FORCE BALANCE.....	143
FIGURE 5-6: SHEAR FORCE COMPONENTS.....	144
FIGURE 5-7: DRAG FORCE AND GRAVITY DIVISION INTO COMPONENTS ALONG THE F_x AND F_y DIRECTION	145
FIGURE 5-8: ELASTICA MODEL PROGRAM FLOW DIAGRAM.....	148
FIGURE 5-9: DISCRETE ELEMENT DIAGRAM.....	149
FIGURE 5-10: FOUR-ELEMENT MOMENT BALANCE FOR DISCRETE TORSION SPRINGS MODEL.....	149
FIGURE 5-11: HORIZONTAL DISPLACEMENT VERSUS VERTICAL DISPLACEMENT FOR SIMPLE CANTILEVER BEAM ANALYTICAL SOLUTION AND APPROXIMATION WITH INCREASING NUMBER OF SECTIONS.....	150
FIGURE 5-12: NUMBER OF SECTIONS VERSUS PERCENT ERROR OF SIMPLIFIED SPRING MODEL.....	151
FIGURE 5-13: ELEMENT DISCRETIZATION	152
FIGURE 5-14: NODE EQUILIBRIUM AT ROTATIONAL SPRING NODE.....	153
FIGURE 5-15: KLARBRING CONTACT MODEL.....	154
FIGURE 6-1: INTEGRATED PROTOTYPE EXPERIMENTAL SETUP.....	157
FIGURE 6-2: INTEGRATED PROTOTYPE EXPERIMENTAL SETUP.....	158
FIGURE 6-3: MODULE BREAK DOWN AND ANALYSIS FOR EACH MODULE.....	159
FIGURE 6-4: HOUSING MODULE IN DETAIL.....	160
FIGURE 6-5: DYNAMIC BEARING CONFIGURATIONS AND O-RING SPECIFICATIONS.....	161
FIGURE 6-6: DYNAMIC SEAL WITH A KNOWN BACK PRESSURE PUSHING AGAINST THE O-RING SEAL, WHICH IMPARTS A FORCE ON THE SHAFT THAT REDUCES THE TORQUE POTENTIAL.....	161
FIGURE 6-7: THRUST LOAD STRUCTURAL LOOP GOING THROUGH SHAFT, BEARING, MOUNT CAP, AND DRIVE INTERFACE PORT.....	162
FIGURE 6-8: SOFT KINEMATIC INTERFACE BETWEEN FEEDER INTERFACE PLATE AND HOUSING MODULE SHOWING BALL AND GROOVE INTERFACES. FOR A TRUE KINEMATIC ORIENTATION THE ORIENTATION OF THE GROOVES NEED TO BE ROTATED BY NINETY DEGREES.....	163
FIGURE 6-9: QUASI-KINEMATIC INTERFACE ASSEMBLY IN ARBOR PRESS USED TO CLOSE THE GAP AND PRESS FIT THE SPHERES INTO THE FEEDER PORT.....	163
FIGURE 6-10: WIRE FEEDER SUB MODULES.....	164
FIGURE 6-11: ASSEMBLY OF WIRE FEEDER MAIN BODY TO LINEAR STAGE	165
FIGURE 6-12: FEEDER MAIN BODY MOUNT PLATE WITH ALL KEY PORTS LABELED. ALSO INCLUDES THE TWO SETUPS USED TO MANUFACTURE THE UNITS.....	165
FIGURE 6-13: PROBOSCIS HEAD DETAILS.....	166
FIGURE 6-14: PROBOSCIS TRANSMISSION SYSTEM.....	167
FIGURE 6-15: ON THE LEFT IS THE DRIVE MODULE ASSEMBLY SHOWING MOUNTING CAP, FLEX COUPLINGS, MOTOR PLATE, AND MOTOR. ON THE RIGHT IS THE MOUNTING STRUCTURE FOR THE DRIVE MODULE TO THE HOUSING VIA TWO 9.5 MM QUICK RELEASE PINS.	168
FIGURE 6-16: RADIAL SPOOL MODULE FIRST AND SECOND ITERATION.....	169
FIGURE 6-17: WIRING DIAGRAM OF THE CONTROLS MODULE. THE POWER SUPPLY (MODEL No FSP018-DEDA2) CONVERTS THE AC SIGNAL TO A 12 V DC WITH 1.5 AMPS.....	170
FIGURE 6-18: IMAGES OF CONTROL BOX SHOWING THE AC INLET, EMERGENCY STOP, MOTOR CONTROL, AND INSTRUMENT SENSORS.	170

FIGURE 6-19: T CONFIGURATION FOR OMEGA PRESSURE SENSOR (PX309-500G-5V) THAT IS INCORPORATE TO THE VALVE IN THE FLOW CHAMBER. THE VALVE (MCMASTER PART : 4912K99) IS A MINIATURE CHROME- PLATED BRASS VALL VALVE WITH HALF AN INCH NPT FEMALE AND MALE CONNECTION RATED TO 450 PSI AT 100 F. 171

FIGURE 6-20: TURBINE FLOW METER CONFIGURATION 172

FIGURE 6-21: WIRE SIZE REQUIREMENT FOR EXPERIMENTAL SETUP BASED ON THE NON-DIMENSIONAL STIFFNESS. THE VALUE CIRCLE IN RED CORRESPONDS THE VALUE USED FOR THE SCALED PROTOTYPE WHICH IS A 0.7 MM RADIUS WIRE OF GALVANIZED STEEL. THE CALCULATION IS MADE FOR ASSUMING A 10.2 CM (4 INCH) WELLBORE DIAMETER, WATER VISCOSITY 1×10^{-3} PA·SEC AND YOUNG'S MODULUS OF 210 GPa. 173

FIGURE 6-22: WIRE SIZE REQUIREMENT FOR OFFSHORE INDUSTRY FOR AN 47.6 CM (18.75 INCH) WELLBORE WITH AN OIL VISCOSITY OF 0.01 PA·SEC, AND DENSITY OF 839 KG/M³, FOR VARYING NON-DIMENSIONAL STIFFNESS VALUES. 174

FIGURE 6-23: SOMERVILLE MASSACHUSETTS PRELIMINARY EXPERIMENTAL RUN ON THE BANKS OF THE MYSTIC RIVER..... 175

FIGURE 6-24: SOMERVILLE PRELIMINARY EXPERIMENTAL RUN SEALING AS A FUNCTION OF PRESSURE FOR A MECHANICAL PLUG INTRODUCED INTO THE FLOW CHAMBER. GALVANIZED STEEL WIRE $D_{WIRE} = 1.55$ MM (0.061 INCH), $D_{BORE} = 10.2$ CM (4 INCHES), ANCHOR MASS $M_E = 0.510$ KG (1.1 LB), MASS PLUG MATERIAL $M_P = 0.875$ KG (1.9 LB), OBSTRUCTION 45 %, ANCHOR COMPACTION MEASURED 22%, PLUG PERMEABILITY 16-22 DARCY 176

FIGURE 6-25: ISOMETRIC VIEW SHOWING THE LOCATION OF THE ENTANGLEMENT EXPERIMENT WITH RESPECT TO THE PIT AND THE PUMP SUPPLYING THE FLOW 177

FIGURE 6-26: SIDE VIEW OF THE ENTANGLEMENT EXPERIMENT SHOWING THE FLOW CHAMBER ANGLED AT 30 DEGREES SUPPORTED BY A MOUNTING FRAME..... 178

FIGURE 6-27: ISOMETRIC VIEW SHOWING THE ENTANGLEMENT EXPERIMENT WITH THE FLOW CHAMBER MOUNTED ON THE FRAME. THE CHAMBER IS GOING TO BE STRAPPED DOWN TO THE FRAME AND THE FRAME TO THE FOUNDATION..... 178

FIGURE 6-28: OVERVIEW OF PRESSURE TEST SHOWING THE SETUP AND HOW THE MECHANICAL PLUG IS GOING TO COMPRESS..... 179

FIGURE 6-29: WIRE ENTANGLEMENT GENERATED BY FEEDING AGAINST THE FLOW AND ORTHOGONAL TO THE FLOW. THE NON-DIMENSIONAL STIFFNESS AT 720 LPM (190 GPM) IS $\Pi_E = 1830$ AND AT 1098 LPM (290 GPM) IS $\Pi_E = 785$ 181

FIGURE 6-30: WIRE ENTANGLEMENT SEALING AT LOW PRESSURES..... 182

FIGURE 6-31: FLOW RATE VERSUS NON-DIMENSIONAL ENTANGLEMENT STIFFNESS SHOWING THAT THE TEST POINTS FOR ENTANGLEMENT ARE IN THE SAME RANGE OF THE SMALLER SCALE EXPERIMENTS..... 182

FIGURE 6-32: PRESSURE EXPERIMENT USING DRILL MUD (9.2 POUNDS PER GALLON) WITH A GENERATED ENTANGLEMENT AND ADDED RIBBON SEALING MATERIAL (HEAT SHRINK) $M_P = 0.875$ KG (1.9 LB) AND APPROXIMATELY ANCHORING MASS OF $M_E = 1.5$ KG (3.3 LB)..... 183

FIGURE 6-33: PRESSURE LOADING IMAGES THROUGHOUT THE LOADING PROCESS 184

FIGURE 6-34: TECHNOLOGY COMPARISON 185

FIGURE 0-1: FLOW RATE VERSUS REYNOLDS NUMBER SHOWING THAT AT ROUGHLY 60,000 BBL./DAY THE REYNOLDS NUMBER IS AROUND 30,000 THUS THE FLOW IS TURBULENT. 197

FIGURE 0-2: FLUID SCHEMATIC IN WIRE GUIDE 198

FIGURE 0-3: FLOW AXIAL VELOCITY AS A FUNCTION OF RADIUS 200

FIGURE 0-4: ENTANGLEMENT STIFFNESS FOR THE SPIDER SILK STRAND BALLOONING PROCESS 207

Conversions

1 barrel = 42 US gallons = 158.99 Liters

1 cp = 1 mPa*sec

1 Darcy $\sim 1 \times 10^{-12} \text{ m}^2$

1 ksi = 1000 psi = 6.894 MPa

1 gal = 3.785 Liter

List of Tables

TABLE 1-1: FUNCTIONAL REQUIREMENTS AND DESIGN CONSIDERATIONS	34
TABLE 2-1: COMMERCIALY AVAILABLE CAPPING STACK COMPARISON MARINE WELL CAPPING STACK AND THE OIL AND GAS UK CAPPING STACK	54
TABLE 2-2: PERMEABILITY RANGES OF SEDIMENTARY AND CRYSTALLINE ROCKS FROM DOMENICO ET AL AND FREEZE ET AL. [127, 128]	71
TABLE 3-1: OIL RIG GENERATION MAXIMUM DEPTH.....	74
TABLE 3-2: BOP STACK HEIGHT (SOURCE: NATIONAL OIL WELL VARCO PRESENTATION).....	77
TABLE 3-3: HYDRIL BOP WEIGHT (LBS.) AS A FUNCTION OF WELLBORE SIZE AND WORKING PRESSURE (SEE BROCHURES FOR DETAILS). SPECIFICATION IN ENGLISH UNITS FOR CONSISTENCY WITH SUPPLIERS.....	78
TABLE 3-4: SUNNDA BOP WEIGHT (LBS.) AS FUNCTION OF WELLBORE SIZE AND WORKING PRESSURE (PARTIAL LIST) AND DOUBLE....	78
TABLE 4-1: WIRE ENTANGLEMENT PARAMETER SYNTHESIS ASSUMING THAT THE DIAMETER OF THE WIRE IS MUCH SMALLER THAN THE WELLBORE DIAMETER, AND THAT THE PRESSURE IN THE MACHINE IS ABOUT EQUAL TO THE PRESSURE IN THE WELLBORE	85
TABLE 4-2: ENTANGLEMENT PLUG SYNTHESIS	86
TABLE 4-3: EXPERIMENTAL ELAPSE IMAGES OF ENTANGLEMENT INITIATION.....	95
TABLE 4-4: ENTANGLEMENT BUCKLING MODELS.....	95
TABLE 4-5: SECTION AND MAX TORQUE TRANSMITTED THROUGH THE ELEMENTS, WHERE THE SHEAR STRESS IS $\tau_v/\sqrt{3}$	107
TABLE 4-6: ENTANGLEMENT TYPES.....	108
TABLE 4-7: ANCHOR MODES	112
TABLE 4-8: FIRST LEVEL PERMEABILITY MEASUREMENTS AND DEVELOPMENT POSITIVE AND NEGATIVE ASPECTS.	124
TABLE 4-9: CHAMBER AND INTERFACE FAILURE MODES AND MAXIMUM PRESSURE RATINGS.....	135
TABLE 4-10: FLANGE FLATNESS MEASUREMENTS FROM COORDINATE MEASURING MACHINE WITH A 3 MM DIAMETER CONTACT PROBE	135
TABLE 5-1 ELASTICA MODEL BACKGROUND SELECTED PAPERS.....	140
TABLE 5-2: KLARBRING'S CONTACT MODEL INTERACTION MODES	154
TABLE 6-1: CHAMBER AND INTERFACE FAILURE MODES AND MAXIMUM PRESSURE RATINGS (* ASSUMES THAT LOAD IS AT FULL BOLT DIAMETER WHICH IS A HIGHLY CONSERVATIVE ESTIMATE)	180
TABLE 0-1: NAVIER STOKES ASSUMPTIONS.....	199

List of Variables

<i>Variable</i>	<i>Unit</i>	<i>Description</i>
a_o	m	Initial Vertical Displacement
A_c	m ²	Cross Sectional Area
A_{obs}	m ²	Obstruction Area
$A_{critical}$	m ²	Critical Obstruction Area
API^o	-	Stock-Tank Oil Gravity
B_r	(kg m) / s ²	Bending Stiffness per Unit Area
B_w	(kg m ²) / s ²	Bending Stiffness per unit width
C	-	Buckling boundary conditions value
C_d	-	Drag Load Coeff
D_{bore}	m	Wellbore Diameter
$d_{bolthead}$	m	Bolt Head Diameter
d_{nom}	m	Nominal Bolt Diameter
dP	kg / (m s ²)	Pressure Differential
d_{pitch}	m	Bolt pitch diameter
d_w	m	Wire Diameter
e	m	Thickness of sand layer for Darcy's initial correlation
E	kg / (m s ²)	Young's Modulus
$E I$	(kg m ³) / s ²	Bending Stiffness
F_{cr}	(kg•m)/s ²	Critical buckling force
F_{clamp}	(kg•m)/s ²	Clamping force
F_x	(kg•m)/s ²	Radial tip load
F_y	(kg•m)/s ²	Axial tip load
g	m / s ²	Gravity
h	m	Height of Column for Darcy's initial correlation
I	m ⁴	Stiffness
k	m ²	Permeability
k_d	m ² /sec	Permeability Coefficient in Darcy's initial correlation
k_{yfy}	N/m	Buckling Stiffness
l_{lead}	m	Lead of a bolt
l_w	m	Length of exposed wire
L_{eff}	m	Effective length
L_p, L_{plug}	m	Plug Length
L	m	Length
m_a	kg/m ²	Mass per unit area of wire
P_{bore}	kg / (m s ²)	Pressure inside BOP wellbore
P_i	kg / (m s ²)	Interior Pressure
P_e	kg / (m s ²)	External Pressure
$P_{Machine}$	kg / (m s ²)	Internal Pressure of Wire Feeder
q	m ³ /sec	Volumetric flow rate
q_f	kg / (m s ²)	Distributive load
r_e	m	External Radius
r_i	m	Internal Radius
r_w	M	Radius of wire
R	m	Radius of BOP Bore
Re	-	Reynolds Number
s	m ²	Surface area for Darcy's initial experiment
t_{cap}	m	Cap Thickness of Flanges
T_R	F, °C	Reservoir Temperature
u_{max}	m/s	Maximum velocity of fluid flow

Variable	Unit	Description
u_y	m/s	Velocity of fluid in the axial direction
V	m/s	Stream Flow velocity
V_f, V_{Flow}	m/s	Fluid mean Velocity
V_r, V_{Feed}	m/s	Wire Feed Velocity
V_{Tot}	m ³	Total volume in the Plug Length
V_{voids}	m ³	Volume of voids
V_{Wire}	m ³	Volume of the wire in the entanglement region
\dot{V}_i	kg/s	Initial flow rate
\dot{V}	kg/s	Flow rate
w	m	Width of element
ΔP_{well}		Well Pressure
α	radians	Rake angle for extrusion, or pitch angle for bolts
μ	kg/ (m sec)	Dynamic viscosity
η	-	Safety Factor
η_c	-	Compaction Efficiency
ρ_f	kg/m ³	Fluid Density
θ	radians	Angle Rotation
ϕ	radians	Angle Azimuthal
Φ	-	Porosity
Γ_{pre}	N•m	Preload Torque on Bolts
λ	radians	Lead angle of threads
μ_i	-	Friction Coefficient Between two surfaces
γ	kg/m ³	Coefficient for correlating the effect of temperature on density
π_s	-	Non-Dimensional Stiffness Coefficient by Shelley for flag waving
π_e	-	Non-Dimensional Entanglement Stiffness (Stiffness per unit area/drag load)
π_w	-	Non-Dimensional Weight to Stiffness Ratio
π_v	-	Non-Dimensional Velocity
Δ	m	Wire tip deflection
u_o	m	Displacement function
ω	-	Non-Dimensional Loading Stiffness
ϵ_v	m ³ /sec	Error is Volumetric Flow Rate measurement
ϵ_L	m	Error in plug length measurement
$\epsilon_{\Delta P}$	N/m ²	Error in pressure measurement
ξ	Rad	Angle of exposure for buckling model

[Left Blank]

Chp 1.

Introduction

As the Deepwater Horizon accident of Spring/Summer 2010 demonstrated, accessing and plugging a damaged underwater oil pipe at depths greater than one kilometer poses a significant engineering challenge. Oil companies continue to plan more wells in deeper waters in order to meet market demand; this, combined with increasingly harsh well environments increases the likelihood of blowout preventer (BOP) failure (resulting in an uncontrolled flow). Therefore, the industry needs an improvement over existing technology to help mitigate the impact of a blowout. The costs associated with a blowout, both from an environmental and litigious standpoint, make it imperative to actively seek out solutions to the problem.

The central hypothesis of this thesis is to create a method and machine to complement existing mitigating capabilities, as recommended by the Deepwater Horizon report [1]. This thesis seeks to develop a machine that feeds a wire (i.e. continuous medium) into a wellbore to form a tangled mass that increasingly obstructs the flow of hydrocarbons in a controlled manner. It is hypothesized that feeding a wire (or ribbon) below the BOP would cause the wire to buckle and entangle inside the BOP, forming an ever growing “bird nest” that would gradually choke off the flow, as shown in Figure 1-1. The tangled mass occlusion (i.e. plug) anchors inside of the BOP on partially deployed rams, bends in the pipes, and other constrictions. Currently, there are four methods utilized in the industry to attempt to obstruct the flow in the event of a BOP failure, which are 1) junk shot, 2) top kill, and 3) drilling a relief well, and 4) capping.

The proposed system has three key advantages over existing methods: 1) minimal risk to the formation, 2) simplicity, and 3) rapid deployment time. The gradual closure of the well reduces the risk of transmitting a pressure shock into the formation that could potentially lead to an uncontrolled fracture. Furthermore, the implementation of this method does not require retrofitting existing BOP units as it can utilize existing ports. Thus, the simplicity of the design will have minimal impact on existing BOP units. Deployment time is shortened by having the technology available as part of a remotely operated underwater vehicle (ROV), delivered by an ROV, or by incorporating it into the BOP stack directly. Incorporating the wire feeding technology into an ROV that can be maneuvered in place to engage an existing BOP port, as illustrated in Figure 1-2, exploits the added versatility of the ROV. A second option is to design an ROV attachment which reduces the complexity of the overall machine at the expense of maneuverability. The third option is to introduce the wire feeding technology as an independent module for the BOP stack thus reducing the activation delay. However,

the cost associated with installing, testing, and maintenance of the integrated unit may deter this approach. As pointed out by Christopher Johnson (Engineering Director at National Oilwell Varco), the faster you respond the better, since a full blowout can endanger the rig crew. On the other hand, the versatility of the ROV unit and the ability to integrate with standard BOP ports makes this configuration desirable.

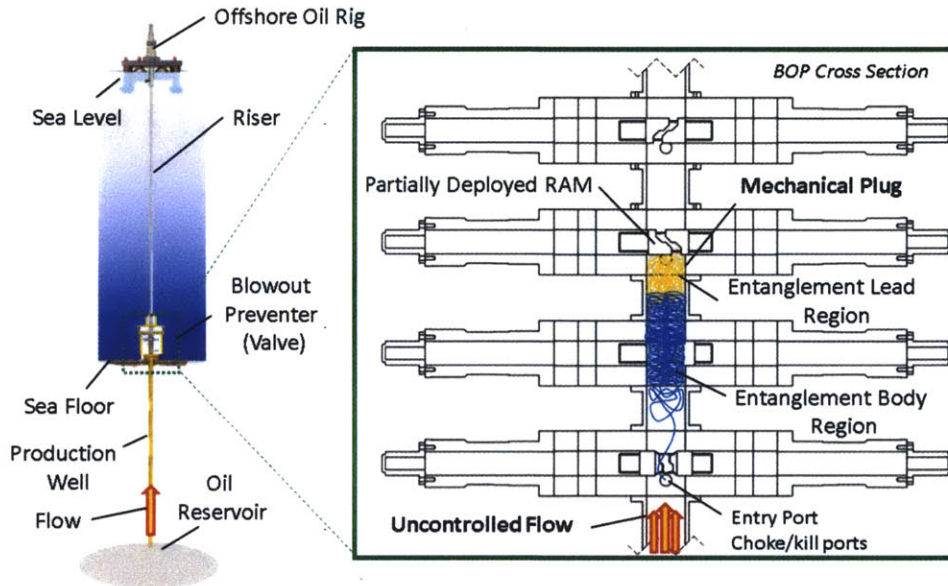


Figure 1-1: Mechanical plug generated inside BOP created by feeding a continuous medium via the existing choke/kill ports (The image on the left showing oil rig from Millheim – Early Reservoir Appraisal)

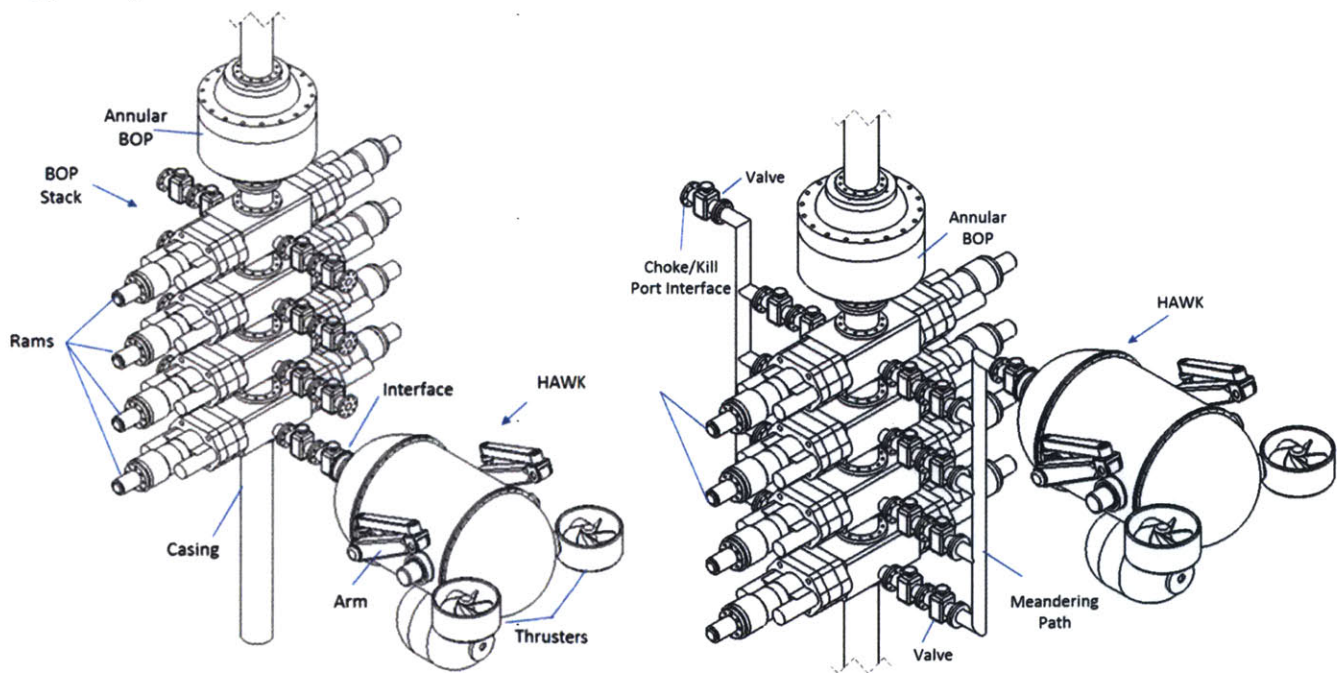


Figure 1-2: Hampering Active Wellbore Kit (HAWK) system incorporated into an ROV and connected in a direct and meandering path to the well bore.

1.1. Background

Control of the well is a crucial aspect of oilfield exploration and production. Devices must be installed to prevent injury or damage to the environment, rig personnel, and drilling equipment. One of the most common well control devices is the Blowout Preventer (BOP), which is generally used to seal a wellbore either temporarily or permanently. Although there are redundancies in the system, sometimes a BOP assembly malfunctions resulting in a blowout and subsequent uncontrolled release of oil/gas into the surrounding environment.

For the extraction of hydrocarbons to take place, a flow channel must be established between the reservoir and the production platform. The open hole (i.e. channel) is created by drilling through a series of geologic layers each consisting of a specific composition (limestone, shale, sandstone, etc.). The equilibrium pressure (formation pressure) increases with increasing depth and can differ drastically among layers due to trapped or embedded fluids/gases. Penetrating from one geologic layer to the next during the drilling process can result in a spike in formation pressure, which can lead to a blowout. One way to mitigate this risk is to increase the pressure in the wellbore to balance the formation pressure using drilling mud of an appropriate density; this serves as a primary defense to protect the well against blowouts given that the adequate density of the drilling column is sufficient to prevent formation fluids/gases from entering the borehole (wellbore). However, the well pressure should not exceed the formation pressure, as it could introduce drilling mud into the formation, thus damaging the well in a process known as "killing the well" [2]. Occasionally there is a large pressure gradient across a layer in the formation; when a substantially high pressure interacts with the well (known as a "kick" on the well) an influx of formation fluids (liquids, gas, etc.) enters the well [3, 4]. The pressure wave can propagate from the point of origin (highest pressure) through the wellbore, across the wellhead, BOP (medium pressure), and to the surface (lowest pressure). At the surface, this pressure spike can have catastrophic repercussions to the drilling rig, equipment, and personnel. Blowout preventers are used to control the well and dampen the transmission of such a pressure spike, effectively reducing inherent risks by controlling the effects of the kick.

BOP's are usually installed at the surface of a well or on the sea floor, to mitigate or filter out pressure spikes that can lead to blowout (uncontrolled flow) or, in the case of a catastrophic failure, to close the well. While there are several styles of BOP configurations, there are only two types of BOP components: annular and ram type as shown in Figure 1-3. Annular BOPs consist of a doughnut-shaped elastomer that is squeezed against the drill pipe and housing to seal off the well. Ram BOPs consist of mirroring plungers that are hydraulically pushed together in the middle of the wellbore. There are also several sub-types within ram style components, which include: 1) pipe rams, 2) blind rams, and 3) shear rams. Pipe rams can seal around wellbore tubulars (drilling tools, measurement devices, etc.) that may be within the BOP's vertical bore. Two semicircular opposing pipe rams can be activated to seal the annulus between the drilling tool and wellbore. Blind rams are used when there is no obstacle in the BOP's bore. Similar to pipe rams, two mating blind rams are typically used to completely seal the wellbore cross section. Shear rams are usually the last resort for

preventing/containing a kick that may cause a blowout. Normally there are two shear rams installed to ensure that the thicker coupling (10% of casing string length) joining two sections of casing will be not be in contact with at least one shear ram [5]. A pair of opposing shear blades engage from either side of the BOP vertical bore to cut through material in the well, and ultimately seal the wellbore [6]. The forces required to shear the a casing inside of the wellbore can be significant. For example, a P-110 grade casing (yield strength 758 MPa) can require in the order of 5×10^6 N of force to shear a casing with an outer diameter of 40.6 cm (16 inches) and inner diameter of 38.1 cm (15 inches).

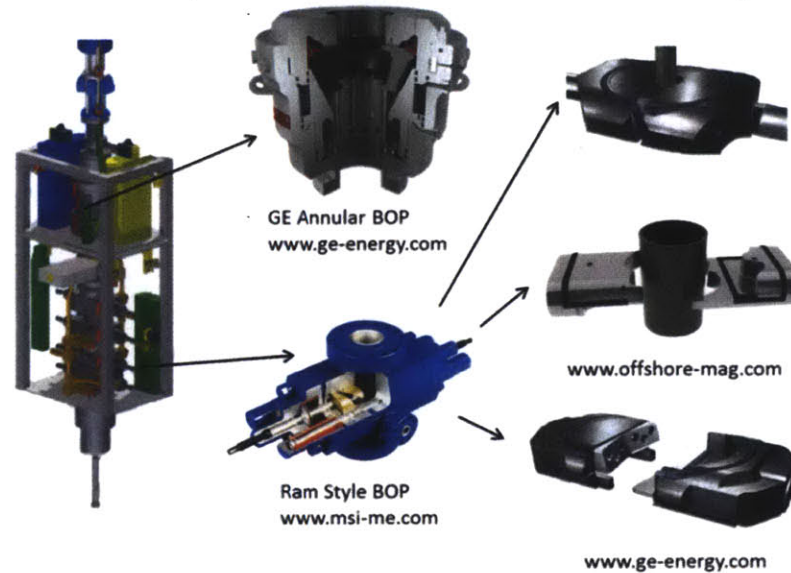


Figure 1-3: Blowout preventer stack components annular and ram style (The image on the left showing oil rig from Millheim – Early Reservoir Appraisal)

Ensuring activation of existing BOPs require frequent monitoring and maintenance. Elastomer seals must be checked between each installation (properly maintained BOPs can be used multiple times) to ensure that the elastomer has not been worn, damaged, or deformed. Furthermore, seals should be replaced every 12-18 months and the whole unit needs to undergo recertification every 3-5 years depending on company or government requirements [7]. Rams must also be inspected and may have to be changed if worn or damaged. Even with continuous maintenance and inspections a BOP can still fail; one current solution in high-risk wells is to use two BOP stacks in series, which is costly and bears others risks.

Aside from capping and drilling a relief well, there are currently two solutions implemented for mitigating the effects of a failed BOP: top kill and junk shot. When a BOP fails, the primary short-term recourse is to attempt to feed heavy drill mud into the wellbore, referred to as top kill. The junk shot approach consists of feeding particulates in with the drill mud that work as a bridging agent to fill in gaps where hydrocarbons are leaking [8, 9]. The implementation of a junk shot requires at least one surface drilling vessel and one ship carrying the mud and feeding material that will be introduced into the wellbore [10]. However, this junk shot approach can have negative repercussions. For example, a sudden stop in the flow from the clogging effect of a junk shot can create a pressure wave that can burst casing components or fracture the reservoir leading to further, even more intense, uncontrolled release of hydrocarbons. An uncontrolled rupture in the casing or formation can lead to a catastrophic

leak to the environment over a wide dispersal area. While the junk shot technique was used to stop wells in Kuwait during the 1991 Gulf War, junk shots have never been used or tested for the offshore industry deepwater wells like the Macondo Canyon [5].

The more-long term solutions are drilling a relief well and capping, but the response time can be significant. Drilling relief well to intersect the original well can take on the order of months to complete, during which time the well continues to release hydrocarbons into the environment. The purpose of the relief well is to access the location where the pressure control was lost and to pump concrete into the leaking well in order to seal the high-pressure region. The capping solutions are covered more thoroughly in the prior art section. In essence, there is a need to rapidly control a deepwater oil well in the event of an unforeseen blowout preventer failure.

1.2. Existing Response Time

As summarized by the International Association of Oil & Gas Producers (OGP) the duration between a well incident and when a containment system is connected and functioning can range from one to ten weeks [11]. The estimated response time for capping is calculated between one and four weeks. In order to establish a containment system the response time can be between four and six weeks. As shown in Figure 1-4, possible response times can extend from four to ten weeks to achieve the closure of a leaking well. Based on these response times, the industry needs an improved short-term solution that can rapidly close off or significantly obstruct uncontrolled flow through a damaged BOP without negative side effects.

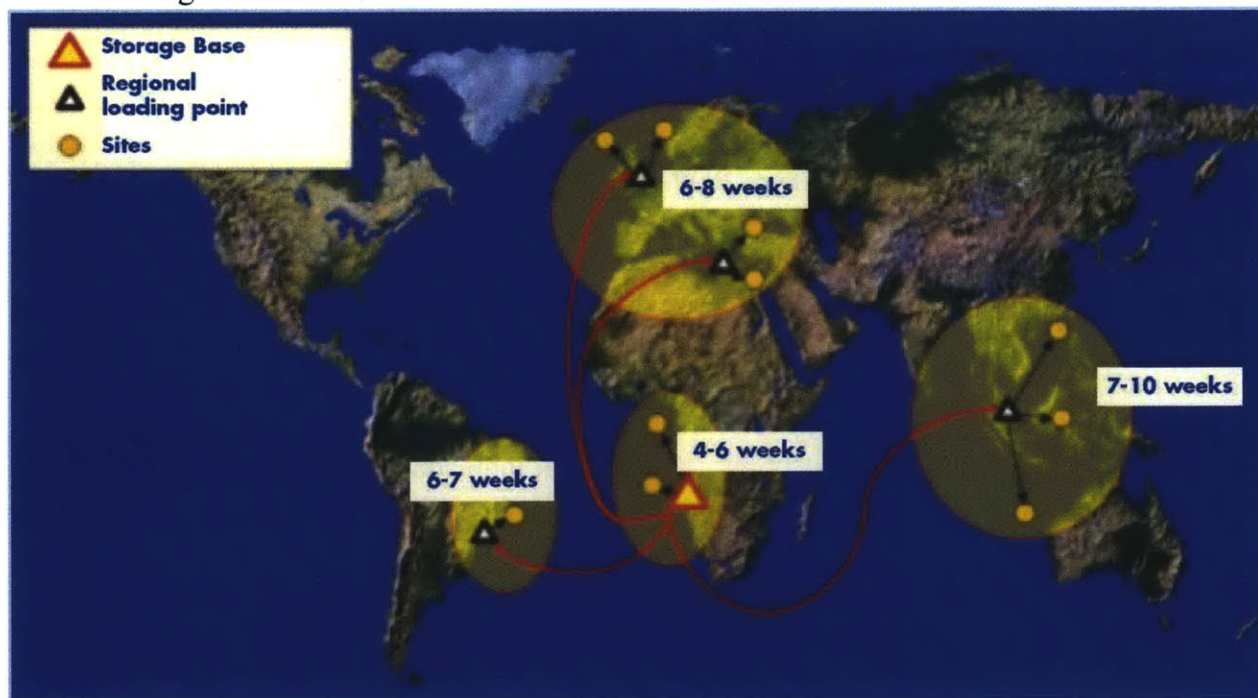


Figure 1-4: Possible response times from the International Association of Oil & Gas Producers – Capping and Containment

1.3. Motivation

Deepwater drilling currently generates approximately 10 percent of worldwide oil production [5]; the number of rigs capable of drilling at depths greater than 1.5 km (5,000 ft) has been increasing dramatically. In the US alone roughly 30 percent of domestic oil production is from deepwater offshore platforms [5]. At the turn of the century, the offshore oil production was 22 percent of the total oil production, with only one percent overall coming from deepwater wells. By 2010, the offshore production rose to 33 percent with 7 percent from deepwater wells [12]. The occurrence of a blowout in a production well is not uncommon. During the ten year period between 1996 and 2006, there were thirty-nine oil well blowouts; as reported by the Minerals Management Service, which has subsequently been divided into two groups, with eighteen of those accidents attributed to cement failures [13].

In the past thirty-three years, three of the top five oil spills were attributed to blowouts [14, 15]. In total, the sum of these blowouts released an estimated 11.7 million barrels of crude oil into the surrounding environment. By comparison the Deepwater Horizon accident released 5.1 million barrels of hydrocarbons. The concern with a damaged BOP is the continual release of hydrocarbons from the formation until repairs are carried forth. Oil released to the environment due to blowouts constitutes twenty nine percent of the top twenty oil spill accidents. The oil released from the Deepwater Horizon's failed BOP dumped about five million barrels into the ocean, at an estimated rate of 60,000 barrels per day, which alone accounts for approximately ten percent of the twenty largest oil spill accidents [1, 16]. Admittedly, the tanker collision between the Atlantic Express and the Aegean Captain in 1979 released a total of ~2.1 million barrels of crude oil; however, there was no risk of continuous release of hydrocarbons as a result of that accident because the tankers carried a finite, albeit substantial, amount of material. Unlike tanker collisions, a failed BOP can lead to the full depletion of an oil reservoir. While future BOP accidents are perceived as unlikely, in the two years since the Deepwater Horizon oil spill, there has been at least one instance, in Brazil, where the probability for another major oil spill was high due a failed blowout preventer [17-19]. As recent as July 24, 2013 another blowout caused the destruction of a natural gas oil rig in the Gulf of Mexico [20].

Currently, several organizations take a remediation approach when addressing the impact of a failed blowout preventer. The Deepwater Horizon accident led to the development of several companies that provide well containment and post-spill cleanup equipment. In July 2010 the Marine Well Containment Company (MWCC) was created as a joint venture between ExxonMobil, Chevron, ConocoPhillips, and Shell to upgrade well containment capabilities; however, despite its goals, the MWCC does not develop new technology for application in industry [21]. Therefore, only existing cap and ram style systems are being examined by MWCC as solutions to address the next deepwater blowout. Another recently created venture is the Oil Spill Prevention and Response Advisory Group (OSPRAG) by *Oil & Gas UK*, which in addition to training and safety preparation also deploys hardware to collect spilled oil and BOP closing units (i.e. caps) in the case of offshore uncontrolled flow [22]. A third group which was recently created is *DeepStar* whose objective is to identify gaps in existing preventative technologies and develop new equipment [23]. Admittedly, effective implementation of legislation may have been able to prevent the series of events that led to an

uncontrolled flow in Macondo. However, accidents will continue to occur because one cannot foresee every possible scenario of operation. The report *Lessons Learned from the Deepwater Horizon Blowout* recommends that advances be made in the "BOP technology from the perspective of overall system safety" [1]. While minimizing risks through legislation and inspections reduces the likelihood of accidents, no efforts are currently underway to improve existing well stabilization technology or help turn off a blown-out well. This in part is due to lobbying by special interest groups that make passing safety legislation related to the oil industry an arduous process. As such new safety technologies are not made mandatory and ultimately lead to increased cost of production. For example, in Norway and Brazil proposals were made to implement a backup activation unit that could detect an acoustic pulse in the water (prelude to a blowout) and activate the rams; however, the oil industry in these countries effectively lobbied against the implementation of such a safeguard and the proposal was abandoned [5].

The resistance to incorporate additional safety measures often comes down to an issue with the associated cost cutting into production profits. While costs associated with a full uncontrolled blowout are greater than implementing additional safety components, most oil companies choose to develop technologies to minimize/prevent the risk of a blowout from occurring. For example, shortly after the Deepwater Horizon accident British Petroleum pledged to create a \$20 billion fund for damage claims [24]. As of February 2013, the Deepwater accident has cost BP ~ 42.2 billion [25]. According to the Clean Water Act Section 311 the maximum fine per barrel is \$1,100 in the "absence of gross negligence" [26, 27]. In the case of negligence, the maximum fine can increase to as high as \$4,300 per barrel. Furthermore, at least in the case of BP, the fines and penalties imposed by the courts are not covered by the "trust fund" [27]. This means that a well leaking 60,000 barrels per day is costing an oil company \$764 USD per second in fines alone, assuming no negligence; this rate increases to \$2,984 USD per second, if the accident occurred due to gross negligence resulted in the accident occurring. An uncontrolled well releasing crude oil for 7.5 hours (the length of an average workday) costs twenty million dollars in fines; this is approximately the total cost of developing a new technology in the oil industry. Thus, any backup blowout safety tool must be able to close the well faster than existing systems and within by the 7.5 hour mark to justify the initial investment.

Over the next five years, the number of offshore locations where subsea BOPs used is estimated to increase from around a dozen regions (mainly the Gulf of Mexico, Brazil, the Mediterranean, West Africa, and Australia) to approximately thirty-four, with the largest increase being off the coast of West Africa [11]. The question is not when or where the next offshore deepwater blowout will take place, but whether tools will be available to bring the well under control within a short time frame.

1.4. Thesis Scope

The work presented shows the development of the proposed technology from the experimental stage to the generation of a proof of concept prototype. The approach taken to develop the occlusion-generating machine for the oil industry is to first perform a series of small-scale experiments in order to identify key parameters. These bench-level experiments will serve to guide the creation of an analytical model for wire entanglement that can then be validated using data collected from a scaled-model experimental prototype. The research is divided into three phases: 1) preliminary experiments on wire entanglement behavior: anchoring and sealing, 2) development and testing of a prototype machine; and 3) factoring system design based upon operating conditions and industry requirements.

The focus of the experiments is to identify the critical parameters required to generate an entanglement within in a free flowing conduit in order to bring a flow under control. The preliminary experiments establish feasibility of all components independently, as illustrated in Figure 1-5. The first part in developing the proposed technology requires a better understanding of the physics of wire entanglement. At present, the relationship between the critical parameters of the wire (stiffness, geometry, feed velocity, etc.) that lead to wire entanglement given the environmental conditions (flow rate, viscosity, operating pressure) is unclear. The focus of the experiments is to identify the critical parameters necessary to generate an entanglement in a free flowing conduit. For example, a non-dimensional stiffness of the wire may be the most dominant factor leading to entanglement as it directly affects the ability of the wire to be molded and bent. However, there are several other parameters that could be used to promote or deter entanglement, such as: feed to flow velocity ratio, entry angles, Reynolds number, surface roughness, and geometric features. The second part of the preliminary experiments is to demonstrate that the generated entanglement can be used as scaffolding supported on the partially deployed RAMs. The entanglement is responsible for anchoring against the existing obstruction and transferring the axial load to the supporting structure. The third part consists of determining the sealing potential of the mechanical plug. An array of permeability experiments is used to quantify the permeability of the wire plug as a function of the total length of wire introduced, type of wire, and compaction. The data collected from the permeability experiments will be used to create a model for flow through a continuous entanglement medium based on the Darcy Equation for flow through porous media. The permeability of the plug is calculated by measuring the pressure and flow rate in a known geometry before and after introduction of the plug. The calculated values can be compared to existing flow models through porous media (i.e. packed spheres, fibrous beds, etc.). Determining compaction due to the flow forces will be done experimentally as well. The theoretical values for the pressure differential are calculated for a given wire length and geometry of the plug; however, the flow stream may not be able to compact the wire above a certain threshold. Therefore, further experimentation related to compaction by flow is required to determine feasible compaction at full scale.

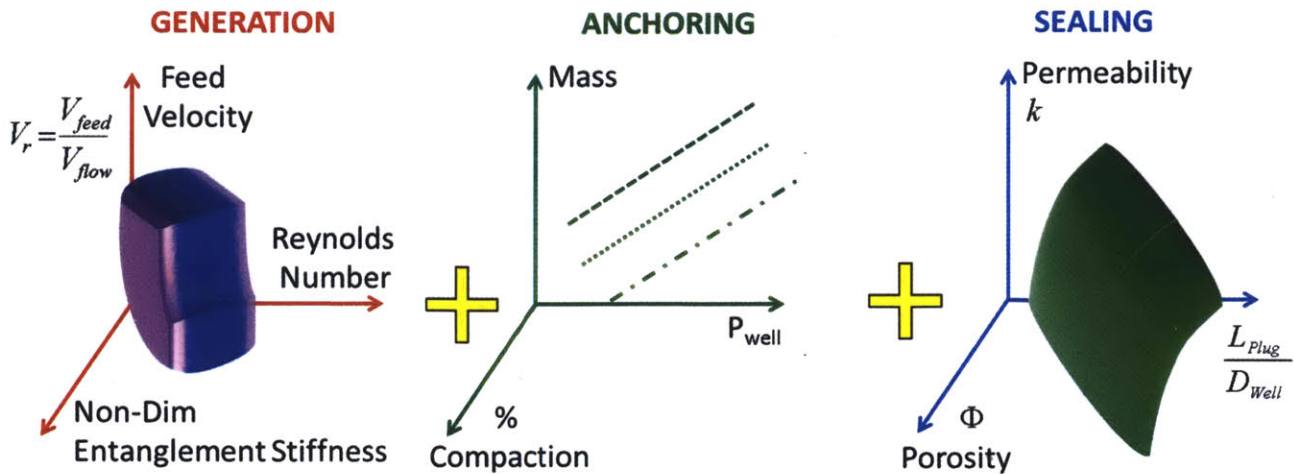


Figure 1-5: Preliminary experiment subsection: generation, anchoring, and sealing. Process for finding the operating parameters.

Phase two is the development of a scaled functional prototype based on the preliminary experiments. The design includes structural analysis, failure modes, manufacturability, and dynamics required to generate a mechanical plug in a free flowing stream. Many other options will later be developed, but the intent here is to show how the fundamental results and knowledge obtained from these experiments can be used to guide the design of the HAWK prototype and later for a scaled version.

Lastly, the third phase entails obtaining feedback from industry leaders to develop an approach that is feasible given industry considerations. Scaling parameters are also considered throughout the process to develop a machine that will work given the operating conditions. The sum of this work is the development of a method and machine to create an occlusion inside the BOP that can control a free flowing well, as rapidly as possible, in the event of a full blowout.

1.5. Functional Requirements

The overall goal is to develop a system that in a controlled manner creates a mechanical plug inside of a failed BOP by continually feeding a “wire” into the well below the BOP rams to slowly increase the well resistance and bring the flow under control. The machine must be evaluated by the drill rig safety operations specialist to ensure that it does not endanger people’s lives, lead to further environmental damage, or create additional damage to the BOP structure and assets. The system must also be simple enough so that it can be a standard feature on new BOP's and easily retrofitted onto current BOP models. Further, it must be accessible via remote access. The proposed system should not increase the risk of an even larger well failure and should not inhibit any existing remediation approaches. Table 1-1 is a summary of the functional requirements and design considerations used to guide the development of this work.

Table 1-1: Functional requirements and design considerations

Functional Requirements			Design Considerations	
	Parameter	Value		
1.	Working Depth	3.5 km > Depth > 1 km	1.	Minimize time to delivery to 2/3 days
2.	Working Pressure	6.89 MPa – 103.4 MPa (1-15 ksi gauge)	2.	Minimize risk to formation by implementing a gradual flow reduction to minimize pressure waves generated
3.	Fluid Temperature	< 150° C	3.	Develop entanglement inside BOP wellbore used to determine the critical parameters
4.	Access to BOP Bore	Choke/Kill lines 7.6 cm (3 inch) ID	4.	Quantify plug efficiency by comparing unrestricted flow rate to obstructed conditions
5.	Bore Diameter	47.3 cm (18.625 inch) wellbore diameter	5.	Design for scaling and manufacturing to reduce costs
6.	Flow rate	184 L/sec (max) 110 L/sec (avg) (100,000 bbl/day (max) 60,000 bbl/day (avg))	6.	Evaluate possible plug removal methods
7.	BOP effective height	10-15 diameters (max)		

Chp 2.

Prior Art

The concept of inhibiting a flow by introducing an occlusion has been used in multiple different disciplines over the years. For example, in medicine one for treating aneurysms (berry or other) in the Circle of Willis, is via a technique that feeds discrete wire coils into the affected blood vessel, as shown in Figure 2-1 [28]. The wire is delivered to the aneurysm site via a catheter and struts are used to anchor the wire coil tower in the aneurysm site. This approach of placing discrete wires within a basilar tip aneurysm is analogous to a junk shot delivery approach for well sealing. While existing occlusion generating mechanisms exist, they are not designed to withstand high pressures (physiologic pressure encountered in treatment of brain aneurysms typically fall between 1.9 to 3.8 psi or 100 and 200 mmHg).

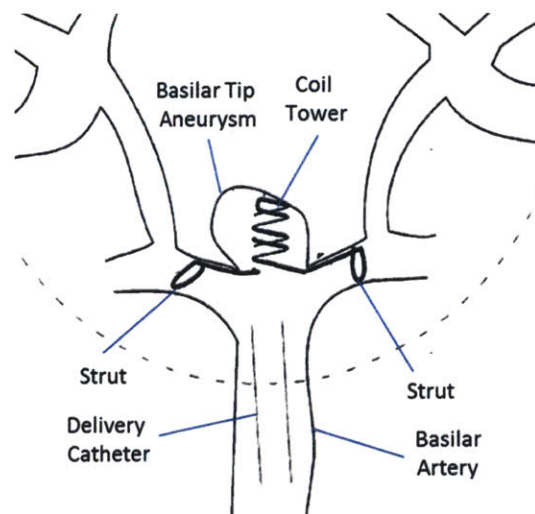


Figure 2-1: Insertion of wire coil tower into basilar tip aneurysm where it promotes the generation of a thrombus (blood clot) (U.S. Pat. No. 6,183,495 B1)

Designing a prototype machine to feed wire into an oil wellbore to generate an occlusion that can block high pressures requires an evaluation of existing technology related to the different aspects of the machine; this will help constrain the design space for the new technology and guide the design process. Topics related to wire feeding machines for subsea oil production include: 1) blowout preventers, 2) wire feeders, 3) wire buckling, 4) axially moving structures with fluid structure

interactions, 5) spontaneous knotting, 6) flow through porous media, and 7) wellbore post clogging procedures. A deterministic breakdown of prior art, with subsections, is illustrated in Figure 2-2.

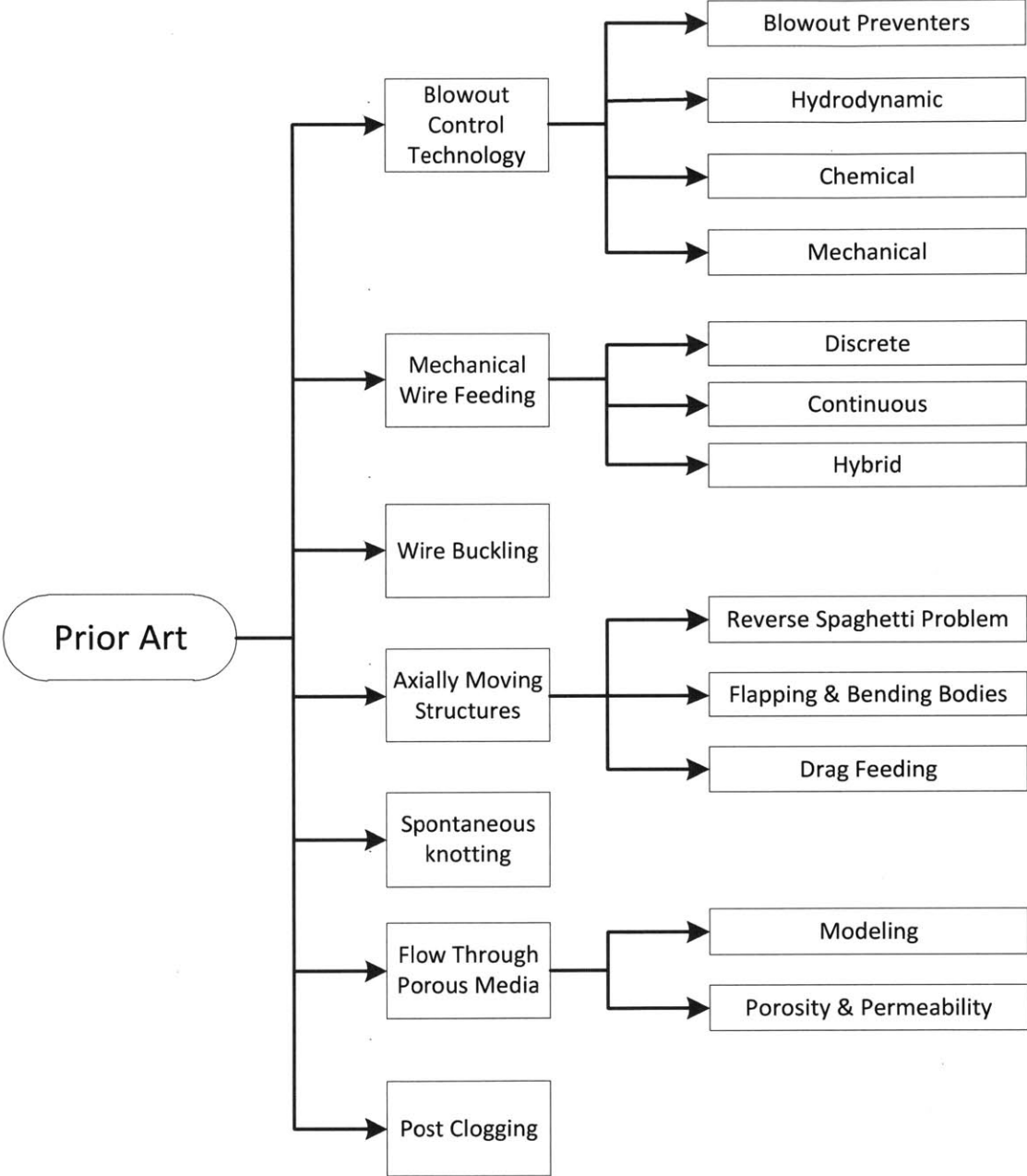


Figure 2-2: Prior art flow chart which deterministically identifies areas contributing to the design space.

2.1. Blowout Control Technology

Conventional approaches to blowout prevention in a well rely upon the successful activation of the blowout preventer (BOP). Yet, there are circumstances when the blowout preventer fails to adequately activate leading to an uncontrolled flow of hydrocarbons. The main causes of BOP activation failure include: 1) loss of power, 2) material degradation, and 3) jamming of the rams. While, blowout preventers are the primary technology for well control, there are alternative approaches to close off an uncontrolled flow through a damaged BOP. These alternative approaches fall under three areas: hydrodynamic, chemical, and mechanical.

2.1.1. Blowout preventers

A subsea BOP assembly is comprised of two structural sub-assemblies, the BOP stack and the lower marine riser package (LMRP), as shown in Figure 2-3. In the case of an emergency, the LMRP is disconnected from the BOP stack and allowed to move away, assuming that the rams in the BOP stack have sealed the well prior to disengagement. Disengaging the LMRP from the BOP stack is necessary to ensure that the oil platform is not transmitting forces to the BOP stack, potentially bending the casing below the BOP. The BOP is also equipped with two onsite control pods whose purpose is to activate the shear rams in an emergency and disconnect the LMRP from the BOP stack.

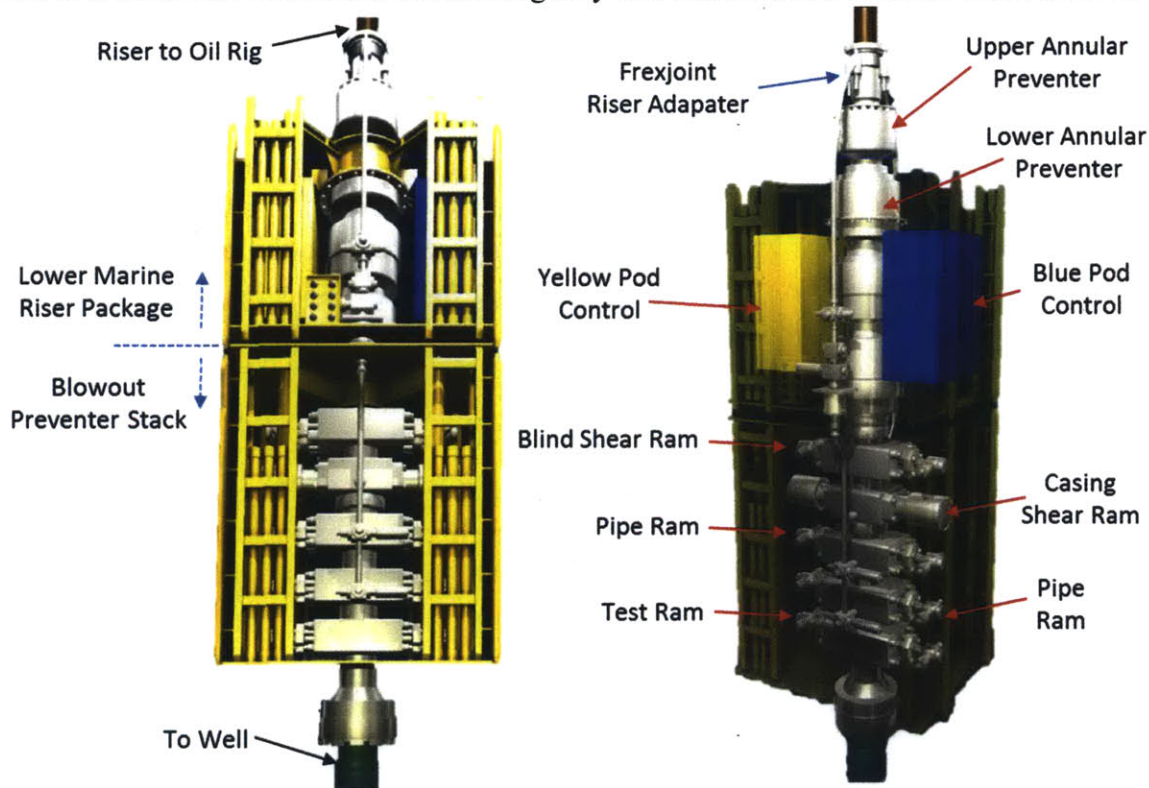


Figure 2-3: Deepwater Horizon BOP assembly (Source: Chief Counsel Report - Trial Graphix) [29]

The LMRP has nominally two annular BOPs, comprised of elastomer rings used to close the annulus between the wellbore and any tubing/casing that may be within the wellbore at the time of the kick. The BOP stack houses a series of ram style BOPs (usually four) two pipe rams of different

diameters (standard tool diameters) and two blind shear rams. An uncontrolled flow of hydrocarbons occurs when all of the BOP components fail to control the flow.

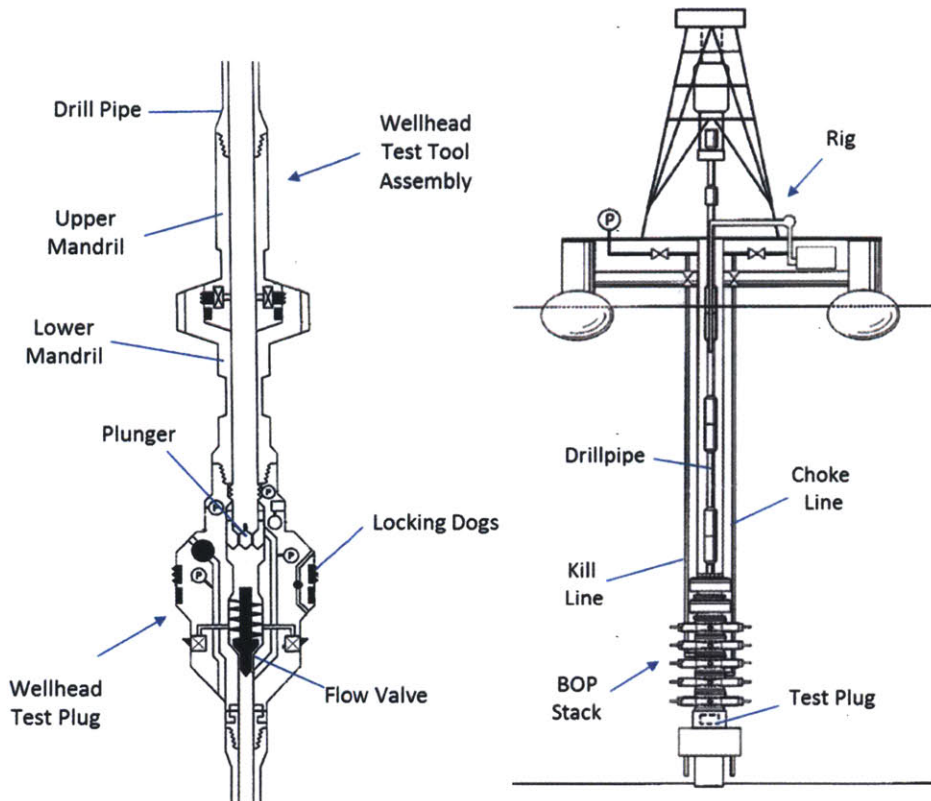
Since BOPs are the primary control method for blowouts, there are continuous improvements being made to BOP technology to increase safety and reliability. At the system level, improvements include having activation redundancies, and full unit testing. At the component level, improvements are also being made to predict failure and develop improved components for ram enclosures, elastomer seals, and shear ram blades.

2.1.1.1. System Redundancy

Backup systems are implemented to ensure that the BOP deploys when needed. In some configurations several blowout preventers are put in series; however, the cost associated with additional BOP components makes this approach unfavorable for companies focused on profit. Therefore, the industry has adopted the practice of trying to ensure that a single BOP stack is sufficiently reliable. As mentioned earlier, one potential failure mode is power loss to the BOP stack. An industry solution for power loss to surface wells is implementation of a secondary power unit that can engage the rams when the primary power conduit fails [30]. Currently, some BOPs used in subsea oil production can rely on supply signals and activation power from drill rigs at sea level. The current power redundancy for these systems is a set of batteries incorporated into the LMRP, which may prove insufficient given that power signals can fail to trigger the shear rams [7, 31]. Thus, an independent power source is required for any new technology.

2.1.1.2. Full System Testing

While in operation the BOP assembly can be tested to ensure all of the components are up to standard. This testing consists of lowering a wellhead tool assembly into the wellbore below the BOP stack and isolating the formation from the BOP assembly, as shown in U.S. Pat. No. 7,062,960 B2 (*Couren et al.*) and No.7,706,980 B2 (*Winters et al.*), each illustrated in Figure 2-4 [32, 33]. *Couren et al's* patent shows a detailed wellhead tool assembly with a test plug that allows the BOP assembly to be isolated from the formation, which is then used to create a simulated kick to test BOP components. *Winter et al's* patent illustrates the infrastructure required to test a BOP stack on the sea floor and implements a similar isolation unit. While the benefits of executing a full system test are significant, the costs are commensurate. In this instance, estimating the lifetime of system components is essential to reducing cost and effectively utilizing trial tooling so that the minimum number of tests are required.



A) Couren et al. (U.S. Pat. No. 7,062,960 B2) B) Winters et al. (U.S. Pat. No. 7,706,980 B2)

Figure 2-4: BOP stack testing units. The unit described by *Couren et al's* patent is the tool that is lowered into the BOP wellbore where it is used to simulate a pressure spike inside the BOP. The unit described by *Winter et al's* patent goes over the infrastructure required to execute the full system test.

2.1.1.3. Ram Enclosure

At the component level, improvements in modeling, maintenance, and development of new control methods are being made to ram assemblies to ensure successful deployment.

Finite Element Analysis (FEA) is used to improve rams by identifying and strengthening regions where stress concentrations are predicted to develop. BOP rams are modeled to identify stress concentrations and perform fatigue analysis [34]. FEA has also been used to selectively reinforce the regions of high stress in ram blowout preventers [35]. One benefit of using finite element analysis, especially multiphysics FEA, is the ability to model varying types load types including; thermal loads, pressurized loading, and acoustic vibration. While a design may satisfy each load independently, the interaction between the loads can lead to failure. The accuracy of the finite element models can only be accurate if an appropriate model is developed that factors all necessary loading parameters. Experimental analysis should always be performed to help develop an intuitive understanding of the fundamental physics involved and, more importantly, to validate or identify areas where the model is lacking. In conjunction with initial analysis, finite element modeling was used in the development of the Cameron EVO (deepwater BOP stack rated for 137.9 MPa (20 ksi) subsea wells), results of which were validated experimentally [36].

As shown in several patents improvements to existing technologies, like locking mechanisms, energizing rams and rail seal actuators have been implemented recently to further improve BOPs. For example, U.S. Pat. No 6,554,247 describes a bonnet lock mechanism using a radial lock with at least one lock actuator [37]. The new bonnet lock mechanism allows for access to the interior of the BOP body using a set of sliders with a mounting system as shown in Figure 2-5.

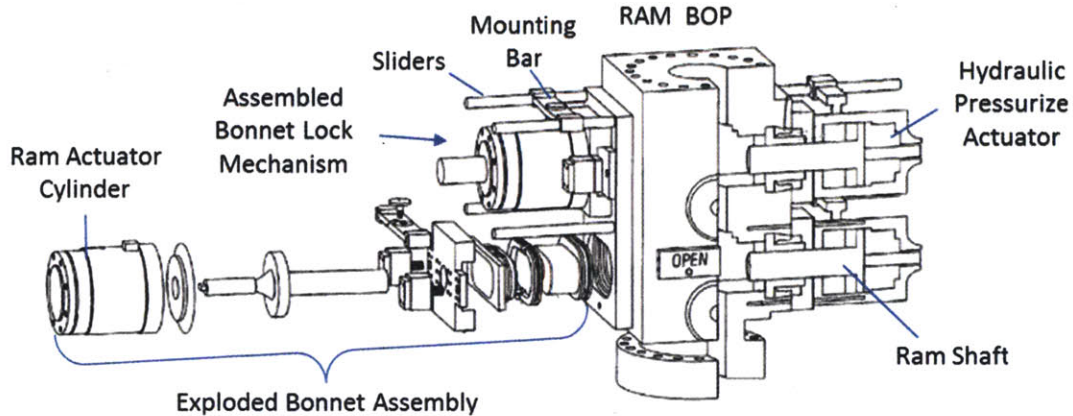


Figure 2-5: Bonnet lock mechanism with radial lock (U.S. Pat. No. 6,554,247)

Other improvements to ram assemblies include the development of an electromagnetic control system with minimal moving parts. The proposed solution, U.S. Pat. No. 2011/0297394 A1, seeks to minimize the moving part count within a ram style BOP. This is achieved through the use of magnets in conjunction with magnetic particulates in the drill mud to prevent a kick from causing a blowout [38]. This approach attempts to control the flow of hydrocarbons through use of a “magnetically pluggable fluid” (magnetorheological fluid). The magnetic field established in the wellbore is used to “solidify” the magnetorheological fluid into a plug that can be strengthened using a mechanical piston assembly which decreases the distance between the magnets, as shown in Figure 2-6. For existing units that do not have the proposed magnetic ram system, it has been proposed that this can be “jury-rigged” by inserting the magnetic fluid into the well and placing solenoids around the casing to induce a magnetic field thus activating the fluid and sealing the wellbore. The implementation of the electromechanical BOP will depend greatly on the density of the magnetic particles in the drill mud, which will determine the amount of power required to generate the plug in the given area. The proposed method also has the added complications of needing a core cooling conduit and requiring continuous power, which cannot be effectively supplied by battery-powered backup units.

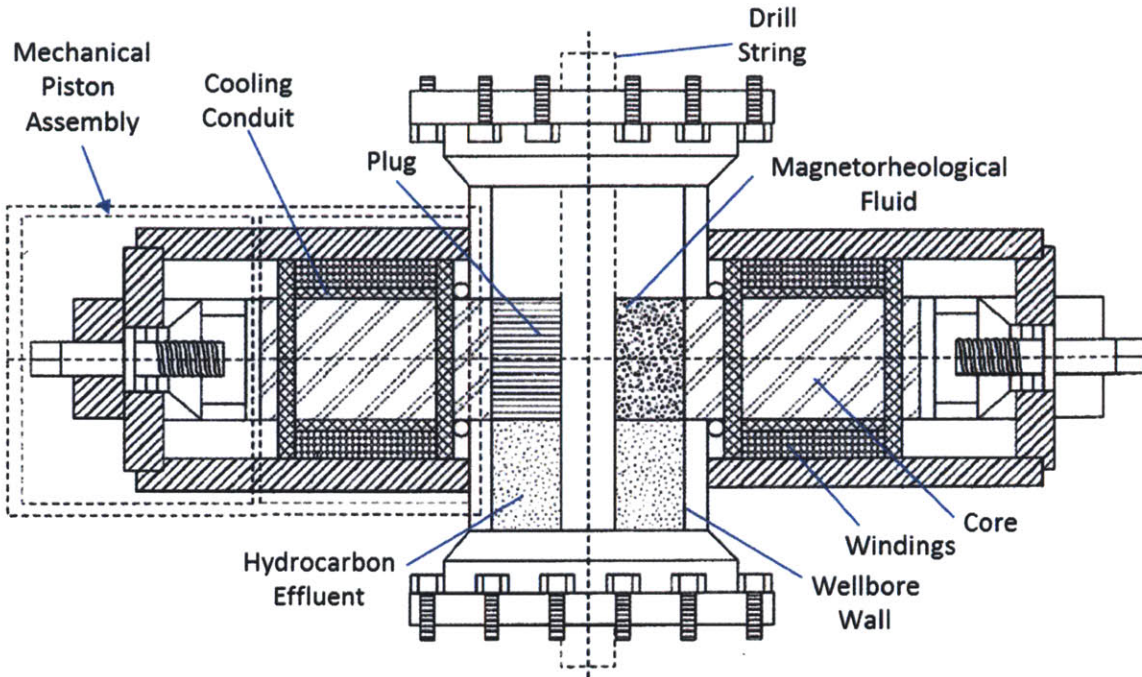
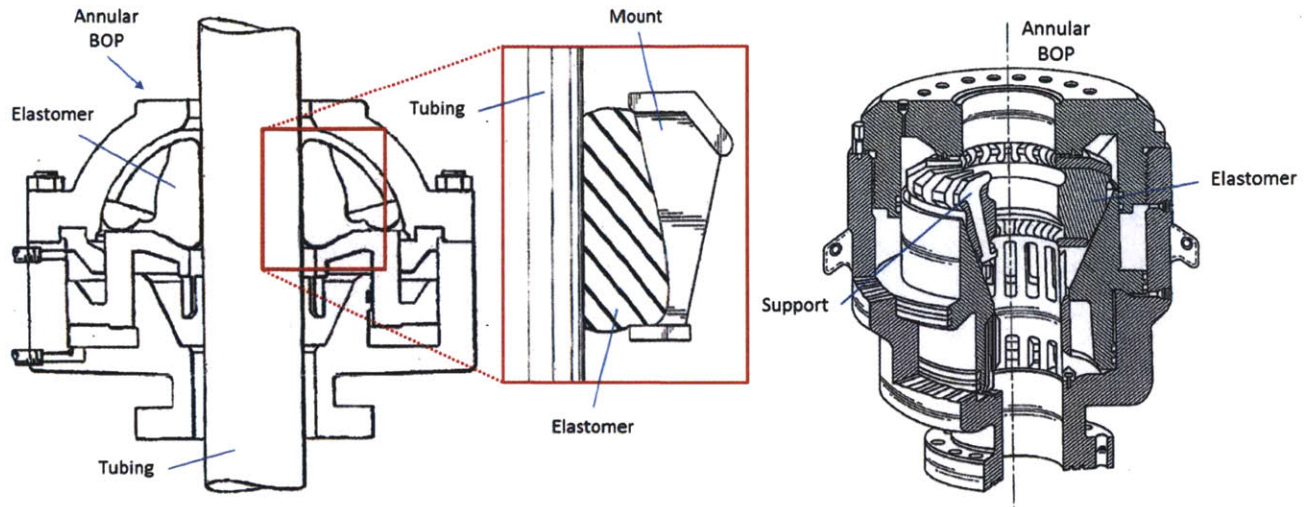


Figure 2-6: Magnetorheological blowout preventer (U.S. Pat. No. 2011/0297374 A1)

2.1.1.4. Elastomer Development

There are several areas within a BOP assembly in which elastomers are used including the annular ring, O-ring seals, etc. However, due to harsh operating conditions these components may deteriorate over time and thus require inspection during use and require replacement of potentially damaged parts. One way to ensure elastomer reliability is to determine how frequently replacement may be required. This is accomplished by modeling the loading and environmental factors that can lead to failure. In cases where replacement frequency is deemed too frequent, improvements can be made during the design process, including strengthening of high stress regions and development of more wear resistant materials.

Finite element analysis is used to identify areas prone to failure in seals due to temperature, wear, and loading. For example, finite element models have been used to produce strain plots of seals essential to identifying strain concentrations that may lead to failure [39, 40]. As shown in Figure 2-7, elastomer seals in an annular BOP press against a pipe or casing in the wellbore, which deforms the elastomer. The pipe/casing imparts a shear loading on the elastomer seal that can lead to wear and eventual failure to bring a well under control [41].



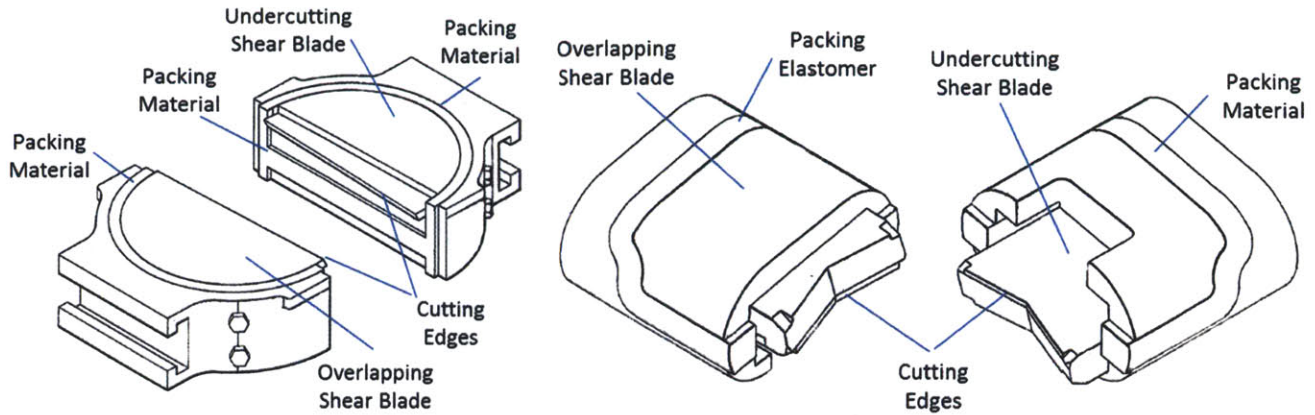
A) Khandoker (U.S. Pat. No. 2008/0027693 A1) B) Butuc (U.S. Pat. No.2010/0140516 A1)

Figure 2-7: Annular BOP elastomer seal finite element analysis

Improvements to materials have been made by controlling the manufacturing process and by developing new techniques that enable seals to withstand the harsh conditions of the BOP environment [40]. U.S. Pat. No. 2010/0140516A1 discloses the use of electron beam radiation to increase the density of crosslinks in BOP seals [40]. Another method proposed, U.S. Pat. No 2012/0000644, is to create a fluorocarbon layer on the surfaces of the nitriles to protect against micro-cracks, thus improving wear resistance and providing “better retention of tensile [stress] and elongations” [42].

2.1.1.5. Shear Blade Obstruction

The primary purpose of the ram shear blade is to cut drill string, casing, and anything else that may be inside the wellbore at the time of a blowout. Some ram shear blades have the dual function of both shearing and sealing the hydrocarbons in the formation. One of the earlier patents (*Nicolson's* 1959 patent U.S. Pat. No. 2,919,111), illustrated in Figure 2-8, illustrates a design consisting of a scissor like mechanism [43]. Gradually, the technology has morphed from a straight design to one in which a V-shape centers in the cutting tube as part of the cutting process. The thickness of the blades has also increased to compensate for the need to seal under higher pressures as shown in U.S. Pat. No. 4,347,898 (Jones) [44]. *Jones' patent* also discloses the use of a seal between the faces of the shear (not shown in illustration) in order to further seal any gaps between the blades.

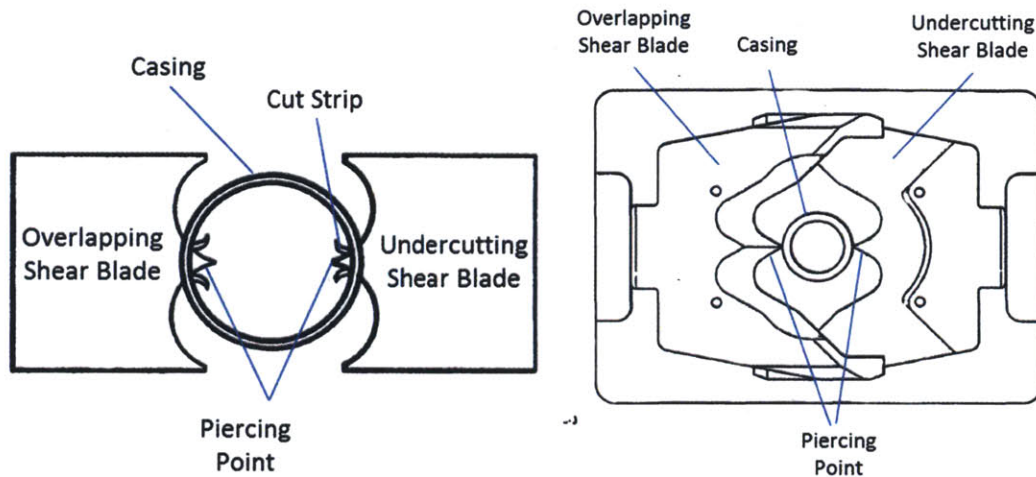


A) Nicolson (U.S. Pat. No. 2,919,111)

B) Jones (U.S. Pat. No. 4,347,898)

Figure 2-8: Straight and V shaped shear blades

Following the development of centering shear blades, a further innovation was the introduction of a piercing point, as disclosed in U.S. Pat. No. 4,549,349 (Harrison) [45]. The idea was later implemented in the industry as shown by U.S. Pat. No. 5,237,899 (Schartinger), which is illustrated in Figure 2-9 [46]. There is a need, as described in Schartinger's patent, to cut any obstruction in the wellbore "without substantially deforming the structure adjacent to the cut" [46]; therefore, by minimizing the deformations of the overall structure the energy of shearing is reduced. A similar system is disclosed by Springett et al. in U.S. Pat No. 7,814,979 B2 granted in 2010 [6].



A) Schartinger (U.S. Pat. No. 5,237,899)

B) Springett et al. (U.S. Pat. No. 7,814,979 B2)

Figure 2-9: Shear blade with piecing point

Since the introduction of the initial "piercing point" concept, several other shear blade geometries have been investigated with the intent to further reduce cutting forces. As shown in patents by Springett et al. (Figure 2-10A) and Yadav et al. (Figure 2-10B) the cutting geometry can be altered to enhance alignment, cutting, and sealing [6, 47]. Yadav et al. hypothesized that the shearing operation can be separated into two steps: securing the position of the material, performed with a V shaped ram, and then puncturing the material with a complementary shape to the V ram combined with a sharp puncture tip.

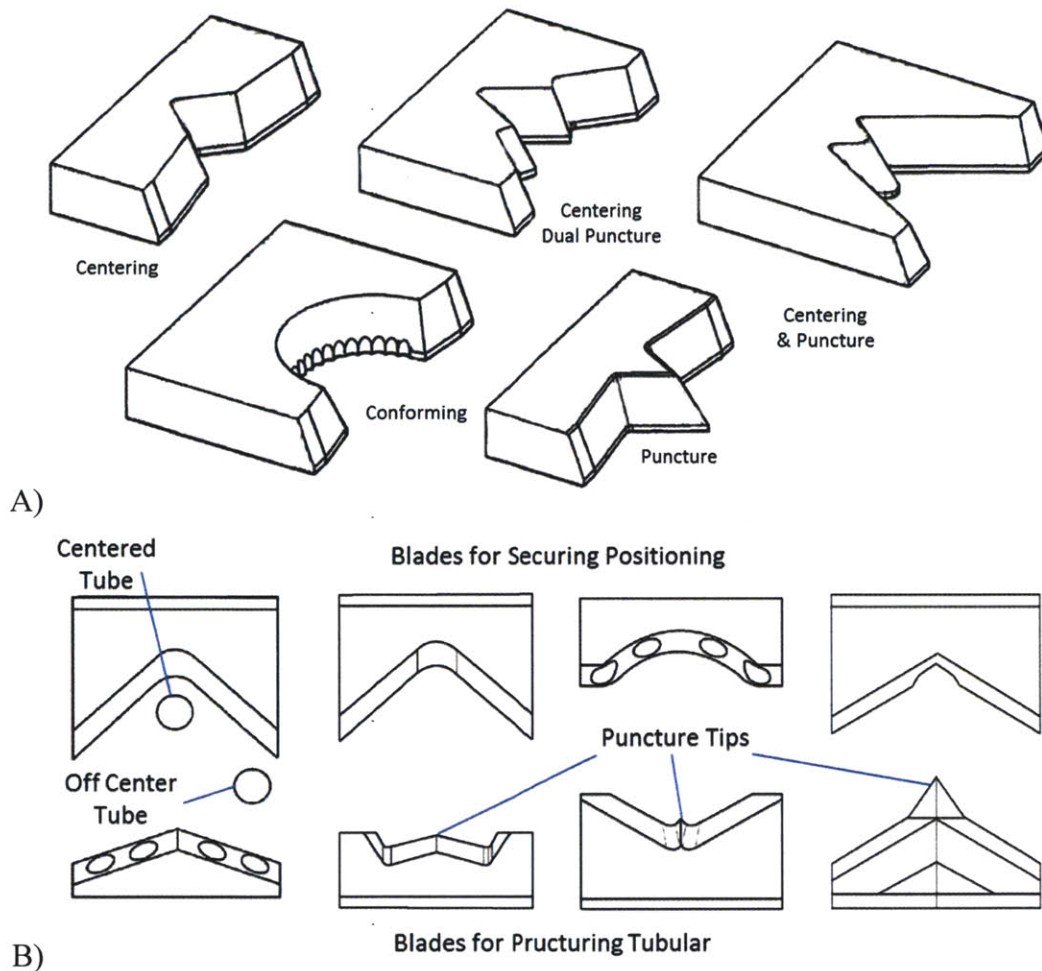


Figure 2-10: A) Ram blade assortment for puncturing tubular members (U.S. Pat. No. 7,814,979 B2). B) Shear blades where one blade is used to secure the position of the tubular and the second blade promotes puncturing through the use of puncturing tips (U.S. Pat. No. 2012/0193556 A1)

Given the plethora of design parameters for shear blades, a method for modeling the energy required to shear the pipe and find the optimal angles for shearing based on material behavior needed to be discerned. Recent work done by Koutsolelos utilized Finite Element Analysis to evaluate the shaping of the shear blades to optimize cutting efficiency [48]. Koutsolelos' experimental and numerical simulation revealed that the Modified Mohr-Coulomb (MMC) fracture criterion provides accurate results. The numerical modeling is used to determine the energy required for shearing given a specific blade geometry and shows how each section of the tubing would look after undergoing shearing.

Other improvements to the shear blades include designing a means to seal the well, while at the same time, pushing the sheared tubing out of the way during the shearing process. U.S. Pat. No. 2006/0113501 A1 discloses a shear blade assembly that includes rail actuators and guide grooves that allow for the compression of the rail seal actuators, thus enhancing the blade-to-blade seal, as well as a seal protector to lift the sheared tubing during the cutting process, as shown in Figure 2-11 [4]. The patents illustrated herein related to shear blade technologies represent a small portion of the total number of patents in the industry and are meant to serve merely as an example of prior art.

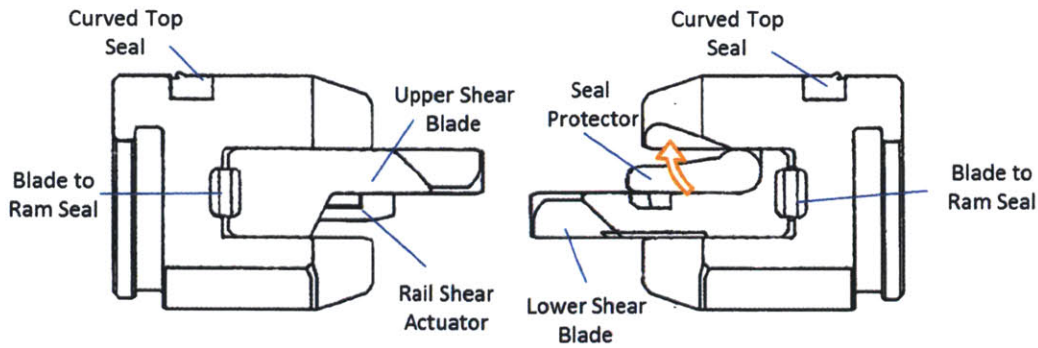


Figure 2-11: Ram bodies blade-to-blade seal enhancement (U.S. Pat. No. 2006/0113501 A1)

2.1.2. Hydrodynamic Obstruction

Well control can also be accomplished hydrodynamically by rerouting high-pressure fluctuations away from the drill platform. U.S. Pat. No. 6,367,566 describes a blowout prevention method using a system of multiple interconnected fluid pathways that allow the recirculation of down hole hydrodynamic fluid to prevent wellbore blowouts under any drilling condition [2]. A detailed description of rerouting kicks to prevent blowouts can be found in Guide to Blowout Prevention [49].

In the case of a blowout, one hydrodynamic operation often performed to control the well is referred to as a “top kill,” a procedure in which drill mud is fed into the well in an attempt to reduce the flow of hydrocarbons to the point where the well can then be safely closed off mechanically. Once the well is under control, a sealing process using cement can then be executed to permanently close the well. The execution of the “top kill” operation requires deployment of at least one drilling vessel and one service vessel to supply mud to the drill rig. Additional service vessels may be required depending upon the volume of mud warranted to kill the well, as shown by Figure 2-12 [10]. At the sea floor, a drill rig supply line connects to a manifold that feeds the kill medium into the choke and kill lines of the BOP.

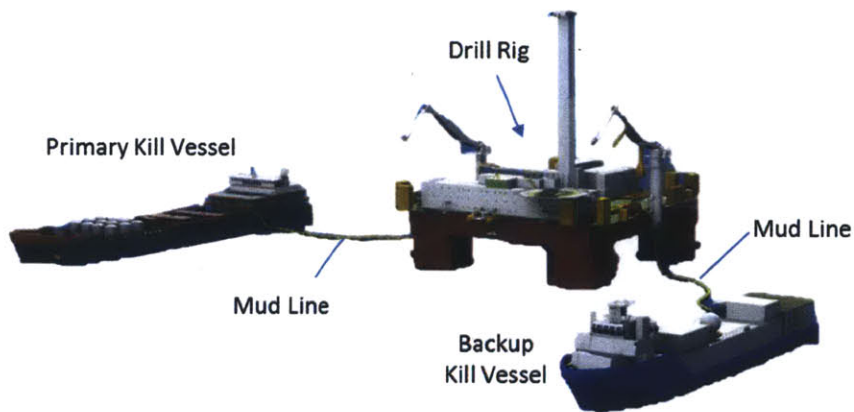


Figure 2-12: Top kill operation vessel requirement (Source BP Briefing May 2010) [10]

2.1.3. Chemical

Proposed chemical blowout control methods include the introduction of two-phase fluids, transition alloys, shear thickening fluids, and/or temperature varying materials into the wellbore. U.S. Pat. No. 4,275,788 discloses a method for plugging a well using a pipe within the open hole to deliver varying density fluids and hardening plug material, as shown Figure 2-13 [50].

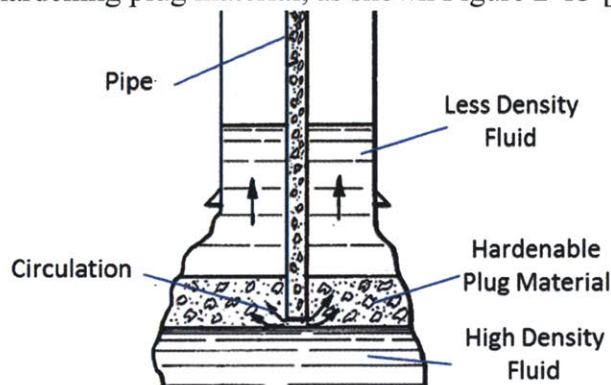
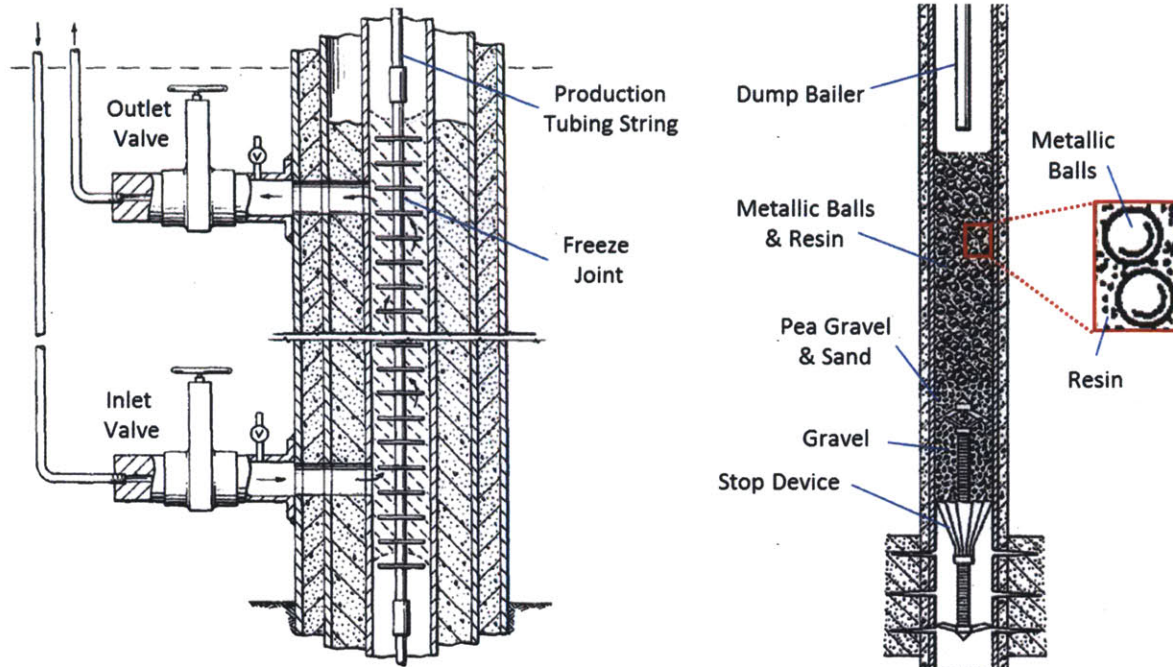


Figure 2-13: Plug forming using two-phase fluids in wellbore and hardenable plug material (U.S. Pat. No. 4,275,788)

Analogous work is also found in U.S. Pat. No. 4,489,784, which proposes the use of low melting alloy metals (or liquid alloy) fed through the active string or hot taping to fill and close the well [51].

As early as 1984, shear thickening fluid (STF) was proposed as an effective means of bringing a well under control [52-54]. Inducing high shear rates to the STF, composed of an expanding material (e.g. clay), shatters the clay particles allowing them to mix with water droplets and resulting in swelling of the subsequent hybrid mixture. As shown by experimental tests discussed in work by Hamburger et al, STFs can be effectively used to “stop unwanted flows” from gas wells.

Another solution proposed by *Osmun et al.* (U.S. Pat. No. 3,738,424) is to drill holes below the exiting region through which nitrogen can be fed and used to freeze the hydrocarbons and plug the well, as shown in Figure 2-14 [55]. To assist in the cohesion of the ice plug, a freeze joint structure must be inserted into the flow stream using standard production tools. One issue not mentioned in the patent is that feeding liquid nitrogen (i.e. -196°C) into the wellbore makes the casing brittle, a side effect of exposing steel to low temperatures, which can lead to brittle fracture in the casing and result in catastrophic failure of the assembly. Furthermore, U.S. Pat. No 3,170,516 (I), describes the means to isolate a region of the well that has ceased to produce by using thermosetting resins that are embedded within support materials (i.e. balls) to allow for the generation of a strong bridge plug, also shown in Figure 2-14 [56]. Both of the techniques, discussed by *Osmun et al.* and *Holland et al.* are limited by the need to access the interior of the wellbore.



A) Osmun et al (U.S. Pat. No. 3,738,424) B) Holland et al (U.S. Pat. No.3,170,516)

Figure 2-14: Chemical means of plugging a wellbore

Another temperature varying solution is proposed in U.S. Pat. No. 4,133,383, whereby a low viscosity gelling agent is introduced into the formation via a separate well [57]. The viscosity of the gelling agent (e.g. hydrated polysaccharide) increases when heated above a threshold temperature thus restricting the uncontrolled flow. Unlike *Hamburger et al.* this proposed temperature controlled shear thickening medium requires use of a relief well, which takes a significant time to drill and is further complicated by the limited accuracy with which it can be drilled. Such a solution is described as akin to hitting a dinner plate sized target more than two miles underground [58].

One of the more recent chemical solutions proposed in U.S. Pat. No. 2012/0285683 A1 (*Hermes*) is the introduction of 2-cyanoacrylate ester monomer into the uncontrolled fluid stream [59]. Due to the rapid interaction of the chemicals, they have to be introduced into the BOP via two separate pipes from a surface vessel so that the subsequent reaction takes place inside the BOP wellbore, as shown in Figure 2-15. This solution is based on bench level experiments performed without a significant pressure load. The test mentioned in the patent describes inverting a 2.5 cm diameter test sample to demonstrate that the plug anchors. In order for this approach to be used in the industry, a thorough understanding of the mixing mechanics of the two compounds inside of a fluid stream must be acquired; this is directly related to the time constants associated with the reaction, which also must be determined.

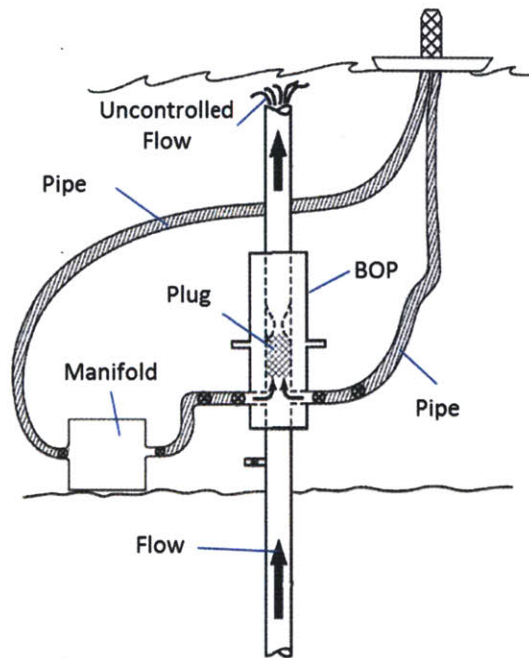


Figure 2-15: Plug generated by introducing 2-cyanoacrylate ester monomer into wellbore (U.S. Pat. No. 2012/0285683 A1)

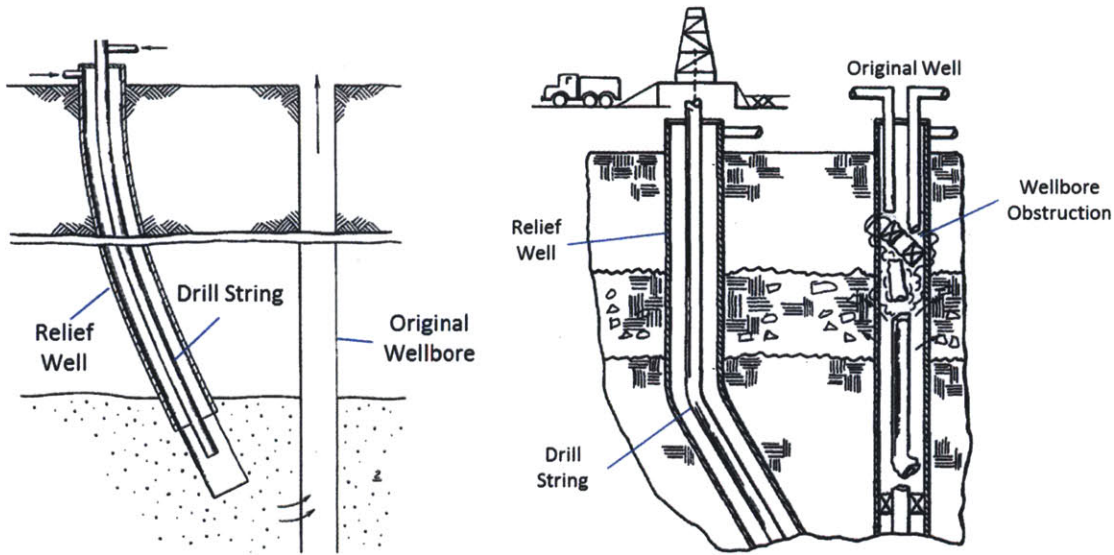
While chemical solutions for well control have been proposed, the oil industry has hesitated to further research and development in these areas, due to challenges associated with implementation and/or potential environmental repercussions. For example, the introduction of thermosetting resins, thickening fluids, etc. into the wellbore may result in the release of those substances into the ocean, where they must then be retrieved. The oil industry is also hesitant to implement any technology that involves retrofitting or altering existing BOPs unless the technology has been rigorously tested and proven to be effective.

2.1.4. Mechanical Obstruction

By far the most widely implemented methods for controlling wells (after a blowout) are mechanical solutions, for example drilling a relief well, capping the well, or injecting a junk shot. Note that the solutions presented are post-closing of the BOP, after the drillers have exhausted all other means of controlling the well.

2.1.4.1. Relief Well

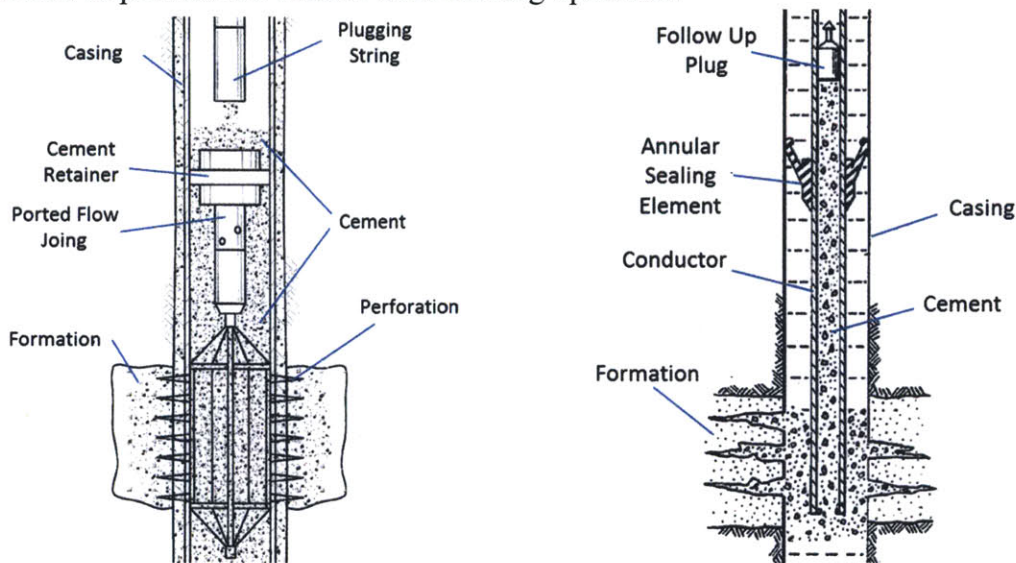
The most time-consuming mechanical solution for well control is the drilling of a relief well. This well must be drilled parallel to the original well and must intercept the primary well at a juncture below the damaged region, as shown in Figure 2-16. The relief well can then be used to syphon hydrocarbons from the uncontrolled flow, thus reducing the flow through the damaged region and allowing for the sealing of the primary well using conventional methods [60, 61]. The binding agents can also be introduced into the primary well via a relief well, used to control and eventually seal the well.



A) Blount (U.S. Pat. No. 4,224,989) B) Vann et al. (U.S. Pat. No. 4,436,154)

Figure 2-16: Relief well patents

During normal operation, cementing is used to isolate regions of production by squeezing cement through perforations in the casing into the formation and allowing it to harden as described in U.S. Pat. No. 6,595,289 B2 (Tumlin et al.) [62]. One of the earliest patents related to cementing wells, U.S. Pat. No. 2,743,779 (Brown), emphasizes the need to consolidate the plug region in order to be effective [63]. As illustrated by the work of Brown and Tumlin's et al. in Figure 2-17, the cement is introduced into the formation to anchor the plug to both the casing and the formation itself. In those instances where casing perforations are not present in the anchoring region, explosive charges can be deployed to generate the perforations. A cement retainer or annular sealing element is usually implemented to prevent the cement from moving upstream.



A) Tumlin et al. (U.S. Pat. No. 6,595,289 B2) B) Brown (U.S. Pat. No. 2,743,779)

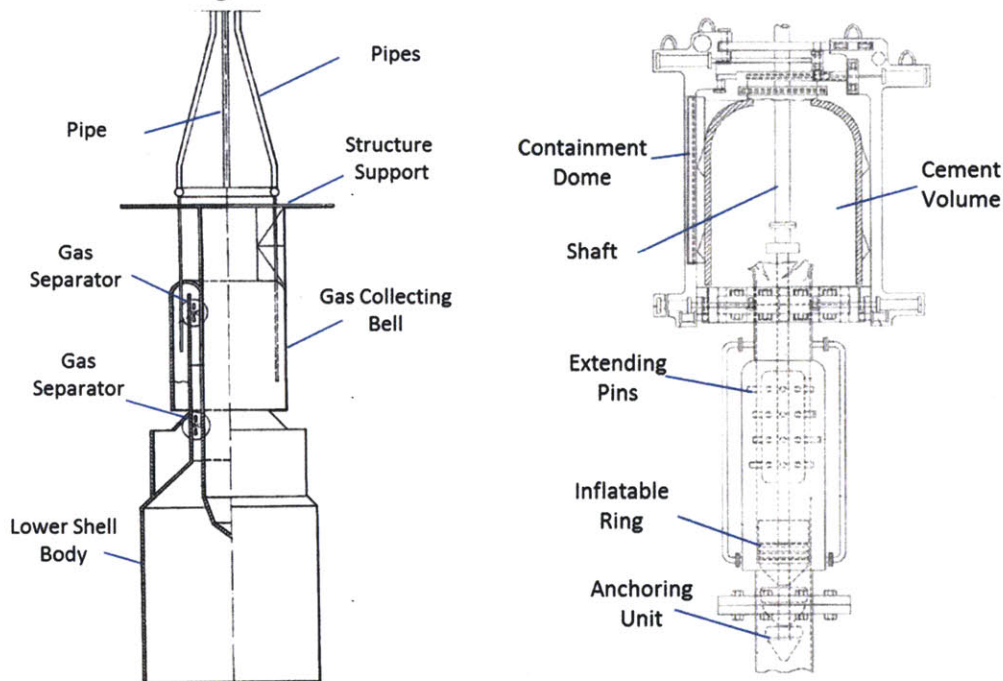
Figure 2-17: Isolation zones patents

During a blowout, hydrocarbon fluids moving through the wellbore push cement upstream not allowing it to cure. Conventional sealing elements (e.g. retainers, plugs, etc.) used during the normal cementing conditions are also not as successful during blowout conditions due to hydrodynamic loading on the tool.

2.1.4.2. Capping

Capping a well is one of the most rapid mechanical solutions used to obstruct the uncontrolled flow of hydrocarbons. Most caps tend to be heavy since they are designed to withstand the high operating pressures of the well and in some cases may contain seal rams as part of the structure. In general, there are two types of caps: localized, and dome structure. The localized caps are connected directly to the casing above the BOP stack, while the dome approach encapsulates the entire BOP stack.

An early cap solution proposed in 1984 in U.S. Pat. No. 4,447,247 (*Naess et al.*) consists of a tubular shell body that is mounted on a platform above the BOP, as shown in Figure 2-18 [64]. Seals are used to prevent hydrocarbons from escaping. *Naess et al.*'s patent also discloses a way of separating gas and liquid hydrocarbons as part of the extraction, but does not propose a solution for sealing the well. One well sealing solution proposed by U.S. Pat. No. 2012/0285704 A1 (*Mothaffar*) is to deploy a similar bell-shaped chamber that can be filled with cement after the well is brought under control [65]. *Mothaffar*'s method includes equipping the cap with an inflatable plunger that can be used to go into the wellbore and anchor against the pipe to prevent the unit from being pushed upward, also illustrated in Figure 2-18.



Naess et al. (U.S. Pat. No. 4,447,247) *Mothaffar (U.S. Pat. No. 2012/0285704 A1)*

Figure 2-18: Local cap bell shaped for production and cementing

The cap solution can temporarily divert the flow of hydrocarbons in the process of closing the well. One solution proposed in U.S. Pat. No. 8,371,373 B2 (*Ba-abbad*) entails a structure of pipes that connect to the well casing to extract effluents, as shown in Figure 2-19 [66]. Another proposed solution places a “diverter unit” at the outlet of the BOP that allows for fluid to pass the diverter temporarily while the flow is brought under control. The diverter unit can also have a ram style BOP unit that can be used to close the well as proposed by U.S. Pat. No. 2012/0318520 (*Lugo*) and illustrated in Figure 2-19 [67]. *Lugo*’s patent can be incorporated into a standard BOP stack or placed on top of a BOP stack.

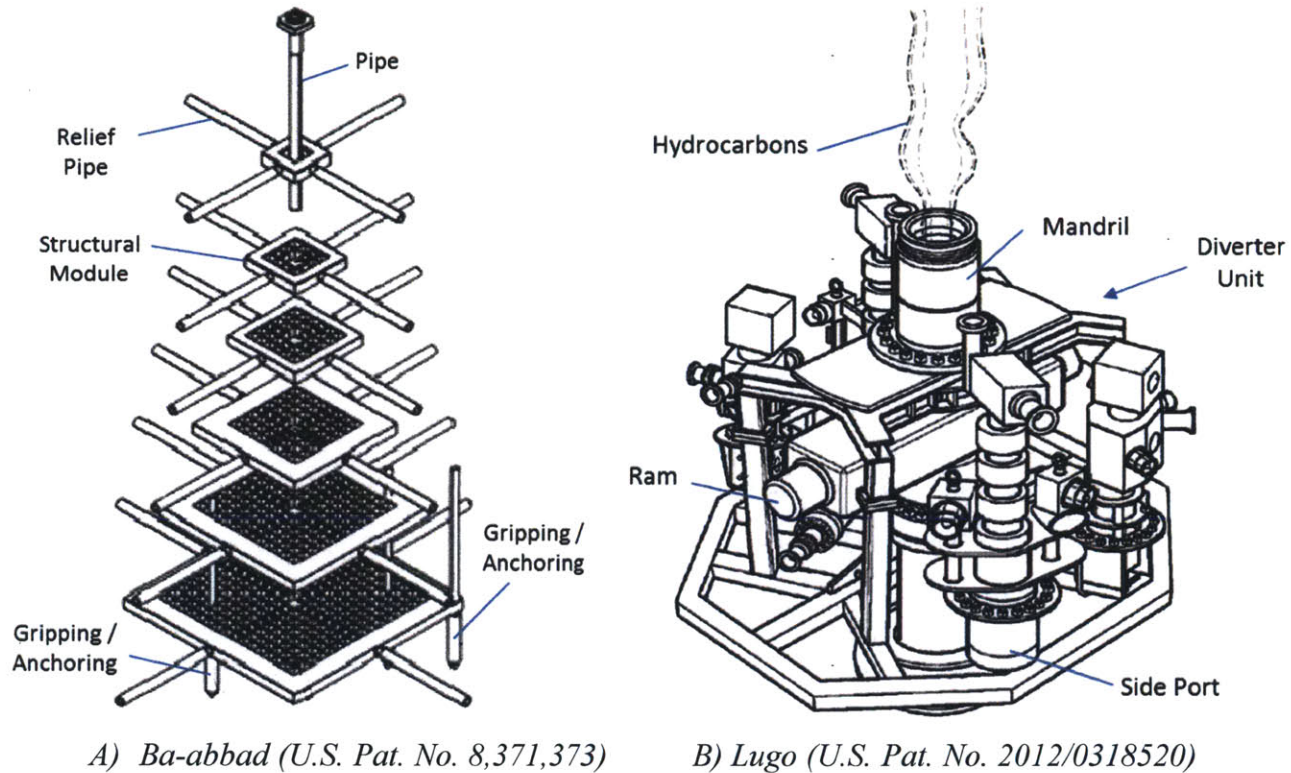


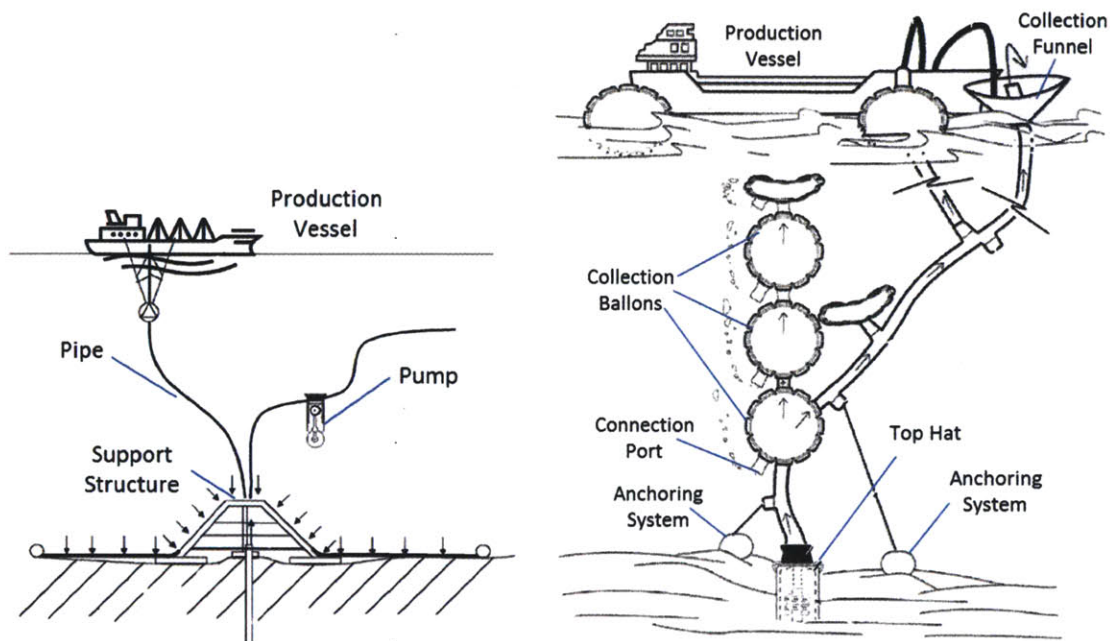
Figure 2-19: Sample diverter patents

Other proposed cap solutions include: 1) a hood like structure that can store the hydrocarbons in inflatable balloons [68]; 2) an inverted funnel and conduit held by a barge that carries hydrocarbons onto a production vessel [69]; and 3) a dome structure sealed by a compression locking mechanism and housing propellers that allow the dome to function like an ROV [70].

The larger version of a cap is referred to as a dome or containment tank that can surround the BOP stack. In U.S. Pat. No. 2012/0241160 one proposed solution involves sizing the dome unit at forty feet in diameter and sixty feet high with integrated anchoring and piping to bring the well under control [71]. A further solution proposed in U.S. Pat. No. 8,025,103 B1 involves a similarly sized system in which the structure consists of a hollow wall which is filled with reinforcement material (e.g. cement) [72]. Fastening elements (e.g. hooks) at the bottom of the containment assembly are used to adhere the unit to the sea floor.

Yet another solution, as proposed in U.S. Pat. No. 2013/0126178 A1, E.P 25885676 A2 (*Kagi*), is to place a “support structure with surrounding foil over the leaking oil well” where liquid below the

foil can be pumped away with the assistance of the hydrostatic loading on the foil, as shown in Figure 2-20 [73]. U.S. Pat. No. 2012/0152560 A1 (*O'Malley*) addresses the storage of such a capping method for collection balloons used for storage while simultaneously collecting from a sea level funnel system, also shown in Figure 2-20 [74].



A) *Kagi* (E.P. Pat. No. 20110725463) B) *O'Malley* (U.S. Pat. No. 2012/0152560 A1)

Figure 2-20: Flexible dome structures and riser with collection balloons

Unlike the cap structure, the oil industry is not currently developing the proposed dome solutions. While expanding the area of collection, dome structures would also increase the area of a pressurized container thus intensifying the overall forces exerted on the structure. Starting with the assumption of a thin walled vessel, a ~12 m (40 ft) diameter dome would require a wall thickness of ~2.5 m to support the hoop stresses required to cap a well with a 103.4 MPa (15 ksi) back pressure, if it were made out of structural steel ($\sigma_y = 290$ MPa) assuming a safety factor of 1. Upgrading to high strength structural steel ($\sigma_y = 690$ MPa) would reduce that thickness to ~0.9 m. Therefore, the assumption of thin walled vessel cannot be used for the dome. Furthermore, ability to quickly transport such a large structure would prove its own engineering challenge.

2.1.4.3. Commercially Available Caps

Capping the well presents several challenges, including the forced removal of the cap via hydrostatic forces and the formation of methane hydrate crystals in the production pipe. The combination of cold water with the gases from the well can form methane hydrate crystals that can clog the cap and impeded the collection of the hydrocarbons. The first issue can be solved with an anchoring system. The second challenge (i.e. hydrate crystal formation) can be addressed by introducing a hydrate inhibitor (e.g. methanol) as is done by some available units.

One commercially available cap is the UKCS Well Capping Device by *Oil & Gas UK* [75]. The unit, shown in Figure 2-21, is rated for wells flowing up to 138 L/sec (75,000 barrels per day) at a maximum 103.4 MPa (15 ksi) back pressure and can be deployed at a maximum depth of ~3 km

(10,000 ft.) [76]. The cap weighs approximately 355 kN (40 tons) and is 7.14 meters tall and has a roughly 4.26 m x 3.97 m cross sectional area. The cap is delivered by ship to the offshore location where it is lowered onto the BOP stack (after the removal of the LMRP) where the systematic closing of the four-valve system is performed to gradually close off the well. The system includes two methanol ports that are used as a hydrate inhibitor during operation.

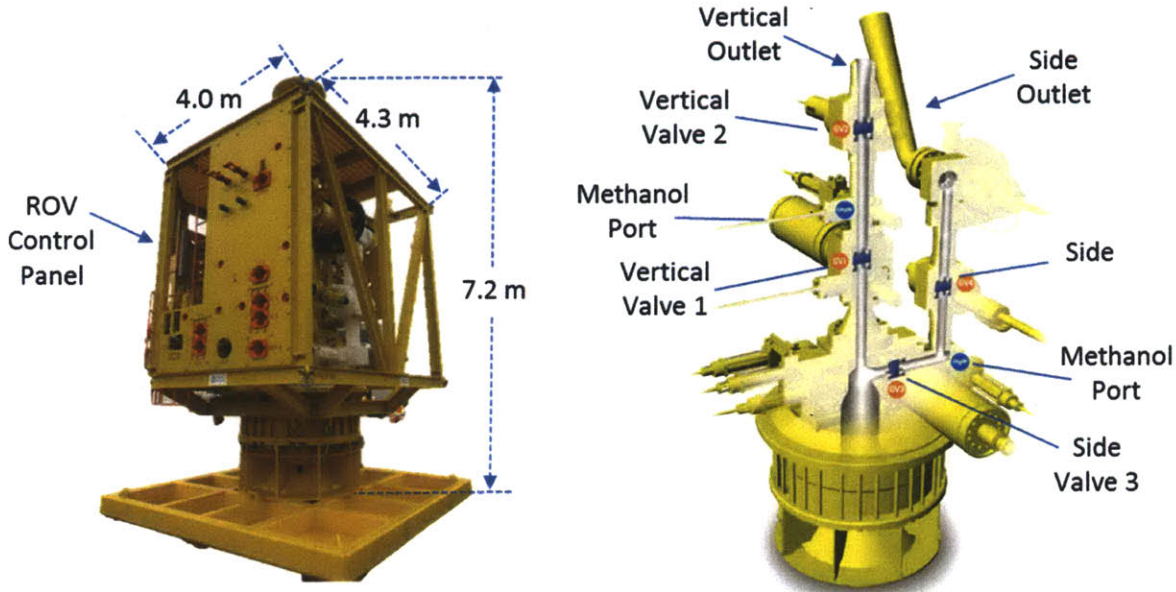


Figure 2-21: OSPRAG capping device dimensions and port system [76]

Another existing cap device made by the *Marine Well Containment Company* is comprised of single ram capping stack plus a containment cap, as shown in Figure 2-22. The current cap can be deployed down to depths of ~3 km (10,000 ft.) with a capacity of 110.4 L/sec (60,000 barrels per day) of oil plus $3.39 \times 10^6 \text{ m}^3$ (120×10^6 cubic feet) of gas per day.

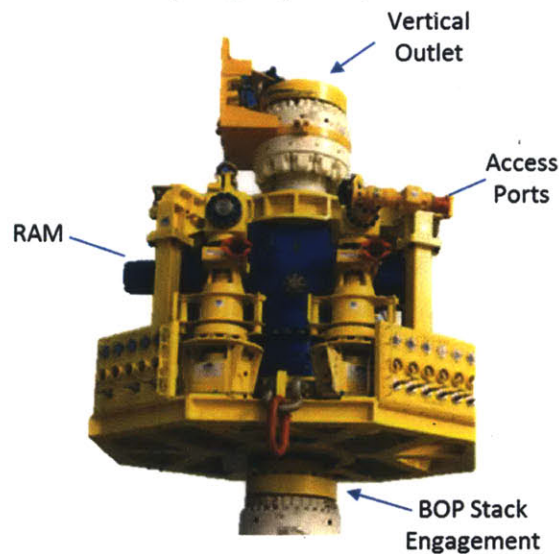


Figure 2-22: MWCC capping device with a single blind ram to control the flow

It is expected that in June 2013, MWCC will have a 68.9 MPa (10 ksi) capping stack as an addition to the 103.4 (15ksi) capping stack. The cap is currently in the process of being expanded to

have a capacity of up to 184 L/sec (100,000 barrels per day) plus an additional $5.6 \times 10^6 \text{ m}^3$ (200×10^6 cubic feet) of gas per day with a capture vessel capable of liquid storage for seven days. A comparison between the Marine Well capping stack and the UK capping stack is shown in Table 2-1.

Table 2-1: Commercially available capping stack comparison Marine Well capping stack and the Oil and Gas UK capping stack

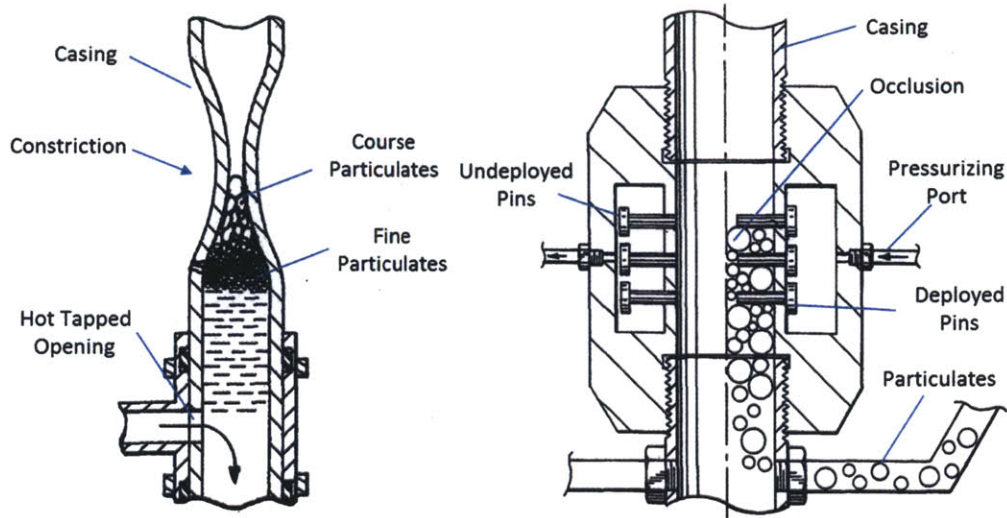
Capping Stack	MWCC (Interim Cap)	UKCS
Working Pressure	103.4 MPa (15 ksi)	103.4 MPa (15 ksi)
Depth	~ 3.0 km (10,000 ft.)	~3.0 km (10,000 ft.)
Capacity	110.4 L/sec (60,000 bbls/day) Gas Oil Ratio 2,000*	138.0 L/sec (75,000 bbls/day) Gas Oil Ratio 3,000
Mass	$90.7 \times 10^3 \text{ kg}$ (100 tons)	$36.3 \times 10^3 \text{ kg}$ (40 tons)
Dimensions (LxWxH)	~4.3 m x 4.3 m x 9.2 m (14 ft. x 14 ft. x 30 ft.)	4.6 m x 4.0 m x 7.2 m (15.1 ft. x 13.1 ft. x 26.6 ft.)
Mechanism	Single Bore/ Single Ram	Dual bore / Dual Barrier
Other	In the process of upgrading	Hydrate Inhibitor / 121° C Temp

2.1.4.4. Junk Shot

One mechanical means to control a well is using a junk shot, which introduces drill mud containing binding agents into the wellbore. The infrastructure needed to implement the junk shot solution is the same as the top kill operation, with additional particulates (i.e. bridging agents) used in the medium being fed into the wellbore. The particulates fed into the wellbore to induce clogging are made up of an array of materials such as golf balls, pea gravel, pebbles, chopped rope, and rubber pieces. Junk shots can be subcategorized into two groups: static components, and reactive particulates. Static components include an assortment of different sized objects, while reactive components include magnetic and swelling materials that are activated in the wellbore.

One of the primitive solutions proposed by U.S. Pat. No. 3,384,175 was to feed pea gravel into the wellbore to temporarily plug a well, an early version of the junk shot [77]. The implementation of junk shots at the time required creating an opening port below the BOP to introduce material into the wellbore. This opening was created using by hot tapping the casing. The area above the insertion point would also need to be constricted in order to help choke the flow and aggregate material, as shown in Figure 2-23 [78]. When greater anchoring force is required, *McCall* suggests implementing an array of extending pins into the wellbore passage that would serve to accrue sealer material, also illustrated in Figure 2-23 [79]. Another solution proposed by U.S. Pat. No. 8,215,405, is the use of a deployable grid within the wellbore in which where the junk shot material could would consolidate and clog [80]. Both the extending pins and deployable grid solutions are not viable since the oil industry is typically hesitant to make any changes to the BOP.

* Calculated from specification using Gas Oil Ratio equation



A) Rowley et al. (U.S. Pat. No. 3,647,000) B) McCall (U.S. Pat. No. 3,926,256)

Figure 2-23: Improving junk shot using casing constriction and deployable pins

A more recently proposed solution presented in U.S. Pat. No. 8,205,677 B1 is to insert heavy metal javelins into the wellbore to accrete and obstruct the flow [81]. These javelins are inserted at the top of the wellbore and are allowed to travel into the wellbore until “some of them come to rest”[†] While inserting 500 to 1000 javelins (diameter 2.5 – 3.8 cm, and length $\frac{1}{4}$ - $\frac{1}{5}$ of the wellbore diameter) may create an array of cohesive needle like structures, the pore size created between the javelins may result in a highly permeable plug that is thus unable to bring the well under control. Further development related to the anchoring and packing of the javelin nest would be required to make such a solution viable.

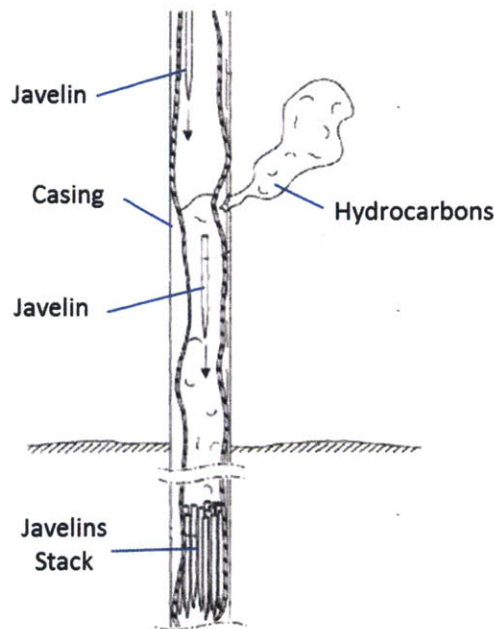


Figure 2-24: Javelin inserts into the wellbore to control the well (U.S. Pat. No. 8,205,677 B1)

[†] From original patent U.S. Pat. No. 8,205,677 B1

There have also been enhancements made to the materials fed into the wellbore to improve the clogging by active means. For example, U.S. Pat. No. 2012/168,161 discloses the favorable use of expandable swelling particulates to replace the conventional discrete materials of tires and metal spheres [82]. The introduction of materials that swell in contact with the hydrocarbons improves packing, thus allowing the plug to withstand higher pressures. Another patent, W.O. 2011153245 A1 proposes to feed permanent magnets of varied sizes to stimulate an attractive force between the particles thus improving plug the cohesion of the plug [83].

While improvements have been made to the junk shot approach, further developments are needed in order to achieve the goal of readily creating/forming a cohesive plug within a wellbore during blowout conditions.

2.2. Mechanical Wire Feeding

Wire feeding technologies are evaluated to identify potential designs for feeding a continuous medium into an uncontrolled wellbore. Mechanical feeding mechanisms are categorized into two primary groups: drive rollers, and continuous chains. These methods are used across a wide range of industries, including but not limited to: welding, coiled tubing, surgical tooling, and snubbing (oil industry). For example, MIG welders feed wire through a rolling set of dies into a flexible hose structure without buckling the wire. The manufacturing industry often makes use of rolling wheels to move, deform, and manipulate materials. One such example is the ring rolling operation that uses a rounding roll pressed against an idler roll to deform the work piece until the desired cross section is obtained. In fact, the technology to feed wire into a pressurized container can be modeled from the existing technology of coiled tubing used in oil field services. The technology exists to feed wire into the wellbore without it buckling during the travel path, but the components have not been incorporated and sized to feed a wire in a manner that would enable entanglement to control a flow.

2.2.1. Mechanical Rollers (Roll)

The most common mechanical wire feeding systems uses rollers to move a wire along a path. For example, drive rollers are used in MIG welders to engage the wire and move it along the liner as shown in Figure 2-25 [84, 85]. Both Miller and Lincoln welders use similar mechanical rollers on their push-pull welding guns to reduce buckling within the hose line when welding aluminum. The configuration of the rollers and mechanism can be altered to attain favorable characteristics such as self-aligning drive, adjustable diameter feeder, and variable grip force.

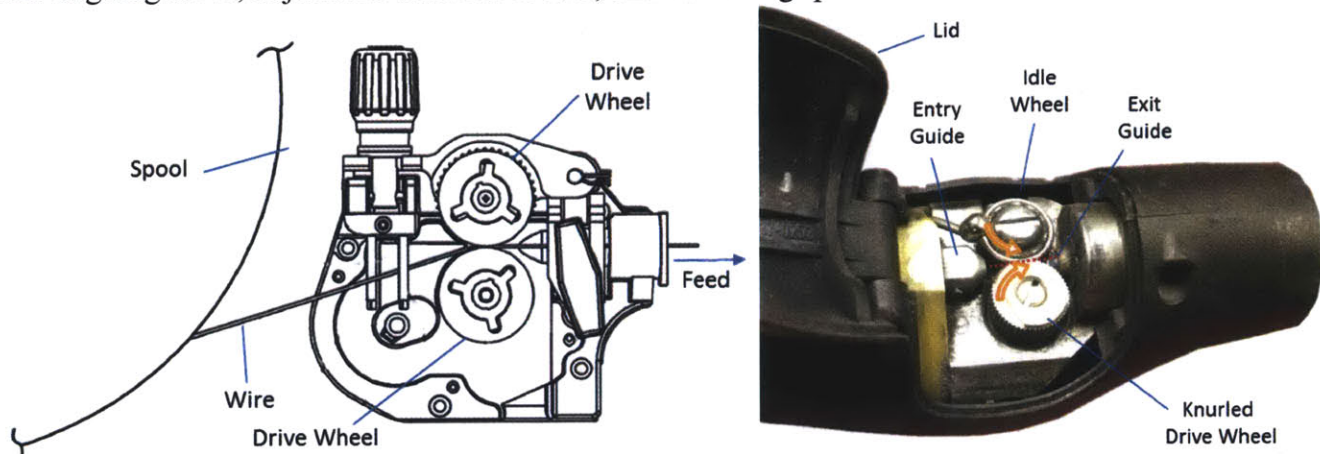


Figure 2-25: MIG welder wire feeders (U.S. Pat. No. 2013/0048621 A1) and Miller Python Push-Pull head for welding aluminum

One favorable characteristic of a wire feeder is self-alignment that does not allow the wire to travel along the length of the rollers. One example of a self-aligning wire feeder is from Miller's patent (U.S. Pat. No. 5,934,537), which is comprised of a three wheel roller arrangement, as shown in Figure 2-26 [86]. Two of the rollers are used to create a groove where the tubing/wire would sit and the third roller is used to grab and feed the wire. Another configuration uses two sets of wire rollers coupled with a guide plate structure to accomplish the self-aligning feature [87]. The use of the guide plate allows for minimal alignment error of the grooved rollers; therefore, this method depends on the

machining accuracy. Miller's approach, on the other hand, self-aligns the wire with respect to the rollers based on elastically averaging the loads on the wire.

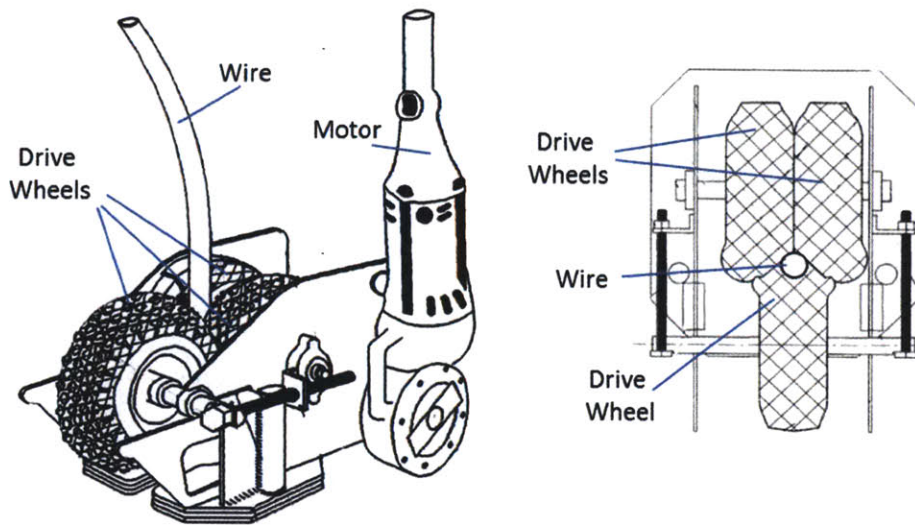
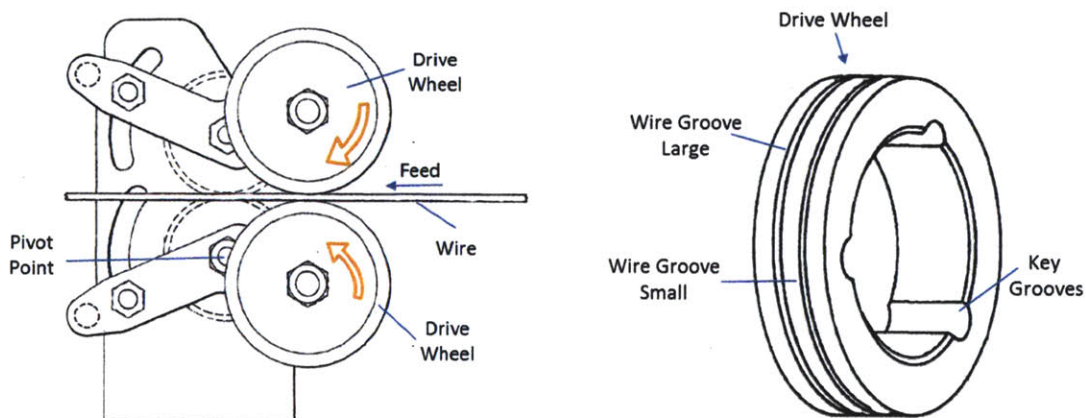


Figure 2-26: Self-aligning wire feeder (U.S. Pat. No. 5,934,537)

Accommodations can also be made to drive wires with different diameters. One of the simpler solutions was to change the hard rollers to elastically deforming rollers. An early design for variable feed apparatus for wires and tubes is from the 1946 *Collins* patent (U.S. Pat. No. 2,525,590), which involves a drive wheel pair mounted on arms that rotate about pivot points [88]. By adjusting arm location the separation between the drive wheels can be increased or decreased accordingly. Other features include circumferential grooves (U.S. Pat. No. 5,816,466) in the driving wheels to feed different diameter wires [87]. Therefore, there is an entire range of incremental or discrete methods to feed wires of different diameters.



A) *Collins* (U.S. Pat. No. 2,525,590)

B) *Seufer* (U.S. Pat. No. 5,816,466)

Figure 2-27: Gradual and discrete wire feeders for varying wire diameter

The variable wire diameter feeder can also be adjusted dynamically as shown in Figure 2-28 by Jeannette's spring loaded split groove wire feeder for the arc welding industry [89]. As the wire diameter changes along the length, the pair of splitting rollers separates allowing for a larger diameter

wire to be fed. As the wire diameter decreases the springs on the exterior of the splitting rollers close the groove thus allowing for a smaller diameter wire to be fed with the same mechanism.

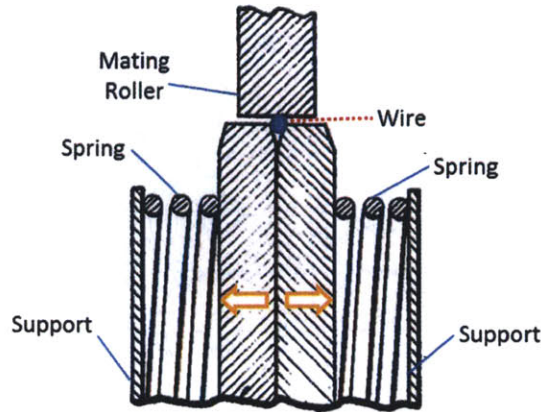
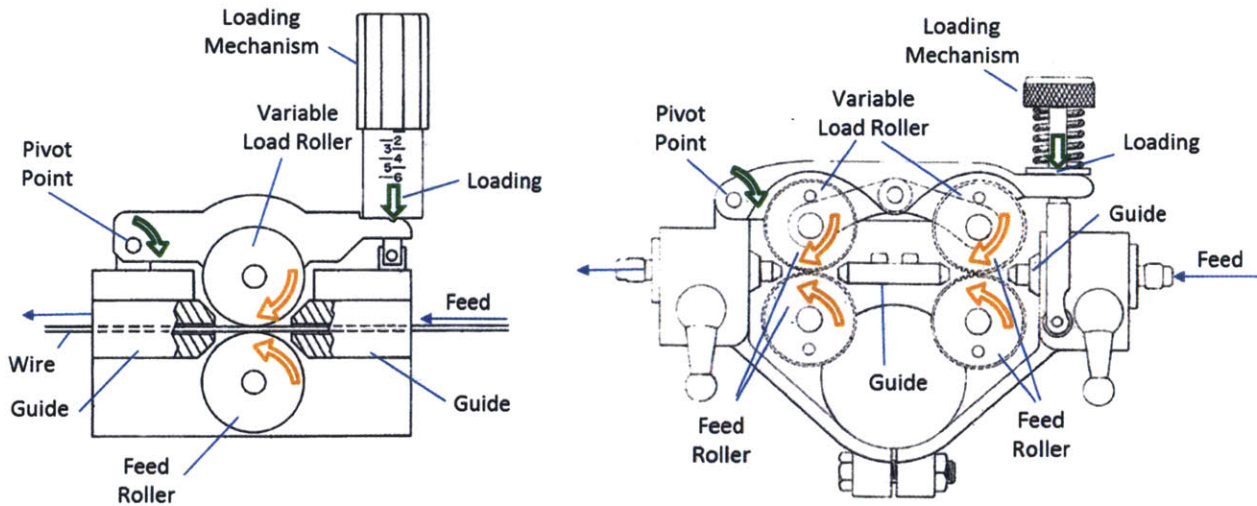


Figure 2-28: Dynamic variable diameter split roller mechanism (U.S. Pat. No. 3,447,730)

During the feeding operation adjusting the force on the wire can permanently deform the wire. Mechanical elements (springs, flexures, etc.) can be used to compensate for wire stiffness, varying diameter size, and compressibility. For example, U.S. Pat. No. 2,786,674 illustrates the use of feed rollers to feed a ribbon as part of a melt spinning process for manufacturing threads from thermoplastics [90]. Another example from the welding industry uses springs to provide a grip force and push the wire without deforming [91]. Increasing the gripping force can also be accomplished by meshing gear teeth into the roller [92]; however, wire deforming gear teeth can induce deformations in the wire, which reduces the force required to buckle. Figure 2-29 shows the variable gripping force cantilever design for both a single and double roller pair.



A) Belfiore et al. (U.S. Pat. No. 7,026,574 B2) B) Olivieri (U.S. Pat. No. 3,331,545)

Figure 2-29: Variable gripping force mechanism

Wire drive rollers also feature adjustable locking incorporated into the feeding mechanism as shown by U.S. Pat. No. 6,427,894 B1 (Blank et al.), illustrated in Figure 2-30 [93]. The overall complexity of such a unit increases as additional features such as ability to feed variable wire diameter, dynamic adjustment, and locking mechanism are introduced.

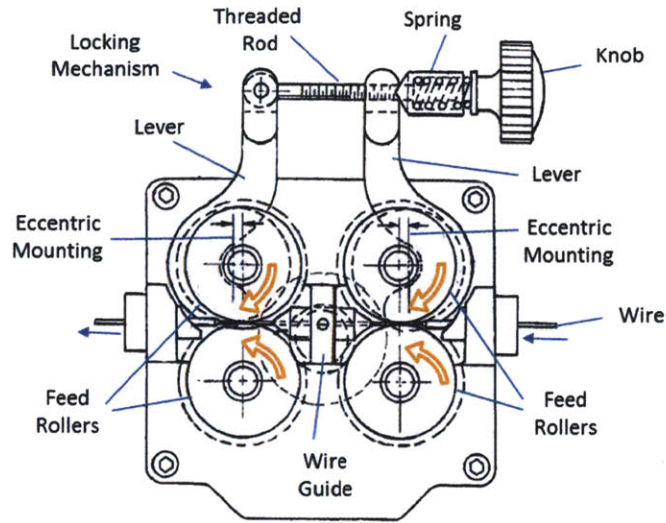


Figure 2-30: Locking mechanism (U.S. Pat. No. 6,247,894 B1)

2.2.2. Continuous Chain

Feeding a wire into the wellbore can also be done with a continuous feed system, including an elastomeric belt driven by rollers and an endless chain with gripping pads. One advantage of a continuous feed system is the ability to push the wire with a greater force without causing localized wire deformations. A pair of parallel, endless, flexible belts (continuous chain) has been used to feed an elastomeric hose through a pressurized chamber, as shown in Figure 2-31 [94].

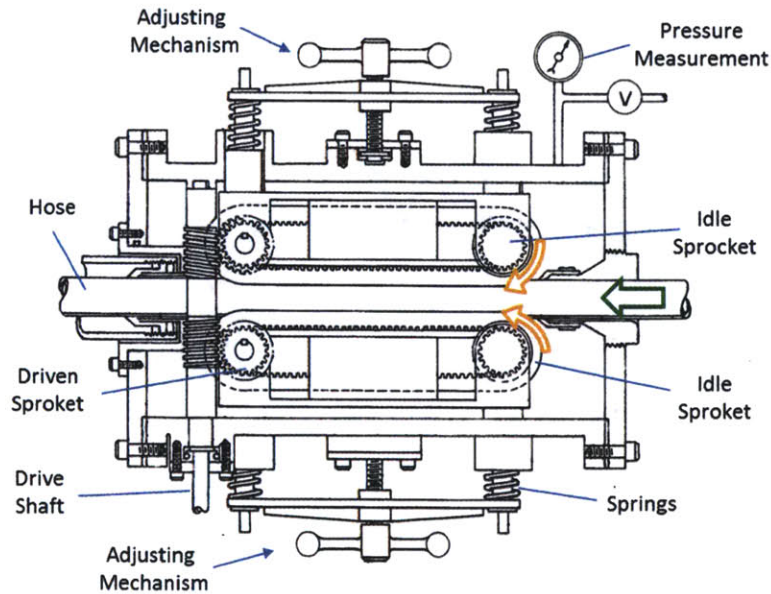
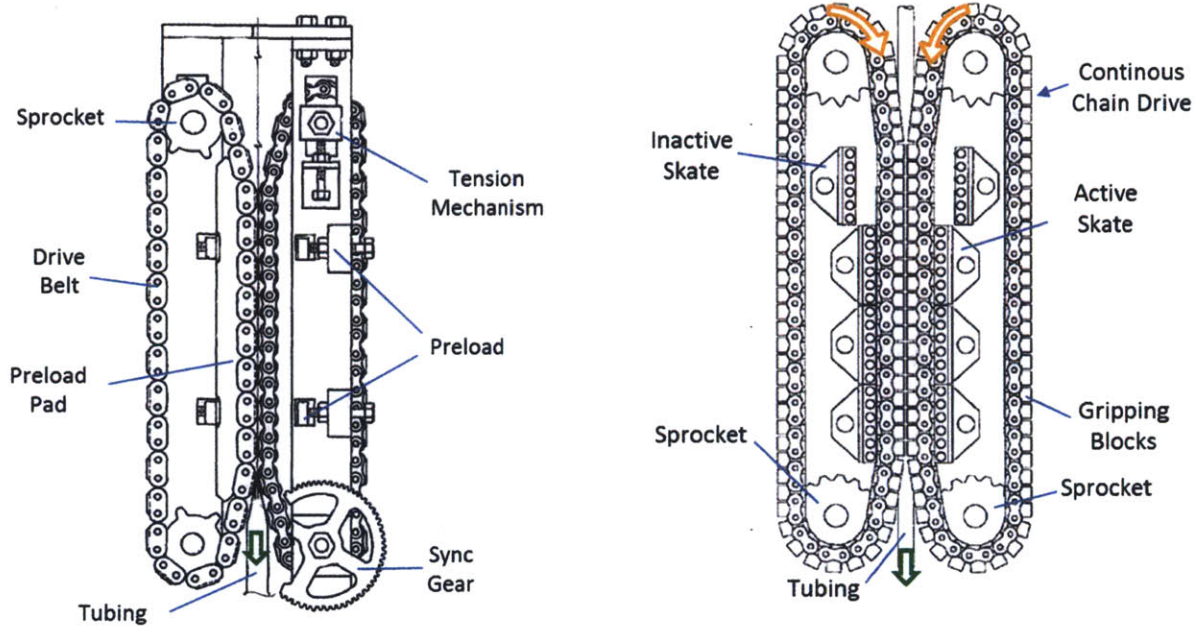


Figure 2-31: Hose feeder into pressurized chamber (U.S. Pat. No. 3,946,918)

As disclosed in *Lyon's et al.*, U.S. Pat. No. 4,585,061, the oil industry frequently makes use of an endless flexible conveyor system to feed and remove coil tubing from a well [95]. A key characteristic of *Lyon's et al.* invention is the "reliable and automatic compensation of chain tensioning" and the ability to handle multiple diameter sizes. One of the earlier patents, U.S. Pat. No. 2,567,009 (*Calhoun et al.*), discloses equipment used for inserting small flexible tubing into high pressure wells using a pair of continuous chain drive systems, as shown in Figure 2-32 [96]. The continuous feeding can also be integrated with gripper blocks that work in opposing pairs to minimize misalignment as shown by Bridges et al [97].



Calhoun et al. (U.S. Pat. No. 2,567,009) *Bridges et al.* (U.S. Pat. No. 5,918,671)

Figure 2-32: Continuous drive system with gripping blocks that press onto tubing

2.3. Wire Buckling Considerations

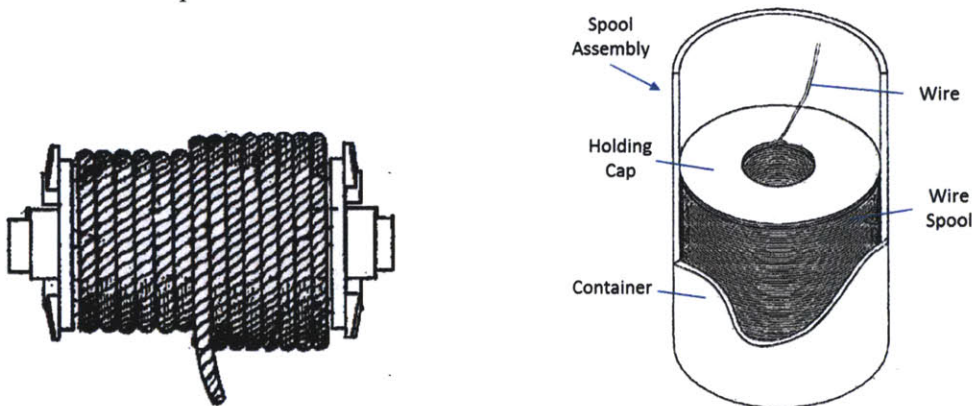
The objective of this system is to generate an entanglement in the wellbore, while at the same time preventing wire buckling inside of the wire feeding machine. Creating those distinct regions requires understanding of the critical parameters (material properties, loading, and geometry) that lead to buckling. The buckling analysis starts with the implementation of the Euler Column Formula, Equation 2.1, where E is the Young's Modulus, I is the moment, L is the effective length, and C depends on the boundary conditions [98]. Buckling has been used in the medical industry to design a clutch based needle insertion method to detect a transition from a high to low tissue resistance [99].

$F_{cr} = \frac{C \cdot \pi^2 E \cdot I}{L^2}$	Equation 2.1
--	--------------

For this application buckling is the onset of the entanglement behavior. The goal will be to design a machine that will preferentially buckle and deform the wire in the flow stream. Therefore, entanglement avoidance must be considered in all modules inside of the machine: storage, feeding, and guides.

2.3.1. Storage

There are several methods for storing the wire (i.e. continuous strand), including use of spools, and woven balls. Winding wire around a spool, as shown in Figure 2-33, is one of the most conventional ways of storing wire free of entanglements as the wire is pulled tangentially to the radius of the spool. Another method is to wind the wire around a spool and then remove the spool core, also shown in Figure 2-33 [100]. The advantage of removing the spool core and stacking the wire in continuous plural loops is that the wire can be pulled from the axial direction and no moving parts are necessary to wind the spool.

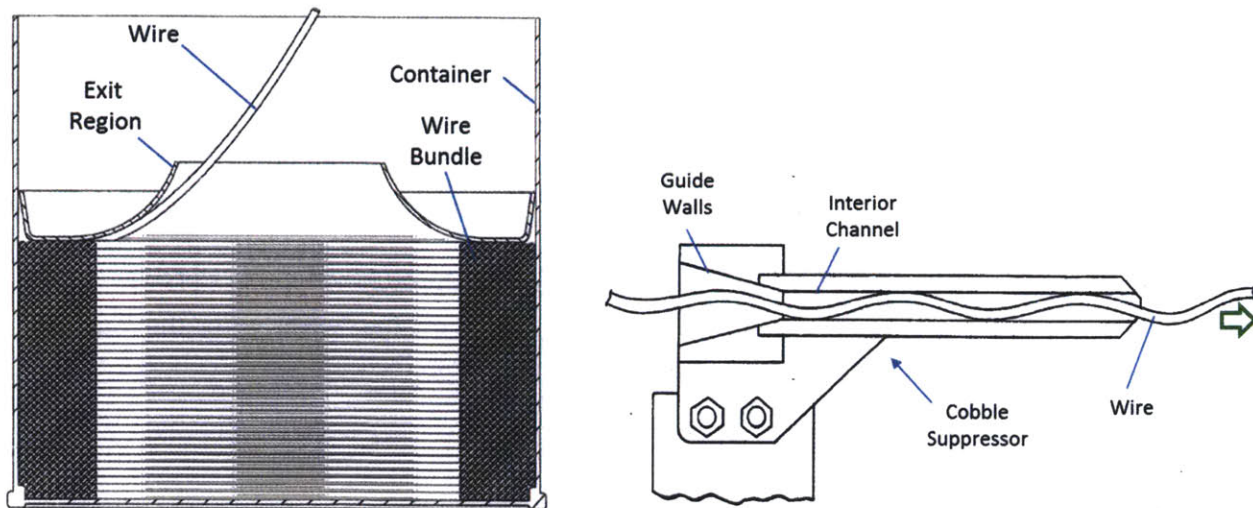


Bae (U.S. Pat. No. 2012/0006802 A1)

Figure 2-33: Wire storage configurations including radial and axial spools

2.3.2. Guides

As the wire leaves the storage area it may be necessary to use guides to reduce entanglements potential particularly after the wire exits the feeding mechanism and before it enters the wellbore. Storage containers can also be used to minimize entanglements by controlling how the wire unravels, as shown in Figure 2-34 by U.S. Pat. No. 2009/0014579 A1 [101]. Wire guides serve to reduce entanglements by limiting the motion of the wire to a preset path, as shown in U.S. Pat. No. 4,450,702, as a cobble suppressor.



Berner et al (U.S. Pat. No. 2009/0014579 A1)

Larson (U.S. Pat. No. 4,450,702)

Figure 2-34: Welding wire guide ring

While a guide serves to reduce buckling, it also adds a frictional force component on the length of contact, which increases the likelihood of creating a birds-nest like structure. Bird nesting occurs when frictional force is greater than the buckling force. Therefore, the wire buckles inside or prior to insertion into the channel, which can prove difficult to clean up. Taylor et al. describe a wire roller mechanism that uses vibrations to minimize if not eliminate "bird-nesting" [84]. Bernat's work utilize resonant vibrations to release the static friction on coiled tubing guides [102]. The methodology used to free stuck or jammed tubulars within a well can be modified to reduce buckling inside of a wire-feeding machine. Another way to minimize buckling is to remove misalignments and other features that can produce kinks in the wire that lead to buckling [87]. Once within the flow stream the wire can buckle in a lower energy mode thus generating an entanglement.

2.4. Axially Moving Structure with Fluid Interactions

The model for inserting the wire into the wellbore can be complex; however, discretizing the wire behavior using existing approaches may be used to model each section independently as shown in Figure 2-35. The following models can serve as a starting point to predict the behavior of the wire: Navier-Stokes (viscous feeding), reverse spaghetti problem, and flapping and bending bodies. The Navier-Stokes equations may be used to model the dynamics of the wire within the guide as an axially moving structure with fluid interaction if the gap between the wire and the channel is small. The reverse spaghetti model may be used to study the interactions of the wire exiting the guide as fed into the wellbore, referring to the ejection of a slender member through an orifice into an environment (e.g. printer paper exiting rollers). The reverse spaghetti problem complements the spaghetti model consisting of pulling a single strand of spaghetti into a cavity. As the wire is exposed to the flow stream, the model can change based on wire stiffness compared to flow loading. For a low stiffness wire (i.e. drag forces \gg wire rigidity), where the length of exposed wire is much larger than the wire diameter, the interactions between the surrounding flow and wire can be modeled as a flapping and bending body, similar to *Shelley et al* paper on *Flapping and Bending of Bodies* [103]. For high stiffness wires, buckling is induced through the interaction of the wire with the surrounding environment (i.e. casing and obstructions). The three regions described are used to begin to develop an understanding of wire behavior within a flow stream.

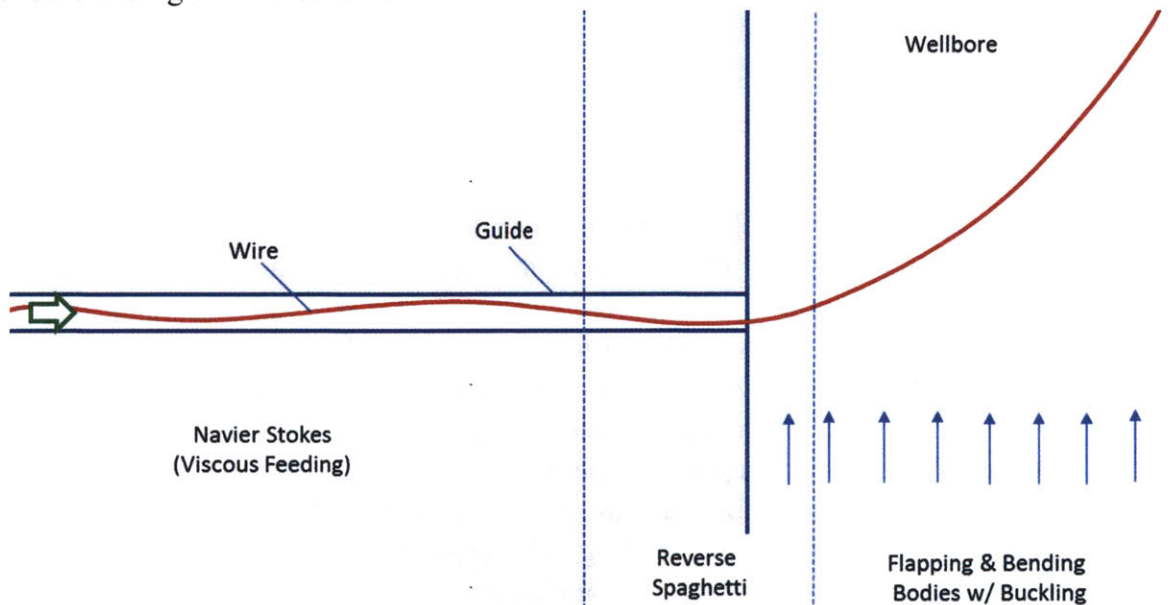


Figure 2-35: Potential physical models for determining wire interaction through different areas along the feeding process

2.4.1. Drag Feeding

Feeding wire into the BOP wellbore region can also be assisted by drag force, generated by a pressure differential between the wellbore and the internal pressure of the wire feeder. This pressure differential can create a flow into the wellbore, effectively assisting in the feeding process. A similar technique has been used by the fiber optic industry to feed fiber optic lines into tubes over long distances with compressed air [104]. Fiber optic lines were inserted with minimal strain on the fiber using 1.03 MPa (150 psi) of air for distances of 2 km link [105]. The applications of drag feeding has led to the development of analytical models and experimental work for straight sections and coiled tubing [106, 107]. Hence the feeder should maintain an internal pressure higher than the wellbore to help ensure that the wire appropriately feeds into the wellbore.

2.4.2. Spaghetti Problem

In 1949, Carrier published a paper: *The Spaghetti Problem* in the journal of American Mathematical Monthly [108]. Carrier's paper examines the vibrations of a string as it is accelerated through an orifice. Since the original paper, extensive research and mathematical modeling has been done on both the forward and reverse Spaghetti Problem [109].

The topic of interest related to this research is the reverse spaghetti problem, which also has numerous applications including rolling processes, spacecraft antennas, cable tramways, printing machines and band saws. The governing equation, the linear sliding beam equation of motion, is too complicated to obtain an analytical solution; therefore, a numerical solution must be used to explore the system dynamics. Discrete [110], close form [111] and numerical [112] solutions have been used to model the dynamics of flexible sliding beams. The approach used by *Kobayashi et al.* [110] is similar to *Sugiyama's* finite element discretization where the string/paper is divided into rigid sections joined by torsional elements. While the mathematical model used by Kobayashi et al. couples the structural dynamics with the fluid force (drag), expanded to include a flow field, it does not include large deformation non-linearities. On the other hand, the model used by *Behdinan et al.* [111] is a comprehensive formulation that takes non-linearities due to large deflections into account; however, this approach is only valid for axially inextensible beams. Another numerical model is proposed by *Mansfield et al.* in which numerical solutions are used to capture the drooping motion of an elastica exiting a horizontal guide [112]. The non-dimensional parameters identified in the Mansfield paper, shown in Equation 2.2 and Equation 2.3, are used to characterize the reverse spaghetti dropping dynamic model. The dimensionless weight-to-stiffness ratio (Equation 2.2) characterizes the gravitational forces on the exiting beam to the bending stiffness. The dimensionless velocity (Equation 2.3) characterizes the exiting velocity with the bending stiffness of the axially moving beam/wire.

$\pi_{\omega} = \frac{m_a \cdot g \cdot L^3}{B}$	Equation 2.2
--	--------------

$\pi_v = V_{feed} \cdot L \sqrt{m_a / B}$	Equation 2.3
---	--------------

The parameters in Equation 2.2 and Equation 2.3 have the following dimensions: m_a [kg/m²] is the mass per unit area, g [m/s²] is the acceleration of gravity, V_{feed} [m/s] is the constant velocity of the moving member, L [m] is the length of extending member, and the bending stiffness B [kg·m²/s²][‡].

The bending stiffness used by Mansfield is not the standard definition used in the mechanical engineering field, which is the Young's modulus E [N/m²] multiplied by the moment, I [m⁴] [112]. A literature review into bending stiffness can be used to clarify the bending stiffness definition dilemma. The bending stiffness used by *Mansfield et al.* [112] and *Shelley et al.* [103] paper is the bending stiffness per unit width (w) of the rectangular piece, as shown in Equation 2.4.

$B_w = \frac{EI}{w}$	Equation 2.4
----------------------	--------------

2.4.3. Flapping and Bending Bodies

For cases where the fluid drag is much greater than the stiffness of the wire, the wire may behave like a flapping of a flag. In 2010 *Shelley et al* published a paper titled *Flapping and Bending of Bodies* which presented detailed analysis on the behavior of a flag flapping in the wind [103]. Shelley's paper uses the non-dimensional stiffness shown in Equation 2.5 to characterize the dynamics of the flag and fluid. Once again, the bending stiffness defined has units of N·m not kg·m²/s² as the classical EI. The following are parameters in Equation 2.5: bending stiffness B [kg·m²/s²], fluid velocity V_{flow} [m/s], density of the surrounding fluid ρ_f [kg/m³], and length of the extending wire L_m [m].

$\pi_s = \frac{B}{\rho_f \cdot L^3 \cdot V_{flow}^2}$	Equation 2.5
---	--------------

For wires with circular cross sections, the bending stiffness is defined as the stiffness divided by the radius of the wire (Equation 2.6).

$B_r = \frac{EI}{r}$	Equation 2.6
----------------------	--------------

For consistency the bending stiffness per unit thickness/radius (B) is to be referred as “bending stiffness, while the classic definition of the bending stiffness (EI) is to be referred as just the “stiffness.”

[‡] The bending stiffness in the Mechanical Engineering context does not have the same units they are related by 1/r

2.5. Spontaneous Knotting

Knotting and entanglement research is separated into two fields: detrimental and favorable. There is, of course, a third section of entanglement, scientific curiosity, which focuses on understanding the pure science behind entanglement irrespective of material properties or the environment.

On one hand, research in the detrimental field is aimed at preventing entanglement situations in manufacturing operations like wire drawing and rolling mills. The rolling mill industry sometimes experiences "cobbling" during the production of stock, caused by the compression of rods between adjacent stands that are used to reduce the diameter of the material from a billet [113]. While cobbling is not a desired effect in the mill industry, it is a prime example of how spontaneous knotting and entanglement can occur due to unforeseen and unwanted buckling forces. Spontaneous knotting or entanglement has also been observed in the oil industry after cutting the wireline, which is a set of electric cables used for collecting well data. Wire entanglement occurs when the wireline (suspended measurement tools) is cut in the middle of an operation (i.e. in the case of an emergency); the unsupported string in the wellbore falls to the bottom of the well, where it buckles and locks leading to clogging.

On the other hand, the textile and medical industries view entanglement favorably, especially in cases where the objective is to generate entanglements to adhere strands of fiber into a continuous filament in order to seal an area by entangling wire and preventing blood flow, respectively. In the textile industry, entanglements have been used to create cohesive fibers that have greater strength than each independent strand [114]. The textile industry uses induced vortices in air jets to adhere loose bundles of continuous multifilament yarn. Even though entanglement is used by various industries, it is not well understood and regarded as "highly unpredictable."

One paper that covers some of the theory of spontaneous knotting of an agitated string is the work by Raymer and Dorian [115]. Although the work presented does not directly develop entanglement theory; the main contribution is that knot formation can be captured in a simple model developed on the basis of random "braid moves" of a string. Research on spontaneous knotting concluded that longer and more flexible strings have a higher probability of knotting.

2.6. Flow Through Porous Media

As the wire entanglement “nest” reaches its terminal compacted state prior to attainment of full clogging (henceforth known as cohesion) the plug can be modeled as a uniform porous medium. Determining the pressure drop across the porous plug can be accomplished in one of three ways: 1) Finite Element Analysis, 2) experimental testing, and 3) analytical modeling.

2.6.1. Finite Element Analysis

The method least frequently used to quantify flow through a porous medium is finite element analysis (FEA). Finite element packages, such as Fluent, can be used to calculate the inertial effects through disordered porous media [116, 117]. Tobacco companies have used FEA to calculate the expected airflow resistance through a cigarette filter which is composed of randomly placed obstacles [118]. Sand control sectors of the oil industry have used FEA modeling to reduce deterioration of the sand formation surrounding the entry region near the bottom of a well. Although finite element codes have proved useful for some industries, any application in which the results need to be accurate require the use of experimental data in conjunction with fundamental theory to validate the model.

2.6.2. Experimental Data

There is an abundance of experimental data available to calculate the pressure drop in a formation without needing to resort to a large finite element computation. The data is used to identify the governing parameters required to develop a model. The first known experimental work aimed at understanding flow behavior through a porous medium is found in *Les Fontaines Publiques de la Ville de Dijon*, published in 1856 by Henry Darcy [119]. The setup consists of a 3.5 m column with an internal diameter of 0.35 m filled with silicious sand for porous media, as shown in Figure 2-36 [120, 121]. Darcy came to the conclusion that for sands of similar composition that:

“Le volume débité est proportionnel à la charge et en raison inverse de l'épaisseur de la couche traverse.”

- which translates to:

“the output volume is proportional to the head and inversely related to the thickness of the layer traversed.” [121]

The original form of Darcy's equation modeling the behaviors observed in his experiment is given by Equation 2.7 [120].

$q = k_d \frac{s}{e} (h + e \pm h_o)$	Equation 2.7
---------------------------------------	--------------

where q is the volumetric flow rate per unit time, k_d is the coefficient that depends on the permeability, e is the thickness of the sand layer, and s is the surface area.

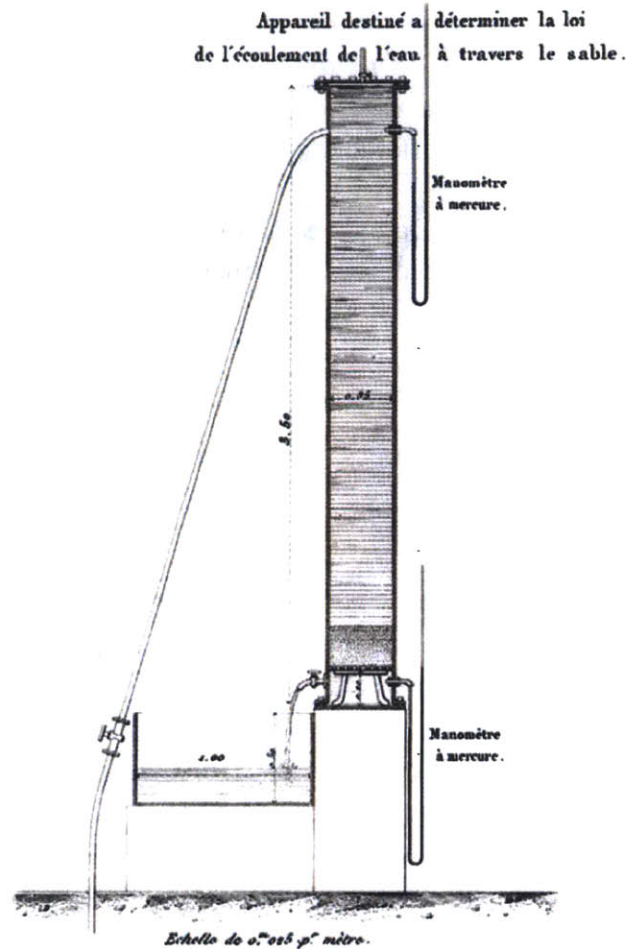


Figure 2-36: Henry Darcy sand column experiment setup from Les Fontaines de la Ville de Dijon [119]

2.6.3. Models

Since 1856, additional experimentation has tests have been performed only to discover different behaviors for varying conditions. Due to the nature Darcy's experimental testing his results are only applicable for systems with the following characteristics [122]:

1. Newtonian fluid with constant viscosity
2. Incompressible (i.e. constant density)
3. Steady State or quasi-steady (i.e. no time dependence)
4. Creeping flow
5. Solid material is not deformable
6. Arbitrary porous medium geometry
7. No slip on the internal solid matrix surface

While Darcy's linear model is not in the form of Equation 2.8, the relation is the same. For the cases where the Darcy equation does not capture the fluid dynamic behavior, additional relationships have been developed. For example, if the streamlines are assumed to be independent of the volumetric flow rate then the resulting filtration law is a power law.

$$\frac{q}{A} = -\frac{k}{\mu} \cdot \frac{dp}{dx}$$

Equation 2.8

Where q (m³/sec) is the volumetric flow rate, A (m²) is the cross sectional area, k (m²) is the permeability, dp (Pa) is the pressure differential, and dx is the length of the column, and μ (Pa*sec) is the dynamic viscosity.

The physical representation of Darcy's equation is illustrated in Figure 2-37, which shows how a permeable membrane with known geometry obstructs a flow of a fluid given a pressure potential (dp).

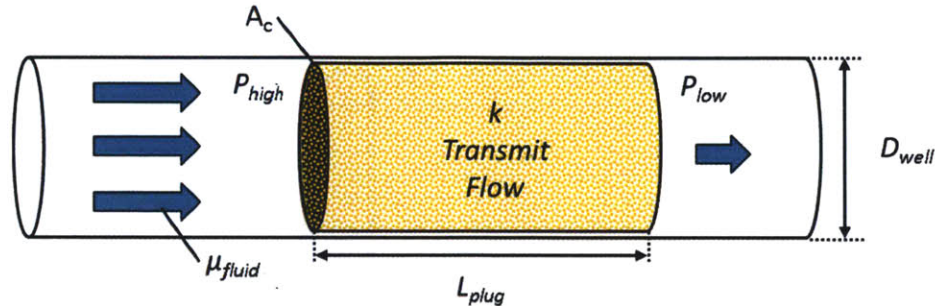


Figure 2-37: Schematic diagram of Darcy's equation showing a permeable plug obstructing flow in a channel

Experimental tests have led to a series of models developed for varying porous media configurations including packed spheres ([123]), fibrous beds, etc. In the event that the existing models do not capture the fluid behavior through a porous medium, there is a series of papers that describe the recipe for modeling the fluid behavior. Tiller's work examines the time dependence of the filtration rate, the role of porosity in filtration with both variable [124] and constant [125] pressure/filtration rate. The work of Tiller et al can be used to create an entanglement resistance theory as the wire nest reaches cohesion [126].

It is important to note that permeability and porosity of a medium/membrane are not equivalent. The permeability refers to the ability of a medium to transmit flow, while the porosity refers to the amount of void space as defined in Equation 2.9.

$$\Phi = \frac{V_{voids}}{V_{tot}}$$

Equation 2.9

Where V_{voids} (m³) is the volume of the voids, and V_{tot} (m³) is the total volume. Therefore, a high porosity consists of a section that has many voids.

The permeability of a rock or medium can depend on the porosity Φ , but the permeability can also depend on coatings and surface features of the porous membrane. The permeability k (m²) is measured in Darcy's where 1 Darcy = 9.869x10⁻¹³ m². Permeability ranges from 10⁵ Darcy for pervious material to 10⁻⁸ Darcy for impervious material. Table 2-2 shows permeability for a range of sedimentary and crystalline rocks collected from various sources [127, 128].

Table 2-2: Permeability ranges of sedimentary and crystalline rocks from Domenico et al and Freeze et al. [127, 128]

	Permeability 10^N [m^2]	Pervious				Semi-Porous				Impervious						
		-7	-8	-9	-10	-11	-12	-13	-14	-15	-16	-17	-18	-19	-20	-21
		10^5	10^4	10^3	10^2	10^1	10^0	10^{-1}	10^{-2}	10^{-3}	10^{-4}	10^{-5}	10^{-6}	10^{-7}	10^{-8}	10^{-9}
Unconsolidated Sedimentary Materials	Gravel															
	Sand															
	Sand Coarse															
	Sand Medium															
	Sand Fine															
	Silty Sand															
	Silt (Loess)															
	Till															
	Marine Clay (NW)															
Sedimentary Rocks	Salt															
	Siltstone															
	Sandstone															
	Limestone, Dolomite															
	Karst															
	Anhydrite															
	Shale															
Crystalline Rocks	Schist															
	Metamorphites & Plutonites (NF)															
	Metamorphites & Plutonites (F)															
	Porous Basalt															
	Basalt															
	Granite (W)															
	Gabbro (W)															

2.7. Post Clogging Procedure

After bringing the well under control, repairs can be made to the existing blowout preventer or a new blowout preventer can be attached to the existing structure above the occlusion. With a working BOP appropriately controlling the well, the partially deployed rams can be retracted to allow for drilling into the occlusion to gain access to the primary wellbore. Standard plug removal tools used to remove broken tools, slick lines, and other obstructions may also be used to remove the entanglement occlusion generated to control the well [129].

Chp 3.

Design Parameters

Design parameters affecting the HAWK can be separated into three categories: environmental conditions, geometry constraints, and flow parameters. The geometric constraints include but are not limited to the range of: wellbore diameter, clearance below the BOP, and BOP stack length. Flow parameters of the wellbore include: mass flow rate, inflow performance relationship⁴, fluid properties, and flow parameters. Figure 3-1 summarizes the requisite design parameters for sizing an experimental unit (all sources are listed in the following text).

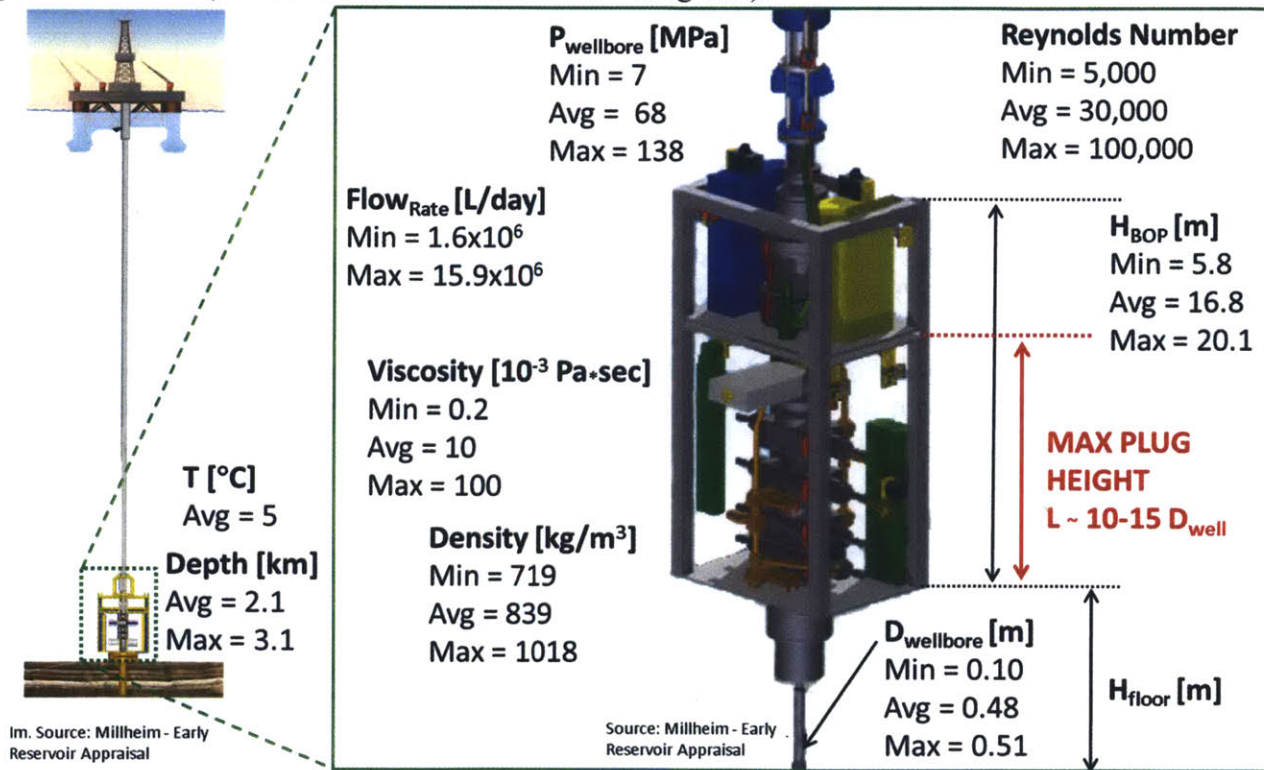


Figure 3-1: Wellbore schematic illustrated design parameters

⁴ Reservoir pressure versus flow rates during normal operation

3.1. BOP Environmental Parameters

There are two primary environmental parameters: depth and temperature. A machine for deepwater operations has an added hydrostatic pressure load in addition to the operating loads. The low temperature of the ocean floor at 3 km below sea level can also affect machine performance since hydrate crystals can form at low temperatures and clog an aperture interface.

3.1.1. Depth

Offshore drilling began with the pursuit to harvest California's Summerland oilfield in 1896 [130]. The first offshore platforms were on pier structures and gradually moved further out to sea with the recruitment of barges. Today, state of the art drilling rigs can reach depths in excess of 3 km below sea level and well depths are divided into three categories: standard, deep, and ultra-deep. "Deep water" drilling is considered anything greater than 305 m (1,000 ft.), and after 1.5 km (5,000 ft.) the well is referred to be in "ultra-deep" water. The depth of offshore wells depends on the specifications of the drill rig. Currently, there are six generations of drill rigs, as detailed in Table 3-1.

Table 3-1: Oil rig generation maximum depth

Generation	Maximum Depth	Build Year
1 st	244 m (800 ft. water – 600 ft)	Early 1960s
2 nd	457 m (1,500 ft. water - 1,000 ft)	1969-1974
3 rd	762 m (2,500 ft. water - 1,500 ft)	Early 1980s
4 th	1,067 m (3,500 ft. water - 3,000 ft)	1990s
5 th	2,438 m (8,000 ft. water - 7,500 ft)	1998-2004
6 th	3,048 m (10,000 ft. water – Source offshore article)	2005-2010

At the turn of the century, Brazil had the drilling depth record of 2,777 m (9,111 ft.) below sea level [131]. According to the Mustang Engineering, as of March 2012, the maximum offshore well depth record is 3,107 m (10,194 ft.) as shown in Figure 3-2. Recently, Hydril Inc., a BOP manufacturer, has released a new BOP designed to work at depths of ~3.8 km (12,500 ft.), where the ambient pressure is on the order of 37.3 MPa (5.4 ksi), but the formation pressure can be as high as 138 MPa (20 ksi) [132]. Even though the maximum drilling depth record continues to increase, the majority of current drilling is performed at depths less 2,134 m (7,000 ft.) [133].

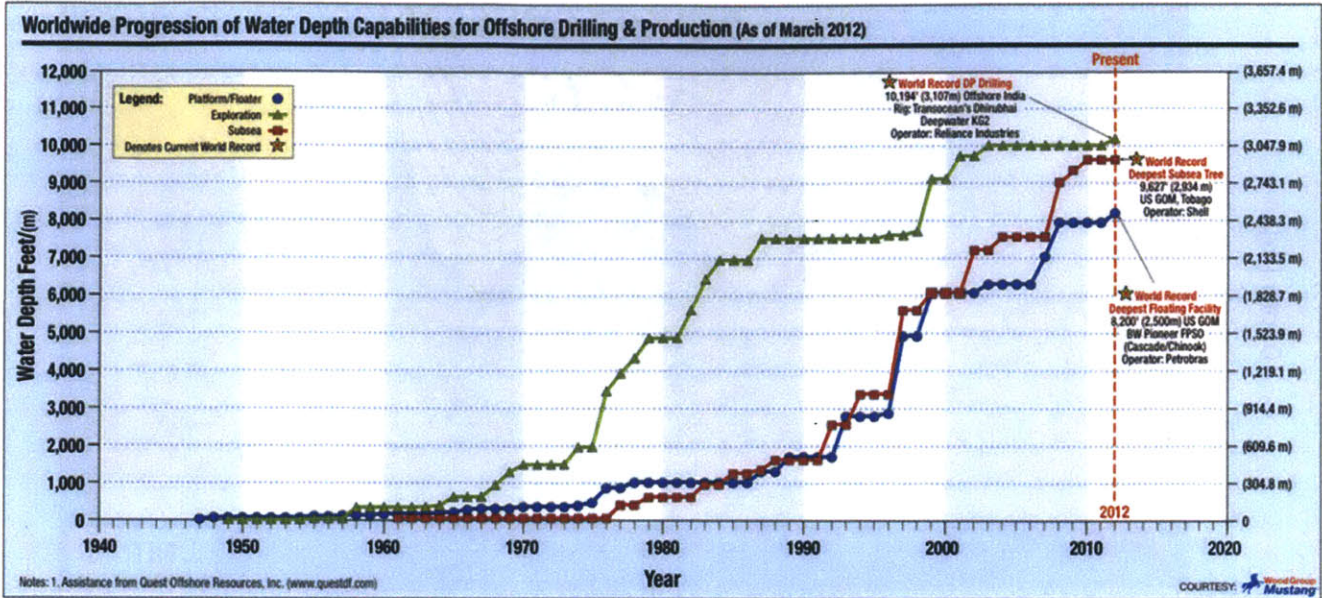


Figure 3-2: Offshore drilling & production depth over time [134]

3.1.2. Temperature

Variance in oceanic temperatures can be affected by seasons, location, and depth. Seasonal temperature changes primarily affect the top 200 meters, known as the Epipelagic zone (sunlight zone). The greatest thermocline is in the Mesopelagic zone, between roughly 200 m and 1 km in depth. After one km, once the Bathypelagic (midnight) zone has been reached, average temperatures are maintained around 3.8° C. Even at the equator, the average temperature below 1 km is 4.9° C and remains fairly uniform throughout the year [135]. Global average ocean temperatures from 1982 to 2004, as illustrated in Figure 3-3, showed a dependence on latitude only in the mesopelagic zone; and after one km depth the temperature remained fairly constant at or below 5° C [136].

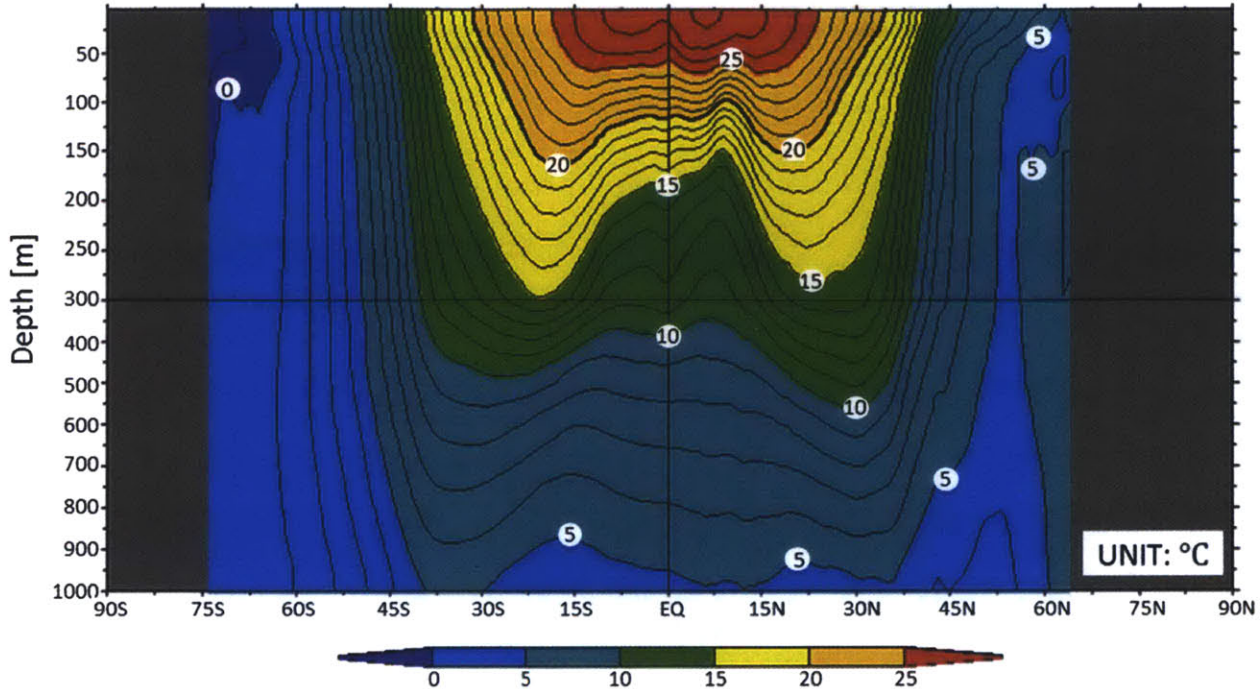


Figure 3-3: Global average ocean temperature dependence on depth from 1982 to 2004 (National Weather Service Climate Prediction Center [136])

3.1.3. Other Environmental Considerations

Other environmental factors to consider may include corrosion, salinity, currents, salt formations, etc. Any system designed to be integrated into the BOP long-term needs to be composed of corrosion resistant components, similar to the BOP stack. Barite and hematite are both corrosive effluents that can be produced from the hydrocarbon production [137]. Salinity should also be considered for systems that are intended to function on the ocean floor for any prolonged period. At 1 km below sea level, the water salinity can range from between 32 and 37 ppt (parts per thousand) with an average salinity of 35 ppt [138]. Methane hydrate crystals (methane clathrate) can also form when methane gas is mixed with water at low temperatures and high pressures, conditions which are common on the sea floor. Depending on the configuration of the mechanism, loading from ocean currents may also need to be considered for supporting the structure and to try to minimize deformations.

3.2. BOP Geometrical Parameters

The top three manufacturers of BOPs include Cameron (Houston, Texas, US) , Shaffer (Houston, Texas, US), and Hydrill (Houston, Texas, US) [139]. The industry produces annular and ram style BOPs, with varying wellbore size and working pressures. The following trend is observed: as working pressure of the components increases, so does the overall height and weight of the unit. This adds to the overall size of the BOP stacks as discussed below.

3.2.1. BOP Stack Height

An array of BOP components is integrated together with a backup power unit and riser interface to create the BOP assembly, as illustrated in Figure 3-1. The BOP assembly typically consists of a combination of both styles, with the rams at the bottom, closer to the well, and the annular BOP towards the top of the assembly. BOP stacks vary in their dimensions predominantly based on the number of components included in the unit as well as its working pressure. As shown in Table 3-2, the heights of highly functioning working pressure BOP stacks (e.g. 103 MPa - 15 ksi and 138 MPa - 20 ksi) range between 15.2 m (50 ft.) and 20.1 m (66 ft.) for a bore diameter of 47.6 cm (18-¾ inch). The height of the Deepwater Horizon, for example, was 16.8 m (55 ft.), with a weight of 4x10⁶ N (450 tons) [1, 5]. There are also 103.4 MPa (15 ksi) subsea BOP stacks that are shorter, and they tend to have smaller bore diameters.

Table 3-2: BOP stack height (Source: National Oil Well Varco Presentation)

	Bore Diameter	Working Pressure	Dimensions (HxWxD)	Estimated Weight
6 Ram	47.6 cm (18-¾in)	15 ksi	600" x 250" x 212"	398 MT
6 Ram	47.6 cm (18-¾ in)	20 ksi	700" x 240" x 212"	496 MT
7 Ram	47.6 cm (18-¾ in)	15 ksi	676" x 240" x 212"	432 MT
7 Ram	47.6 cm (18-¾ in)	20 ksi	762" x 240" x 212"	541 MT
8 Ram	47.6 cm (18-¾ in)	20 ksi	790" x 240" x 212"	562 MT

Source: National Oilwell Varco Presentation (Drilling 20ksi wells with hook loads)

One of the new BOP units designed for higher fluid temperatures (i.e. 200° C) and pressures (i.e. 138 MPa - 20 ksi) is the Cameron EVO with a 47.6 m (18-¾ inch bore), show cased in the Houston Offshore Technology Conference in May 2007. Taking into account the production demand, as well as new BOP stacks introduced into the market, it is estimated that the characteristics BOP stack is approximately 15.2 m (50 ft.).

The weight and height of individual annular and ram components can vary significantly based on the operating pressure and wellbore diameter, as shown in Table 3-3 and Table 3-4 (Hydril and Sunnda manufactured BOPs). The two tables summarizing BOP components are only a representative sample of the items available in the industry.

Table 3-3: Hydril BOP weight (lbs.) as a function of wellbore size and working pressure (see brochures for details). Specification in English units for consistency with suppliers

Company & Working Pressure [ksi]/ Height [inch]		Wellbore Size						
		7-1/16"	9"	11"	13-5/8"	16-3/4"	18-3/4"	21-1/4"
Hydril GK Annular BOP (Brochure)	3	2,715 32"	3,500 37.9"	5,500 39.8"	8,784 45.3"	-	-	-
	5	4,000 36.9"	6,000 41.8"	8,200 48.3"	13,800 54.1"	20,835 61.3"	-	48,000
	10	12,200 48.1"	18,540 55.8"	26,140 63.5"	13,250 54.5"	-	-	-
	15	14,250 54.1"	-	-	-	-	-	-
	20	23,000 59.0"	-	-	-	-	-	-
Hydril Compact Ram BOP	5	-	-	-	-	-	34,000 59.0"	-
	10	-	-	-	-	-	35,000 63.0"	-
	15	-	-	-	-	-	53,100 75.0"	-
Hydril Pressure Control Quik-Loq	10	-	-	-	29,907 62.1"	-	-	-
	15	-	-	-	33,800 68.0"	-	69,100 75.1"	-

Table 3-4: Sunnda BOP weight (lbs.) as function of wellbore size and working pressure (partial list) and double.

Company & Working Pressure [ksi]/ Height [inch]		Wellbore Size						
		7-1/16"	9"	11"	13-5/8"	16-3/4"	18-3/4"	21-1/4"
Annular BOP (Brochure)	2	-	-	-	-	-	-	15,100 52.5"
	3	2,900 29.1"	4,775 32.5"	5,825 32.9"	9,100 40.7"	-	-	-
	5	3,175 30.9"	6,800 36.5"	9,550 41.5"	13,650 45.0"	A	A	A
	10	-	-	23,000 53.0"	32,475 58.8"	-	-	-
LWP, LWS, SL/SLX Style Ram	2	-	-	-	-	-	-	14,455 44.6"
	3	-	2,200 22"	4,096 29.4"	15,350 34"	-	-	-
	5	2,504 26.8"	5,750 29.5"	7,725 33"	15,620 34"	-	-	-
	10	9,900 36.6"	-	20,560 40.9"	23,400 46"	-	-	-
U Style Ram BOP	2	-	-	-	-	-	-	25,150 62.8"
	3	-	-	9,900 49.3"	14,300 53.4"	A	-	-
	5	5,200 44.2"	-	10,200 54.5"	14,800 55.9"	A	A	-
	10	6,400 48.6"	-	11,300 55.9"	18,400 66.6"	A	A	-
	15	-	-	18,400 69.8"	43,250 81.8"	-	-	-

3.2.2. BOP Clearance

The BOP stack clearance refers to the space between the bottom flange of the BOP stack and the seafloor. The clearance is difficult to quantify for all wells due to the fact that silt can accumulate at the base of any given well. Therefore, the system must be designed such that it can be used with no clearance between the BOP stack and the sea floor.

3.2.3. Wellbore Configurations

The objective of this section is to examine the range of two configuration geometries that can occur during a blowout. While there are numerous configurations for failure during blowouts, only the two most predominant configurations are examined here (shown in Figure 3-4). The first configuration consists of having blind rams deploy that are unable to control the flow (i.e. not enough pressure, faulty seals, jammed piston, etc.). As previously mentioned, offshore oil industry wellbores are going towards a standard 47.6 cm (18-3/4 inch) wellbore; thus, the wire entanglement technology should operate at the standard wellbore diameter. The second configuration consists of having an obstruction in addition to the deployed rams. Since frequently the obstructing object consists of tubing with a diameter of approximately 12.7 cm (5 inches), then it is assumed that the average obstruction diameter is 12.7 cm (5 inches) and that the obstruction is somehow interacting with rams [29]. These two configurations can be used to characterize blowout geometries in the the BOP wellbore. The range of each configuration is determined by using the existing geometries of the wellbore, casing, and tubing.

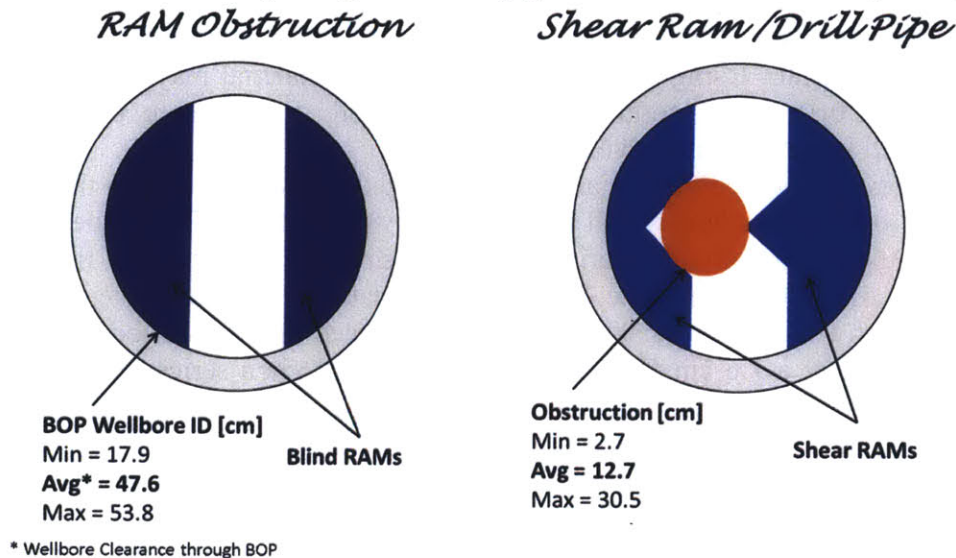


Figure 3-4: BOP obstruction configurations. The clear flow configuration can also have an annular configuration (not shown above).

The interior casing diameter (ID) can range from 9.2 cm (3.64 inches) for a 11.4 cm (4.5 inch) outer diameter (OD) casing up to 48.6 cm (19.12 inch) for a 50.8 (20 inch) OD casing [140]. Variations on the interior casing diameter depend on the stage of construction and depth of the well. Casing diameter must decrease, with constant OD, with the depth of the well due to increases in hydrostatic pressure around the casing and telescoping casing design. For example, while the BOP stack ID and wellhead ID are typically 47.6 cm (18-3/4 inches), the production casing for the Macondo well was 25.1 cm (9-7/8 inch) [1]. Shallow wells can have casings as large as 55.9 cm (22 inches) OD

and 49.5 cm (19.50 inches) ID, which means that the wellbore through the BOP is slightly larger to allow for the casing to be introduced into the open hole.

Casings are normally produced in 12.2 m (40 ft.) sections with double-sided female intermediate joints that connect to standard pipe couplings. Since shearing through the pipe couplings requires more energy, in some BOP stacks there are two shear rams separated by the height of a pipe coupling, guaranteeing that at least one shear ram will not interact with the coupling. The coupling sections make up roughly ten percent of the overall casing length [5]. Tubing can also be inside of the wellbore at the time of blowout and can be used to perform tasks inside of the well like drilling and data collection. The tubing diameter can range from 2.7 cm (1.05 inches) to as large as 17.8 cm (7.0 inches).

3.2.4. Wellbore Interior

Since a continuous medium is to be inserted into the wellbore, the interior surface characteristics of the wellbore are likely to be important. The absolute roughness of carbon steel is 45 um/m according to engineering toolbox but can be as high as 250 um/m. The surface roughness of the interior of the wellbore could affect the interaction of the buckling medium with the wellbore interior. This however will be a topic for future investigation.

3.2.5. BOP Ports

Direct access to the BOP bore is limited. Material can be introduced into the wellbore via one of three methods: the 'top of the bop', a side relief well, or via use of choke/kill ports that are elements of the BOP stack. Inserting material via the top of the well during a blowout can result in the rapid ejection of injected material. Using a relief well to introduce material may not be an option in some cases since it can take up to three months to drill a relief well. Furthermore, drilling a relief well for every production well is not cost-effective.

The third option is to insert material via standardized choke/kill ports on the BOP stack, which are normally used to introduce heavy drill mud into the well at the BOP. Under normal operations drilling mud is circulated through the interior of the drill string to the bottom of the well and exits out of the choke line at the BOP. When the drill string circulation is not available, the kill lines are the auxiliary ports through which additional drill mud is introduced into the wellbore. The choke and kill lines nominally consist of a 7.6 cm (3 inch) aperture accessed via a series of valves. One potential challenge is the meandering path that may be prior to entering the port. The new Cameron Evo BOP has choke valves 7.8 cm (3-¹/₁₆ inches) in diameter and kill valves 10.3 cm (4-¹/₁₆ inches) in diameter [36].

As shown in Figure 3-5, the choke/kill ports are located on the sides of the ram BOPs and provide access to the BOP interior. The mating flange is connected to standard valves where a system can be connected to access the wellbore.

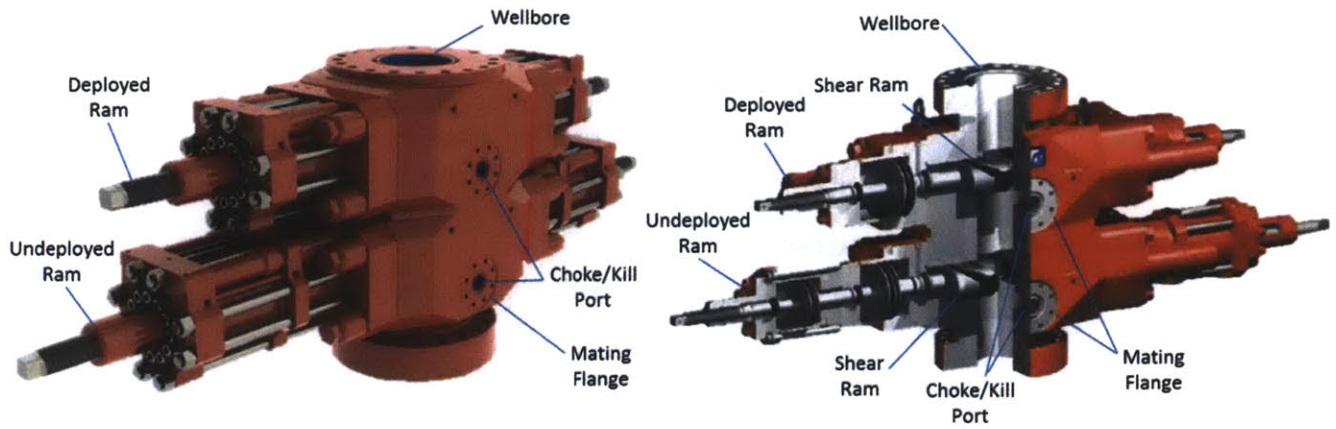


Figure 3-5: Ram BOP from T3 Energy Services showing location of choke/kill ports and cross section of system leading into the wellbore

3.3. Flow Parameters

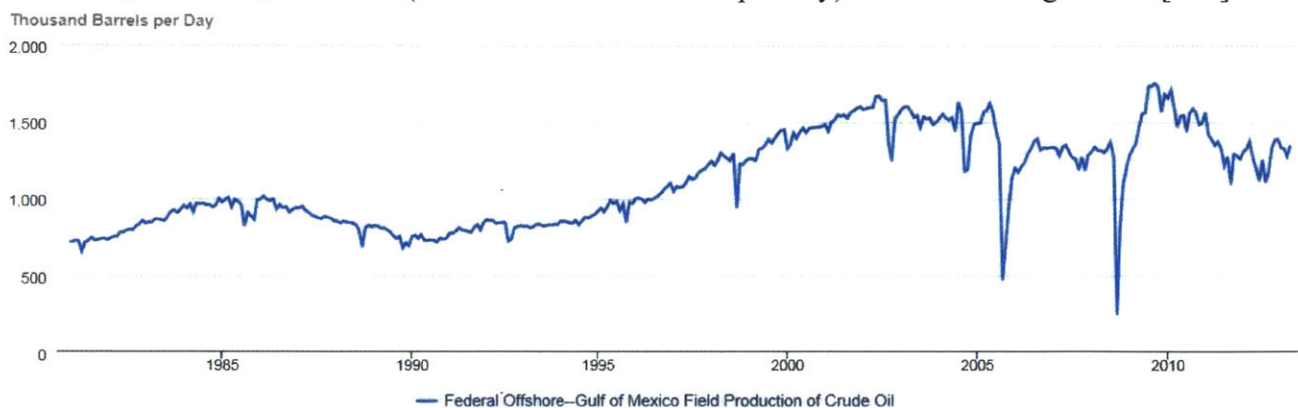
The formation pressure from which the flow is originating, the flow rate, and fluid properties can characterize an uncontrolled flow. The higher the formation pressure, the greater the driving force pushing the fluid medium out of the formation, thus increasing the flow rate.

3.3.1. Formation Pressure

Early oil reservoirs in shallow waters had formation pressures of about 13.8 MPa (2 ksi); current offshore deepwater production pressures can be as high as 138 MPa (20 ksi). Note that formation pressures are provided as absolute pressures. The average offshore deep water BOP is now designed to withstand 103.4 MPa (15 ksi) of pressure at water depths of ~ 3 km (10,000 ft.) [139]. Ultra-deep wells nominally range in pressures from 89.6 MPa (13 ksi) to 124.0 MPa (18 ksi) with temperatures up to 132°C [141]. Between eighty five and ninety percent of the existing wells worldwide have a closed wellhead pressure less than 68.9 MPa (10 ksi), with some deeper wells having pressures as high as 103.4 MPa (15 ksi) according to the International Association of Oil & Gas Producers (IAOGP) [11].

3.3.2. Blowout Flow rates

The production flow rate and the worst-case discharge rate can differ by at least an order of magnitude. The production rate is the quantity of oil produced per day (bbl/day); whereas, the worst-case discharge rate is the free-flowing oil exiting the well in an uncontrolled event. Normal production rate for crude oil wells average between 1,560 and 3,180 liters per day per well (ten and twenty barrels per day per well) [142]. The total offshore Gulf of Mexico crude oil production ranges between 1,840 and 2,760 L/sec (1 and 1.5 million barrels per day) as shown in Figure 3-6 [143].



 Source: U.S. Energy Information Administration

Figure 3-6: Gulf of Mexico crude oil production (Source EIA)

Most wells (i.e. between 85 and 90 percent) have a worst-case discharge pressure flow rate of 184 L/sec (100,000 bbl./day) or less [11]. One reference for the Deepwater Horizon Accident estimated the uncontrolled flow rate at a low of 18.4 L/sec (10,000 bbl./day) and a high of 92 L/sec (50,000 bbl./day) [64]. These flow rates estimates were under constant revision throughout the spill [144]. One reference point for the unrestricted flow can be obtained using the Deepwater Horizon

accident data that released 110.4 L/sec (60,000 barrels per day). At a production well blowout in North Africa the flow rate was determined to be 184 L/sec (100,000 barrels of crude per day) [137].

Therefore, the design should span from a production range of 18.4 L/sec (10k bbl./day) to 184 L/sec (100k barrels per day), which results in Reynolds values from ~6,000 to ~60,000 for an 47.6 cm (18-3/4 inch) wellbore diameter (Refer to Appendix-Calculations-Reynolds Number of Free Flowing Oil Well for details). Thus, under blowout conditions, the flow remains turbulent until it is brought under control.

An independent Reynolds Number calculation performed for the Deepwater Oil Spill accident yielded a Reynolds number of 40,000 at the bottom of the well at a flow rate of 92 L/sec (50,000 bbl/day) at an approximate mean velocity of 3.7 m/s in a 18 cm bore diameter, and a representative kinematic viscosity of crude oil of 10^{-5} m²/s [52].

3.3.3. Fluid Properties

The properties of the uncontrolled flow can vary greatly on the formation, temperature, and pressure. The range of properties is presented here in order to illustrate approximate conditions where wire entanglement is to be generated. The entanglement sensitivity due to variations in fluid properties should be examined in future work.

3.3.3.1. Density

The range in oil density ranges from a low of 719 [kg/m³] and high of 1018 [kg/m³]; however, oil density is assumed to be 839 [kg/m³] on average [49]. For the purposes of this work, the average oil density, independent of temperature, is used unless otherwise stated.

For more detailed calculations the density can be calibrated for temperature using the temperature graphs provided in the Well Production Practical Handbook using Equation 3.1 [140, 145].

$\gamma_o = \frac{141.5}{131.5 + (API^o)}$	Equation 3.1
--	--------------

Where API^o is the stock-tank oil gravity (if the API is greater than 10 it is lighter than water and floats), and specific gravity of oil is referenced to a water density of 1000 kg/m³. Therefore, at 20 API^o, the density is 934 kg/m³ and 1000 kg/m³ at 10 API^o at 15.6° C and atmospheric pressure [140].

3.3.3.2. Viscosity

The dynamic viscosity of heavy crude oil can range from 0.10-10.0 Pa·sec [49, 140]. Anything above 10 Pa·sec (i.e. 1 cp = 1 mPa·sec) is considered tar sand oil, whose viscosity is equivalent to honey at room temperature. The kinematic viscosity of crude oil under blowout conditions is approximately 10^{-5} m²/s, which makes the dynamic viscosity approximately 8.39×10^{-3} Pa·sec (assuming density of 839 kg/m³) [52]. For the purpose of this research, the average dynamic viscosity of crude oil is to be used for first order analysis. The dynamic viscosity of oil (gas free) can also be a function of pressure and temperature of the well. The standard formula for calculating the viscosity of dead oil is known as Beal's correlation, as shown in Equation 3.2⁵ [145]. There are at least two other correlations that can be used Beggs-Robinson and Glaso's correlation that were determined by curve fitting to experimental data.

⁵ Note that the temperature in the equation is to be entered in Fahrenheit, a metric form of the equation was not found in the referenced text.

$$\mu_f = \left[0.32 + \frac{1.8 \cdot 10^7}{(API^o)^{4.53}} \right] \cdot \left(\frac{360}{T_R + 260} \right)^D$$

$$D = 10^{\left(0.43 + \frac{8.33}{(API^o)} \right)}$$

Equation 3.2

Where D is the intermediate power value, API^o is gravity, and T_R (F) is the reservoir temperature. A visual representation of Equation 3.2 can be found in Figure 3-6 for an API ranging between 10 and 60, and temperatures between 37 and 104° C.

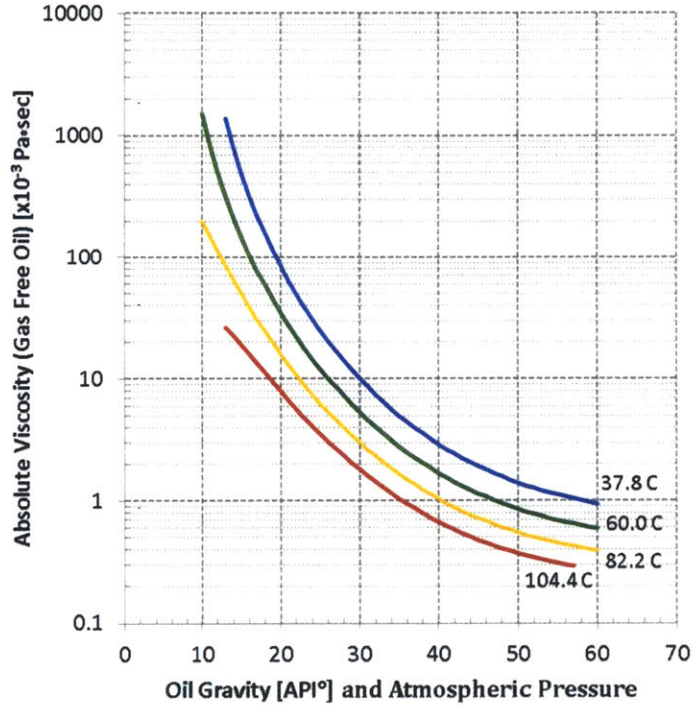


Figure 3-7: Absolute Oil Viscosity as a function of oil gravity and temperature from 37.7 to 104.4° C

3.3.3.3. Temperature

The temperature of the exiting hydrocarbons is a function of the field depth and location, with deeper fields predominantly generating hotter wellhead temperatures. Most wells have a maximum wellhead hydrocarbon temperature of 150° C, as reported by the International Association of Oil & Gas Producers [11]. Therefore, an occlusion medium must be able to withstand pressures and temperatures reaching as high as 138 MPa (20 ksi) and 200° C respectively, for ultra-deep wells [146].

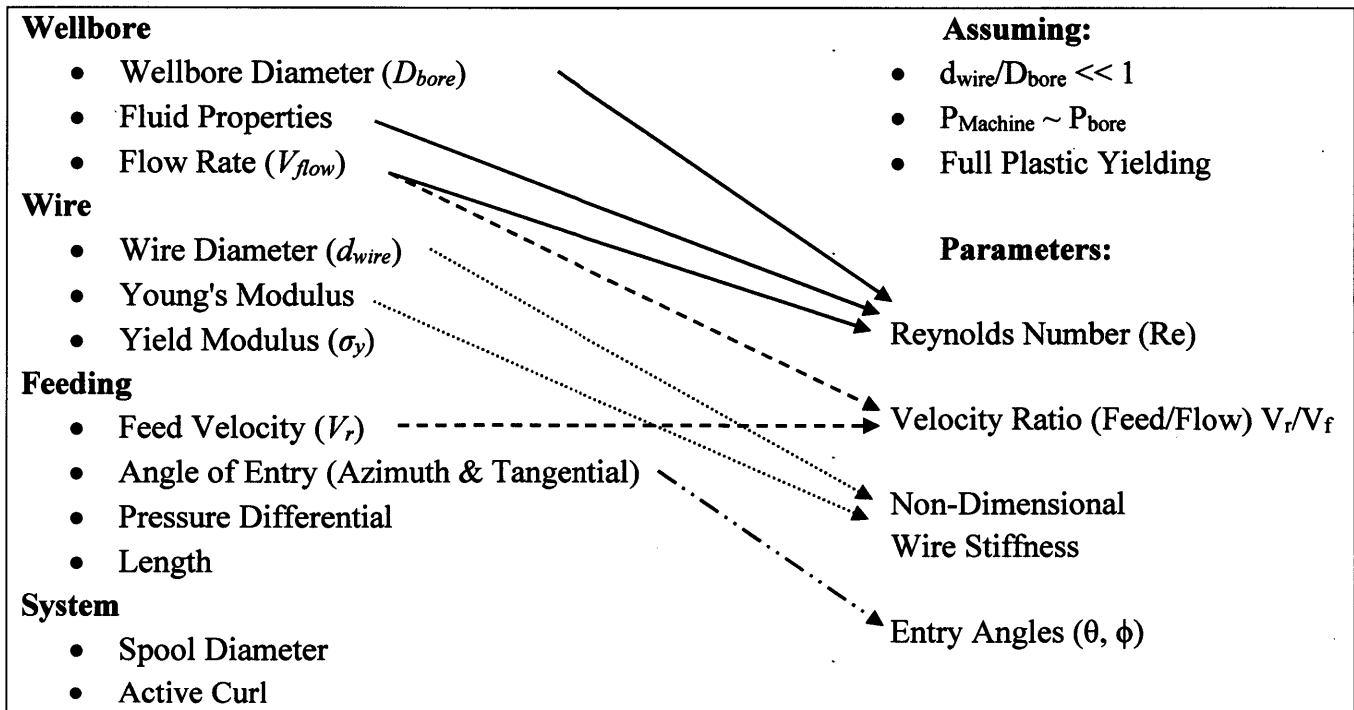
Chp 4.

Bench Level Experiments

Bench level experiments are separated into three sections: generation of wire entanglement, anchoring, and sealing.

The first portion of this chapter focuses on developing an understanding of wire entanglement by identifying all of the parameters that can effect entanglement behavior and consolidating and/or eliminating higher order terms (as shown in Table 4-1). Thus, from a dozen possible parameters the system is reduced to just four parameters for which a sensitivity study can be done while developing an entanglement model. The four parameters evaluated for wire entanglement sensitivity are Reynolds number, velocity ratio, wire stiffness, and entry angles (azimuth & tangential). The velocity ratio is defined by feed velocity of the wire (V_r) to the mean fluid flow velocity (V_f).

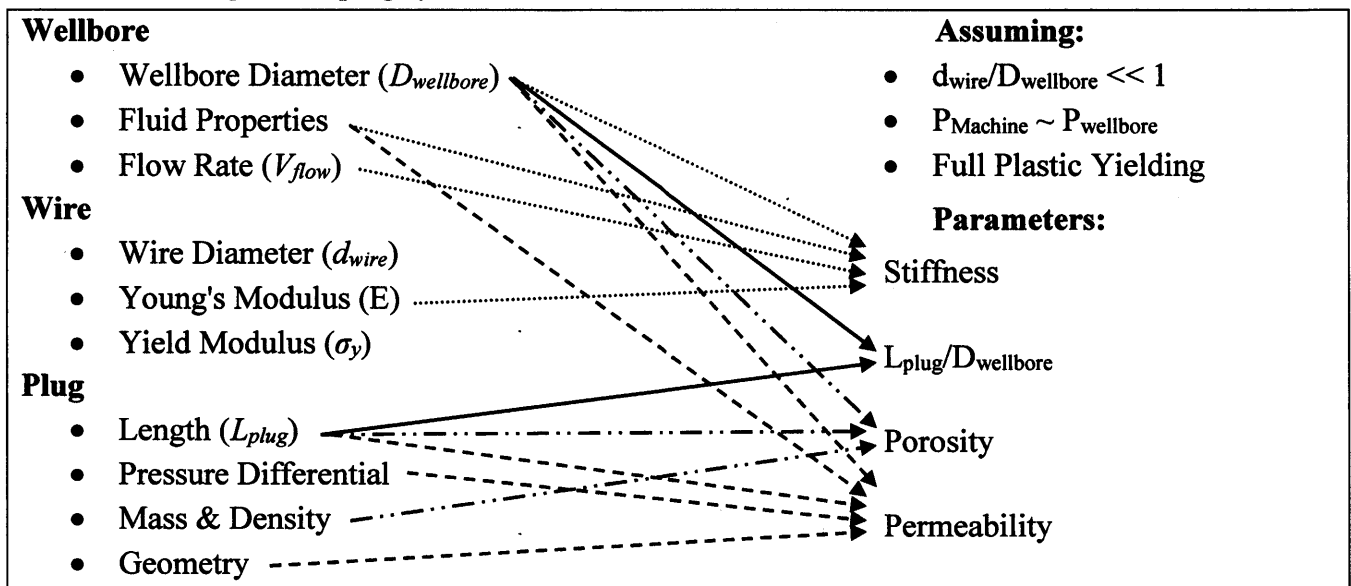
Table 4-1: Wire entanglement parameter synthesis assuming that the diameter of the wire is much smaller than the wellbore diameter, and that the pressure in the machine is about equal to the pressure in the wellbore



The anchoring section pertains to the means by which the mechanical plug is fixed inside of the BOP bore. The loading from the pressure differential is intended to pass through the mechanical plug onto an existing obstruction inside the BOP, such as the partially deployed rams. This section quantifies the geometry and percentage obstruction required to transfer the load from the fluid onto the supporting structure.

The sealing section consists of evaluating the efficiency with which the entanglement can obstruct the flow. This is done by determining an effective permeability of the cohesive mass as well as its ability to resist a pressure head. Three parameters are used to characterize the plug: permeability, porosity, and geometry (as shown in Table 4-2). The assumptions are as follows: 1) wire diameter is much smaller than wellbore diameter, 2) the pressure of the machine is in equilibrium with the pressure of wellbore, and 3) material can undergo fully plastic yielding. Three bench-level experiments were set up at different scales to quantify the nest's ability to seal and withstand the pressure loads.

Table 4-2: Entanglement plug synthesis



4.1. Entanglement Generation in Air Stream

The wire entanglement air stream experiment is used to prove feasibility prior to investing in a fluid system. The objectives of the air experiment are: 1) design a wire feeding mechanism, 2) identify critical components of the design, 3) setup data acquisition, and 4) develop an understanding for entanglement parameters.

4.1.1. Sizing Considerations

Sizing considerations must be considered when designing the experimental setup. The experimental apparatus should be less than 2.5 meters in length, and be designed to operate with both laminar and turbulent flows through varying inlet air pressure (max 0.69 MPa - 100 psi). The calculated maximum pipe diameter is ~ 33 mm, considering two meters (79 in) of length for the developing region and assuming that it requires 60 pipe diameters to reach fully developed flow. A bench level experiment demonstrated that with a 25.4 mm (1.0 in) diameter pipe the average air velocity is around 3.3 m/s, resulting in a Reynolds number of 5,030^{††} at a pressure inlet of 0.48 MPa (70 psi). Therefore, the flow regime at the feeder can be changed from laminar to turbulent and vice versa by changing the source/inlet pressure. The design converged on a 25.4 cm (1 in) pipe interior diameter.

An experimental approach was taken to account for: 1) air compressibility, 2) temperature dependence on pressure, 3) sudden expansion at the inlet, and 4) backflow in the developing region. At the inlet the fluid medium undergoes a rapid expansion; the loss coefficient for the inlet region is $K \sim 1.0$ based on geometry ($d/D \sim 15\%$) [147]. The fluid (air) diffuses into the developing region, eventually leading to a steady state flow. Since air is a compressible fluid whose temperature varies with pressure, it was easier to perform a small-scale experiment to determine if the flow is laminar or turbulent. The steady state fluid velocity is measured with a hot wire anemometer (Omega hot wire anemometer HHF1000R) to ensure that the pipe diameter is small enough for turbulent flow.

As shown in Figure 4-1, the mean air velocity as a function of inlet pressure can change from a mean of 1.3 ± 0.2 m/s to 3.3 ± 0.2 m/s for inlet pressures of 0.14 MPa (20 psi) and 0.48 MPa (70 psi) respectively.

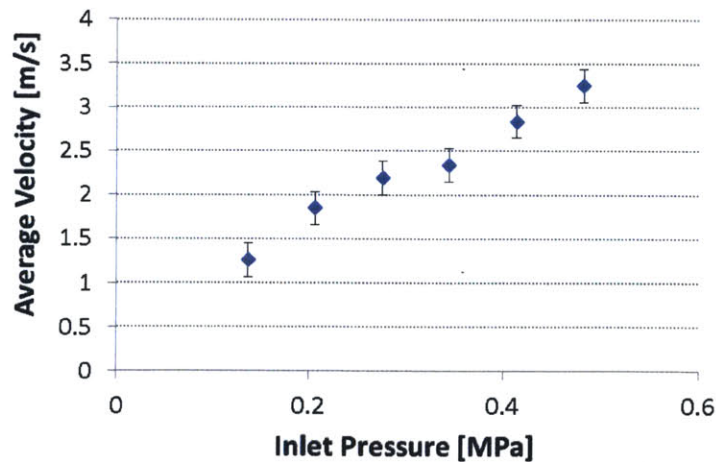


Figure 4-1: Mean air velocity as a function of inlet pressures ranging from 0.14 to 0.48 MPa

^{††} $Re = (1.2 \text{ kg/m}^3 * 3.3 \text{ m/s} * 0.0254 \text{ m}) / (2 \times 10^{-5} \text{ kg/ms})$

4.1.2. Experimental Setup

The experimental setup consists of a device feeding wire into a straight pipe with fully developed flow and a downstream obstruction, representative of a partially deployed ram. Data collection (instrumentation) and hardware make up the two major components of the scale model as shown in Figure 4-2. The following measurements must be taken as part of the experimentation: air pressure, and wire displacement captured via photographs. Pressure is measured prior to the inlet with an analog pressure sensor. Hardware consists of a clear pipe equipped with a custom design wire feeder. The total length of the prototype is two meters. The inlet is for ¼ inch push-to-connect pipe tubing. The main pipe is acrylic round tube with a 3.2 cm (1-¼ inch) OD and 2.5 cm (inch ID). From the inlet to beginning of the wire feeder is a distance of 1.5 m. Instrumentation connections provide a ¼ inch pipe push-to-connect mate, and are secured to the pipe casing via an M5.8 thread. The obstruction section is modular as to allow the tubular sections to be switched. The obstruction can also be placed at a variable distance from the wire feeder using the extension region.

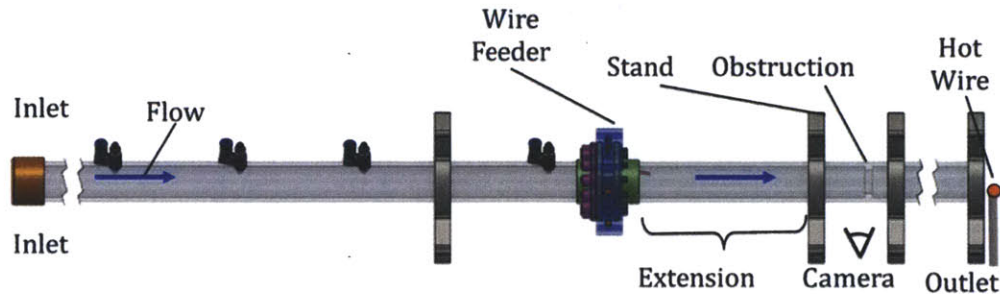


Figure 4-2: Experimental layout and wire system. The diameter of the pipe is 2.54 cm (1 in) and the length is ~ 150 cm.

4.1.3. Feeder Design

The purpose of the wire feeder is to continuously feed wire into the channel. The main housing for the wire feeder is clear to enable visualization of the dynamics of the string entering the (air) fluid flow. There were several design options for feeding the wire into the channel, which will be discussed later; the design chosen to feed wire in this model is comprised of two disks pressing the wire through a guide hole. Figure 4-3 shows a cross sectional view of the wire feeding mechanism. The disks are synchronized via a pair of gears. Setscrews (4-40) secure the disks and gears to the shaft. A hexagonal coupler is used to rotate the driver shaft to spin the disk feeding mechanism. As the disks spin, wire entering from the external guide is gripped by the disks and fed into an interior guide leading into the fluid flow region.

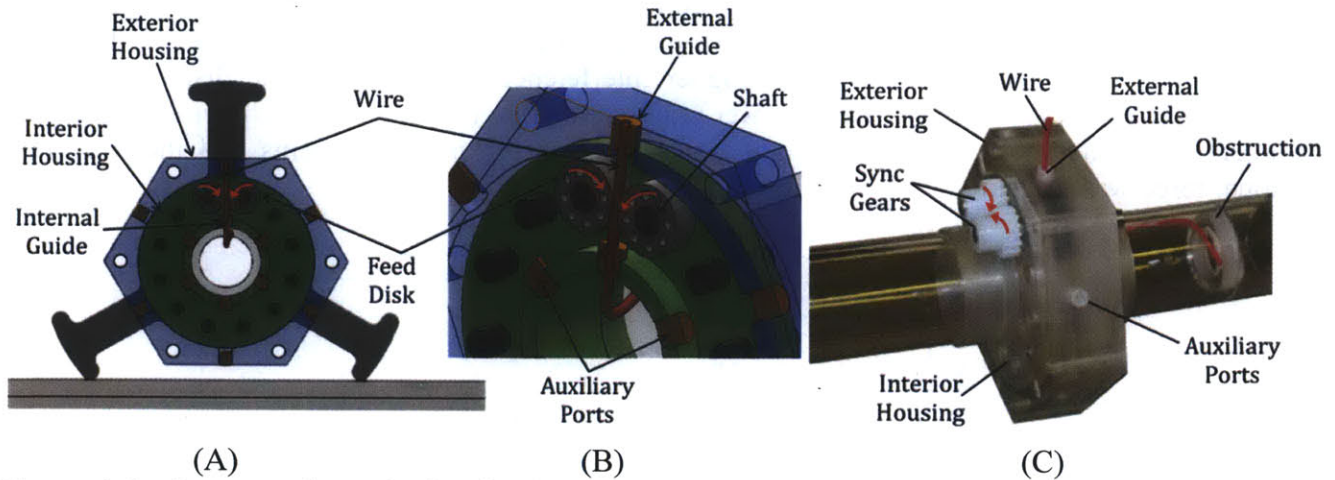


Figure 4-3: Cross section of wire feeding mechanism. A) is the front view showing the exterior housing around the mounting unit containing size entry ports. B) Wire entering through the external guide and being pushed by the drive wheels into the flow chamber through an internal guide. C) Photo of system showing the synchronizing gears that link the motion of the feed disks.

To minimize the number of parts, shaft bearings were incorporated into the plastic housing. The design was made to allow for six wires to be fed simultaneously, driven by a single motor/source. Unused ports can be closed using 10-32 plastic set screws. Open ports consisted of 10-32 plastic set screws with a hole in the center, with the hole sized for the wire gauge being fed. A single shaft connected to a hexagonal coupler, connected to a flexible screwdriver extension, is used to drive the mechanism. As the driver spins the disks rotate in opposite directions due to the gearing, as shown in Figure 4-3.

4.1.3.1. Feeder Disks

The design of the feeder disks is crucial to effective insertion of wire into the channel. The feeder disk must be able to provide a force on the wire that is greater than the buckling force. Several designs have been considered and evaluated as part of the feeding mechanism as shown in Figure 4-4. Initial feeding test using rubber disks showed that unless there is a significant compression force on the wire during feeding the wire slips. The rubber disk tests were performed with a minimally stiff wire ($B_r \sim 3.5 \text{ N}\cdot\text{m}^3$). The wire would slip instead of buckle.

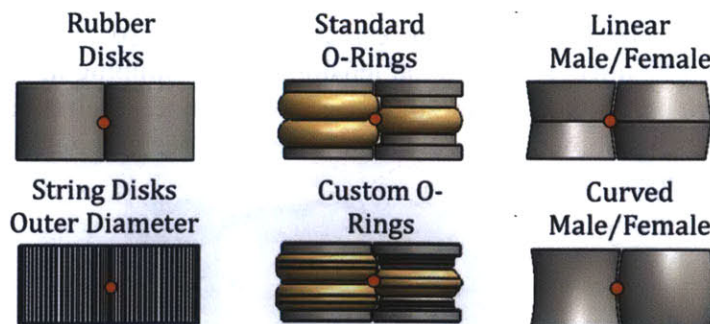


Figure 4-4: Feeder disk concepts

The rubber disks proved to be ineffective, even with centering channels the wire could move along the contact length of the rubber disks. The standard (circular cross section) O-ring design was implemented to correct for the travel; however, the design also depended on compression of the O-

rings to generate enough friction to push the wire to buckle. Since the force required to buckle wire depended on the compression between the disks that are used to push the wire, a series of disk were made with varying interior diameters. A higher interference ratio between the disks, resulted in increased friction but also the amount of power required to drive the motors. As shown in Figure 4-5, the interior diameter holding the O-rings was increased in 0.5 mm increments and the maximum frictional force was measured for two different wires.

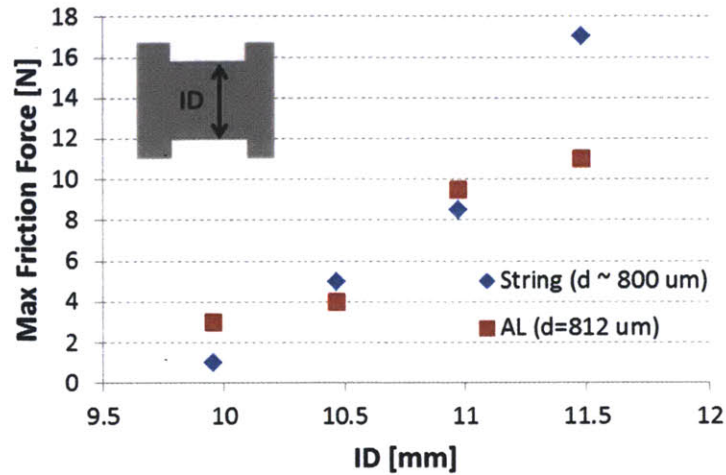


Figure 4-5: Max friction force (N) as a function of interior diameter of the O-ring holder using three standard orings (0.301 IDX0.70W) with an aluminum wire (812 um diameter) and string wire (812 um). Locking the wheels and pulling till slipping measured the maximum amount of force exerted by wheels.

Based on the data above the standard O-ring configuration could be used depending on the buckling force for a given wire. For example, the buckling force for an aluminum wire ($E=70$ GPa) with a diameter of 812 um in a cantilever configuration ($c=2.47$) over the 2.54 cm tube diameter tube is roughly 5.7 N (from theory); however, due to imperfections being developed in the wire after passing through the rollers the required experimental force can be lower than the theoretical value. Preliminary tests also revealed that using the O-ring design to push wire demonstrated the ability feed at low speed (lower than 0.25 m/s); as the speed increased slipping would occur between the roller surface and wire. Therefore, the feeding mechanism needs the ability to push wire at much larger forces with minimal slipping.

The knurled driving wheels proved to be effective against slipping. A pull test showed that an aluminum wire (diameter 812 um) yields in axial tension prior to slipping through two knurled wheels, and the knurled wheels are capable of driving the wire into the tube. Preliminary tests were performed using brass knurled wheels, as shown in Figure 4-6. The final design could also use knurling wheels to establish a consistent pattern.



Figure 4-6: Brass knurled drive disks with a center channel to prevent the wire from traveling

4.1.4. Non-Dimensional Entanglement Stiffness Coefficient

The non-dimensional entanglement stiffness coefficient is derived based on Shelley’s stiffness coefficient for the dynamics of a flag waving. The non-dimensional entanglement stiffness is defined as the rigidity per unit area of the wire compared the fluid loading as shown in Equation 4.1, which is a modified version of that used by Shelley et al [103]. Combining like terms results in Equation 4.2, which is then further broken down to Equation 4.3.

$\pi_e = \frac{\frac{E \cdot I}{2r_w \cdot D_{bore}}}{\frac{1}{2} \cdot \rho_f \cdot C_d \cdot D_{bore} \cdot 2r_w \cdot V_{flow}^2}$	Equation 4.1
---	--------------

$\pi_e = \frac{E \cdot I}{2 \cdot r_w^2 \cdot C_d \cdot \rho_f \cdot D_{bore}^2 \cdot V_{flow}^2}$	Equation 4.2
--	--------------

The drag coefficient C_d for an infinitely long cylinder $L/D > 40$ under turbulent conditions is ~ 1.00 ; therefore the term can drop out for a wire configuration.

$\pi_e = \frac{E \cdot \pi \cdot r_w^2}{8 \cdot C_d \cdot \rho_f \cdot D_{bore}^2 \cdot V_{flow}^2}$	Equation 4.3
--	--------------

4.1.5. Drag Load Deflection

After establishing a reliable feeding system the next step is to characterize wire deflection as a function of wire stiffness (EI) and loading, as shown in Figure 4-7. Since loading is a function of radius, it is non-uniform. For example, as calculated shortly, a laminar flow will impart a fourth order loading along the length of the wire.

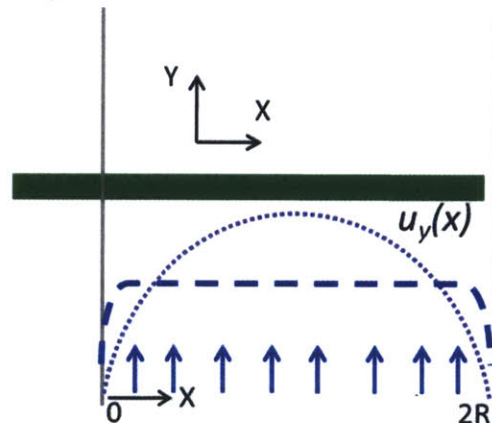


Figure 4-7: Wire deflection induced by drag loading with laminar (purple dotted line) or turbulent (blue dashed line) flow.

4.1.5.1. Laminar

Determining the deflection on the wire starts by first finding the velocity of fluid flow as a function of radius. For laminar flow the velocity is a quadratic function, as shown in Equation 4.4, as a function of radius (r), BOP bore radius (R), and depth into the flow (x) where r equals $x-r$ [147].

$u_y(r) = u_{\max} \left(1 - \frac{r^2}{R^2} \right)$ $u_y(x) = u_{\max} \left(1 - \frac{(x-R)^2}{R^2} \right)$	Equation 4.4
---	--------------

The velocity profile (Equation 4.4) can be combined with the drag force (Equation 4.5) to find the discretized drag load as a function distance into the well as shown in Equation 4.6. For the laminar case the loading on a fully exposed wire length (D_{bore}) is of the shape of a fourth order polynomial, as shown in Figure 4-8.

$F_{drag} = \frac{C_D \cdot d_w \cdot \rho \cdot (u_y(x))^2 dx}{2}$	Equation 4.5
$F_{drag} = \frac{C_D \cdot \rho \cdot d_w \cdot u_{\max}^2 (x^4 - 4x^3R + 4x^2R^2)}{2R^4} dx$	Equation 4.6

The shape of the deformed wire can then be calculated by doing a force and moment equilibrium on the wire, as shown in Figure 4-8.

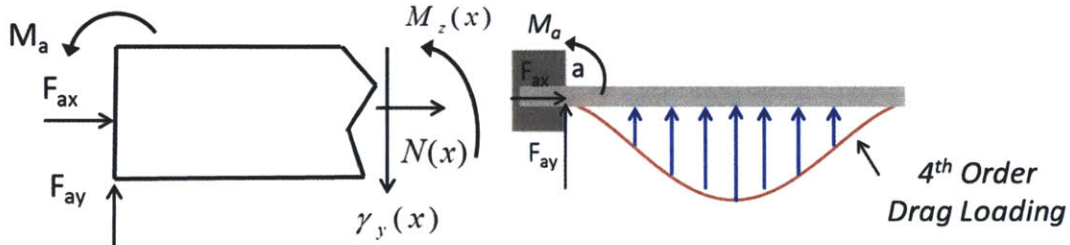


Figure 4-8: Fourth order poly deflection for laminar conditions

The calculated reaction forces and moments at the base for the laminar conditions are shown in Equation 4.7.

$\sum F_x = 0 \Rightarrow F_{xa} = 0$ $\sum F_y = 0 \Rightarrow F_{ya} = -\frac{8}{15} C_D \cdot \rho \cdot d_w \cdot u_{\max}^2 \cdot R$ $\sum M_a = 0 \Rightarrow M_a = -R \int_0^{2R} F_{drag}$	Equation 4.7
--	--------------

A moment balance about the base is used to determine the moment as a function of length along the wire, as shown in Equation 4.8, where x'_R is the equivalent location of the applied load.

$N(x) = 0 \quad \gamma_y(x) = \int_0^x F_{drag} + F_{ay}$ $M_z(x) = x \cdot F_{ya} + (x - x'_R) \int_0^x F_{drag} + M_a$	Equation 4.8
--	--------------

The displacement can be obtained from the moment by integrating twice and applying the following boundary conditions: 1) angle at base is zero, and 2) displacement at base is zero.

As shown in Figure 4-9, the displacement varies with the non-dimensional stiffness which can be altered by changing materials (left) or drag loading (right).

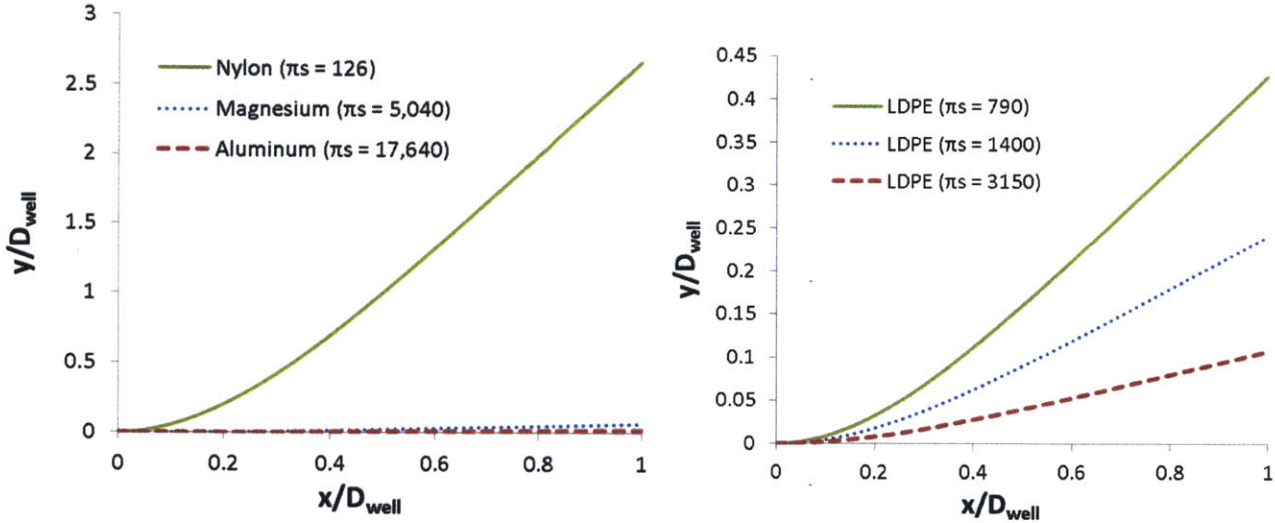


Figure 4-9: Deflection shape for laminar flow conditions. On the left is changing the non-dimensional stiffness by changing materials ($E_{al} = 70$ GPa, $E_{mg} = 45$ GPa, $E_{ny} = 2$ GPa) and keeping the flow rate to 1gmp. On the right is changing the non-dimensional stiffness by changing the flow rate (0.32 L/sec (5 gpm), 0.47 L/sec (7.5 gpm), and 0.64 L/sec (10 gpm)) for a wellbore diameter of 2.54 cm, and wire diameter ($E_{LDPE} = 0.5$ GPa) of 800 μ m.

4.1.5.2. Turbulent

The approach for solving the wire deflection due to turbulent flow is the same as that for laminar flow. The primary change in the solution is replacing the velocity equation to the turbulent velocity profile shown in Equation 4.9.

$u_y(r) = u_{\max} \left(1 - \frac{r}{R}\right)^m \quad \frac{1}{9} \leq m \leq \frac{1}{5}$	Equation 4.9
--	--------------

The calculated reaction forces and moments for the turbulent conditions are shown in Equation 4.10.

$\sum F_x = 0 \Rightarrow F_{xa} = 0$ $\sum F_y = 0 \Rightarrow F_{ya} = -C_D \cdot \rho \cdot d_w \cdot u_{\max}^2 \cdot \frac{R}{(2m+1)}$ $\sum M_a = 0 \Rightarrow M_a = -R \int_0^{2R} F_{drag} = -2R \int_0^R \frac{C_D \cdot \rho \cdot d_w \cdot u_{\max}^2}{2} \left(\frac{x}{R}\right)^{2m} dx$ $M_a = -C_D \cdot \rho \cdot d_w \cdot u_{\max}^2 \cdot \frac{R^2}{(2m+1)}$	Equation 4.10
--	---------------

Due to the asymmetry of the turbulent velocity equation, a set of two independent equations have been used to calculate the drag force as a function of x throughout the entire wellbore diameter extending from zero to two radii, as shown in Equation 4.11.

$F_{drag} = \frac{C_D \cdot \rho \cdot d_w \cdot u_{\max}^2}{2} \left(\frac{x}{R}\right)^{2m} dx \quad 0 < x < R$ $F_{drag} = \frac{C_D \cdot \rho \cdot d_w \cdot u_{\max}^2}{2} \left(\frac{2R-x}{R}\right)^{2m} dx \quad R < x < 2R$	Equation 4.11
---	---------------

As shown in Figure 4-10, the drag loading imparted on the wire due to a turbulent flow is higher than a fourth order polynomial and depends on the m flow parameter.

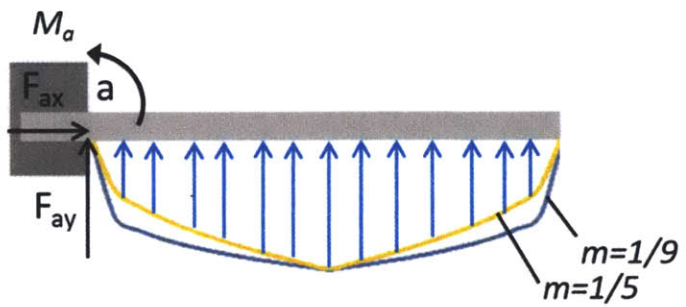


Figure 4-10: Turbulent loading shape over the length of the full wellbore

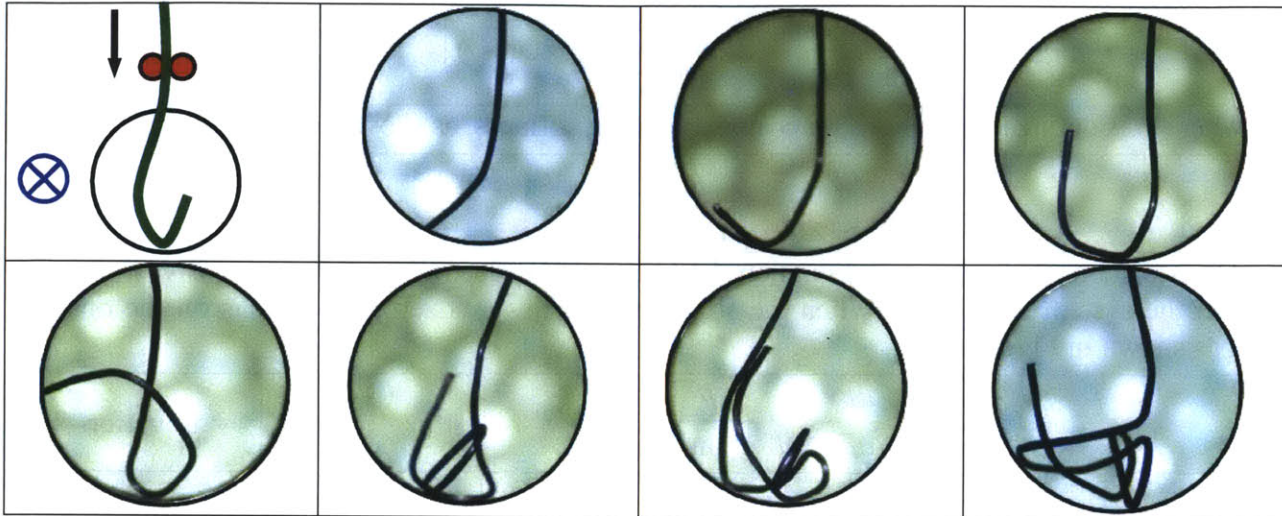
The moment of the wire as a function of length is determined using the same moment balance system as the laminar conditions from Equation 4.8 using the turbulent drag loading equations. However, given that the deflection may be considerable for turbulent flow, then it is best to apply other forms for solving the structure like finite element analysis and discretized solution to account for the change in drag coefficient as a function of the orientation of the wire with respect to the flow.

4.1.6. Entry Buckling Behavior

Prior to looking at the full entanglement configuration, it is crucial to understand how the wire behaves at the onset of buckling which leads to entanglement. As the wire enters touches the opposing surface of the inner tube it can experience three forces: tangential loading, axially compressive loading, and the distributive load from fluid drag. The tangential loading is due to the friction between the wellbore and the wire tip. The compressive loading is the vertical force component on the wire that is a reaction force generated by the feeding operation. Depending on the magnitude of the loading parameters the wire can buckle and deform to the lowest energy state or deflect. Table 4-3 shows

experimental time elapse photos of the initial buckling behavior of the wire in contact with the tube wall, examining the buckling behavior without fluid loading.

Table 4-3: Experimental elapse images of entanglement initiation



4.1.7. Buckling on entry

Three structural models, Table 4-4, are provided to give an insight into the onset of entanglement with varying functionalities. None of the models provided capture the full post buckling behavior. A discrete model may have to be created to model the entanglement buckling behavior.

Table 4-4: Entanglement buckling models.

Model	Onset Buckling	Curved	Fluid Loading	Post-Buckling
Flexural Member	X	0	0	0
Buckling Curved Member	X	X	0	0
Curved Member with Distributive Loads	X	X	X	0

4.1.7.1. Flexure Member

The flexure member model is adequate for a wire that is experiencing a tangential and axial compressive loading, as shown Figure 4-11 [148]. The flexure member applies when the deformed curvature of the wire is small, the stiffness of the wire is large, and the fluid drag negligible.

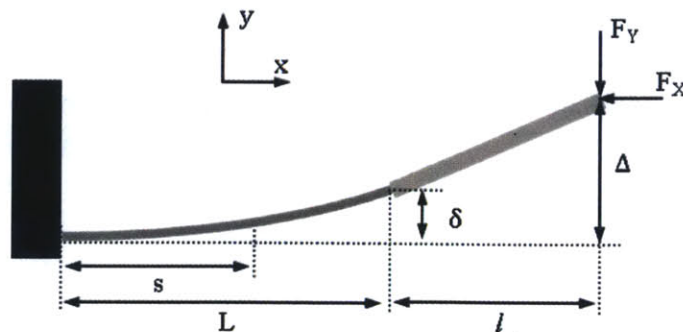


Figure 4-11: Flexure member onset of buckling model

The deflection as a function of length, applied loading, and the geometry is calculated using Equation 4.12.

$y(x) = \frac{L \cdot F_y}{\omega \cdot F_x} \left(\tan(\omega) \cos\left(\omega \frac{x}{L}\right) - \sin\left(\omega \frac{x}{L}\right) + \omega \frac{x}{L} - \tan(\omega) \right)$	Equation 4.12
---	---------------

where ω is defined as the non-dimensional loading stiffness, as shown in Equation 4.13.

$\omega = L \sqrt{\frac{F_x}{EI}}$	Equation 4.13
------------------------------------	---------------

The stiffness of the flexure, Equation 4.14, is used to determine the compressive force that would lead the system to buckle. When the stiffness goes towards zero, the wire is on the onset of buckling as shown in Figure 4-12.

$k_{\delta_y F_y} = \frac{dF_y}{d\delta_y} = \frac{F_x \cdot \omega}{L \cdot (\tan(\omega) - \omega)}$	Equation 4.14
--	---------------

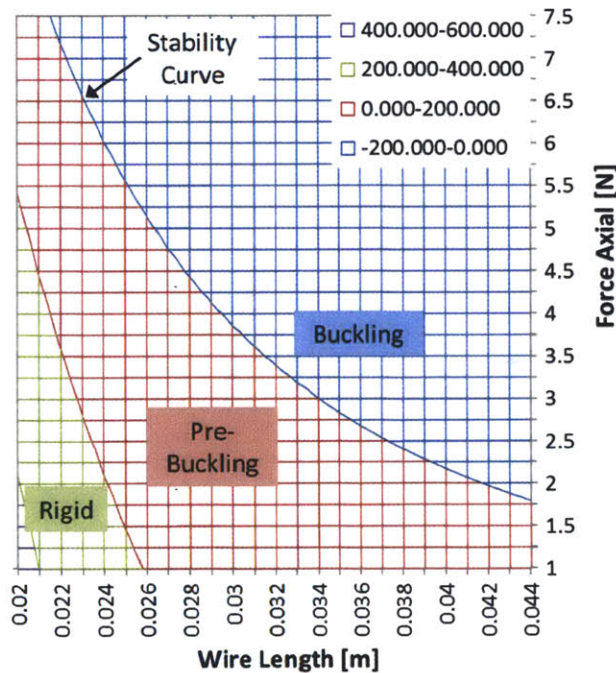


Figure 4-12: Stiffness chart as a function of axial load for ranges in wire length versus axial loads, where the stiffness is in units of [N/m]

Since the flexural model has a limited range of usage, an additional model is presented that accounts for the curvature of the wire.

4.1.7.2. Buckling of Curved Member

The second model is for a purely compressive loading of a pre-curved member with large radius of curvature. The tangential and axial loading can be rearranged, as illustrated in Figure 4-13, to generate a simple curved beam with a compressive load P [98].

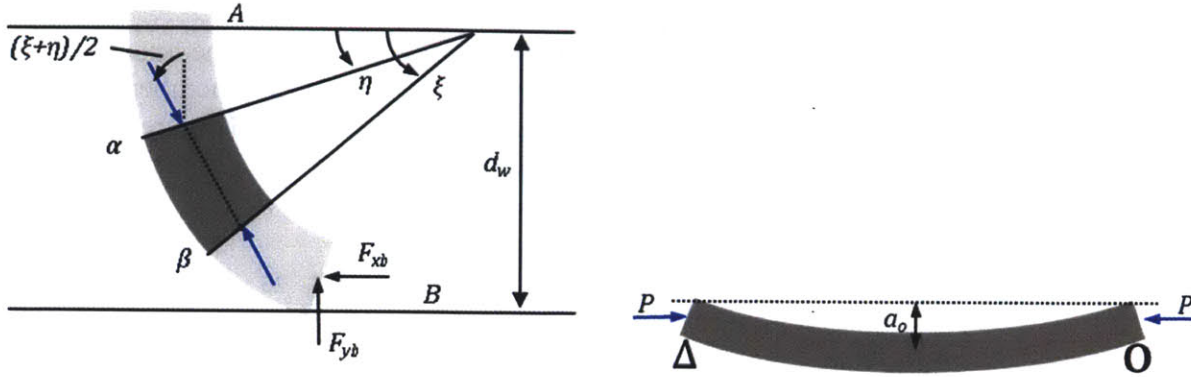


Figure 4-13: Buckling of curved member

In order to use this model the loading must be translated into an axial load across a pre-curved member with a known displacement function. The conversion of the applied loading (F_{xb} , F_{yb}) is converted to vertical an axial force P along the curved member using Equation 4.15.

$P = F_{yb} \cos\left(\frac{\xi + \eta}{2}\right) - F_{xb} \sin\left(\frac{\xi + \eta}{2}\right)$	Equation 4.15
---	---------------

The pre-curved configuration is accounted by a displacement function v_o , Equation 4.16, along the effective length of the beam L_{eff} .

$v_o = a_o \sin\left(\frac{\pi \cdot x}{L_{eff}}\right)$ $L_{eff} = 2 \cdot \frac{d_w}{\sin(\xi)} \cdot \sin\left(\frac{\xi - \eta}{2}\right)$	Equation 4.16
--	---------------

where a_o is the original vertical displacement across the midsection of the beam as calculated using Equation 4.17.

$a_o = \frac{d_w}{\sin(\xi)} (1 - \cos(\xi/2))$	Equation 4.17
---	---------------

The moment balance of the beam for the applied axial load P as a function of the initial shape v_o and additional component v_l is shown in Equation 4.18.

$EI \frac{d^2 v_l}{dx^2} = -P (v_o + v_l) = -P \cdot v$	Equation 4.18
---	---------------

The particular and homogeneous solution for the displacement along the beam is Equation 4.19.

$$v = v_0 + v_1 = \frac{a_0}{1 - (P/P_{cr})} \sin \frac{\pi x}{L_{eff}}$$

$$P_{cr} = \frac{\pi^2 EI}{L_{eff}^2}$$

Equation 4.19

The solution provided can only be used for cases where the P is lower than the buckling force P_{cr} . As the load P approaches critical load the displacement along the pre-curved member increases. The effect of pre-curve radius has is also shown by varying ξ evaluated at 15° (Figure 4-16), 30° (Figure 4-15), and 45° (Figure 4-14) for an aluminum wire (400 μm radius) in a 2.54 cm chamber diameter.

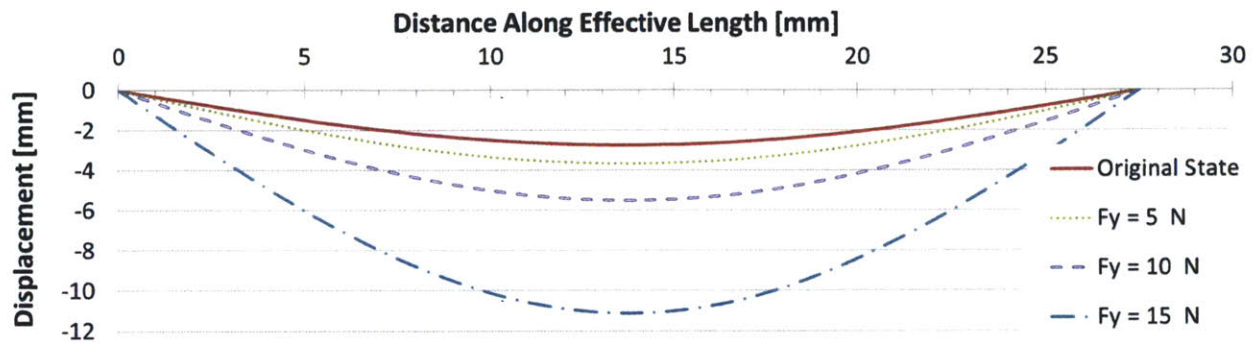


Figure 4-14: Pre-curved member displacement for $\xi = 45$ degree with a 25.4 mm diameter flow channel and aluminum wire 400 μm radius

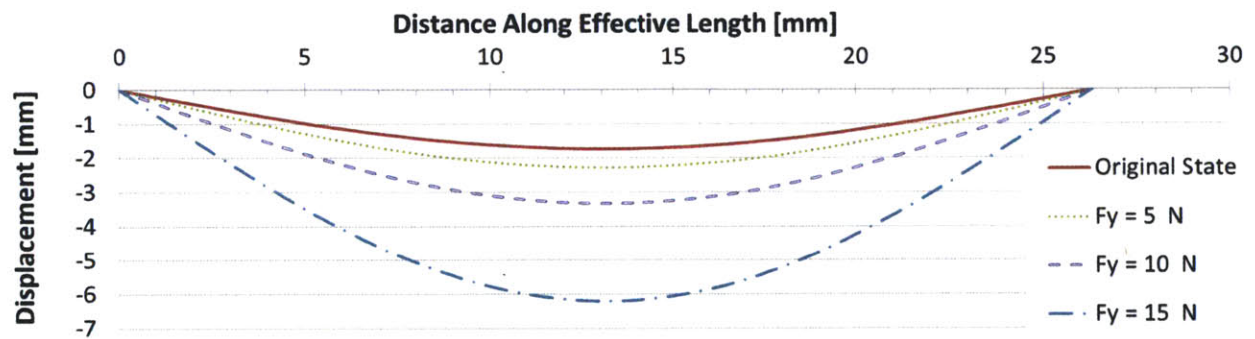


Figure 4-15: Pre-curved member displacement for $\xi = 30$ degree with a 25.4 mm diameter flow channel and aluminum wire 400 μm radius

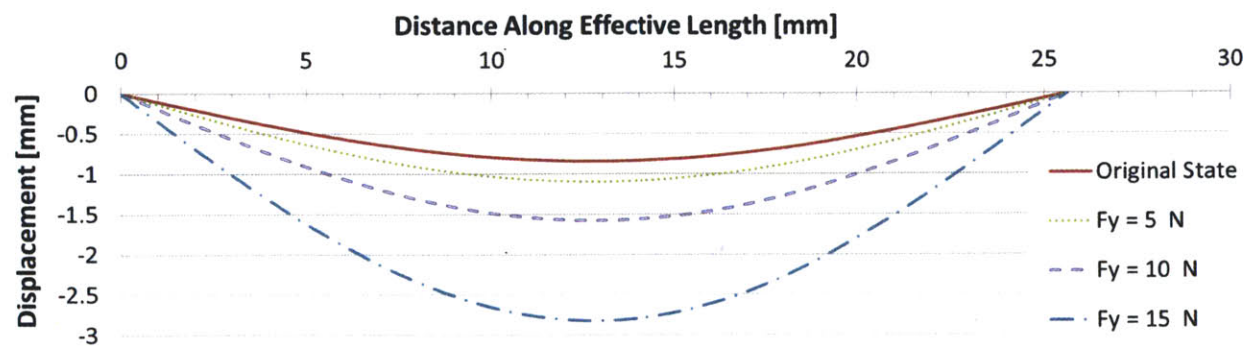


Figure 4-16: Pre-curved member displacement for $\xi = 15$ degree with a 25.4 mm diameter flow channel and aluminum wire 400 μm radius

While the pre-curved model can be used to obtain the shape of the wire due to loading, it is limited to loads below buckling and does not include the drag loading. The buckling of a curved member can be expanded to include fluid drag by adding a distributive load q_f along the length of the beam.

4.1.7.3. Buckling of Curved Member with Distributive Loading

As shown in Figure 4-17, the curved model can be further expanded to include a drag loading as a distributive load.

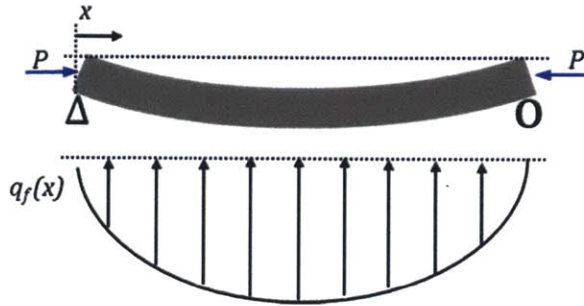


Figure 4-17 Curved member buckling with distributive loading

The challenge of developing this model is quantifying the parameters related to the distributive load q_f for Equation 4.20.

$EI \frac{d^2 v_1}{dx^2} = -P (v_o + v_1) + \frac{q_f x^2}{2} + Ax + B$	Equation 4.20
---	---------------

Due to the growing complexity of the simplified models it is deemed appropriate to move towards finite elements modeling to capture the dynamics of wire.

4.1.8. Results

Different wire inserts were placed inside of the flow stream to capture the behavior of the wire as a function of load.

4.1.8.1. Deflection of wire

The deflection of the aluminum wire (812 μm) into the airflow channel showed no measurable deflection due to the air flow. The non-dimensional entanglement coefficient, Equation 4.2, calculated for this configuration has values greater than 12,700, meaning that the wire stiffness dominates hence why no significant deformation was observed. Therefore, it is expected that as the stiffness of the wire decreases the deflection will increase.

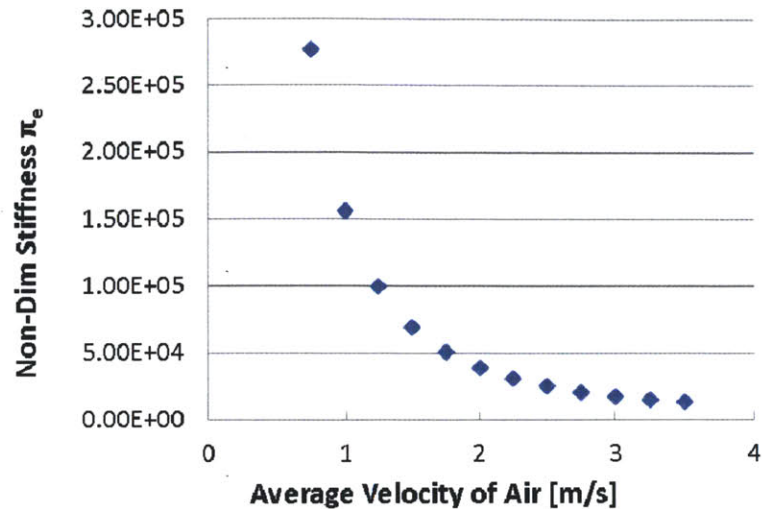


Figure 4-18: Wire non-dimensional entanglement coefficient as a function of the average air velocity for an aluminum wire with a diameter of 812 μm

4.1.8.2. Entanglement modes

Entanglements were observed with both aluminum and nylon wire, as shown in Figure 4-19. The entanglement did not vary with the air speed from flow velocity up to 3.3 m/s due to the drag loading compared to the wire stiffness. Therefore, the models may need to be expanded to include wire dynamics.

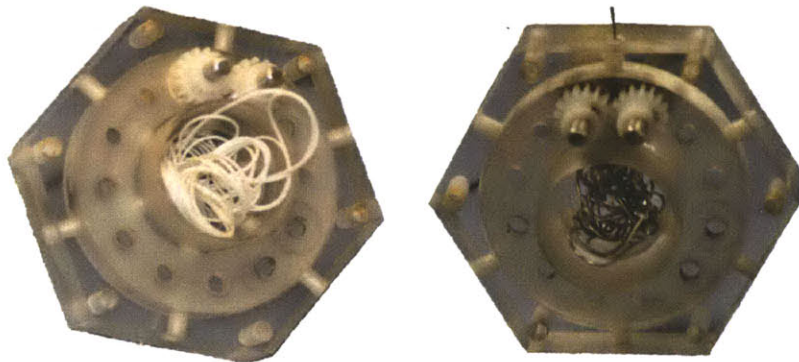


Figure 4-19: String and aluminum wire in air buckling

4.1.9. Discussion

There were several lessons learned from this experimental setup, especially pertaining to the design of the wire feeding unit. The most effective driving wheels for feeding wire into the flow stream are the knurled wheels. The flowing fluid needs to be changed to water to increase the drag loading to obtain a closer non-dimensional entanglement coefficient; therefore, the bearing structural housing needs to be changed from a plastic to an appropriate bearing material such as brass. At high speeds, frictional heat from shaft and bearing heats the surrounding bearing plastic thus leading to wear in the bearing surface. The entanglement also needs to be expanded to include the dynamic interaction of the wire as well as the fluid drag loading.

4.2. Entanglement Generation in Fluid Stream (PI)

The second entanglement experimental setup uses the first prototype to feed wire into a fully developed fluid stream. The wire feeding system can feed at speeds starting at 0.04 m/sec, but due to possible slipping between the wire and the driving wheels the speed must be approximated by measurements. The pump can supply a maximum flow of 37 lpm (9.8 gpm), and min of 2 lpm (2 gpm) thru a 2.5 cm clear pipe. The range in Reynolds number obtained is from 6,300 to 31,000.

4.2.1. Experimental Setup

The functional requirements for this setup include: minimized size, ability to operate in fully developed flow, and ability for controlled feed speed. The flow stream must be fully developed meaning that there must be at least 30 diameters from the fluid entry to the point of insertion. The configuration must be able to provide Reynolds number up to 30,000 with the flexibility to increase using a pump with a higher flow rate. The working fluid must be non-toxic and inexpensive, thus water was chosen as the working fluid. Non-dimensional numbers were used to calibrate the experiment accordingly. To minimize the need for perfect enclosures and watertight seals the feeding assembly is submerged in a tank of water.

The experimental setup is divided into three modules: 1) water flow, 2) wire feeding, and 3) housing. The water flow system consists of a pump pulling water from a reservoir tank and delivering it through a filter, a flow meter, and into the inlet of the housing. After flowing through the housing, the water exits through a flexible hose that ends in the reservoir tank, thus closing the loop. The wire-feeding unit consists of the feeding mechanism, spool, and driving motor. The third module is the housing that directs water flow and keeps the wire feeding mechanism submerged below water.

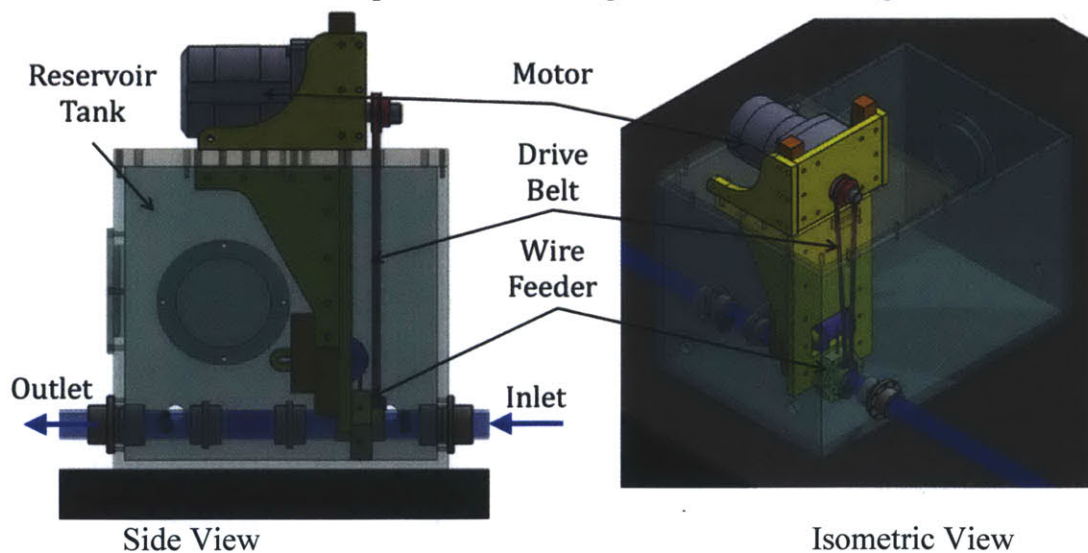


Figure 4-20: Fluid experimental flow layout showing the wire feeding mechanism incorporated into the tank and driven by an external motor.

4.2.1.1. Transmission System

The drive motor is a Bodine brushless DC motor (Model # 3369) with a maximum speed of 500 rpm and torque of 57 N*m (42 ft*lb). A mechanical fuse (10-32 nylon set screw) was introduced in the drive gear to shear off at 4.24 N*m (3.13 ft*lb) of torque, in the case that the drive is jammed. Three belt systems were considered to transmit the torque from the motor to the wire feeder. The first belt used was an mxl timing belt. Initially, the timing belt was selected for its compatibility for water applications; however, at times the belt would skip leading to uncertainties. Therefore the mxl belts were changed for another drive system that would be less sensitive to preloading and misalignments. Posidrive belts were considered to drive the wire feeder without any parasitic skipping. However, fully continuous posidrive (plastic) belts failed over time due to the sudden loads when the wire feeder got jammed. A reinforced posidrive belt (steel core) was also tested and failed as well. The manufacturing process used to make the reinforced posidrive belt leaves a weak area in the belt where the splice is made, which leads to failure. The third timing belt used was a M5 drive chain that proved to withstand the loading and transmit the torque onto the feeder. The disadvantage of using the M5 drive chain is its susceptibility to corrosion over time; thus the system is kept dry until it is used and replaced as needed.

4.2.2. Entanglement Regions

An entanglement is created in a flow field when the stiffness of the wire and drag loads both affect the dynamics of the wire. Therefore, it is hypothesized that there are at least three distinct regions in an entanglement chart: The first region is where the drag loads dominate. The second region is where the stiffness of the wire dominates the behavior. Leaving the third region where both the wire stiffness and drag loading play a role that leads to entanglements. . As shown in Figure 4-21, the regions may be plotted in two different plots Reynolds number versus wire stiffness and Reynolds number versus non-dimensional feed velocity. The goal will be to find the boundary lines of the entanglement regions and the type of entanglements generated.

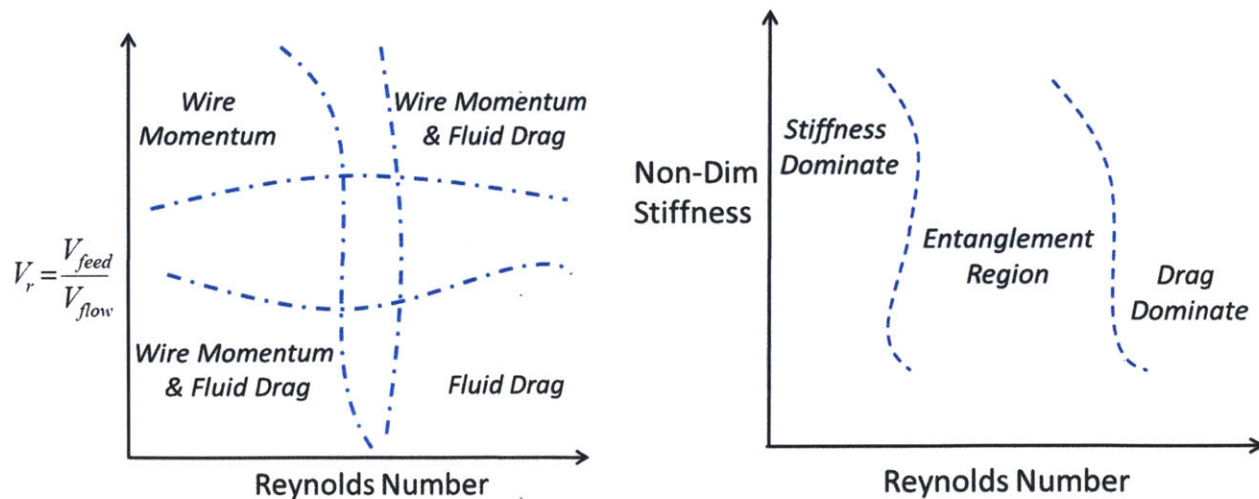


Figure 4-21: Entanglement regions

4.2.3. Experimental fluid data

The initial interaction between the wire and the fluid flow has been characterized into four distinct categories, as illustrated Figure 4-22. In the "streamline" configuration the wire contacts the opposing surface and bends in the direction of the flow stream not generating an entanglement. For the "entry-streamline" configuration an initial entanglement is generated at the leading end but migrates with the flow stream and no further entanglement is created. As the entry velocity increases with respect to the mean flow velocity the wire entanglement enters a "full-still" configuration where the entangled nest is generated in the entry area. As time progress a greater force is required to feed wire into a smaller effective volume (seen experimentally). The preferred entanglement configuration, "full-motion" occurs when there is a balance between the fluid viscous drag forces and the entangled nest generation. The "full-motion" configuration allows for a more uniform entry force to feed the wire and for entanglement growth along the length of the channel.

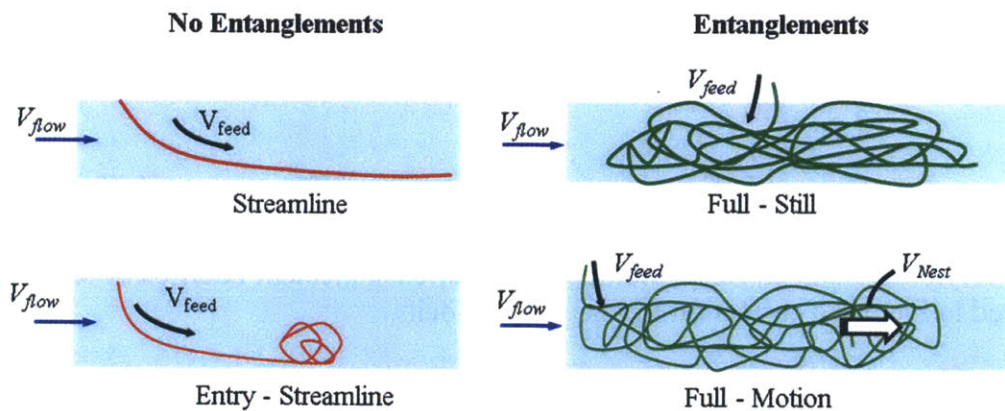


Figure 4-22: Characterization of entanglement behavior

For the small-scale experiments aluminum wire (812 μm diameter) is used to identify the entanglement region. As shown in Figure 4-23, increasing the feed velocity can be used to generate entanglements.

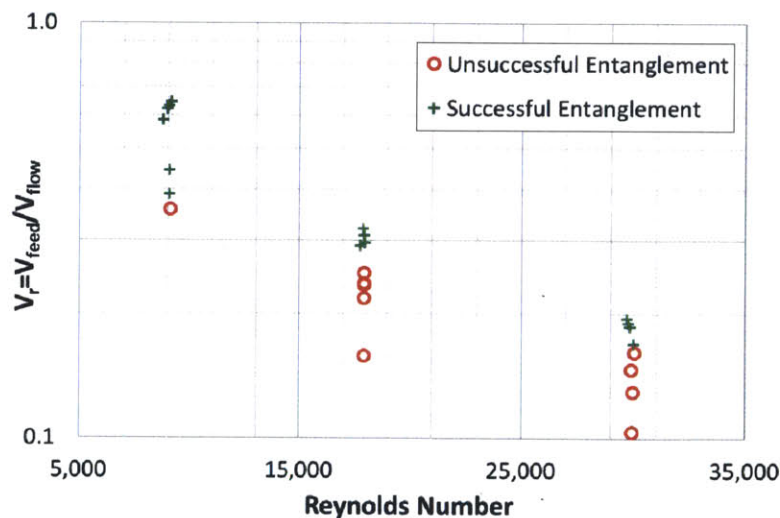


Figure 4-23: Reynolds number versus feed rate for aluminum wire (with a 812 μm radius)

The entanglement stiffness coefficient calculated for the data above is shown in Figure 4-24. Notice that in its current form the non-dimensional entanglement coefficient varies only with flow rate with feed then the non-dimensional stiffness extends from 43,500 at low flow rates ($Re \sim 9,000$) down to 3,950 at higher flow rates ($Re \sim 30,000$). The entanglement values found demonstrates that future work will need to also consider the feed velocity as part of the entanglement coefficient.

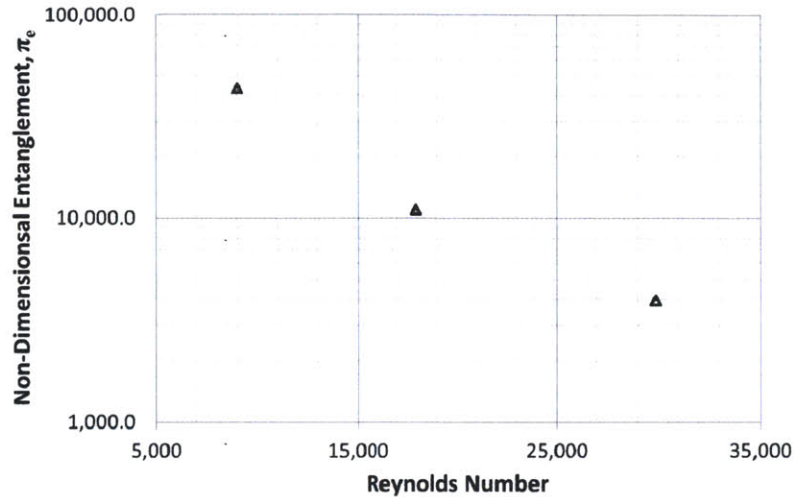


Figure 4-24: Reynolds number versus non-dimensional entanglement coefficient showing that future work may need to include a correction for the entry velocity

4.2.4. Discussion

During the data collection process, it became evident deviations in the entry angle could result in changes in the configuration mode. Therefore, the entry angle of the wire has been confirmed to be a critical parameter that must also be controlled in order to minimize sources of uncertainty. Hence, the second prototype must have a feature that allows for the change in rotation angle and tilt. This work, captured on video, has been captured on video and has been shown to generate a stiff plug with a high porosity (i.e. low compaction). Along with aligning the components it will also be useful to incorporate wire guides that follow the shape of the feeding wheel to further reduce the areas where the wire can buckle and break inside of the machine. Another desirable improvement is to craft the wheels from knurling wheels to avoid inconsistencies in the manufacturing process.

This experimental setup served to identify the regions where entanglement occurs and to emphasize the need to control the entry angle as a critical parameter. The experiments that follow will further explore the angle dependence.

4.3. Entanglement Generation in Fluid Stream (PII)

This section explores the entanglement dependence on entry angles. The following shows the next iteration of the wire feeding prototype using the existing submerged experimental flow loop. The two key features controlled are feeding angle θ and tilt angle ϕ .

4.3.1. Experimental Setup

The experimental setup consists of the feeding machine submerged in a water tank, powered externally by a ~290 W (3/8 HP) motor^{**}. The driving method has been changed to a M25 chain to eliminate issues with slipping between the drive gear and belt. The transmission ratio (driving/driven) from the sprocket on the motor (18 teeth) to the feeding machine (9 teeth) is a half. The flow is changed from 7 lpm (2 gpm) to 36 lpm (9.5 gpm) yielding a Reynolds number range from 6,300 to 31,000. In the case of jamming, a mechanical fuse is triggered in the junction between the sprocket and the motor shaft (done via stripping a key). The key is sized so that it will shear at 3.6 N*m of torque, less than the rated torque of the motor (56 N*m).

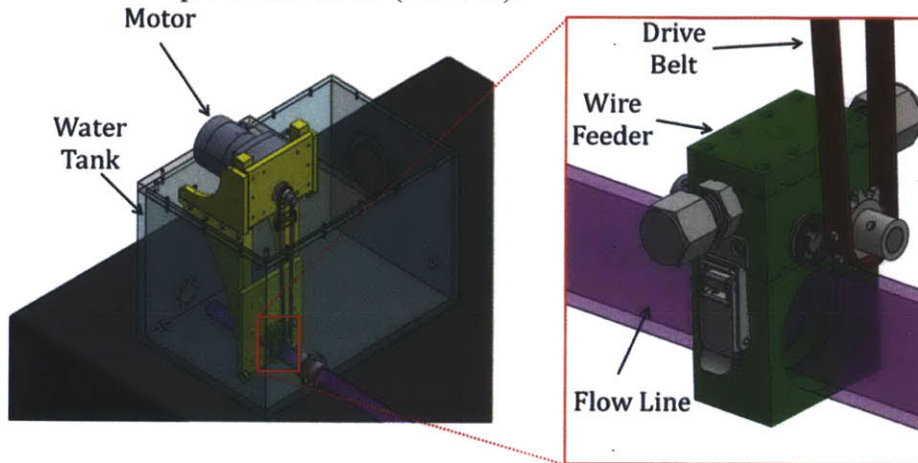


Figure 4-25: On the left is a water tank with a 2.5 cm (1 inch) in diameter pipe that connects to the submerged wire feeder. A motor on top of the tank drives the wire feeder via a belt system.

4.3.1.1. Wire Feeder Design

The wire feeder, illustrated in Figure 4-26, is composed of three stages: 1) entry port, 2) drive stage, and 3) closing cap. The three stages of the wire feeding mechanism are designed to connect with a high degree of precision using a kinematic coupling. Stainless steel spheres 3.2 mm ($1/8$ inch) in diameter are placed in holes 1.9 mm (0.075 inch) deep. The matching 45° v-grooves were made for matching against the spheres. A gap of 250 μ m (0.01 inch) was left to allow for a close fit when the components are assembled and pressed using an arbor press [149]. The result is a highly precise matching between each of the stages, which allows for the centering of the all of the components across all three stages to minimize misalignments that could lead to buckling. For ease of assembly, spring loaded latches are used to easily remove stage two and three from stage one. The spring-loaded latches also provide a preload for aligning the kinematic couplings. Four 6-32 screws 3.2 cm (1.25 inch) long are used to preload all of the stages after initial alignment. The path of the wire inside of

^{**} Parallel Shaft Brushless DC Gearmotor (Model # 3369); Speed (rpm): 500; Rated Torque (lb-in): 42; Rated Voltage: 130V; Amps (24V model): 2.6; Amps (130V model): 2.6; Peak Torque (lb-in): 86; Motor HP: 3/8; Gear Ratio: 5; Radial Load (lbs): 60; Length XH (inch): 8.189; Weight (lbs): 14

the feeding machine is always supported by a wire guide thus increasing the amount of energy required for the wire to buckle inside, as shown in Figure 4-26.

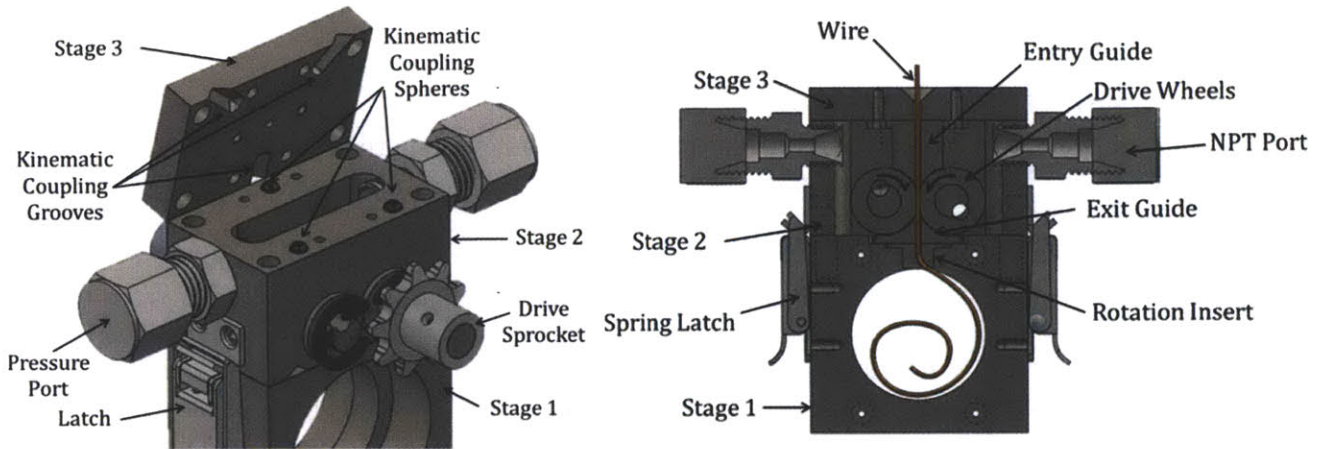


Figure 4-26: Kinematic couplings for stages and drive system

Stage one allows for the change in rotational and tilt angle using an array of inserts with fixed tilt and 30 degree rotation angle increments. The inserts were designed to be machined out of a Delrin or metal in two halves that are joined together. Although 3D printing is also a viable option, there are also additional complications can arise with a varying printing process. The 3D printing components via Polyjet proved to be unsatisfactory at the scale of 1 cm or less, STL printing could be done, but the benefits are not substantial. The inserts used were made using 3D printing technology in stainless steel created by iMaterialize (Belgium, EU), which created inserts with a course surface finish. The finish affected the wire feed for sharp tilt angles of 30 and 50 degrees

Stage one also houses a wire guide that complements the driving wheels to prevent buckling as the wire leaves driving wheels. The distance between the drive wheels and exit port was minimized to deter buckling inside the feeder.

Stage two houses the driving wheels, pressure port, and pressure measuring port. The driving wheels are held by a 1/4 inch diameter shaft and locked with a 6.4 mm (1/8 inch) shaft key. The locking shaft keys are designed to fail at a torque of 12.2 N*m. The feeding wheels are made of high speed stainless steel knurling wheels with twenty five threads per inch *TPI* (can also have 35 *TPI*, and 80 *TPI*). A slight groove was made in the center of the feeding wheels to have the wire self-align preferentially. The knurling wheels provide regular features along the length of the wire. The shafts are driven via a sprocket linked mechanically to the motor via a M25 chain. The two shafts in the wire feeder are synchronized via a set of opposing gears, as shown in Figure 4-27. The synchronizing gears are designed to fail after 4.0 N*m of torque at the teeth interface, the set screw that joins the gear to the shaft has a max torque specification of 5.9 N*m. Bushings are used for holding rotating shafts without wearing down the structure. The shaft diameter was increased to 6.4 mm (1/4 inch) to increase the stiffness of the shaft under tip loading. The prior version had deflections of the shaft that eventually lead to the replacement of the shaft and bearing structure. Spacers are used reduce friction and align the components in the axial direction. E-clips are used to hold the assembly.

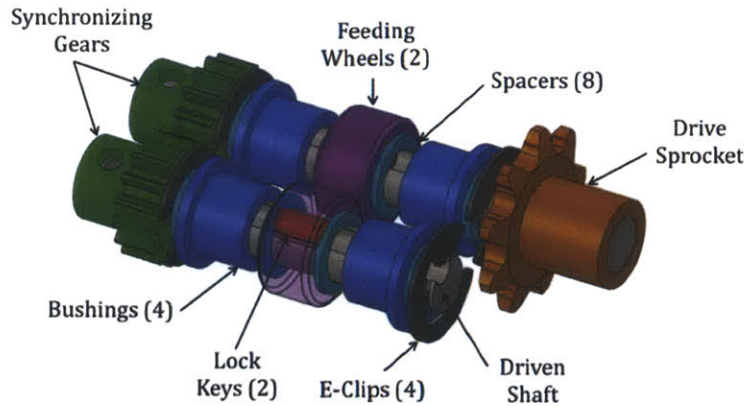


Figure 4-27: Wire drive system housed in stage two

Stage two also has a pair of 6.4 mm (1/4 inch) Yor-Lok fittings (McMaster 5182K702) to allow for pressurizing the machine at a level higher than the flow stream. One port can be used to pressurize the machine while the other can be used to measure pressure. One of the variables that could potentially be examined is the effect of a differential pressure between the machine and the well.

Stage three is a lid for the pressurized enclosure that brings the wire from the external environment and guides the wire to the center of the rollers. The entry guide is crucial as it prevents the wire from wondering along the length of the feeding wheels which has been shown to lead to entanglements inside the machine.

A failure analysis has been performed on the transmission system to prevent failure of critical components or damage to the drive motor. As shown in Table 4-5, the maximum torque rating is calculated for each section of the transmission system and a mechanical fuse has been included as a safety precaution.

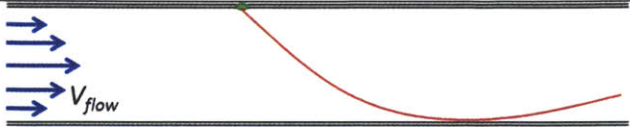
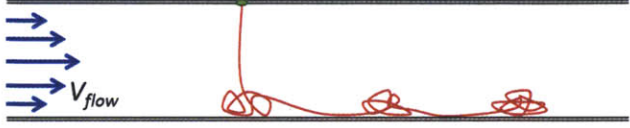

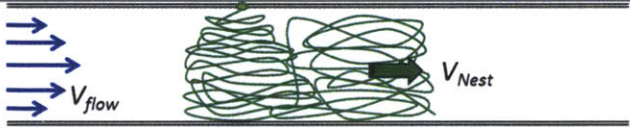
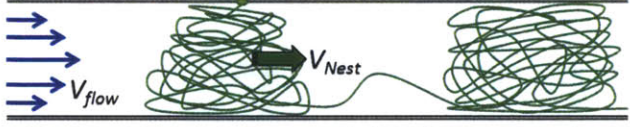
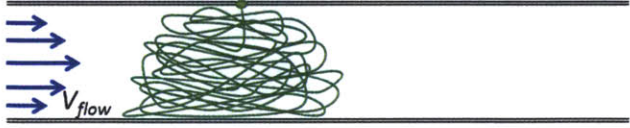
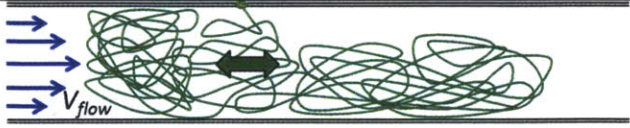
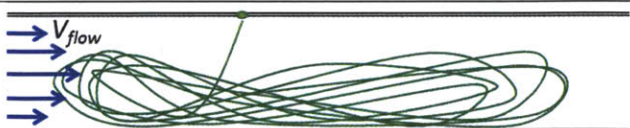


Table 4-5: Section and max torque transmitted through the elements, where the shear stress is $\sigma_y/\sqrt{3}$.

Section	Materials	Mat Properties	Failure mode	Cross Sectional Area	Max Torque Transmitted
Lock Keys (Shaft-drive disk)	Stainless	$\sigma_y = 240$ MPa	Shear ($r_t = 3.2$ mm)	19.6 mm ²	8.6 N*m
Sync Gears Teeth	Carbon Steel	$\sigma_y = 250$ MPa	Shear ($r_t = 6.4$ mm)	6.4 mm ²	5.9 N*m
Sync gear set screw 4-40	Stainless	$\sigma_y = 240$ MPa	Shear ($r_t = 3.2$ mm)	4.6 mm ²	4.0 N*m
Drive sprocket set screw 4-40	Stainless	$\sigma_y = 240$ MPa	Shear ($r_t = 3.2$ mm)	4.6 mm ²	4.0 N*m
Drive sprocket teeth	Aluminum	$\sigma_y = 276$ MPa	Shear ($r_t = 3.2$ mm)	8.4 mm ²	12.0 N*m
M25 Chain	Steel	508 N working load	Tension ($r_t = 9.1$ mm)	2.5 mm ²	9.3 N*m
Motor sprocket teeth	Stainless	$\sigma_y = 240$ MPa	Shear ($r_t = 18.3$ mm)	8.4 mm ²	21.2 N*m
Motor sprocket fuse	Nylon	$\sigma_y = 45$ MPa	Shear ($r_t = 9.5$ mm)	14.5 mm ²	3.6 N*m

4.3.2. Data

Three parameters were varied to identify the regions of entanglement: V_{flow} , V_{feed} , and stiffness. The original four behaviors were extended to ten discrete types of wire behaviors observed during testing as shown in Table 4-6 for varying configuration settings. As shown in Figure 4-28 and Figure 4-29, the feed velocity can be used to generate entanglements. Varying the angle of rotation and tilt angle of wire feeding can also change the type of entanglement behavior, as shown by Figure 4-30, and Figure 4-31.

Table 4-6: Entanglement types

Type	Icon	Behavior	Description
I	○	The wire contacts at a shallow angle and proceeds to exit the flow channel	
II		Entanglements get periodically generated and slips before reaching cohesion, and another entanglement is formed	
III	□	Initial entanglement is created and slips, secondary entanglement is generated and stays at entry regions	
IV	△	Cohesive entanglement is created at entry and moves with the flow slipping and catching	
V	◇	Cohesive entanglement is created and slips downstream eventually catching and allowing a second entanglement to form and move forward	
VI	⋈	Entanglement is generated only at the entry region and does not move forward	
VII	×	Entanglement is generated to move backward by feeding against the stream and the nest proceeds to also entangle downstream	
VIII	∞	Entanglement is generated in a figure eight configuration	
IX	✱	Cohesive entanglement is generated that moves against the flow, usually generated when feeding a stiff wire against the flow stream	
X	○	Wire is fed against the flow but does not entangle and proceeds to move against the flow eventually friction and drag lead to entanglement	

4.3.2.1. Feed Velocity Variations

Nylon wire (812 μm diameter) was fed into a turbulent flow at varying speeds to identify the entanglement region. Due to the motor activation region higher velocity ratios did not generate entanglement, because the wire got displaced by the flow, as shown in Figure 4-28. The same test was performed using aluminum wire (812 μm), as shown in Figure 4-29.

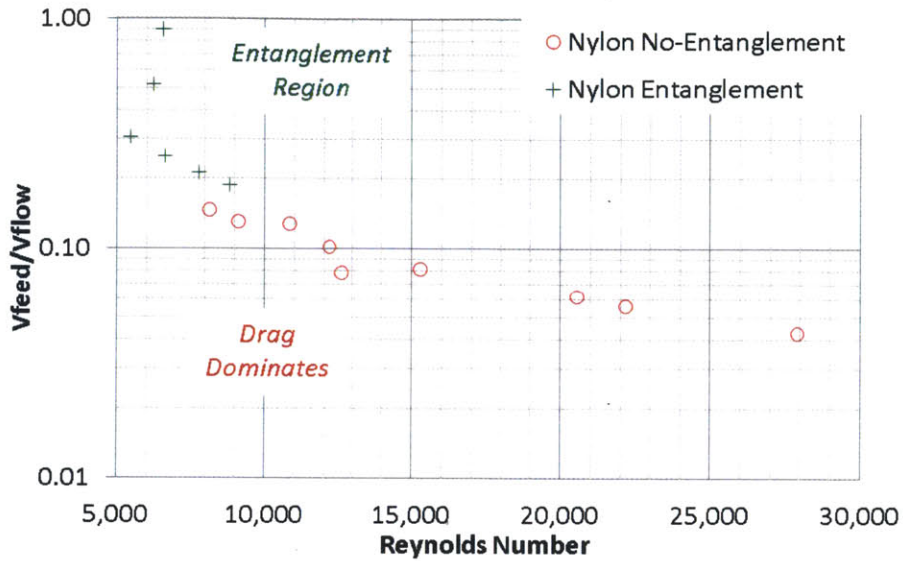


Figure 4-28: Reynolds versus feed rate for nylon wire with a theta of 180 degrees and tilt of 70 degrees

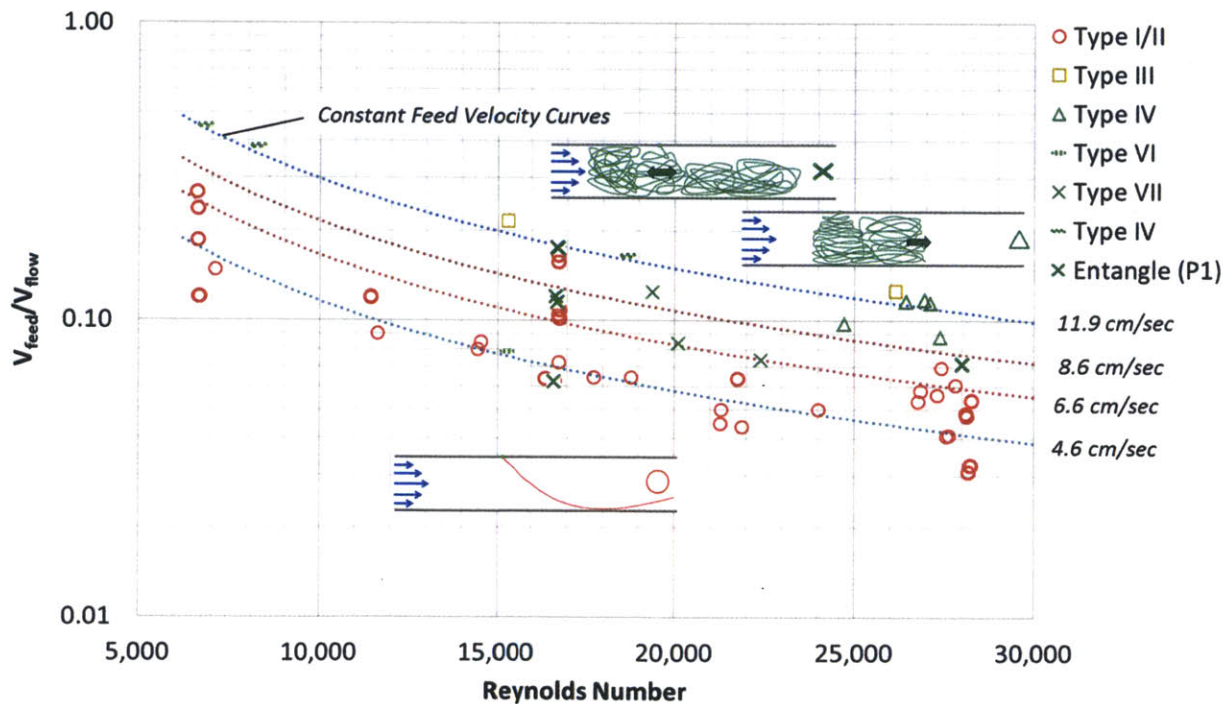


Figure 4-29: Reynolds number versus feed rate for aluminum wire (with a 812 μm diameter) with a theta of 180 degrees and tilt of 70 degrees

4.3.2.2. Rotation and Tilt Angle

A sensitivity study was needed to examine the effect of changing the angle of rotation and tilt on the entanglement behavior. For a fixed tilt angle, tests were performed varying rotation angle to establish a preliminary sensitivity analyses. The plots below, show the Reynolds number versus rotation angle, illustrate the effect of rotation angle on the type of entanglement behavior at first contact. Figure 4-30 and Figure 4-31 are for fixed tilt of 30 and 70 degrees respectively. Due to imperfections in one of the inserts (tilt 50°) the data is not provided.

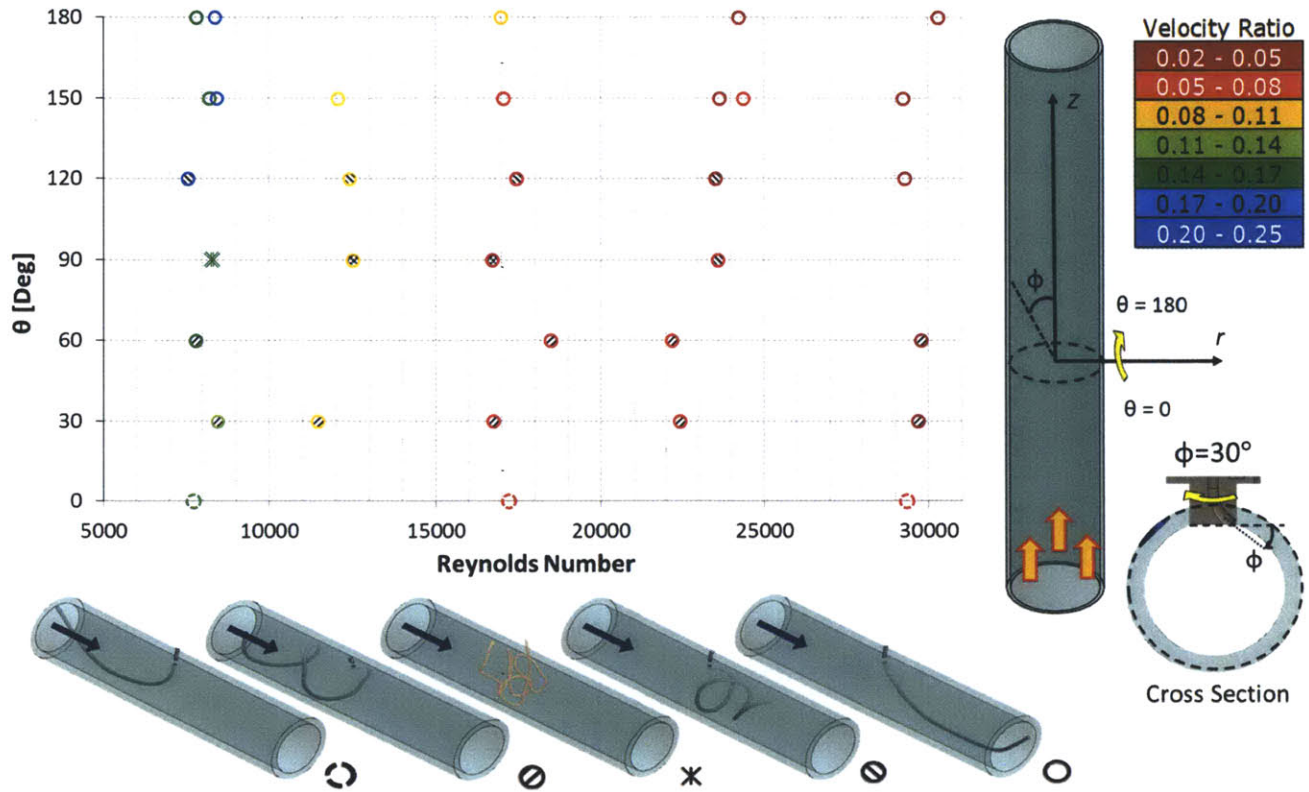


Figure 4-30: Rotation angle for tilt 30 degrees for a given Reynolds Number.

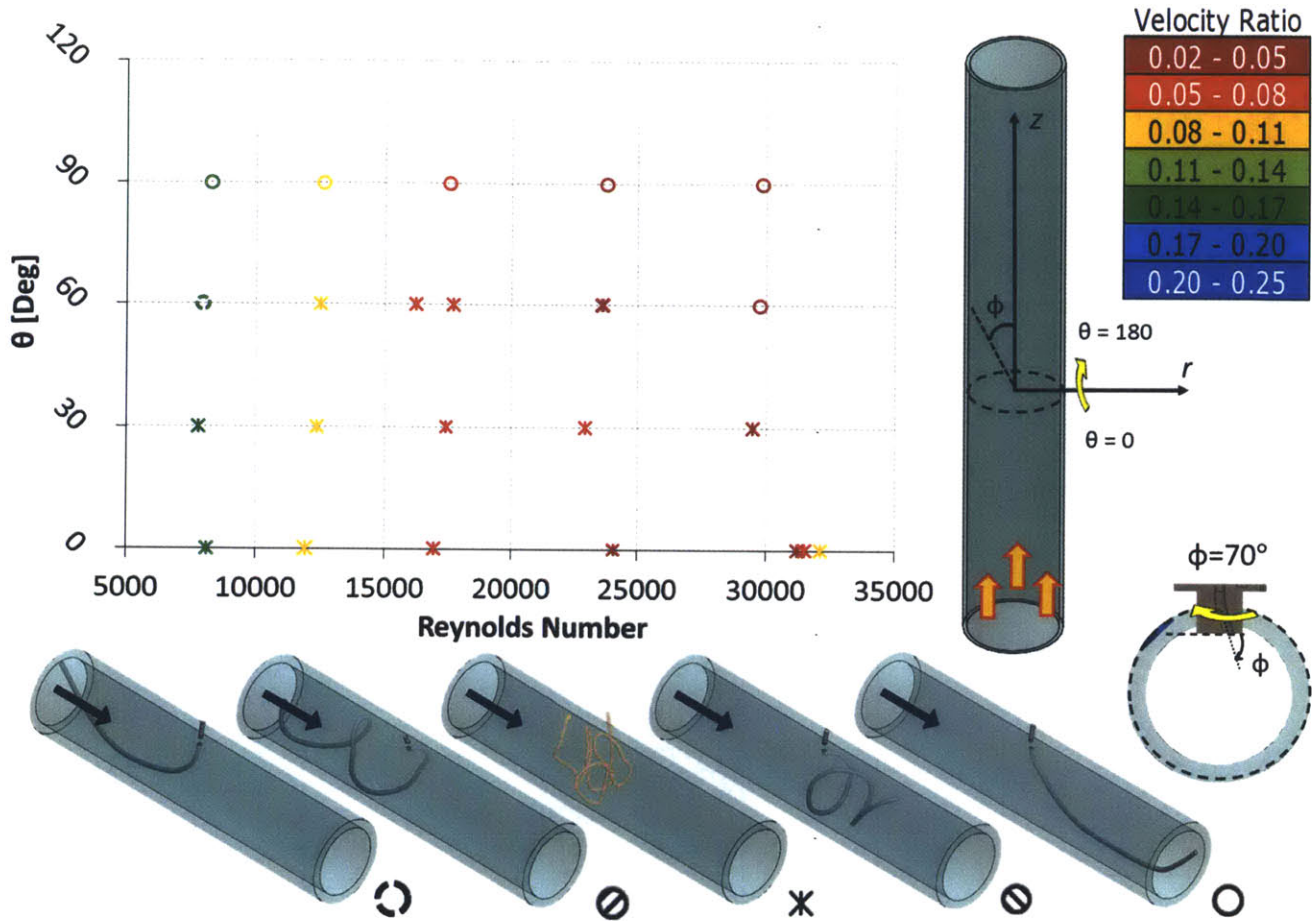


Figure 4-31: Rotation angle for tilt 70 degrees for a given Reynolds Number.

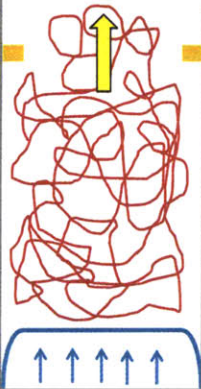

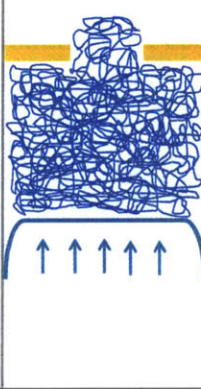
4.3.3. Results

Low stiffness materials such as nylon have a smaller entanglement region since the drag load dominates the wire behavior. As the stiffness of the wire is increased the entanglement region expands to include higher flow regimes. The rotation and tilt angle can also be used to influence the initial entanglement behavior. As the tilt angle decreases, the wire is fed orthogonal to the flow, the region of entanglement shifts to rotation angles below ninety degrees. Given the significant drag loading on the wire, it is best to feed to wire at rotation angles below 90 degrees and with tilt angles less than 50 degrees to induce entanglement. The non-dimensional entanglement coefficient (π_e) of the wire should be kept above 1,000 to obtain the same entanglement behavior as that observed in the experimental setup. Future work should also include performing a feed velocity correction that quantifies dynamic effects.

4.4. Anchoring Entanglement

The interaction between the stiff wire entanglement and existing obstruction determines the anchoring potential of the mechanical plug inside of the BOP. There are three primary interaction modes between the entanglement and the obstruction region, summarized in Table 4-6. The focus of this section is identifying the failure criteria compression of the initial entanglement. In the event where the obstruction area (A_{obs}) is less than the critical area ($A_{critical}$), there is no significant anchoring and the entanglement can be ejected by the flow. For significant aperture obstructions, the anchoring of the entanglement can fail by squeezing/extruding through the aperture; whereas, a fully compressed entanglement can fail in shearing when overloaded.

Table 4-7: Anchor modes

Not Anchoring	Compression Process	Full Compressed Anchor
		
$A_{obs} < A_{critical}$	$A_{obs} > A_{critical}$	$A_{obs} > A_{critical}$
Ejection	Extruded/Squeezing	Shearing

4.4.1. Theory

As the unconsolidated entanglement is compressed by the flow, it can be extruded through the obstruction aperture by the deformation of the structure. As the entanglement is compressed further it reaches cohesion and transfers the load from the well to the existing obstruction where the mode of failure is shearing. A significant load on the entanglement can lead to failure by shearing the material in the plug.

4.4.1.1. Extruded

The initial analysis for determining extrusion force is based on the drawing process illustrated in Figure 4-32. As shown in Equation 4.21, the extrusion force is a function of the compaction of the medium and the area reduction geometry [150]. A more involved analysis, Equation 4.22, shows the dependence on the rake angle and friction between the die and work piece. Figure 4-33 shows the extrusion force as percent compaction and area reduction for the simple geometry.

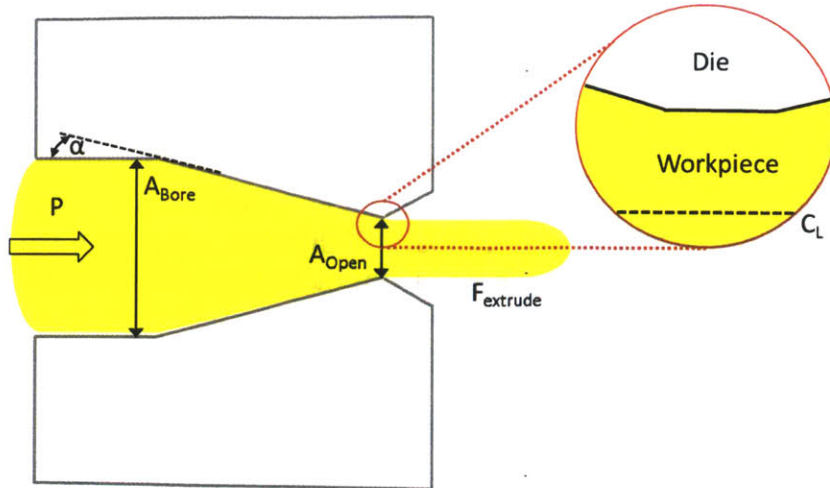


Figure 4-32: Drawing process schematic diagram showing an effective work piece that would be the entanglement nest passing through the restriction

$F_{extrude} = C_{\%} \cdot \sigma_{Y,avg} \cdot A_{Open} \ln \left(\frac{A_{Bore}}{A_{Open}} \right)$	Equation 4.21
---	---------------

Where A_{Bore} is the initial cross sectional area, and A_{Open} is the reduced cross section.

$F_{extrude} = C_{\%} \cdot \sigma_{Y,avg} \cdot A_{Open} \left[\left(1 + \frac{\mu}{\alpha} \right) \cdot \ln \left(\frac{A_{Bore}}{A_{Open}} \right) + \frac{2}{3} \alpha \right]$	Equation 4.22
---	---------------

Where α is the die angle, and μ is the friction coefficient between extruded material and die.

A visual representation of Equation 4.21 is shown in Figure 4-33 illustrates the drawing force required (N) as a function of compaction and area reduction.

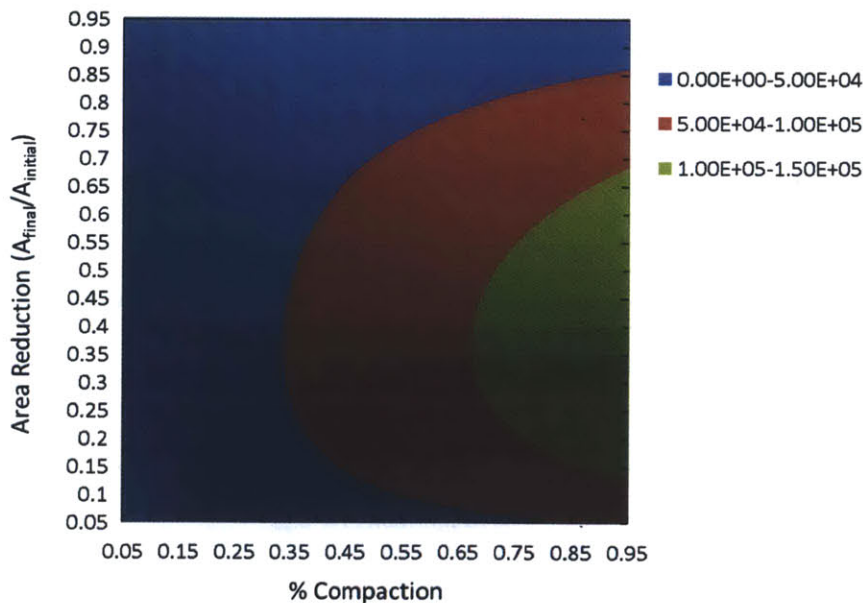


Figure 4-33: Drawing force in Newtons as a function of percentage compaction and area reduction calculated using Equation 4.21. The calculation is for a 50 MPa yield stress material with a bore diameter of 10.2 cm (4 inches) with varying compaction percentage.

The behavior depicted above; however may not be an appropriate model for the extrusion of the wire entanglement. The tapered angle used on dies in the drawing process is not present in the existing obstructions inside the BOP or in the obstruction caps that represent the rams.

4.4.1.2. Shearing

The first level analysis for shearing is done by determining the force required to shear the compressed entanglement given an applied load. If the load is less than the shearing potential then anchoring is achieved, otherwise, material failure of the entanglement occurs leading to the extrusion of compressed entanglement. The first order calculation, shown by Equation 4.23, relates axial loading to the strength of the plug, estimated using the percentage compaction of a homogenous plug.

$F_{axial} = \Delta P \cdot A_c < \sigma_s \cdot p \cdot h_c \cdot C_{\%} = F_{shear}$	Equation 4.23
--	---------------

Where ΔP [N/m²] is the maximum differential pressure across the entanglement, A_c is the full cross sectional area, σ_s [N/m²] is the shear strength of the material, p [m] is the active perimeter, h_c [m] is the effective height of the entanglement, and $C_{\%}$ is the compaction of the entanglement as defined in Equation 4.24.

$C_{\%} = \frac{m_{wire} / V_{plug}}{\rho_{wire}}$	Equation 4.24
--	---------------

Where the m_{wire} is the mass of the wire in the effective height, V_{plug} is the volume of the plug, and ρ_{wire} is the density of the wire.

As shown in Figure 4-34, the maximum operating pressure that a partially compacted mechanical plug can withstand proportional to the percentage compaction, geometry, and material strength.

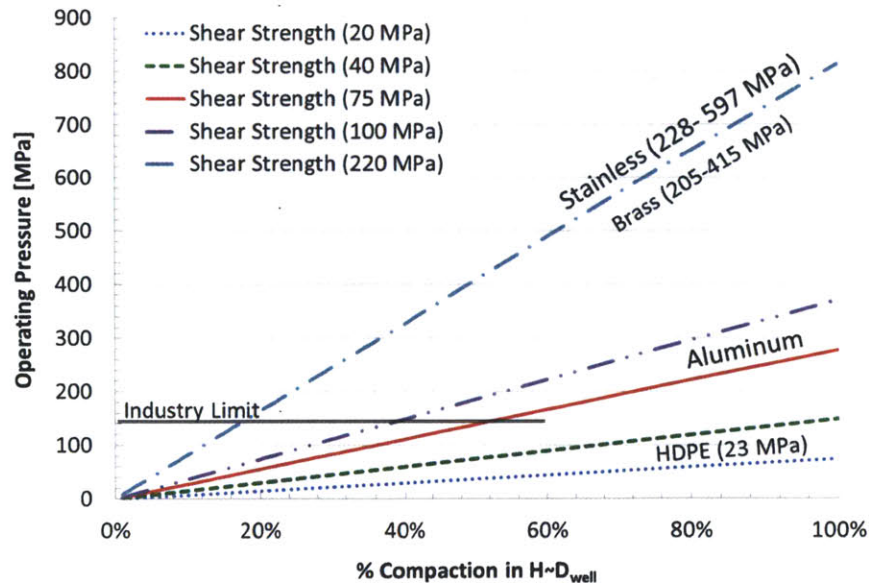


Figure 4-34: Max operating pressure of a partially compacted mechanical plug prior to shear failure for varying material properties with the following geometry $D_{bore} = 47.6$ cm (18.75 inch), effective height $h_c \sim 47.6$ cm (18.75 inch) using Equation 4.23

4.4.2. Experiment Setup

A wire entanglement compression experiment was conducted to determine the critical obstruction area needed for anchoring. As shown in Figure 4-35, the experimental setup consisted of a plunger that is connected to a universal testing machine with a 20kN load cell. The plunger moves axially in the negative z direction to compact the anchor and try to eject or extrude it through the obstruction cap at the bottom.

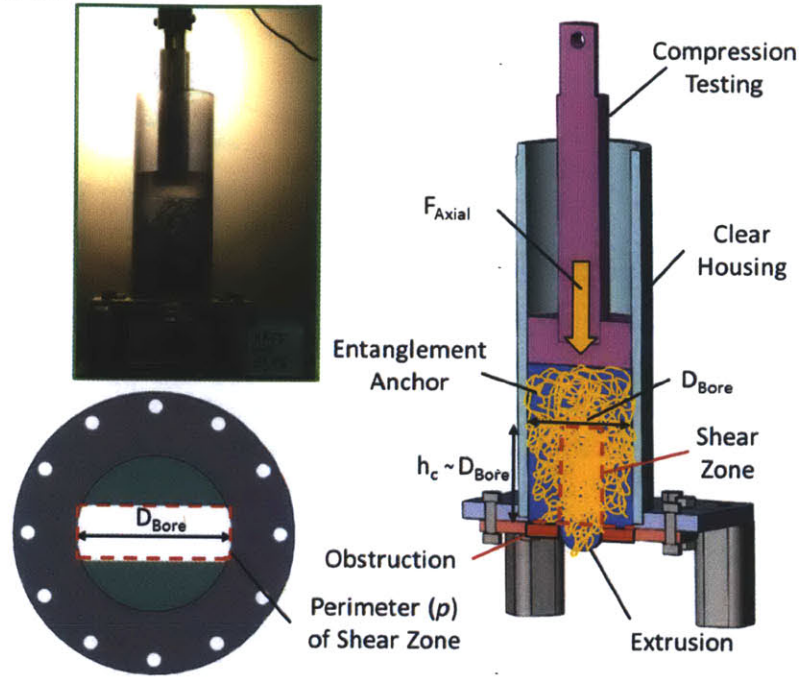


Figure 4-35: Anchor loading preliminary experiment

4.4.2.1. Materials Considerations

Using the critical stiffness parameter needed to generate entanglements, the wire diameter required depends upon the material properties of the wire. As shown in Figure 4-36, the wire diameter needed for a high Reynolds number flows (25,000 to 30,000) is ~ 0.5 mm for steel wire. One of the smallest commercially available (Home Depot) wire is a 16 gauge galvanized steel wire (1.55 mm diameter - gauge 16). This higher entanglement stiffness wire value will allow for significant higher flow conditions.

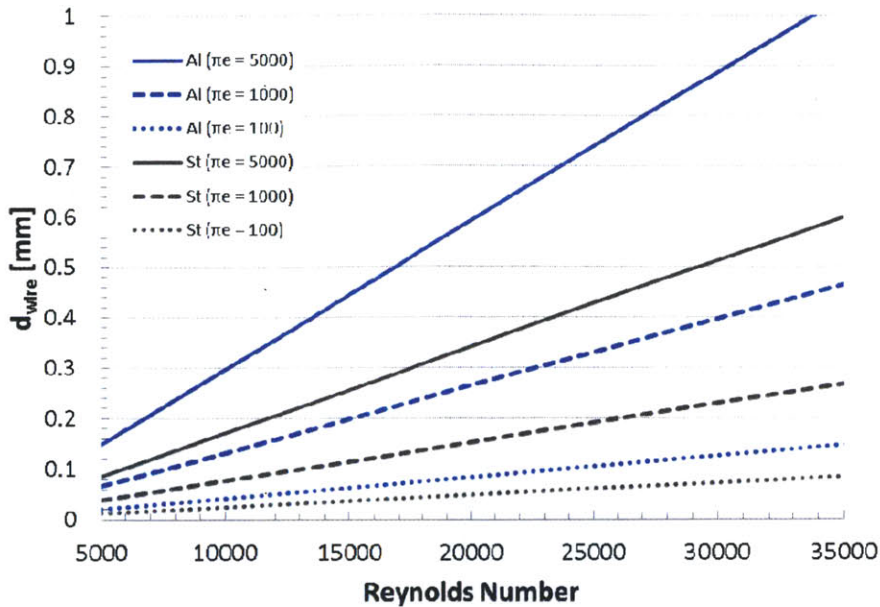


Figure 4-36: Theoretical wire diameter for the experimental test showing the effect of the non-dimensional entanglement coefficient on the wire diameter for given geometric and material properties: $D_{\text{bore}} = 10.2$ cm, $E_{St} = 210$ GPa, $E_{Al} = 70$ GPa, using water.

4.4.2.2. Sample Preparation

Uncompressed entanglements were created by bending galvanize wire to wavelengths lengths of about 50 mm which is about one half of the diameter of the clear cylinder. The mass of each uncompressed entanglement was measured to $m_a = 170 \pm 14$ g. The exterior surface of the wire is smooth and un-knurled. Each uniform uncompressed entanglement is loaded into the chamber (height = 26.4 cm (10.375 inches)) with a given RAM geometry obstruction aperture. The plunger is placed above the entanglement and the compression is initiated thus pushing the entanglement against the obstruction disks.

4.4.3. Galvanized Steel Wire Compression Data

As shown in Figure 4-37, the preliminary compression experiments show that the entanglement is subject to partial ejected for low obstruction (i.e. such as 25% RAM geometry) since a low axial load yielded more than ninety percent axial travel with partial ejection. For obstructions of forty five percent and greater it is evident that a significant amount of axial load is transferred via the compressed entanglement and on to the supporting structure.

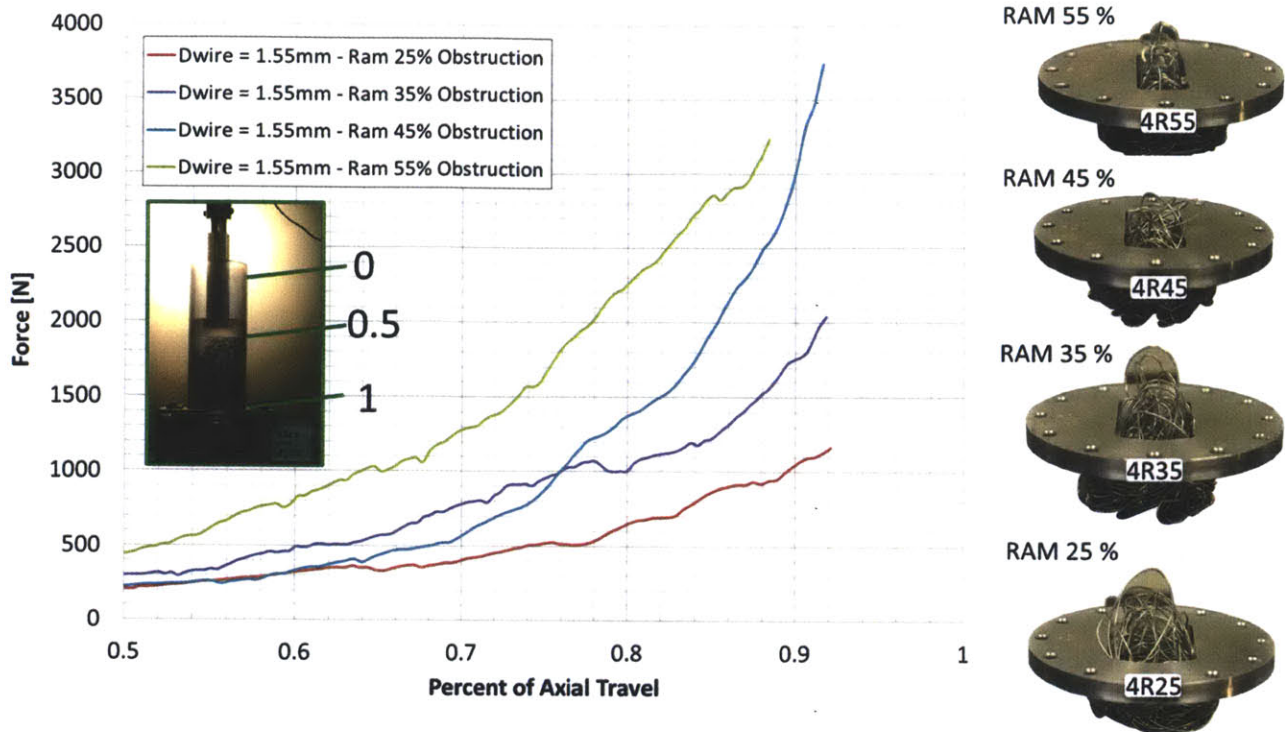


Figure 4-37: Mass entanglement $m_e = 170 \pm 14$ g (3/8 lb), $D_{bore} = 9.5$ cm (3.75 inches), Galvanize steel wire $d_{wire} = 1.55$ mm

4.4.4. Anchoring Test Discussion

For RAM obstructions of 35% or lower the unconsolidated entanglement undergoes partial ejection during the loading process, while at higher obstruction coverage the plug anchors and the load is transferred onto the supporting structure. Given that the load applied is uniform additional testing must be done with a deformable plug to ensure that the loading behavior is the same. Further anchoring compression tests using an axial load machine were deferred in the interest of loading using a compressible sealing material backed by fluid pressure. This approach is considered a more representative test to capture the actual dynamics of the compression of the mechanical plug inside of the wellbore.

4.5. Sealing by Porous Occlusion 2.5 cm Bore

As the wire entangles and anchors it begins to behave as a semi porous plug. The permeability of the entangled wire is characterized experimentally as a function of plug length, and porosity. The objectives of this experiment are to determine how the wire occlusion can be modeled and to identify the type of wire occlusion with the lowest permeability. The goal is to quantify the amount of wire required to hold a certain pressure with minimal to zero flow in order to size the wire feeder accordingly.

4.5.1. Experimental Setup

The experimental setup consists of a flow loop with a cylindrical channel where a porous plug is inserted to measure its permeability by measuring the flow rate and pressure, as shown in Figure 4-38.

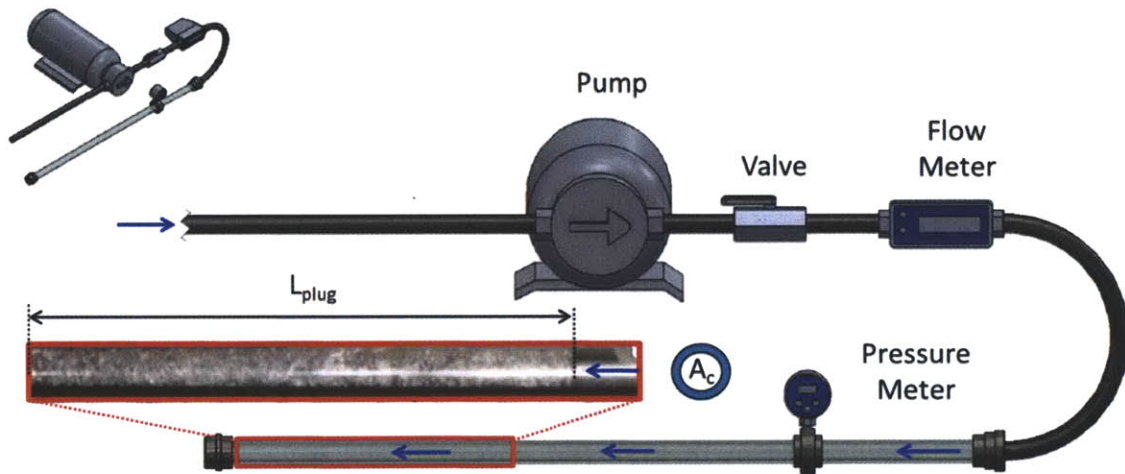


Figure 4-38: Porous occlusion experimental setup consisting of a pump, Omega flow meter (FTB791), and a pressure meter (MG1-200-A-9V-R). The interior diameter of the pipe is 2.5 cm (1 inch).

The first order approach is to assume a linear permeability model, based on the Darcy equation, is rearranged to solve for the permeability of the porous plug as a function of the measured values and the errors associated with the measurements as shown in Equation 4.25. All of the factors in the equation can be quantified (viscosity) or measured (pressure, flow rate, plug length, area). The objective is to determine the model type of the porous plug whether it is a linear, power, etc.

$$k = \frac{(\mathcal{V} + \varepsilon_{\mathcal{V}}) \cdot (L + \varepsilon_L) \cdot \mu}{A_c \cdot (\Delta P + \varepsilon_{\Delta P})}$$

Equation 4.25

Where the main sources of error for the permeability k [m^2] are from the following measurements: flow rate \mathcal{V} , plug length L , and pressure ΔP . For the Omega flow meter FTB791 (range 3.8 to 38 lpm (1 – 10 gpm)) the error is 2 % of the measurement; therefore, the higher the flow rate the higher the error in measurement. The pressure meter (1.4 MPa (200 psi) max) has an error of ± 1 percent of the full scale; therefore, at low pressures the error dominates the signal and decreases with the pressure.

4.5.2. Data

An array of continuous media was tested to determine geometry and features that are favorable along the wire. The following materials were evaluated as part of this experiment in compaction to find the porosity and permeability of the plug: aluminum wire (0.8 mm (0.032 inch) diameter), bread wire and rubber wire. The permeability as a function of flow rate is plotted in Figure 4-39 for the three materials whose permeability's were below 10,000 Darcy: aluminum wire (AL), rubber (SI), and a ribbon core (RC) design. The ribbon core design was inspired by a sea slug (*Cromodoris willani*) that has a stiff core member across the center and flexible extensions like wings across the entire length of the body. As shown in Figure 4-39, changing the L/D ratio can affect the permeability measurements. Ideally, each experimental configuration should consist of a single point (permeability); however, as the plug length increases the permeability measurements do converge as expected. The current test setup is limited by the pump specifications.

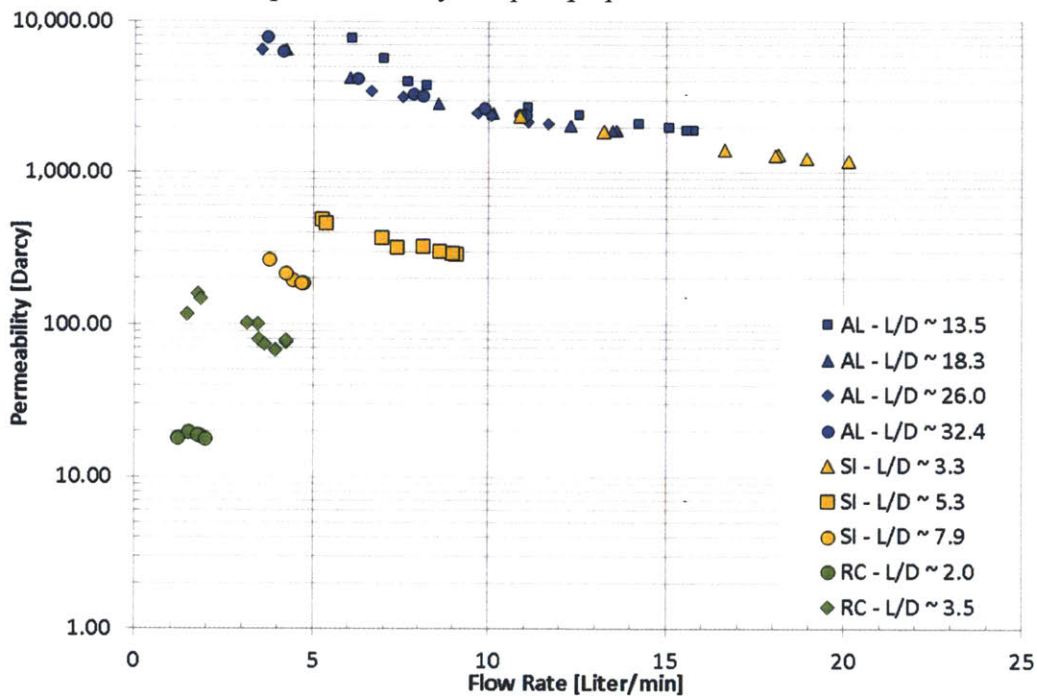


Figure 4-39: Permeability experiment summary for aluminum (AL), nitrile rubber (SI), and ribbon core design (RC) with varying length to diameter ratio. Due to pump limitations of the experimental setup additional flow rate measurements for low permeability's cannot be obtained with this setup.

The detailed flow rate versus pressure plots is shown in Figure 4-40, Figure 4-42, and Figure 4-44, for the aluminum wire, nitrile rubber, and ribbon core (slug) designs respectively. For each material, the permeability is calculated using Equation 4.25 and traced as a function of flow rate for each of the three cases respectively as shown in Figure 4-41, Figure 4-43 and Figure 4-45.

The error in the flow rate increases with the measurement since the flow meter has a two percent error of measurement. The error bars in the pressure decrease with increasing pressure because the error in the measurement is a function of the full scale of the measurement. The error is a larger portion of the low-pressure measurements.

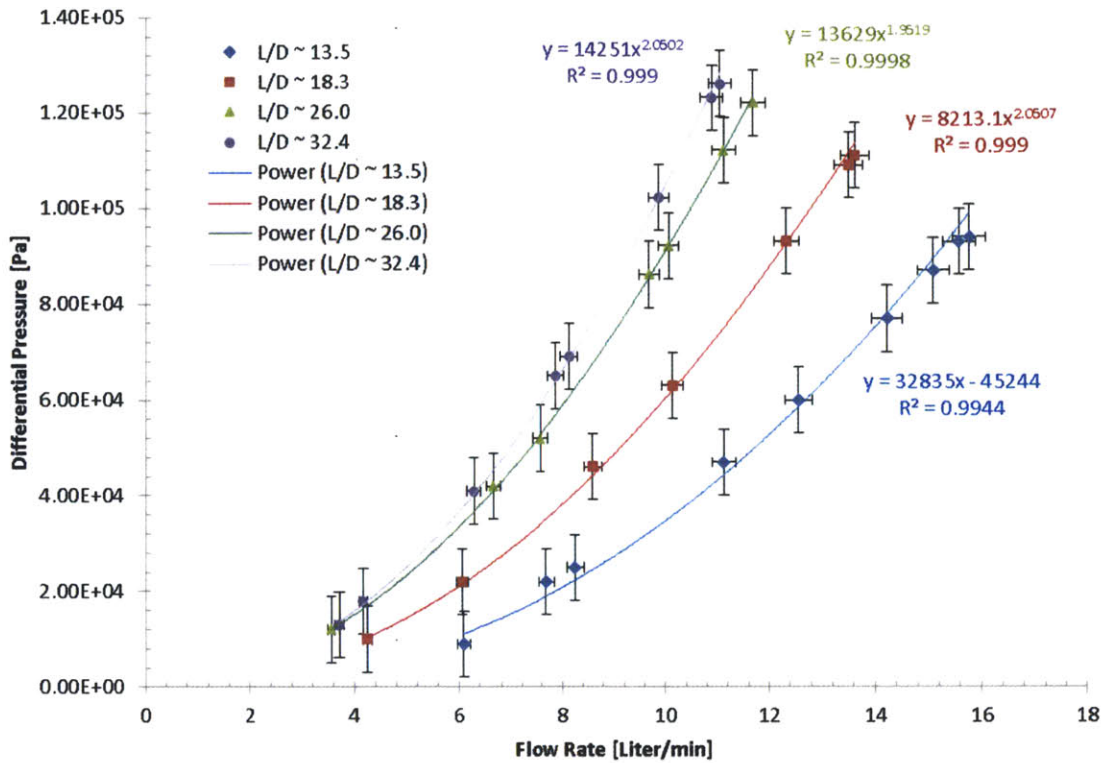


Figure 4-40: Aluminum wire 0.8 mm (0.032 inch) with porosity of 73%

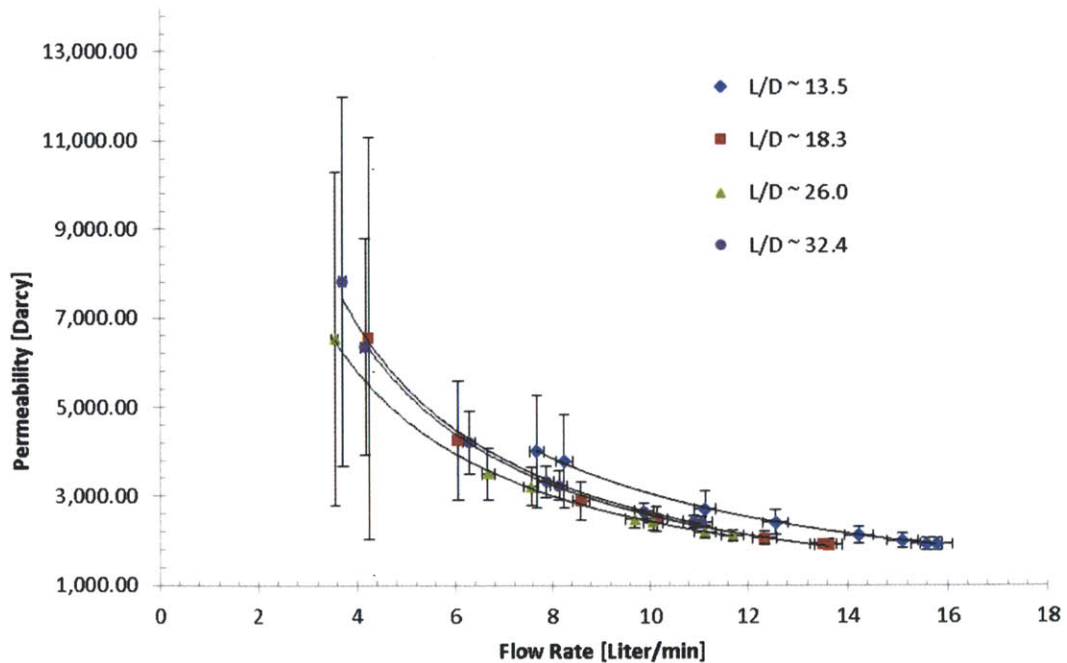


Figure 4-41: Permeability (Darcy) for Aluminum wire (porosity of 73%) with varying geometry configurations

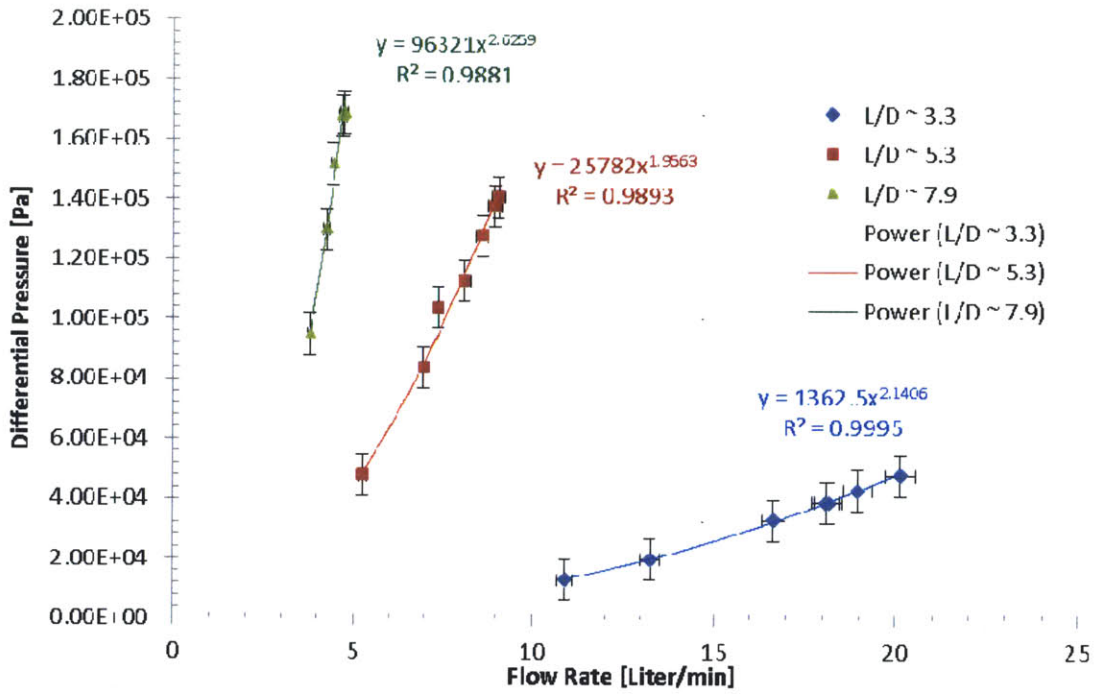


Figure 4-42: Buna O-ring wire 1.8 mm (0.070 inch) with porosity of 40% to 15%

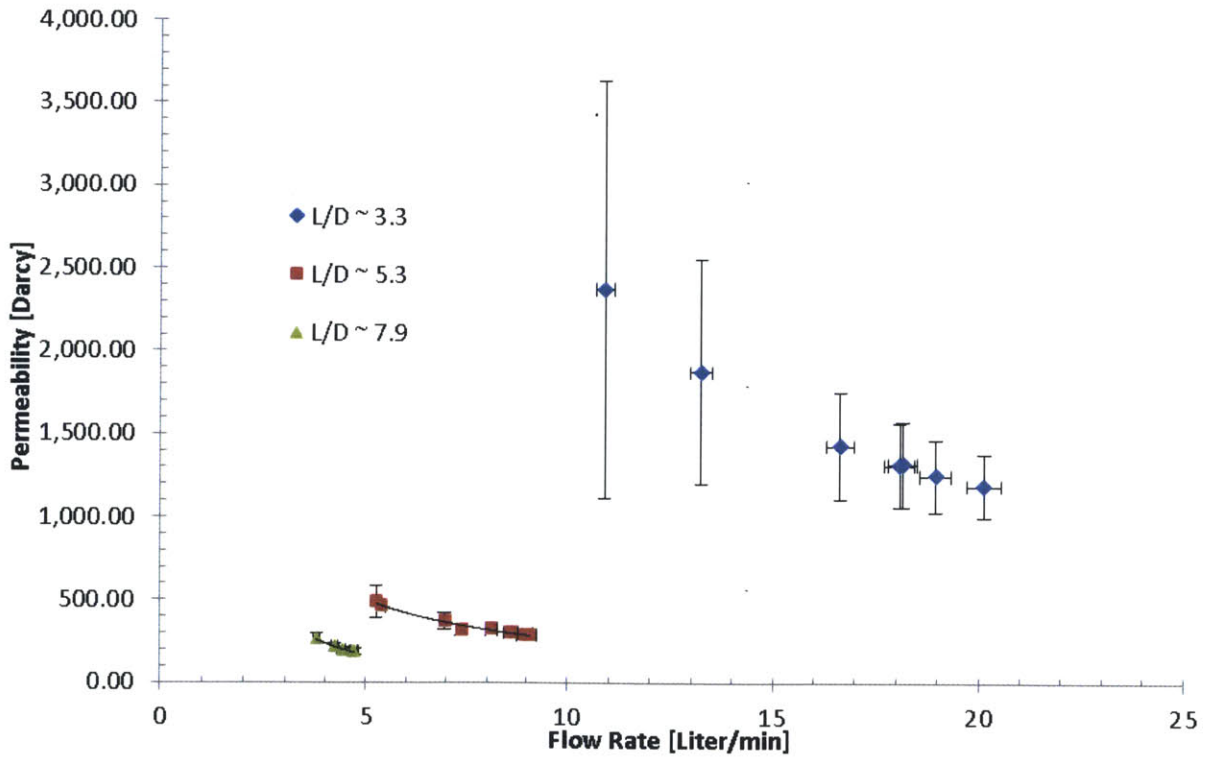


Figure 4-43: Permeability (Darcy) for Buna O-ring wire (porosity of 73%)

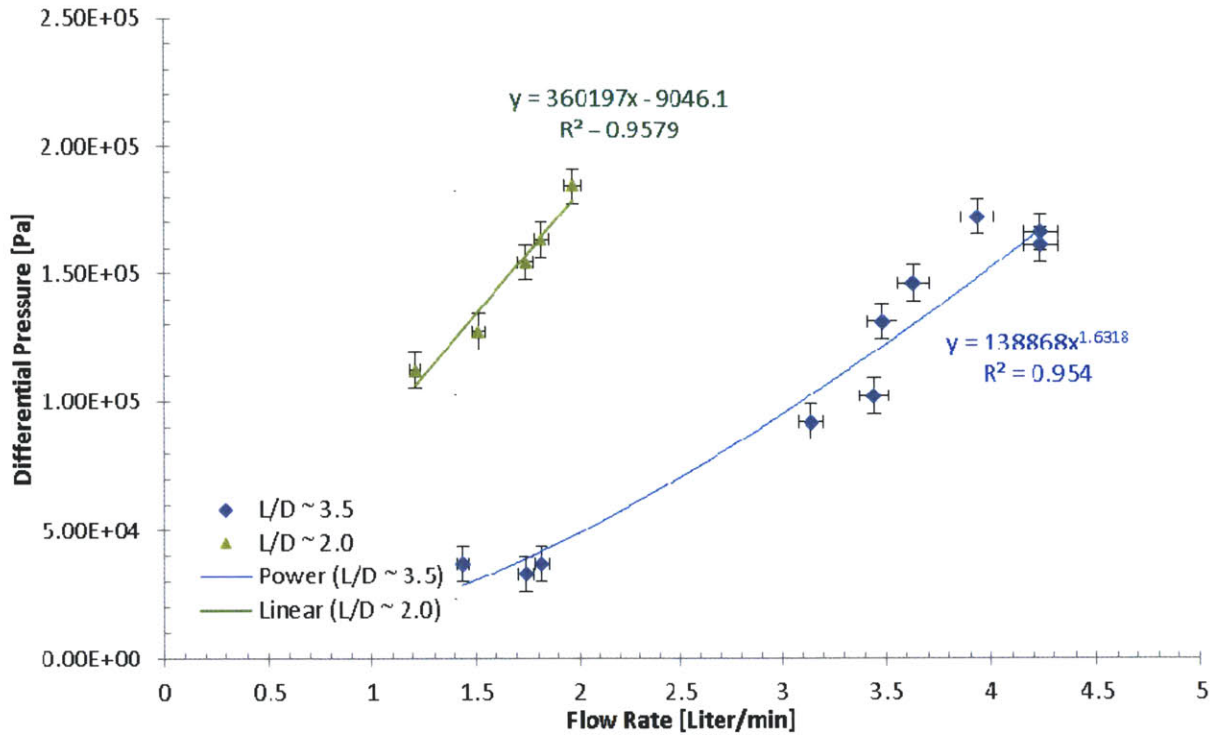


Figure 4-44: Slug design flow rate trend. The error for the flow measurement is 2% of the measurement; whereas the pressure measurement has an error of $\pm 1\%$ of the full scale.

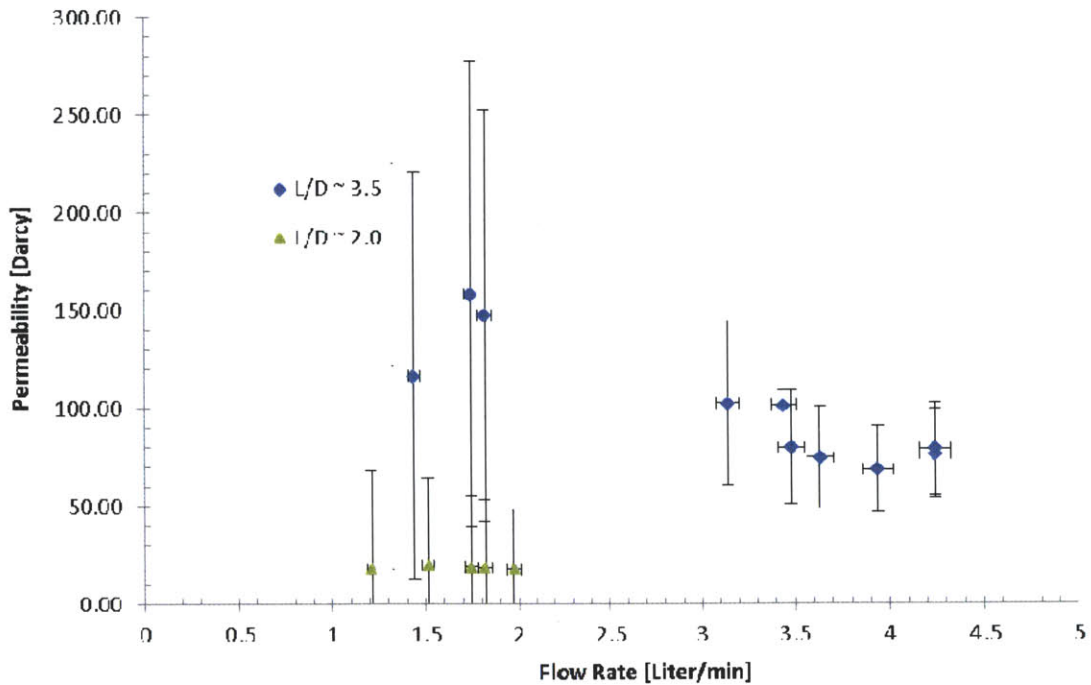


Figure 4-45: Slug design changed the compression by the flow

4.5.3. Performance Calculations

The calculated closure efficiency is used to determine the plug characteristic necessary (i.e. length and permeability) to control a flow releasing a max of $V_i = 15.9 \times 10^3 \text{ m}^3/\text{day}$ (100,000 bbl./day) of hydrocarbons. As shown in Figure 4-46, for three standard well diameters a ninety percent closure can be achieved with plug lengths of less than ten diameters, assuming a plug permeability of 30 Darcy, which is experimentally achievable. Therefore, less material is needed to achieve ninety percent closure for wells with smaller diameters. Similarly, a decrease in permeability will also reduce the plug length required to close the well as shown in Figure 4-47.

$\% \text{ Sealing} = \frac{V_i - \frac{\pi \cdot D_{\text{well}}^2 \cdot k \cdot P_{\text{well}}}{4 \cdot \mu_{\text{fluid}} \cdot L_{\text{plug}}}}{V_i}$	Equation 4.26
---	---------------

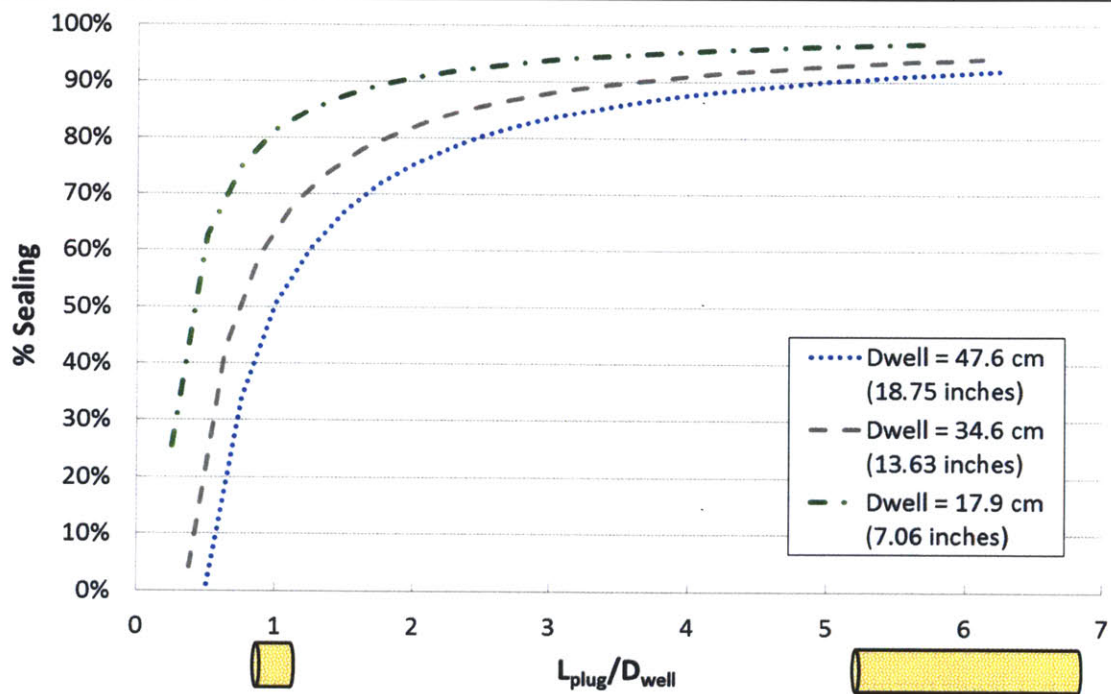


Figure 4-46: Effectiveness of a plug with an Ranges of $L_{\text{plug}}/D_{\text{well}}$, $\mu_{\text{fluid}} = 0.010 \text{ Pa}\cdot\text{sec}$, Well Pressure $P_{\text{well}} = 68.9 \text{ Mpa}$ (10ksi) Permeability ($k = 30 \text{ Darcy}$) experimentally reasonably achievable, Initial Volumetric Flow Rate $V_i = 15.9 \times 10^3 \text{ m}^3/\text{day}$, Well Pressure $P_{\text{well}} = 68.9 \text{ Mpa}$ (10 ksi)

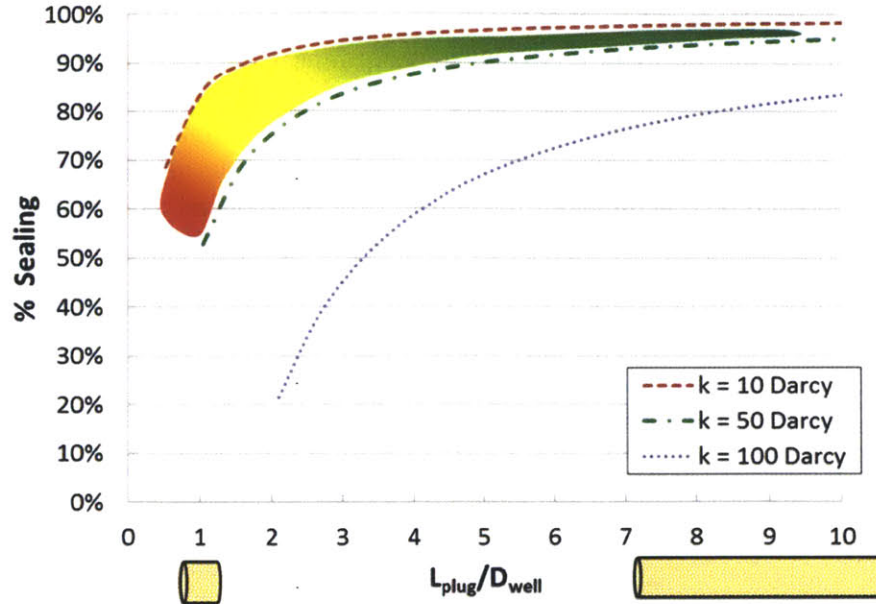


Figure 4-47: Permeability sensitivity for an 47.6 cm (18.75 inch) bore diameter with an uncontrolled flow rate of 100,000 bbl/day, viscosity 8.39×10^{-3} Pa sec. Ranges of L_{plug}/D_{bore} , BOP bore diameter (D_{bore} (18.75 inches)), $\mu_{fluid} = 0.010$ Pa*sec. Initial Volumetric Flow Rate $V_i = 15.9 \times 10^3$ m³/day (100,000 bbl./day), Well Pressure $P_{bore} = 68.9$ MPa (10ksi)

4.5.4. Results

In an attempt to improve the permeability of the continuous wire it was found that the ribbon core design has measured permeability's that are two orders of magnitude better than the aluminum wire, and also has the added advantage of $1/25$ the mass as shown in Table 4-8. As shown in Figure 4-48, the measured permeability using a 2.5 cm (1 inch) wellbore range from 18 Darcy for the ribbon core design to 1896 Darcy for aluminum wire packed to seventy percent porosity. The desired occlusion should be below ten wellbore diameters in length and have a permeability of less than fifty Darcy.

Table 4-8: First level permeability measurements and development positive and negative aspects.

Material	Min. Permeability [Darcy]	Mass [grams]	Advantages	Disadvantages	Comments
Wire Al (0.8 mm)	1896	300	Anchoring	High Porosity	Equivalent highly fractured rocks and sorted sand.
Rubber (1.8 mm)	186	94.6	Compressibility Friction along walls	Minimal Anchoring	Better for sealing but not for withstanding loads
Ribbon Core	18	12.5	Low permeability, high porosity	Complex shape, No anchoring	Hybrid between sealing and anchoring

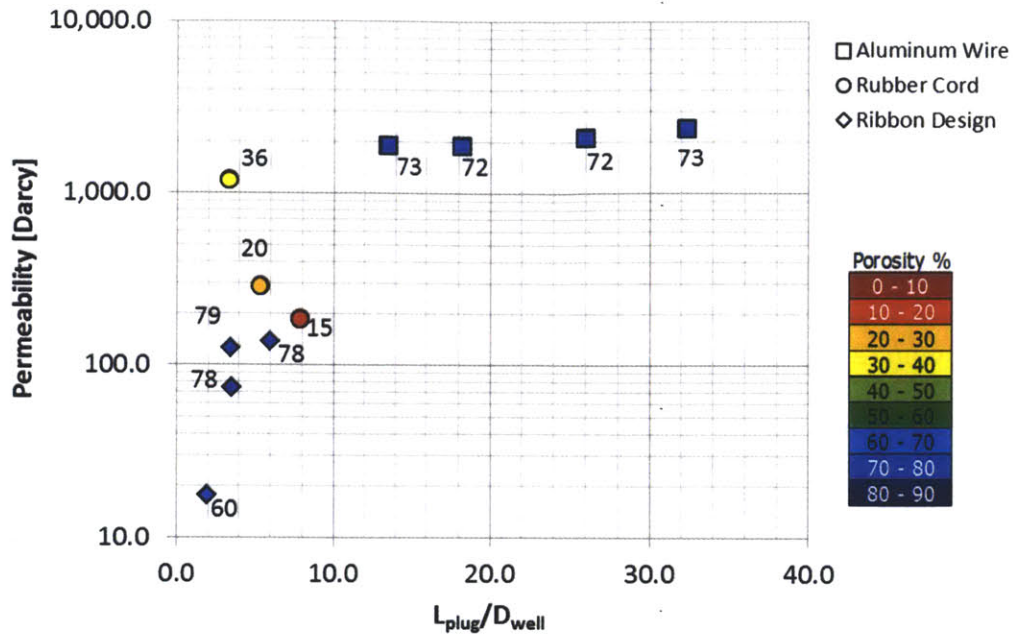


Figure 4-48: Permeability results for a 2.5 cm diameter channel with at most 38 liter/min flow rate with varying initial porosities

4.6. Sealing by Porous Occlusion 10.2 cm Bore

The objective of this section is to determine the effect of increasing the wellbore diameter on the permeability of different plug materials. As shown by the performance calculations, the permeability of each of the mechanical plug must be below 50 Darcy in order to work with the geometry of the BOP.

4.6.1. Experimental Setup

As shown in Figure 4-49, the 10.2 cm (4 inch) permeability experiment is composed of four components: 1) pump, 2) flow meter, 3) pressure meter, and 4) plug chamber. The pump used is a Fluid O-tech pump powered by a Leeson electric motor that was available in lab with a maximum pressure head of 0.4 MPa (60 psi). Connected to the pump is the Omega flow meter FTB791 (range 4 – 38 lpm) and pressure meter (MG1-200-A-9V-R). The connections and chamber were sized for 20.6 MPa (3,000 psi) internal pressure. The chamber is made from aluminum 10.2 cm (4 inch) interior diameter pipe with a wall thickness of 12.7 mm (0.5 inch). At the exit location of the chamber there is a honey comb crate that is used to hold the plug with minimal flow interference. The crate covers a 17.7 % of the cross sectional area.

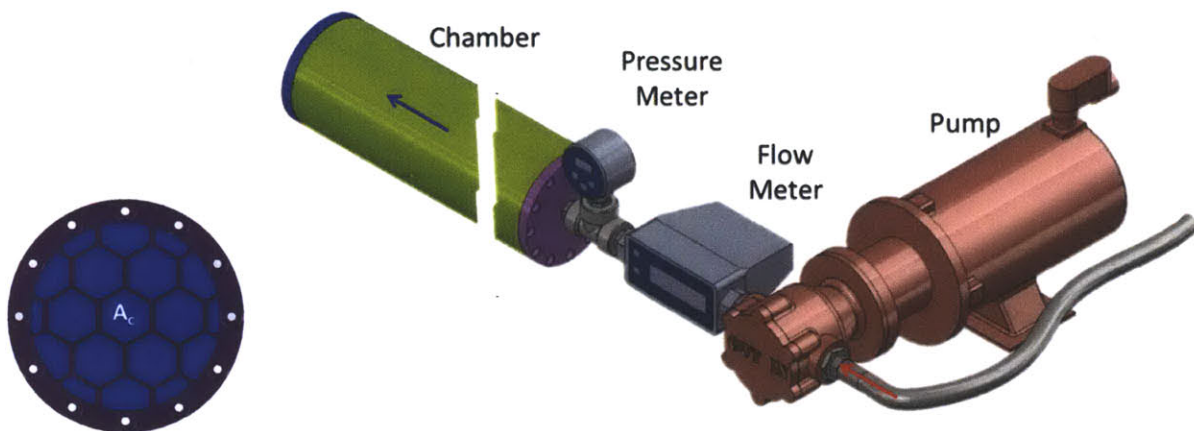


Figure 4-49: Four inch permeability experimental setup

4.6.1.1. Test Procedure

The chamber is filled with the continuous material to be tested and compacted against the crate cover with approximately 900 N of force. The mass of the plug is measured before insertion, while the height of the plug is measured in the compressed state to determine the porosity. The flow chamber closed with a cap that connects to the flow loop. The pump is turned on allowing the chamber to fill with water and pressurize. The pressure and flow are recorded to calculate the permeability of the medium

4.6.2. Data

The two additional materials that were tested with the chamber: foam square extrusion, and flat ribbon. As shown in Figure 4-50, the permeability of the flat ribbon design were below 100 Darcy, whereas the permeability of the foam square extrusion was larger. Bread wire was also measured to have higher permeability than 1000 Darcy, similar to the aluminum wire (800 um diameter).

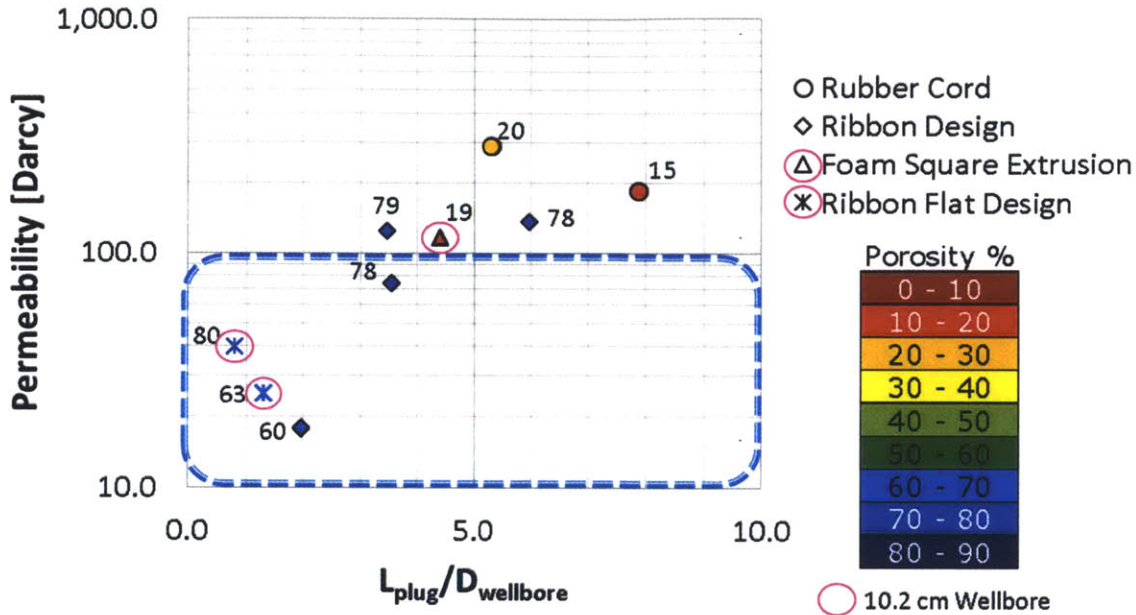


Figure 4-50: Permeability experimental results for 10.2 cm wellbore scale

4.6.3. Results

As shown by the permeability data, the flat ribbon design was scalable to the 10.2 cm (4 inch) diameter aperture chamber. Note that the permeability experiments assume a linear relation based on Darcy's law and it should be a matter of further testing. The compressible sealing material can undergo non-linear compression. The measured permeability for the flat ribbon design is below 50 Darcy, which makes it feasible to significantly obstruct the flow within the BOP geometry. The material may need to be used in conjunction with a stiffer and stronger material that would function as the scaffolding to hold the flexible structure formed by the flat ribbon.

[Left Blank]

4.7. Anchoring and Sealing At High Pressure

A high-pressure flow rate loop, provided by a fire truck engine, is used to test a mechanical plug's ability to anchor and seal.

4.7.1. GAS Method

Based on the sealing experiments, the approach to bring the well under control is a three-step process, whose acronym is GAS, which stands for generation, anchoring, and sealing. The first step is to generate a stiff entanglement inside the free flowing uncontrolled stream. As the entanglement reaches cohesion it is pushed by the flow towards an existing obstruction inside of the BOP. With a critical entanglement mass in place, a more compressible material is introduced/fed into the wellbore. The sealing material would then be pushed onto the entanglement using it as the scaffolding of the plug. As more sealing material is introduced the entanglement is compressed and anchors itself axially in the wellbore. Sealing is achieved as more and more soft material is compressed due to the significant pressure differential between the wellbore and environment. This method allows for significant sealing of the well with only a small amount of material compared to existing technologies.

4.7.2. Experiment Design

This section discusses the experimental setup and detailed pressure chamber design for testing anchoring and sealing (effective permeability) of a plug with varying aperture restrictions. The setup consists of a custom flow chamber connected to a fire truck to provide the uncontrolled flow. The permeability of the mechanical plug inside the chamber is measured under high pressures, as shown in Figure 4-51 by measuring the flow rate and pressure.

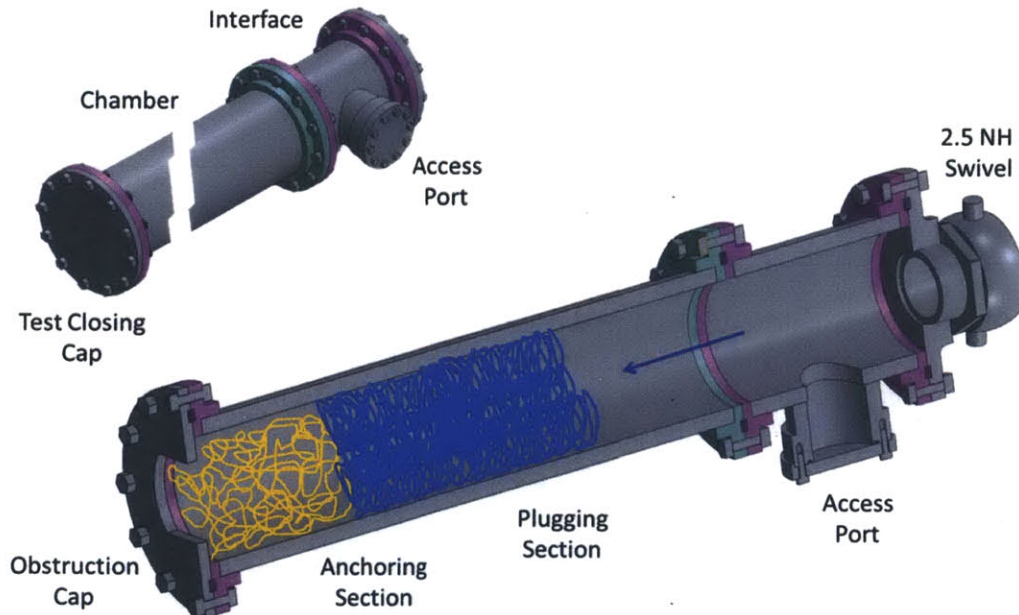


Figure 4-51: Custom flow chamber with interface region. The chamber is connected to the outlet of a fire truck hose via a 2.5 NH swivel connector.

4.7.2.1. Pressure Rating for Fire Truck

The experiment is designed to operate in an open flow loop configuration with a fire truck supplying a pressurized flow to the experimental setup. The maximum pressure that can be provided by a fire truck is 2.76 MPa (400 psi) dead stall pressure, and 1.03 MPa (150 psi) for a flow rate of 5,678 L/min (1,500 gal/min). Therefore, for a 10.2 cm (4 inch) bore diameter the minimum axial force that will be required from the obstruction caps is $\sim 27.9 \times 10^3$ N at full closure with an internal pressure of 3.45 MPa (500 psi). To account for any potential pressure spikes in the system, all of the flanges and connectors need to be rated to at least 6.8 MPa (1,000 psi) to obtain a safety factor of two. The interface for the fire truck can be either a 5-inch NH female thread or a 2.5-inch NH (National Hose) female thread, preferably with a swivel connection. The connection used will be a 2.5-inch NH (7.5 threads per inch, 3.068 inch outside diameter male) connection to keep the overall size of the interface smaller.

4.7.2.2. Flow Channel

In the case of full obstruction the flow channel needs to be rated to a pressure of 2.8 MPa (400 psi). An extra 0.7 MPa (100 psi) is added to account for any pressure fluctuation that may happen as part of the loading process, increasing the minimum pressure rating for the channel to 3.4 MPa (500 psi). A safety factor of 1.5 is added to the overall specifications to account for any material imperfection or micro cracks that could be present in the chamber as part of the manufacturing process. For perspective this is about the same safety factor used for airplanes. The thick-walled cylinder equations used to calculate the radial σ_{rr} , hoop $\sigma_{\theta\theta}$, and axial stress σ_{zz} are shown in Equation 4.27, Equation 4.28, and Equation 4.29 respectively [98].

$\sigma_{rr} = \frac{P_i \cdot r_i^2 - P_e \cdot r_e^2}{r_e^2 - r_i^2} - \frac{r_i^2 \cdot r_e^2 \cdot (P_i - P_e)}{r^2 (r_e^2 - r_i^2)}$	Equation 4.27
$\sigma_{\theta\theta} = \frac{P_i \cdot r_i^2 - P_e \cdot r_e^2}{r_e^2 - r_i^2} + \frac{r_i^2 \cdot r_e^2 \cdot (P_i - P_e)}{r^2 (r_e^2 - r_i^2)}$	Equation 4.28
$\sigma_{zz} = \frac{P_i \cdot r_i^2 - P_e \cdot r_e^2}{r_e^2 - r_i^2} - \frac{F_z}{\pi \cdot (r_e^2 - r_i^2)}$	Equation 4.29

Where r_e is the external radius, r_i is the internal radius, r is the location where the stress is being calculated, P_e is the external pressure, and P_i is the internal pressure. Therefore the axial force F_z on the cylinder is generated by an internal pressure differential on the cap as defined in Equation 4.30 using the mid radius to calculate the area.

$F_z = (P_i - P_e) \cdot \pi \cdot \left(\frac{r_e + r_i}{2} \right)^2$	Equation 4.30
--	---------------

The calculated von Mises yield stress for the aluminum chamber Al 6061 T651 ($\sigma_y = 276$ MPa @ 24° C)[151] is $\sigma_{vm} = 17.7$ MPa for a channel with an interior radius $r_i = 50.8$ mm (2.0 in), exterior radius $r_e = 63.5$ mm (2.5 in), and a pressure differential of $P_i - P_e = 3.45$ MPa (500 psi). At the maximum operating pressure the von Mises stress is at 9.6% of the yield, with the safety factor $\eta = 1.5$. The maximum pressure rating for this flow channel, with a safety factor of 1.5, is 184 MPa (5.20 ksi).

4.7.2.3. Seal Interfaces

Water-tight face seals between interfaces are achieved using O-rings.^{§§} It was not advisable to use gaskets, as they are prone to leaking. The O-ring used between the cap plate and flange is size 430 (5 1/8 inch ID, 5 5/8 inch OD, and 1/4 inch thick) with actual dimensions of 12.9 cm (5.1 inch) ID, 14.3 cm (5.65 inch) OD, and 6.9 mm (0.275 inch) thickness. The recommended gland depth, in Machinery's Handbook, for a static seal of a 1/4 inch thick o-ring is between 5.7 to 5.8 mm (0.226 to 0.229 inches) [152]. The recommend groove width for a 430 O-ring without backup rings is 9.5 mm (0.375 inches), with a bottom groove radius between 5.1 to 8.9 mm (0.020 to 0.035 inches). Therefore, the O-ring groove will has interior diameter of 12.7 cm (5.0 inches), exterior diameter of 14.6 cm (5.75 inches), with a gland depth of 5.6 mm (0.22 inches). The 150 um (0.006 inch) additional O-ring compression is used to maintain contact between the O-ring and both faces of the mating components. Conventional face seals have the O-ring groove on one of the components while keeping the mating component flat. In an effort minimize raw materials costs through use of on-site supplies, the O-ring gland depth was divided amongst both faces of the mating components. Admittedly, separating the groove adds complexity to multiple parts, but in this case the added benefit of such complexity is the ability to protect the sealing surface from scratches during assembly.

4.7.2.4. Seal Cap

The seal caps for testing the pressure vessel have to withstand the maximum shear force created from the internal pressure of the flow channel. The cap is made from Al 6061 T651 9.5 mm (3/8 inches) thick due to the onsite availability of the material. The operating shear stress (based on a 3.4 MPa (500 psi) internal pressure) on the cap is 13.8 MPa (8.7 % of yield with safety factor included) was calculated using Equation 4.31 with a safety factor of 1.5. The maximum rating for the cap geometry is 39.7 MPa (5.75 ksi) of internal pressure acting on a 101.6 mm diameter bore with a safety factor of 1.5. However, the partial O-ring groove on the seal cap reduces the effective thickness of the seal cap, thus reducing the maximum operating specifications as follows. The maximum shear stress at the operating conditions is 119.5 MPa (12.2 % of yield with safety factor included). The adjusted maximum pressure rating for the cap with the O-ring groove is reduced to 28.2 MPa (4,090 psi).

$$\tau_{flange} = \frac{F_z \cdot \eta}{2\pi \cdot t_{cap} \cdot r_i}$$

Equation 4.31

4.7.2.5. Bolt Circle Design

The purpose of the bolt circles that secure the cap is to transfer the axial loads created by the internal pressure of the chamber on the seal cap onto the flange while maintaining a preload on the o-ring interface to prevent leakage. The spacing between the bolts should be kept between three and five bolt diameters to abide by Saint-Venant's principle of characteristic dimensions and must also take into account wrench a clearances as well as a flange clearance. The bolt circle design that satisfies the functional system requirements consists of twelve bolts evenly distributed at a 16.5 cm (6.5 inches) along the circle. The distance between the bolts is 4.8 characteristic dimensions, assuming a 9.5 mm (3/8 inch) bolt diameter, thus abiding by Saint-Venant's Principle. The provided bolt circle is for a

^{§§} Please note that English units are provided since they are the standard dimension on the components and the references used.

flange wall thickness equal to the channel wall in order to minimize distortions during the welding process.

4.7.2.6. Bolt Preloading

The array of bolts must be preloaded to maintain the seal interface and keep the O-ring under compression. The preloading is nominally provided by a torque specification, even though the critical parameter is the tension of the bolt that matters. One way to calculate the torque preload is to use the torque tension relationship provided in Machinery's Handbook (Equation 4.32) and Shigley's Mechanical engineering design (Equation 4.33), which account for the axial load, thread friction, and face contact friction [152]. The second method is based upon fundamental principles and use experiments to determine the preload force; however, this method relies on measuring the elongation of the bolt for a given preload. Since the preferred method is to use a torque wrench, friction coefficients between the components will be estimated to calculate the torque required to achieve given preload. Notice that both of the equations below do not depend on the number of threads in contact, this is because the threads over one bolt diameter of length take the entire load [153].

$\Gamma_{preload} = F_{clamp} \left(\frac{l_{lead}}{2\pi} + \frac{d_{pitch} \cdot \mu_t}{2 \cos \alpha} + \frac{(d_{nom} + d_{bolthead}) \cdot \mu_f}{4} \right)$	Equation 4.32
--	---------------

Where F_{clamp} is the vertical clamping force, l_{lead} is lead of the screw, d_{pitch} is the pitch diameter of the threads, d_{nom} is the nominal diameter of the screw, $d_{bolthead}$ is the effective outer diameter of the bolt head, α is the thread pitch angle (60 deg for standard threads), μ_t is the thread interface friction coefficient, and μ_f is the friction coefficient for the flat contact interface between the bolt and flange.

$\Gamma_{preload} = \frac{d_{nom} \cdot F_{clamp}}{2} \cdot \left(\frac{\tan \lambda + \mu_t \cdot \sec \alpha}{1 - \mu_t \cdot \tan \lambda \cdot \sec \alpha} \right) + \frac{F_{clamp} (d_{nom} + d_{bolthead}) \cdot \mu_f}{4}$	Equation 4.33
--	---------------

Where λ is the lead angle defined as $\tan(\lambda) = l_{lead} / \pi \cdot d_{nom}$.

Figure 4-52 shows a plot of the preload required calculated both of the equations using $3/8$ -16 bolts with a ten percent additional clamp force estimating $\mu_t \sim 0.8$ (steel on steel) and $\mu_t \sim 0.45$ (steel and aluminum).

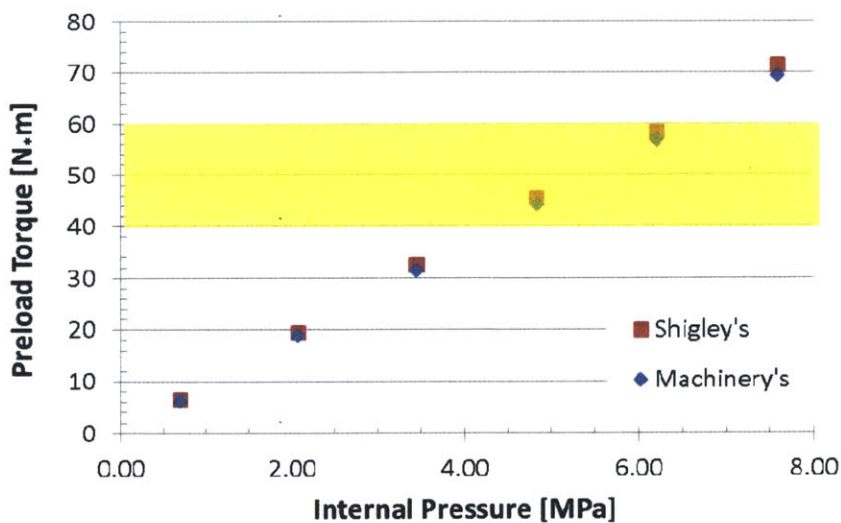


Figure 4-52: Bolt minimum preload required for range internal pressures calculated using two equations in literature

4.7.2.7. Flanges

The flange was designed with features for alignment and manufacturing. The weld interface between the flange and the channel was raised by 1.3 cm (0.5 inches) to minimize distortions of the flange face, otherwise the deflections of the flange face could lead to a poor seal leading to leakage. The interior of the flange also has an internal alignment face where the channel tubing rests to align the components. The thickness of the weld region was set to the same thickness of the channel wall to improve welding of the two units.

The flange receives the loads from the seal cap and transfers those loads to the channel via a weld. The first mode of failure of the flange is in shear from the axial loads. A similar calculation for the shear loads on the cap is done. The effective flange thickness is 9.9 mm (0.39 inches), which includes the reduction from half the O-ring groove gland depth. At the operating load of 3.4 MPa (500 psi) the flange maximum shear is 19.2 MPa, which is operating at 12.0% of the yield with a safety factor included. The maximum operating pressure of the flange is 29.6 MPa (4,150 psi), assuming a rated yield strength of 276 MPa.

The second mode of failure of the flange is shearing at the weld joint. The heating process during the welding process can soften the local region thus effectively annealing the local area and reducing the yield stress properties of the material. Therefore, without heat treatment post-welding the chamber, the maximum pressure rating is 7.34 MPa (1,070 psi), and with heat treatment after welding the pressure rating increases would increase up to 36.5 MPa (5,300 psi) for Al 6061 T651.

4.7.2.8. Obstruction Cap Sizing

The ram caps are to represent partially deployed ram structures at varying closure states. There are two types of obstructions: annular and rectangular. The annular geometry is used to model the behavior of a partially deployed annular ring or a pipe ram; while the rectangular geometry is used to model the partial closure of the blind shear rams. The obstructions were designed to cover from 25 to 55 percent of the cross sectional area of the flow channel, as shown in Figure 4-53.

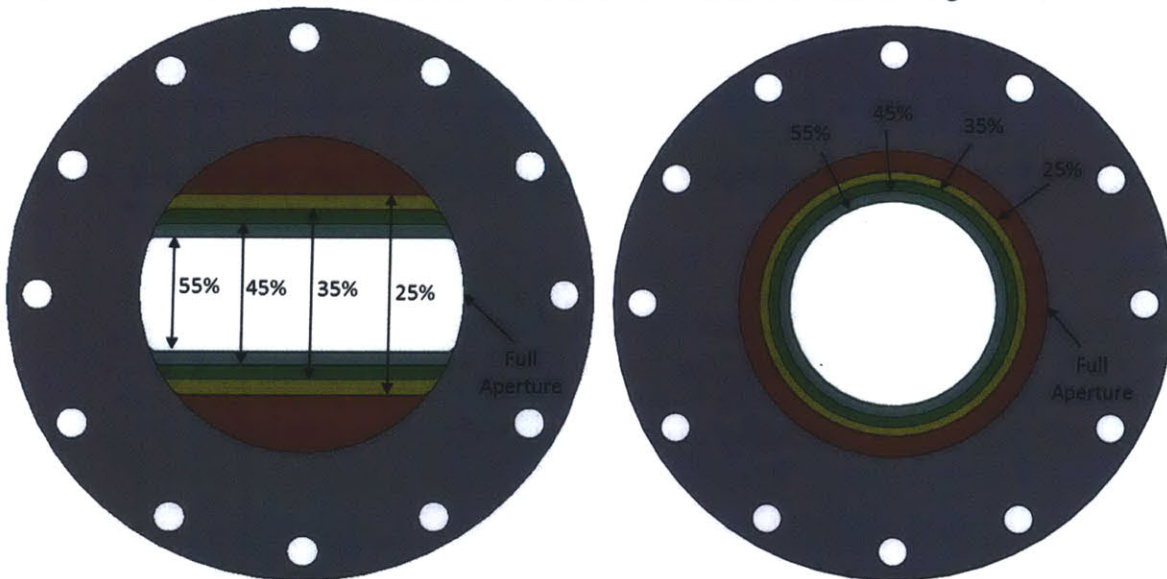


Figure 4-53: Ram and annular obstruction apertures

4.7.2.9. Interface Port

The interface section consists of a short channel section with a 5.4 cm (2.125 inch) access port into the flow region. The access port serves as both an instrumentation port and a possible wire feeding port similar to the choke/kill port on BOPs. The maximum rating of the port is 17.2 MPa (2,500 psi) with a safety factor of two. The mode of failure of the system the interface section is the blind thread on the port face. Therefore, when testing for higher pressure this section should be replaced and the port flange would also be changed accordingly.

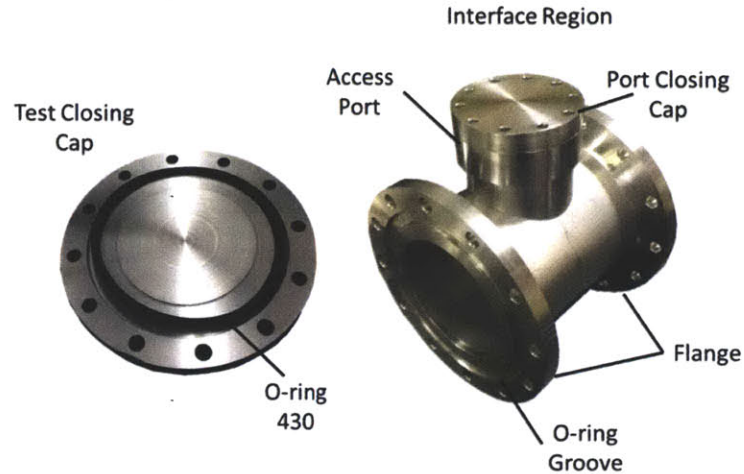


Figure 4-54: Interface region and bolt region

4.7.2.10. Summary

The maximum operating pressure of the unit is 7.34 MPa (1.07 ksi) with a safety factor of 1.5, which is limited by the strength of the untreated flange weld and the tensile strength of the access port bolts as shown in Table 4-9. At the expected operating pressure of 3.45 MPa (500 psi), all of the components are below 50 percent of the maximum allowable load before yield, which includes a minimum of 1.5 safety factor. For the pressure rating, the flange bolts ($3/8$ -16) are torqued to 60 N*m, while the access port bolts ($1/4$ -20) are torqued to 7 N*m. The calculated torque measurements are within the expected industry values, 50 ± 10 N*m for $3/8$ -16 threads for a high material strength, and 6 ± 1 N*m for $1/4$ -20 threads for low strength material.

Table 4-9: Chamber and interface failure modes and maximum pressure ratings

	Component	Failure Mode	Factor of Safety	Maximum Pressure rating	Operating to Yield % (500psi)
Chamber	Channel	Hoop and Axial	1.5	31.8 MPa (4.62 ksi)	10.8%
	Seal Cap	Shear	1.5	15.6 MPa (2.26 ksi)	22.1 %
	Bolts	Thread/Nut Shear	2.5	21.8 MPa (3.16 ksi)	15.9%
		Head Shear	2.5	17.4 MPa (2.53 ksi)	19.8%
		Body Tensile	2.5	9.58 MPa (1.39 ksi)	36.0%
	Flange	Shearing	1.5	28.7 MPa (4.16 ksi)	12.0%
	Flange Weld Untreated (20%)	Shearing	1.5	7.34 MPa (1.07 ksi)	46.9%
Flange Weld Heat Treated	Shearing	1.5	36.8 MPa (5.34 ksi)	9.4%	
Interface	Port Cap	Shear	2.5	39.6 MPa (5.75 ksi)	8.68 %
	Clamping bolts	Shear Thread	2.5	12.0 MPa (1.74 ksi)	28.8%
		Shear Head	2.5	12.9 MPa (1.87 ksi)	26.7%
		Tensile	1.5	7.5 MPa (1.09 ksi)	45.9%

4.7.3. Pressure Vessel Testing

Prior to welding, all four flanges were tested for flatness to quantify any distortions caused during the welding process. As shown in Table 4-10, the faces of the flanges were all within 50 um flatness prior to welding with the main source of error coming from the deformations caused by the chucks during the turning process, as shown by Figure 4-55. However, the flanges can distort during the welding process, which can lead to leakage. The measurements from flange three and four after welding revealed that the deformations were as great as 390 um across the face of the flange and 108 um in the O-ring groove. The warping from welding, however, did not affect the integrity of the seal.

Table 4-10: Flange flatness measurements from coordinate measuring machine with a 3 mm diameter contact probe

	Flange 1	Flange 2	Flange 3	Flange 4
Face (µm) [Post Welding]	43.9	44.8	42.1 [391.2]	33.9 [177.7]
O-ring Groove (µm) [Post Welding]	22.1	18.5	15.7 [107.8]	40.3 [79.7]

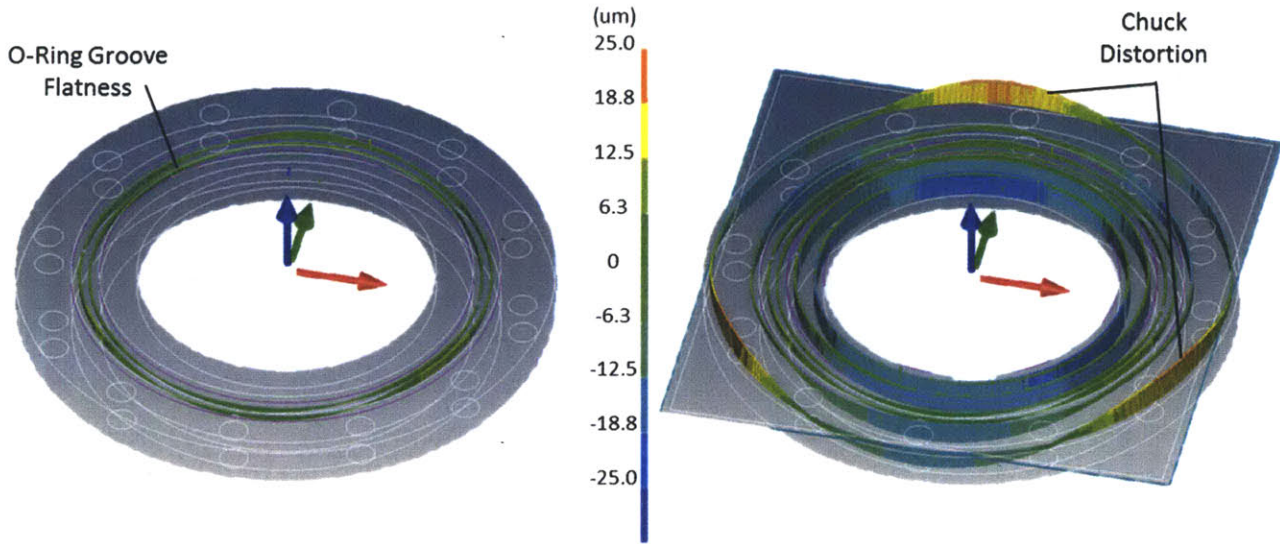


Figure 4-55: Flange flatness measurements for flange 3 showing the O-ring groove flatness profile and the overall plate flatness

The system was assembled and pressured tested using a hydrostatic test pump (Richard Dudgeon, Model 7555.1, Pressure Rating 6000 psi, S/N 9346) up to 6.7 MPa (1,000 psi) without leakage by Ramsay Welding where the flanges were welded together. After an hour there was still no leakage, but the pressure dropped to 5.5 MPa (800 psi) which is attributed to the seals in the test pump.

4.7.4. Experiment Setup

As discussed earlier, the flow chamber is connected to a fire truck with a max pressure rating of 1.52 MPa (220 psi) via a 2.5 NH hose as shown in Figure 4-56. The permeability of the mechanical plug is calculated based on the measured flow rate, pressure, fluid properties, and geometry.

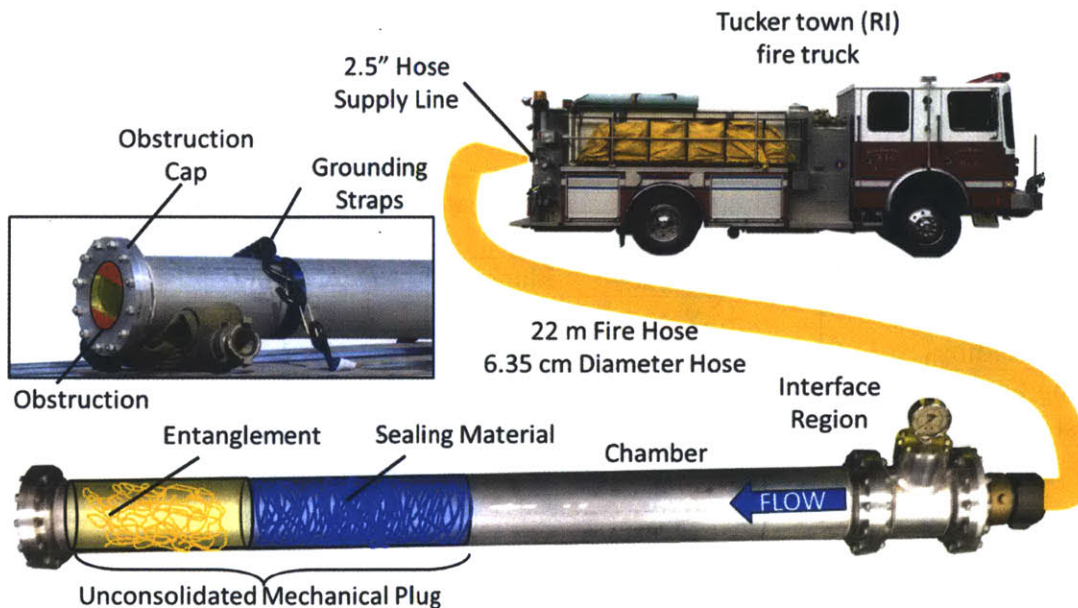


Figure 4-56: Fire truck permeability experimental setup

The chamber is filled from the open end with unconsolidated plugging material followed by a pre-formed stiff entanglement. An obstruction cap is used to close the open end. The fire truck is used to deliver a flow to the chamber, thus pushing unconsolidated plugging medium against anchor and compressing the anchor to the obstruction cap axially. In cases where the anchor does not catch on the obstruction the plugging material and anchor are ejected from the flow chamber. It is expected that for small obstructions the anchor will not have enough surface area to catch and will be ejected. As the obstruction percentage increases the entanglement is expected to catch and anchor on the obstruction.

For each obstruction cap the maximum pressure and flow rate are measured for a given entanglement and plugging medium. The wire selected for this set of experiments is made from galvanized steel wire (1.95 mm in diameter). A preliminary anchor loading experiment, see section 4.4.2 for details, was performed to determine the anchor type and expected behavior as it is compressed.

4.7.5. Fire Truck Permeability Test Data

Prior to investing in a high-pressure flow meter rough measurements were made to verify that the mechanical plug could reduce the flow of the channel in a significant manner with a substantial back pressure. Therefore, using a known quantity of sealing material we measured the flow rate at pressures higher than 0.69 MPa (100 psi) to calculate the percent sealing for the array of obstruction geometries. As shown in Figure 4-57, closure efficiencies above 70 percent was measured for obstructions 35% or larger. At lower obstructions, the entanglement does not have enough material to catch and anchor. As shown in Figure 4-58, at 25% obstructions the entanglement fails to anchor and is ejected below the maximum pressure rating of the flow loop. The experiments at obstruction coverage 35% and higher demonstrated that an entanglement can withstand the full pressure of the flow loop, tested up to 1.4 MPa (200 psi), without ejecting or extruding.

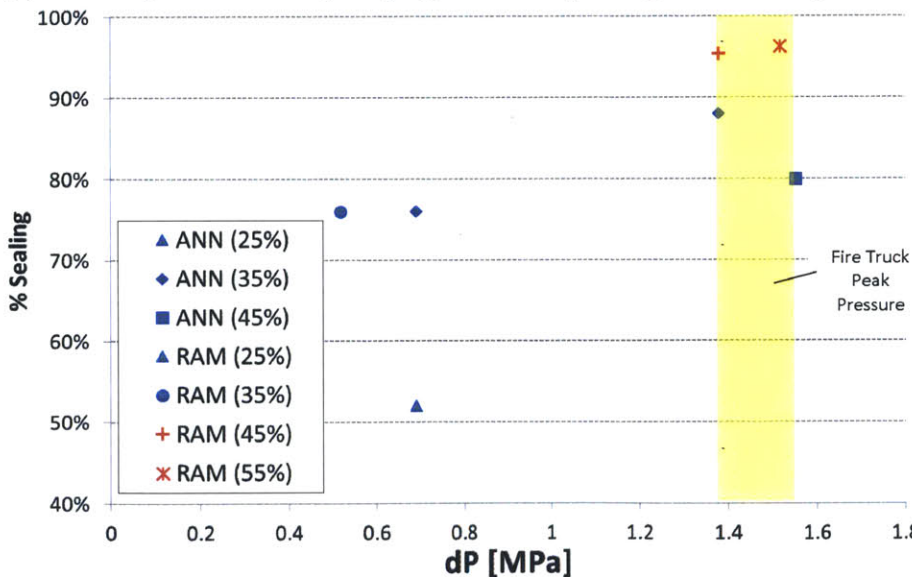


Figure 4-57: Pressure difference across plug versus percent closure for annular (ANN) and ram (RAM) obstructions with varying amount of plugging material. Blue labels are for 0.412 kg of heat shrink plugging material. Red labels are for 0.812 kg of heat shrink as plugging material. The entanglement used is a galvanized steel ($m_e = 0.32\text{kg}$) with a wavelength of ~ 1.5 inches (roughly $1/3$ of the wellbore diameter).

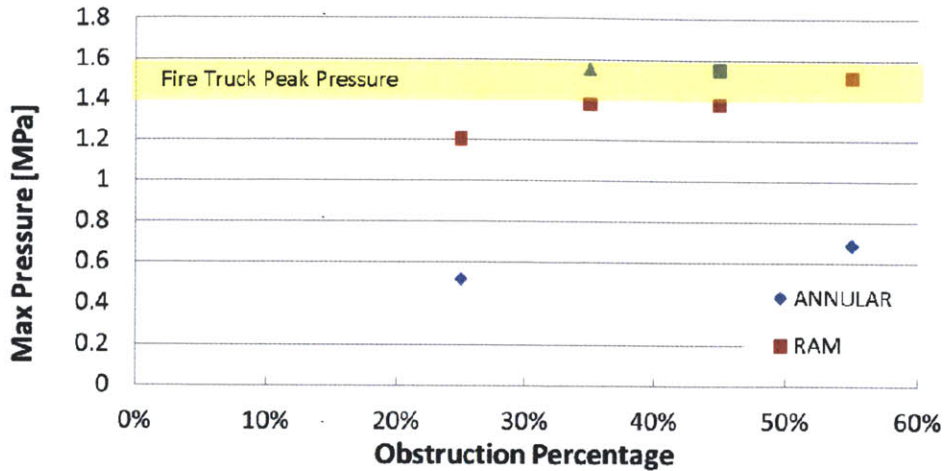


Figure 4-58: Maximum pressure differential measured for a given obstruction percentage of the annular and ram geometry for the data presented in Figure 4-57.

4.7.6. Conclusion

The permeability results proved that a significant obstruction could be generated with very little obstruction material. A minimum of 35 percent annular and ram obstruction is necessary to withstand a significant amount of back pressure. The ram obstructions were better for catching the plugging material and transferring the pressure load to the structure. Ram obstructions are much more efficient for anchoring than annular cross sections.

Chp 5.

Entanglement Model

An analytical wire entanglement model, proved intractable at this stage, but the methods to begin the study are presented herein as a basis for future work.

Modeling an entanglement generated by inserting a wire in a flow stream can begin by first modeling the dynamic behavior of a wire entering the wellbore at a known velocity and arbitrary entry angle (α), as shown in Figure 5-1. The formulation presented is primarily based on the work done for high speed printing, but other applications include tape, transponders, cloth handling equipment, telescoping robotic arms, spacecraft deployable sections, etc.. Since the wire can be considered highly flexible member that will undergo large deflections, linear models will not be accurate. The foundation of the work above is based on the early work modeling elastica developed by a series of scientist and engineers such as Galileo, Hooke, Bernoulli, and Euler [154]. The topic is commonly referred to as “elastica” theory. Another nonlinear model technique that can be used for an inextensible member undergoing large deformation is a springs/chain model consisting of rigid elements joined by rotation springs. Both the elastica and the spring model should agree in the region where drag forces dominate. The spring model, however, can continue to be used to model an entanglement undergoing complete plastic deformations. The models that follow examine the dynamics of a flexible continuous structure with a varying cross flow derived using elastica theory and element discretization.

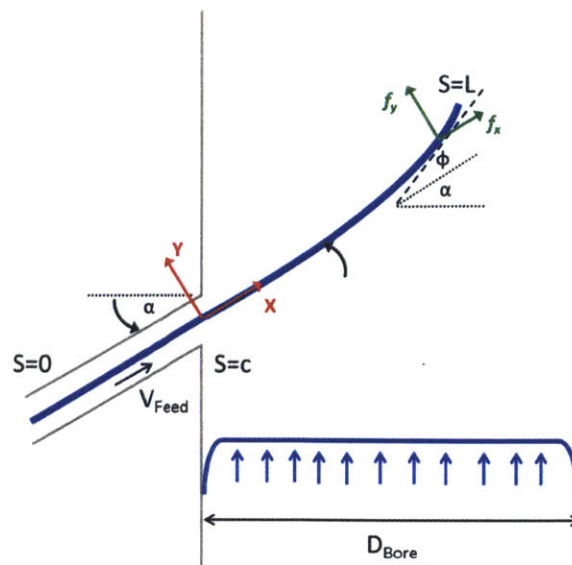


Figure 5-1: Flexible wire entering the wellbore

5.1. Background

The study of high of thin structures undergoing large non-linear deformation has been a study of interest to many fields. Table 5-1 shows some of the work developed over the years and their corresponding solution approach.

Table 5-1 Elastica model background selected papers

Year	Author	Discrete	Closed Form	Numerical	Inextensible	Gravity	Drag	Contact	Title
1945	Bisshop and Drucker		X		X				Large Deflection of Cantilever Beams
1956	Conway				X				Nonlinear Bending of thin Circular Rods
1959	Mitchell		X						The Nonlinear Bending of Thin Rods
1959	Newmark	X		X					A Method of Computation for Structural Dynamics
1962	Frish-Fay		X		X				Flexible Bars
1974	Nordgren	X		X			X		On Computation of the Motion of Elastic Rods
1979	Sinclair		X						The Non-Linear Bending of a Cantilever Beam with Shear and Longitudinal Deformations
1981	Benson		X					X	The Deformation of a Thin, Incomplete, Elastic Ring in a Frictional Channel
1985	Buffinton and Kane		X	X	X				Dynamics of a Beam Moving Over Supports
1987	Kokarakis & Bernitsas		X	X					Effect of Extensibility on Large Deformation Three-Dimensional Static Behavior of Beams
1987	Mansfield and Simmonds	X			X	X			The Reverse Spaghetti Problem: Drooping Motion of an Elastica Issuing from a Horizontal Guide
1988	Bauchau and Hong	X		X					Nonlinear Response and Stability Analysis of Beams Using Finite Elements in Time
1986a	Simo and Vu-Quoc	X		X	X				On the Dynamics of Flexible beams Under Large Overall Motions
1992	Stolte and Benson		X	X	X				Dynamic Deflection of Paper Emerging from a Channel
2007	Hong et al			X		X	X	X	Dynamic Analysis of Flexible Media by Dynamic Elastica Theory with Aerodynamic Effect

5.2. Derivation

The derivations for both elastica and spring model are each provided without interaction (i.e. buckling) in this section. Subsequent sections expand on the interaction between the wire and the wellbore which can lead to buckling of the structure.

5.2.1. Elastica Model without interaction

The formulation of the elastic model is based on the prior work of predominantly three papers Mansfield et al. [112], Stolte et al [155], and most recently Hong et al. [156]. This is for a thin flexible wire inserted into a flow stream at an arbitrary angle of injection with gravitational loads. While this derivation will follow their general approach, it is sub divided into sub sections.

5.2.1.1. Coordinate System

The coordinate system shown in Figure 5-2 illustrates a wire exiting an arbitrary angle (α) relative to global reference frame (\bar{x}, \bar{y}) , where $x(s)$ is the projected distance of the wire onto the x axis, similarly $y(s)$ is the projected distance of the wire onto the y axis. Therefore, $\alpha=0$ feeds the wire orthogonal to the flow. While and $\alpha>0$ will feed wire with the direction of the flow, thus positive angles are measured in the counter-clockwise from horizontal. The origin of the fixed coordinate frame (x, y) is at the entry where the wire enters the wellbore. The secondary coordinate system also used is s , which is measured along the length of the wire with the leading edge at $s=L$, lagging edge at $s=0$, and location at the clamp (i.e. entry) is at $s=c$. Therefore, the location of any point on the curve outside of the channel can be expressed in terms of $x(s)$ and $y(s)$ as shown in Equation 5.1 and Equation 5.2 respectively, where $\phi(s)$ is the angle from x direction.

$x(s) = \int_c^s \cos(\phi(\bar{s})) d\bar{s}$	Equation 5.1
$y(s) = \int_c^s \sin(\phi(\bar{s})) d\bar{s}$	Equation 5.2

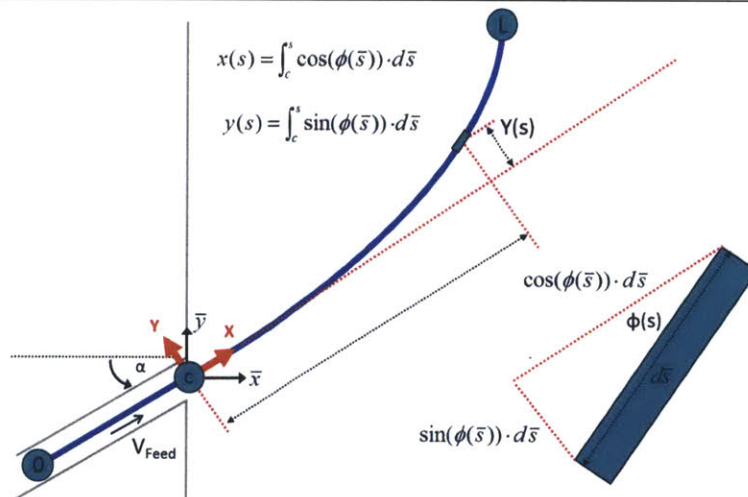


Figure 5-2: Coordinates on any point in the active region as a function of $\phi(s)$.

5.2.1.2. Deformation Potential

The deformation potentials, Equation 5.3 and Equation 5.4, are used to accomplish the “analogous reduction of dynamic problems” but are best understood using Figure 5-3 [112].

$u = \int_s^L x \cdot d\bar{s}$	Equation 5.3
$v = \int_s^L y \cdot d\bar{s}$	Equation 5.4

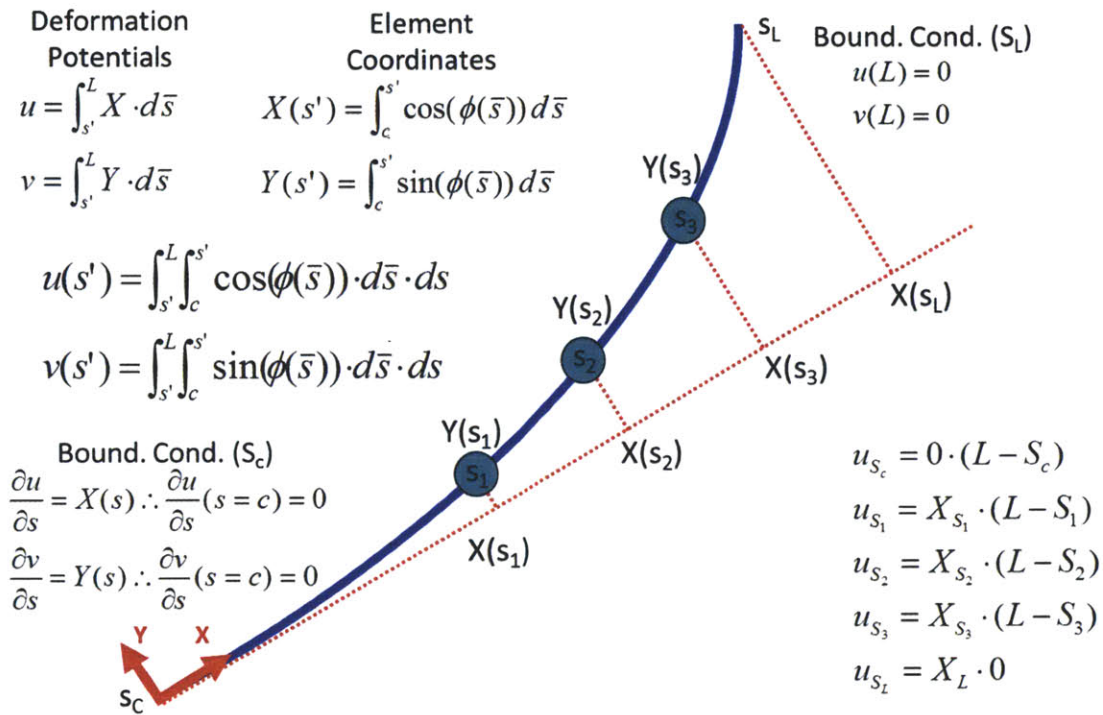


Figure 5-3: Deformation potential with boundary conditions

Taking the second derivative of the deformation potential, as shown in Equation 5.5 and Equation 5.6, yields a simplification that will later be used on the governing equations of the system.

$u = \int_s^L x \cdot d\bar{s} \Rightarrow u = \int_s^L \left(\int_c^{\bar{s}} \cos \phi \cdot d\bar{s} \right) ds \Rightarrow \frac{\partial^2 u}{\partial s^2} = -\cos \phi$	Equation 5.5
$v = \int_s^L y \cdot d\bar{s} \Rightarrow v = \int_s^L \left(\int_c^{\bar{s}} \sin \phi \cdot d\bar{s} \right) ds \Rightarrow \frac{\partial^2 v}{\partial s^2} = -\sin \phi$	Equation 5.6

5.2.1.3. Curvature Derivation

The curvature ($\kappa=1/r$) of the wire can be derived using small angle approximation, with the Pythagorean*** Thm as shown in Figure 5-4 to obtain the final form of the curvature equation shown in Equation 5.7.

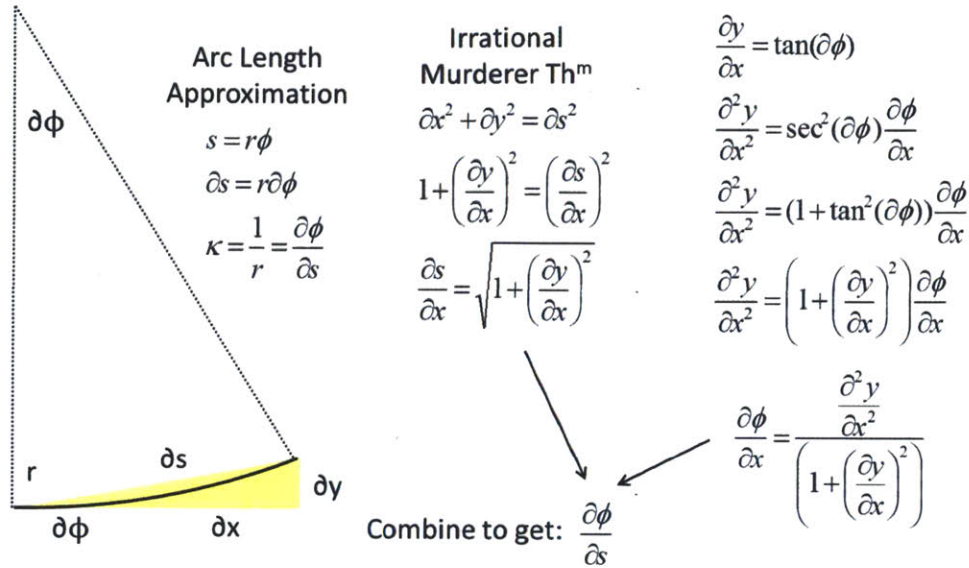


Figure 5-4: Curvature derivation

$\kappa = \frac{d^2 y / dx^2}{\left[1 + (dy / dx)^2\right]^{3/2}} \approx \frac{d^2 y}{dx^2}$	Equation 5.7
---	--------------

5.2.1.4. Governing Equations

The governing equation for the behavior of the wire ejected into the wellbore starts with the fundamental beam equation based on a force balance of an element as shown in Figure 5-5 that yields to Equation 5.8.

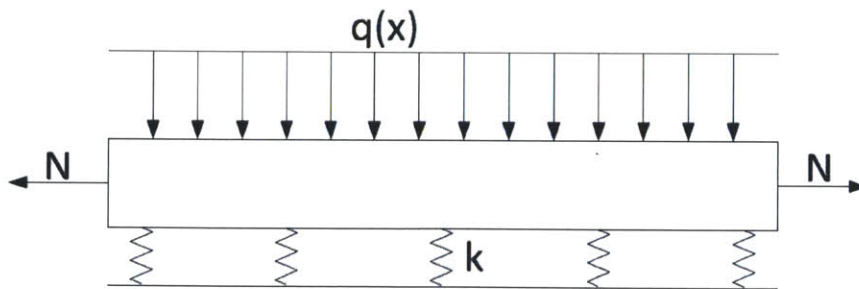


Figure 5-5 Element force balance

$E \cdot I \cdot w'''' - N \cdot w'' + k \cdot w = q(x)$	Equation 5.8
--	--------------

The first term that is eliminated is the elastic foundation represented by the k since there is no support on the other side of the applied load. Since, the wire is assumed to be inextensible (i.e. length is constant) then the term with the N drops out as well, leaving the reduced form as Equation 5.9.

*** Also can be referred to as the murder of Hippatus after he could not disprove the existence of irrational numbers.

$E \cdot I \cdot w'''' = q(x)$	Equation 5.9
--------------------------------	--------------

Integrating the equation above and putting in term of the angular rotation ϕ (i.e. $\phi = w'$) yields Equation 5.10 that is similar to that used by Stolte et al. [155]. The integral term on the right is the shear stress, and where bending rigidity D was replaced by EI since D is the bending rigidity used for wide beams [98].

$E \cdot I \cdot \frac{\partial^2 \phi}{\partial s^2} = \int_s^L q(s) ds$	Equation 5.10
---	---------------

Where s is the arc length along the wire. Stolte et al.'s governing equation (Equation 5.11) is found by separating the distributive loads into the shear components on the element as shown in Figure 5-6.

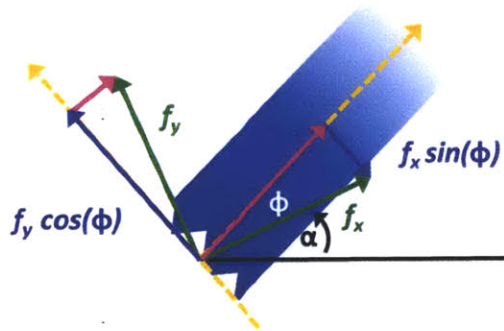


Figure 5-6: Shear force components

$E \cdot I \cdot \frac{\partial^2 \phi}{\partial s^2} = V_x(s) \cdot \sin(\phi) - V_y(s) \cdot \cos(\phi)$	Equation 5.11
--	---------------

Where $V_x(s)$ and $V_y(s)$ are the shear forces from integrating the distributive loads f_x and f_y , respectively as shown in Equation 5.12 and Equation 5.13.

$V_x = \int_s^L f_x(\bar{s}) d\bar{s}$	Equation 5.12
--	---------------

$V_y = \int_s^L f_y(\bar{s}) d\bar{s}$	Equation 5.13
--	---------------

5.2.1.5. Distributive Loads

The distributive loads f_x and f_y can be composed of gravity, inertial loads, and exterior loading such as the cross flow drag force generated from cross fluid flow as shown in Equation 5.14 and Equation 5.15.^{†††}

$f_x = -mg \sin \alpha - m\ddot{x} + F_{d,\bar{x}}(\bar{x}, \phi) \sin \alpha$	Equation 5.14
--	---------------

$f_y = -mg \cos \alpha - m\ddot{y} + F_{d,\bar{x}}(\bar{x}, \phi) \cos \alpha$	Equation 5.15
--	---------------

While the gravitational term (mg) and inertial terms ($m\ddot{x}, m\ddot{y}$) are covered in prior derivations, the drag term ($F_{d,x}$) is added here to account for the loading imparted by the flow on the wire. Note

^{†††} The derivation done in Hong et al defines the angle α from the plane of the ejection, thus making their α negative; while α is defined here as positive being counterclockwise and negative being clockwise. This little negative sign was a source of confusion for some time.

that the drag load depends on the global coordinates since the drag force varies along the radius of the wellbore. The loading variables are derived from the geometry shown in Figure 5-7.

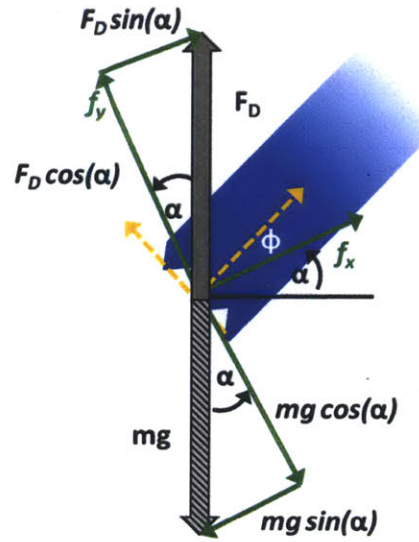


Figure 5-7: Drag force and gravity division into components along the f_x and f_y direction

In reality there can be two type of drag loading: shear and cross flow. Shear drag is induced by the resistance of the fluid along the length of the wire during the feeding process, as the insertion velocity increases so does the effect of shear drag force. The cross flow drag refers to the force imparted on the wire by the flow (shown as F_D in figure above). The cross sectional drag load can differ for each section of the wire depending on the orientation, wire geometry, and location along the channel. Thus it is recommended that finite element models have a sub-routine for calculating the force of drag for each individual element over each iteration.

Note that one assumption made here is that the shear drag force on the wire as it is fed into the flow is assumed to be small compared to the cross flow drag force. In the case that the fluid velocity is zero, it has been shown by Kobayashi et al. that the shear fluid force can play an important role for the reverse Spaghetti problem [110].

5.2.1.6. Partial Differential Equations

This is the set of three partial differential equations to be solved simultaneously.

$\frac{\partial^2 u}{\partial s^2} = -\cos \phi$	Equation 5.16
$\frac{\partial^2 v}{\partial s^2} = -\sin \phi$	Equation 5.17
$EI \frac{\partial^2 \phi}{\partial s^2} = -\sin \phi m \ddot{u} + \cos \phi m \ddot{v} + mg(L-s)\{\cos \phi \cos \alpha - \sin \phi \sin \alpha\} + \sin \phi \int_s^L F_D ds - \cos \phi \int_s^L F_D ds$	Equation 5.18

In order to solve the system the acceleration terms and the terms related to $\cos(\phi)$ and $\sin(\phi)$ must be approximated.

5.2.1.7. Quasi-linearization

A quasi-linearization technique is used in Stolte et al. and Hong et al. to make the system of equations easier to solve through the iteration process. As shown in Equation 5.19 and Equation 5.20, $\sin(\phi)$ and $\cos(\phi)$ are approximated to a linear system of the previous value. In the equations the star (*) implies the last known value in the iteration process.

$\sin \phi \approx \sin \phi^* + (\phi - \phi^*) \cos \phi^*$	Equation 5.19
$\cos \phi \approx \cos \phi^* - (\phi - \phi^*) \sin \phi^*$	Equation 5.20

Similarly, the acceleration terms also undergo the quasi linearization process as shown in Equation 5.21 and Equation 5.22.

$\begin{aligned} \ddot{u} \sin \phi &\approx (\ddot{u}^* + (\ddot{u} - \ddot{u}^*)) \cdot (\sin \phi^* + (\phi - \phi^*) \cos \phi^*) \\ &\approx -\ddot{u}^* \phi^* \cos \phi^* + \ddot{u}^* \phi \cos \phi^* + \ddot{u} \sin \phi^* \end{aligned}$	Equation 5.21
$\begin{aligned} \ddot{v} \cos \phi &\approx (\ddot{v}^* + (\ddot{v} - \ddot{v}^*)) \cdot (\cos \phi^* - (\phi - \phi^*) \sin \phi^*) \\ &\approx \ddot{v}^* \phi^* \sin(\phi^*) - \ddot{v}^* \phi \sin \phi^* + \ddot{v} \cos \phi^* \end{aligned}$	Equation 5.22

5.2.1.8. Finite Difference

Applying the finite difference to the spatial and time domain is used to develop an iterative solution. The center difference technique is applied to the spatial domain (Equation 5.23 and Equation 5.24); while, a back difference approximation is performed for the time domain (Equation 5.25).

$\frac{\partial^2 u}{\partial s^2} = \frac{u_{i-1,j} - 2u_{i,j} + u_{i+1,j}}{\Delta s^2}$	$\frac{\partial^2 v}{\partial s^2} = \frac{v_{i-1,j} - 2v_{i,j} + v_{i+1,j}}{\Delta s^2}$	Equation 5.23
$\frac{\partial^2 u}{\partial t^2} = \frac{u_{i,j} - 2u_{i,j-1} + u_{i,j-2}}{\Delta t^2}$	$\frac{\partial^2 v}{\partial t^2} = \frac{v_{i,j} - 2v_{i,j-1} + v_{i,j-2}}{\Delta t^2}$	Equation 5.24
$\frac{\partial^2 \phi}{\partial s^2} = \frac{\phi_{i-1,j} - 2\phi_{i,j} + \phi_{i+1,j}}{\Delta s^2}$		Equation 5.25

5.2.1.9. Matrix Form for System of Equations

Applying the quasi-linearization and the finite difference approximation to set of partial differential equations yields the matrix system shown by Equation 5.26, Equation 5.27, and Equation 5.28, to be solved simultaneously.

$\frac{\partial^2 u}{\partial s^2} = \frac{u_{i-1,j} - 2u_{i,j} + u_{i+1,j}}{\Delta s^2} = -\cos \phi^* + (\phi - \phi^*) \sin \phi^*$	Equation 5.26
--	---------------

$\frac{\partial^2 v}{\partial s^2} = \frac{v_{i-1,j} - 2v_{i,j} + v_{i+1,j}}{\Delta s^2} = -\sin \phi^* + (\phi - \phi^*) \cos \phi^*$	Equation 5.27
--	---------------

$EI \frac{\partial^2 \phi}{\partial s^2} = -\sin \phi m \ddot{u} + \cos \phi m \ddot{v}$ $+ m g (L - s) \{ \cos \phi \cos \alpha - \sin \phi \sin \alpha \}$ $+ \sin \phi \int_s^L F_D ds - \cos \phi \int_s^L F_D ds$ $EI \frac{\phi_{i-1,j} - 2\phi_{i,j} + \phi_{i+1,j}}{\Delta s^2} = -(\sin \phi^* + (\phi - \phi^*) \cos \phi^*) m \left(\frac{u_{i,j} - 2u_{i,j-1} + u_{i,j-2}}{\Delta t^2} \right)$ $+ (\cos \phi^* - (\phi - \phi^*) \sin \phi^*) m \left(\frac{v_{i,j} - 2v_{i,j-1} + v_{i,j-2}}{\Delta t^2} \right)$ $+ m g (L - s) \{ \cos \alpha (\cos \phi^* - (\phi - \phi^*) \sin \phi^*) - \sin \alpha (\sin \phi^* + (\phi - \phi^*) \cos \phi^*) \}$ $+ (\sin \phi^* + (\phi - \phi^*) \cos \phi^*) \int_s^L F_D ds - (\cos \phi^* - (\phi - \phi^*) \sin \phi^*) \int_s^L F_D ds$	Equation 5.28
---	---------------

5.2.1.10. Flow Diagram for Elastica Model

A matlab code was written in an attempt to solve this system of equations. The flow diagram for solving the system of equations is illustrated in Figure 5-8.

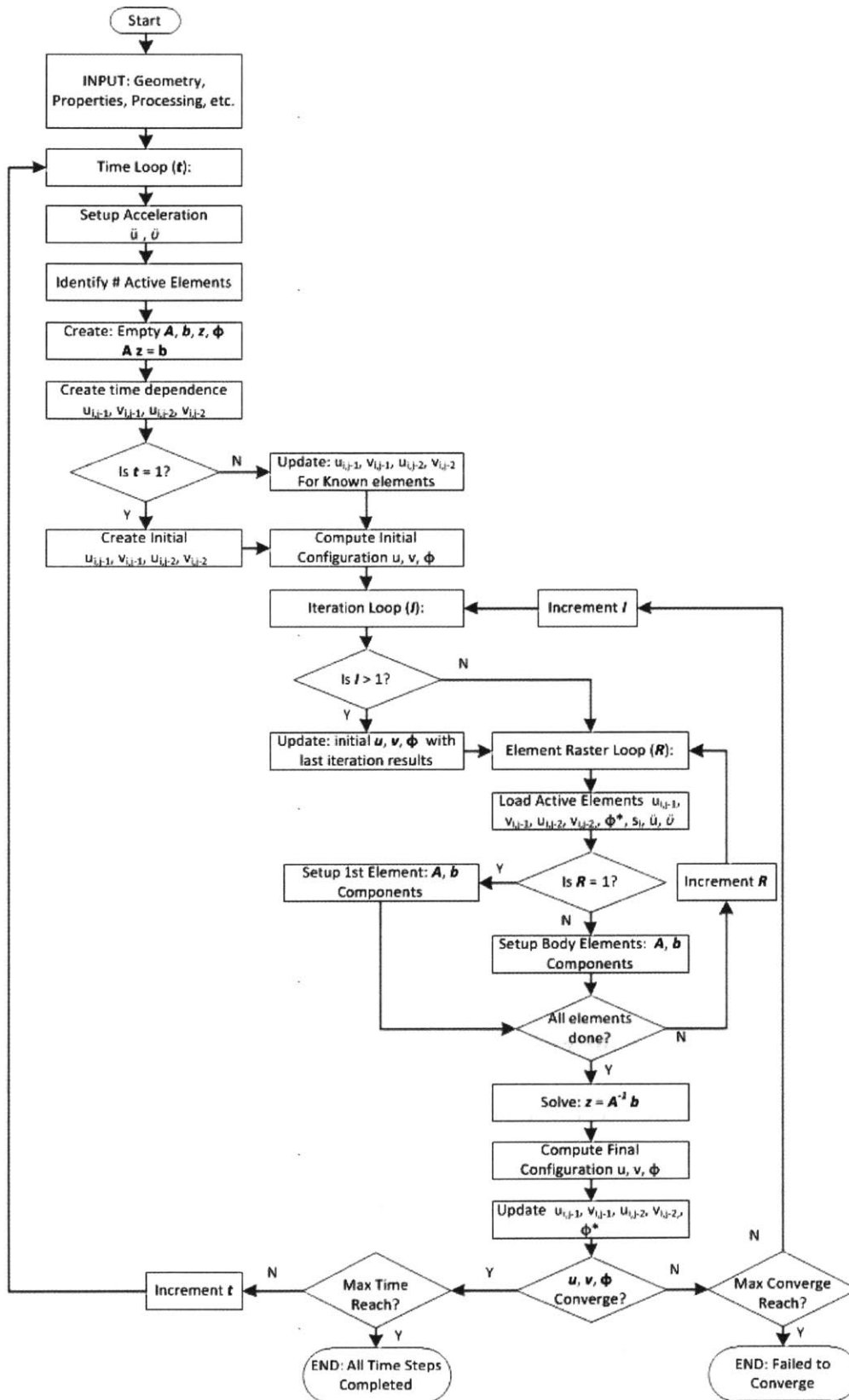


Figure 5-8: Elastica model program flow diagram

5.2.2. Simplified Spring Model without Interaction

The rotational spring model starts with the discretization of wire into n rigid elements with connecting $(n-1)$ rotational spring as shown in Figure 5-9. The rotation springs represent the rotation stiffness of the wire for that section. The loading on each element can be gravitational, inertial, or externally applied. The only force considered in this section is the drag force imparted onto the wire elements from the cross sectional fluid flow.

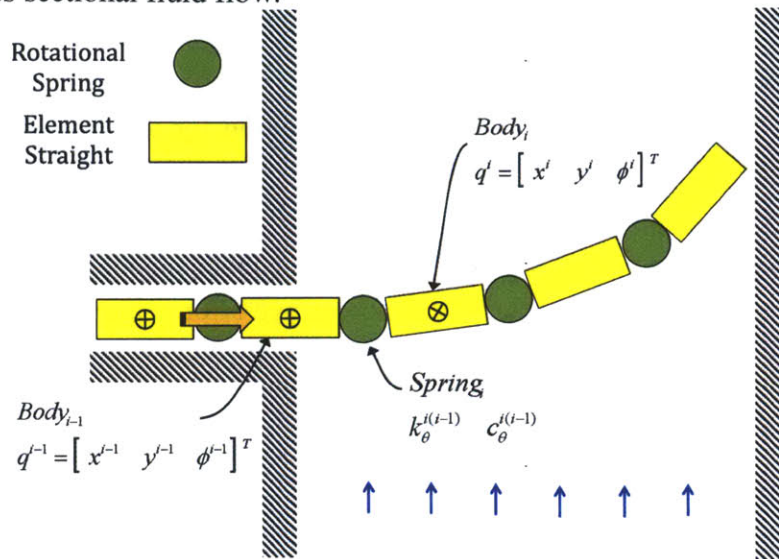


Figure 5-9: Discrete element diagram

The angle between elements can be determined from first doing a moment balance on each element as shown in Figure 5-10. One underlying assumption is that the system is in steady state such that the dynamic loads are small. This assumption can later be revised. Another assumption is that the difference in angle between the elements is small such that there is no need to account for the torque generated by the shear and normal components rotated about the spring node (this will not be the case in the model that follows). The system of torque equations can then be solved in matrix form by arranging the equations in the form $A\tau = b$. In this case the τ is the unknown torques matrix, A is the relation between the elements, and b is torques from the applied loads as shown in Equation 5.29.

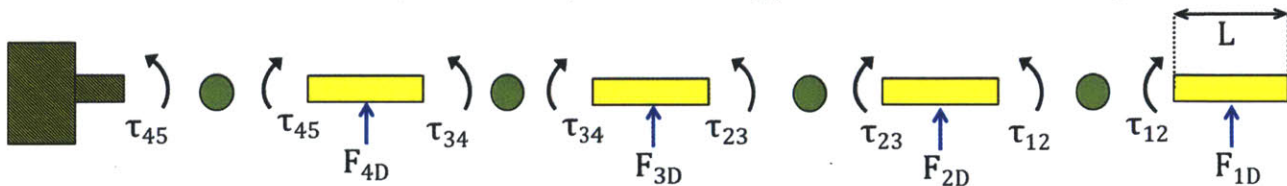


Figure 5-10: Four-element moment balance for discrete torsion springs model

$\begin{bmatrix} 1 & 0 & 0 & 0 \\ -1 & 1 & 0 & 0 \\ 0 & -1 & 1 & 0 \\ 0 & 0 & -1 & 1 \end{bmatrix} \cdot \begin{bmatrix} \tau_{12} \\ \tau_{23} \\ \tau_{34} \\ \tau_{45} \end{bmatrix} = \frac{L}{2} \begin{bmatrix} F_{1D} \\ F_{2D} \\ F_{3D} \\ F_{4D} \end{bmatrix} + L \begin{bmatrix} 0 \\ F_{1D} \\ F_{1D} + F_{2D} \\ F_{1D} + F_{2D} + F_{3D} \end{bmatrix}$	Equation 5.29
--	---------------

The relation between change in angle of rotation ($\Delta\phi_i$) and torque of each element is shown in Equation 5.30.

$$K_i \cdot \Delta\phi_i = \tau_i$$

Equation 5.30

Where K_i is the effective rotational stiffness given by Equation 5.31.

$$K_i = \frac{E_i \cdot I_i}{L_i}$$

Equation 5.31

Through an iteration process the rotation angles vector (ϕ) can be found. At each iteration the drag load is adjusted accordingly to the geometry.

5.2.2.1. Validation

This method was compared as the analytical solution for a simple cantilever beam with tip loading to ensure that in the static configuration of both models agrees. The test model consisted of an aluminum beam ($E = 70 \times 10^9 \text{ N/m}^2$, $\sigma_y = 500 \text{ N/m}^2$) with the following geometry base 25.4 cm, height of 10 cm, and length 0.25 m. The beam was subjected to 845 N at the tip to yield the maximum moment at the base of 211.3 N*m, where the moment at yield is equal to 211.6 N*m. As shown in the displacement (Figure 5-11) and tip displacement percentage error (Figure 5-12) plots, subdividing the beam into a low number of elements has a significant amount of error in the solution. As the number of elements increases to one hundred the error drops to 1 percent.

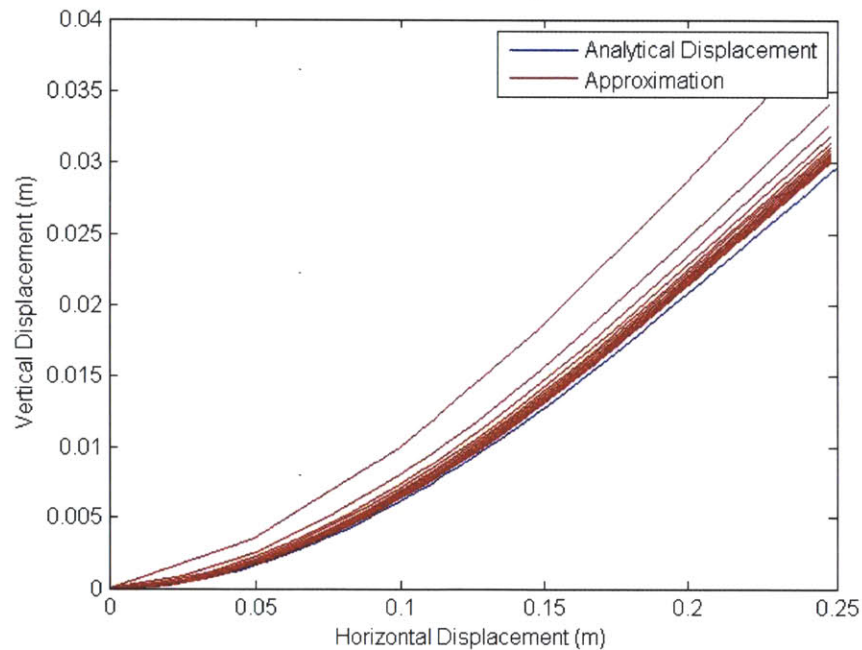


Figure 5-11: Horizontal displacement versus vertical displacement for simple cantilever beam analytical solution and approximation with increasing number of sections

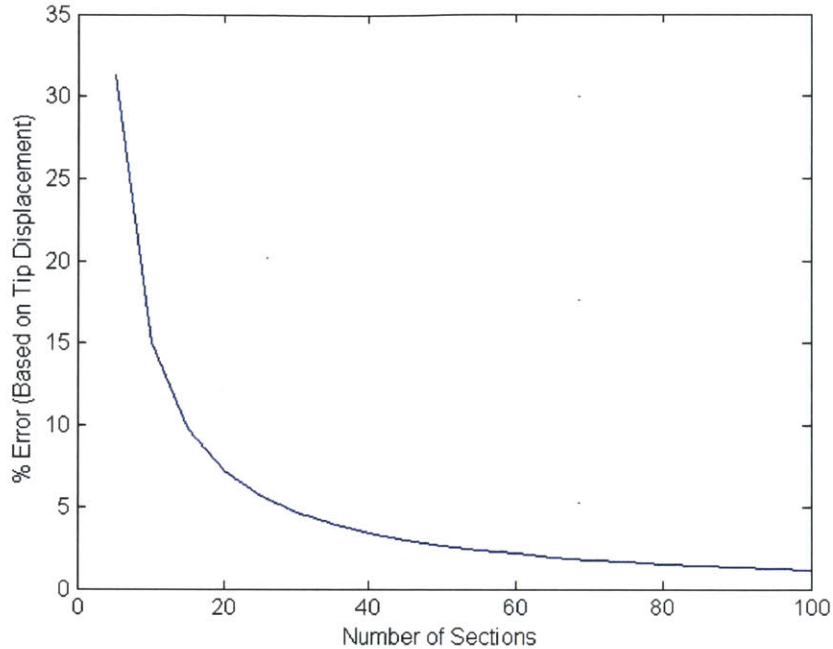


Figure 5-12: Number of sections versus percent error of simplified spring model

The spring model can be used to predict the shape of a wire that is fed into a pipe with fluid flow to determine the parameters that lead to entanglement. The deformation on the wire is assumed to be purely bending for the first order model, which implies that the stiffness of the wire is comparable to the loading applied. The model works by stepping through a discretized time step and imposing a deformation on each element. One limitation of this model is capturing the dynamic effect of the wire as the set of equations is a balance of forces and moments.

5.2.2.2. Discussion

The simplified spring model serves only as a first order approximation. The inherent assumption in the model above is that the angle change is small such that it is not a significant effect. As the angle between the elements increases, the shear and normal components can create a pseudo-torque on the following element; therefore, this model needs to be further refined to keep track of the orientation between the elements and rotate the shear and normal forces accordingly. This is the equivalent of making sure that each node is in equilibrium and that each element is in equilibrium without assuming a small angle approximation.

5.2.3. Springs Model with Angle Correction and without Interaction

As shown in Figure 5-13, the spring model can be modified to account for an arbitrary drag angle, and large angle distortions between the elements. With this approach; however, the solution requires finding the normal and shear components as well as the torques for each element.

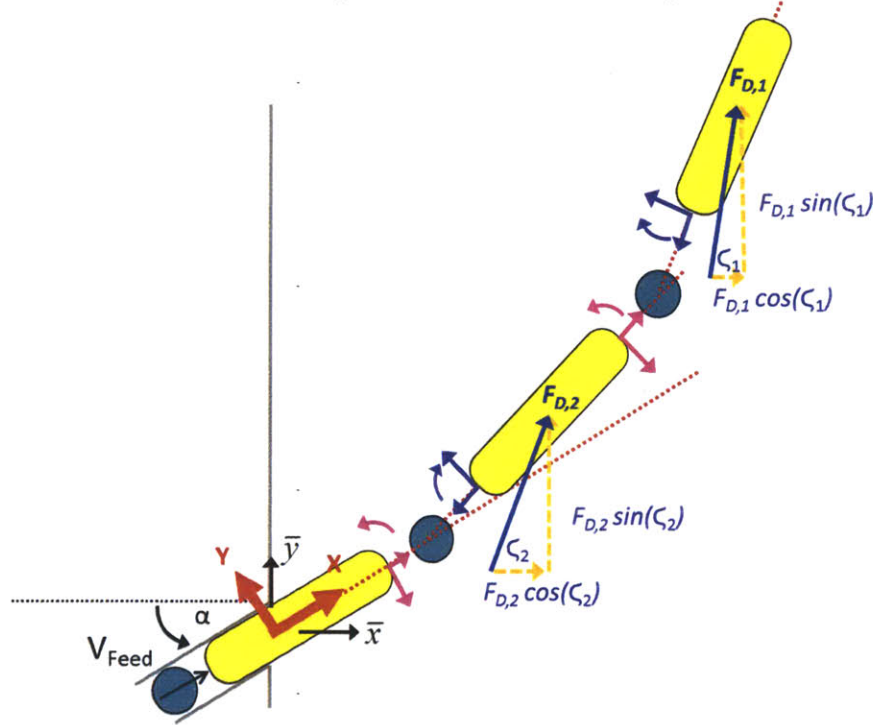


Figure 5-13: Element discretization

The original loading for the normal, shear, and moment at the rear of each element (i.e. purple) can be found using Equation 5.32, Equation 5.33, and Equation 5.34 respectively. The drag force is calculated for each section using the location along the \bar{x} direction and tilt ($\phi_i + \alpha$) as described later in the loading section.

$N_{i,o} = F_{D,i} \cos \zeta_i \cos(\phi_i + \alpha) + F_{D,i} \sin \zeta_i \sin(\phi_i + \alpha) + N_{i-1,f}$	Equation 5.32
$\gamma_{i,o} = -F_{D,i} \sin \zeta_i \cos(\phi_i + \alpha) + F_{D,i} \cos \zeta_i \sin(\phi_i + \alpha) + \gamma_{i-1,f}$	Equation 5.33
$\tau_{i,o} = -rF_{D,i} \sin \zeta_i \cos(\phi_i + \alpha) - rF_{D,i} \cos \zeta_i \sin(\phi_i + \alpha) + \tau_{i-1,f} - 2r\gamma_{i-1,f}$	Equation 5.34

The translation between the initial or original (o), and final loading (f) for the next element is done by setting the torsion spring node at equilibrium. As shown in Figure 5-14, the original normal ($N_{i,o}$) and shear ($\gamma_{i,o}$) components from the previous element are rotated accordingly to final normal ($N_{i,f}$) and shear ($\gamma_{i,f}$) components of the current element by imposing equilibrium at the spring node using Equation 5.35 and Equation 5.36 respectively.

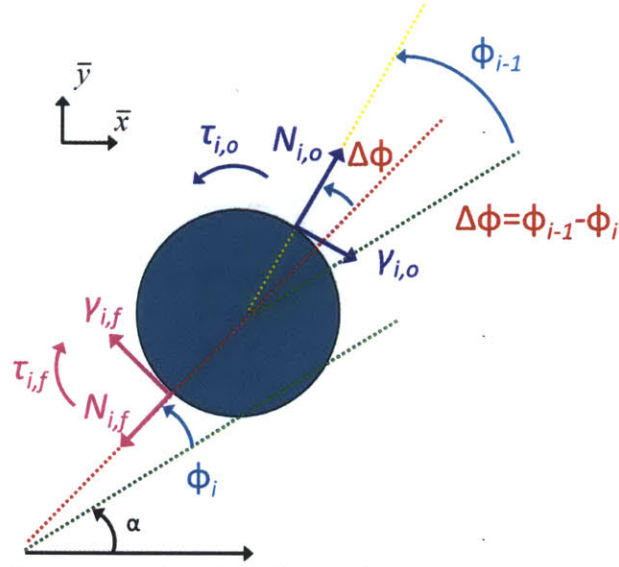


Figure 5-14: Node equilibrium at rotational spring node

$$N_{i,f} = \gamma_{i,o} \sin(\phi_{i-1} - \phi_i) + N_{i,o} \cos(\phi_{i-1} - \phi_i)$$

Equation 5.35

$$\gamma_{i,f} = \gamma_{i,o} \cos(\phi_{i-1} - \phi_i) - N_{i,o} \sin(\phi_{i-1} - \phi_i)$$

Equation 5.36

The system of equations, assuming in a quasi-static domain with negligible mass, is in the form of $Az = b$ where A has the relation between all of the shear, normal, and moment parameters, z is the vector of the unknown parameters (Equation 5.37), and b is the loading from the drag loads.

$$z = \{N_{1,o} \ \gamma_{1,o} \ \tau_{1,o} \ \dots \ N_{i,o} \ \gamma_{i,o} \ \tau_{i,o} \ \dots \ N_{n,o} \ \gamma_{n,o} \ \tau_{n,o}\}^T$$

Equation 5.37

For a three elements system the stiffness matrix A_3 multiplied by the parameter vector z_3 is shown in Equation 5.38.

$$A_3 z_3 = \begin{bmatrix} 1 & 0 & 0 & 0 & 0 & 0 & 0 & 0 & 0 & 0 \\ 0 & 1 & 0 & 0 & 0 & 0 & 0 & 0 & 0 & 0 \\ 0 & 0 & 1 & 0 & 0 & 0 & 0 & 0 & 0 & 0 \\ -\cos \Delta\phi & -\sin \Delta\phi & 0 & 1 & 0 & 0 & 0 & 0 & 0 & 0 \\ \sin \Delta\phi & -\cos \Delta\phi & 0 & 0 & 0 & 1 & 0 & 0 & 0 & 0 \\ -2r \sin \Delta\phi & 2r \cos \Delta\phi & -1 & 0 & 0 & 0 & 1 & 0 & 0 & 0 \\ 0 & 0 & 0 & -\cos \Delta\phi & -\sin \Delta\phi & 0 & 1 & 0 & 0 & 0 \\ 0 & 0 & 0 & \sin \Delta\phi & -\cos \Delta\phi & 0 & 0 & 1 & 0 & 0 \\ 0 & 0 & 0 & -2r \sin \Delta\phi & 2r \cos \Delta\phi & -1 & 0 & 0 & 1 & 0 \end{bmatrix} \begin{bmatrix} N_{1,o} \\ \gamma_{1,o} \\ \tau_{1,o} \\ N_{2,o} \\ \gamma_{2,o} \\ \tau_{2,o} \\ N_{3,o} \\ \gamma_{3,o} \\ \tau_{3,o} \end{bmatrix}$$

Equation 5.38

The incremental rotation angle ($\Delta\phi_i$) of each element can be found using Equation 5.39 after separating the moments from the z vector. The resulting answer is re-entered into the system of equation until the solution converges on the rotation angle.

$$\phi_i = \frac{\tau_i}{\frac{E_i \cdot I_i}{L_i}}$$

Equation 5.39

5.2.3.1. Discussion

The initial process described is similar to that used in commercial finite element packages. An evaluation of commercially available finite element packages demonstrated limitations capturing the high nonlinearities of the entanglement process. The finite element packages, however, can be used to model the initial deformation of the wire as a function of the drag loading. Once the wire makes contact with the pipe wall the model changes to a buckling configuration. While there is software like ANSYS that can be used to model large plastic deformations, the chaotic generation of the entanglement process is not captured. Therefore a discrete model composed of springs and rigid elements was used to model the wire interacting with the flow but had challenges with code convergence.

5.3. Interaction Loading

The contact/interaction between the wire and the inner surface of the wellbore can determine the type of entanglement that is generated. The work done in Klarbring PhD Thesis can be used as a foundation to model the interface. Klarbring's model has already been incorporated in the modeling of elastica by Cho et al. in 1998 to capture the interaction between a guide and an ejected elastica. As shown in Figure 5-15, when the wire contacts the opposing wall of the wellbore it is subjected to a normal and a frictional force.

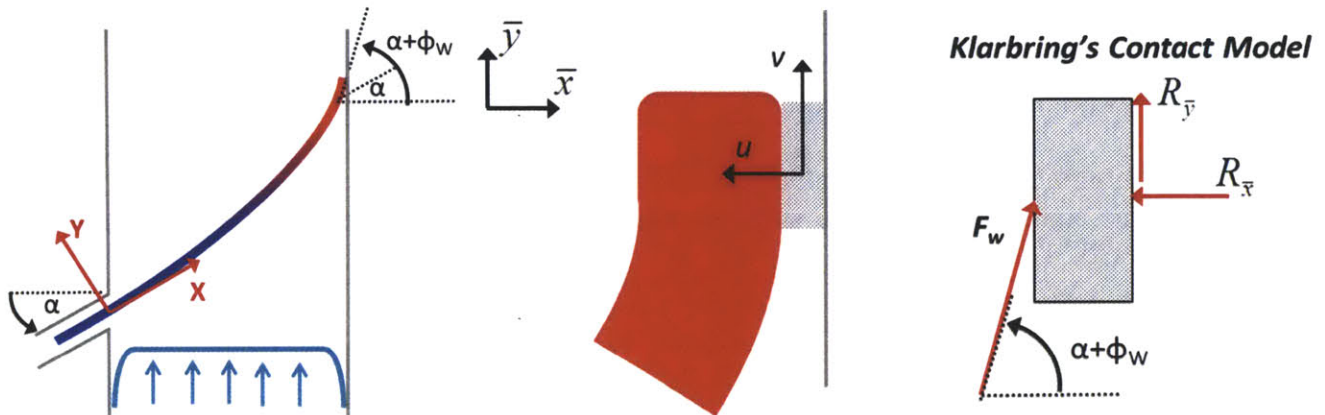


Figure 5-15: Klarbring contact model

As identified in Klarbring's contact model there are four modes of interaction between the wire and the wall depending on the loading and magnitude of the frictional force as shown in Table 5-2.

Table 5-2: Klarbring's contact model interaction modes

Parameter	Stick	F. Slip	B. Slip	Separation
U	0	0	0	> 0
v'	0	> 0	< 0	> 0
$R_{\bar{x}}$	> 0	> 0	> 0	0
Other	$ R_{\bar{y}} < f \cdot R_{\bar{x}}$	$R_{\bar{y}} = -f \cdot R_{\bar{x}}$	$R_{\bar{y}} = f \cdot R_{\bar{x}}$	$R_{\bar{y}} = R_{\bar{x}} = 0$

As anticipated the frictional coefficient between the wire and the wellbore interior can play a significant role in the mode of entanglement generated in the absence of an obstruction.

5.4. Model Discussion

The development of a model for full entanglement is a mathematically intensive endeavor that on its own can be made into the theses of several PhD students. The roadmap presented in this chapter is one possible approach by which to model the system. The numerical approach was attempted as part of the development of this work, but did not yield adequate results due to issues with convergence. Thus, an experimental approach is used to scale the entanglement behavior.

The more appropriate software that may be used for this application is crash-modeling software for large distortion high stresses, which occurs during the entanglement process.

[Left Blank]

Chp 6.

Machine Design

This chapter discusses the development of an integrated prototype wire feeder using the knowledge from the bench level experiments for testing in a high pressure flow loop system. The machine presented, as shown in Figure 6-1, is divided into four modules: housing, spool (inside housing), wire feeder (inside housing), and drive system. The support structure for the experimental setup consists of a rigid flow channel with exchangeable obstruction caps, which is representative of a partially deployed BOP rams. The complete assembly has maximum pressure rating is 7.52 MPa (1090 psi) limited by the bolt circle of the interface region. The maximum pressure rating of the feeder prototype is 6.2 MPa (900 psi), limited by the O-ring dynamic seal to the external drive interface.

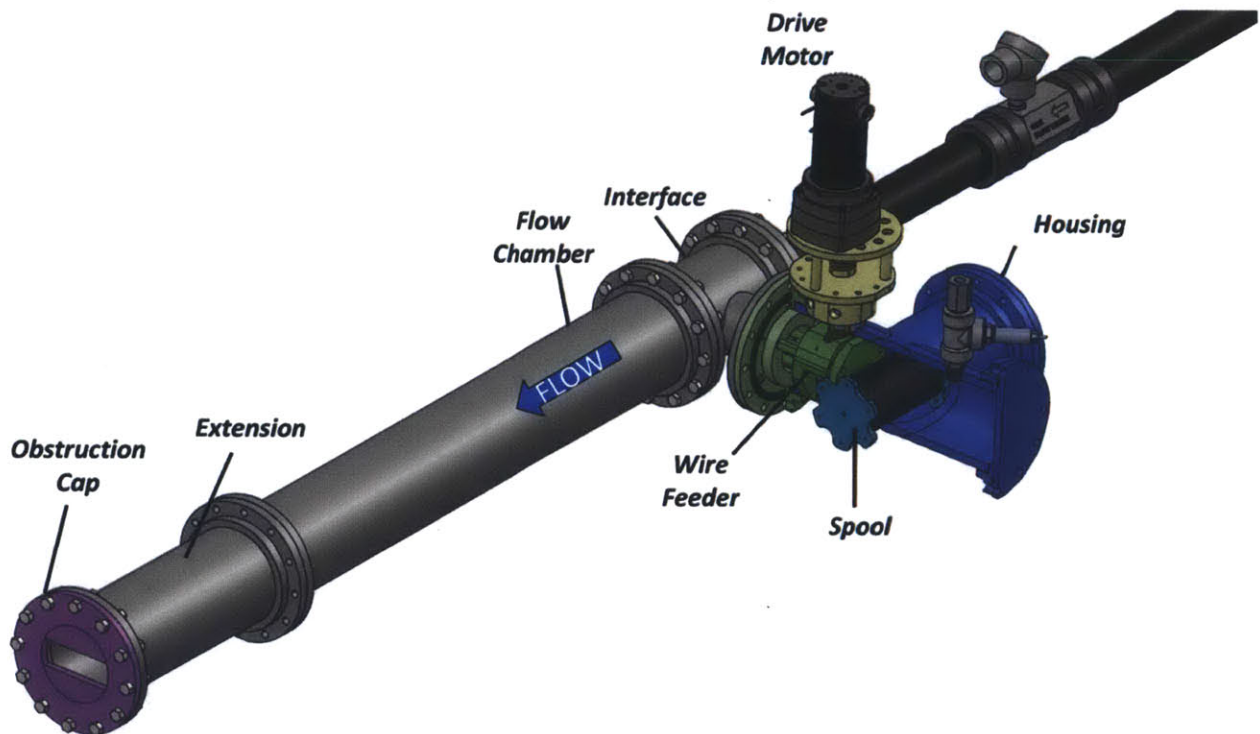


Figure 6-1: Integrated prototype experimental setup

6.1. Prototype Functional Requirements

The functional requirements for the scaled experiment wire feeding unit are summarized in Figure 6-2. Additional requirements include power delivery and data acquisition units. To minimize cost, the drive system (motor) is external to the pressure chamber which requires designing a dynamic seal.

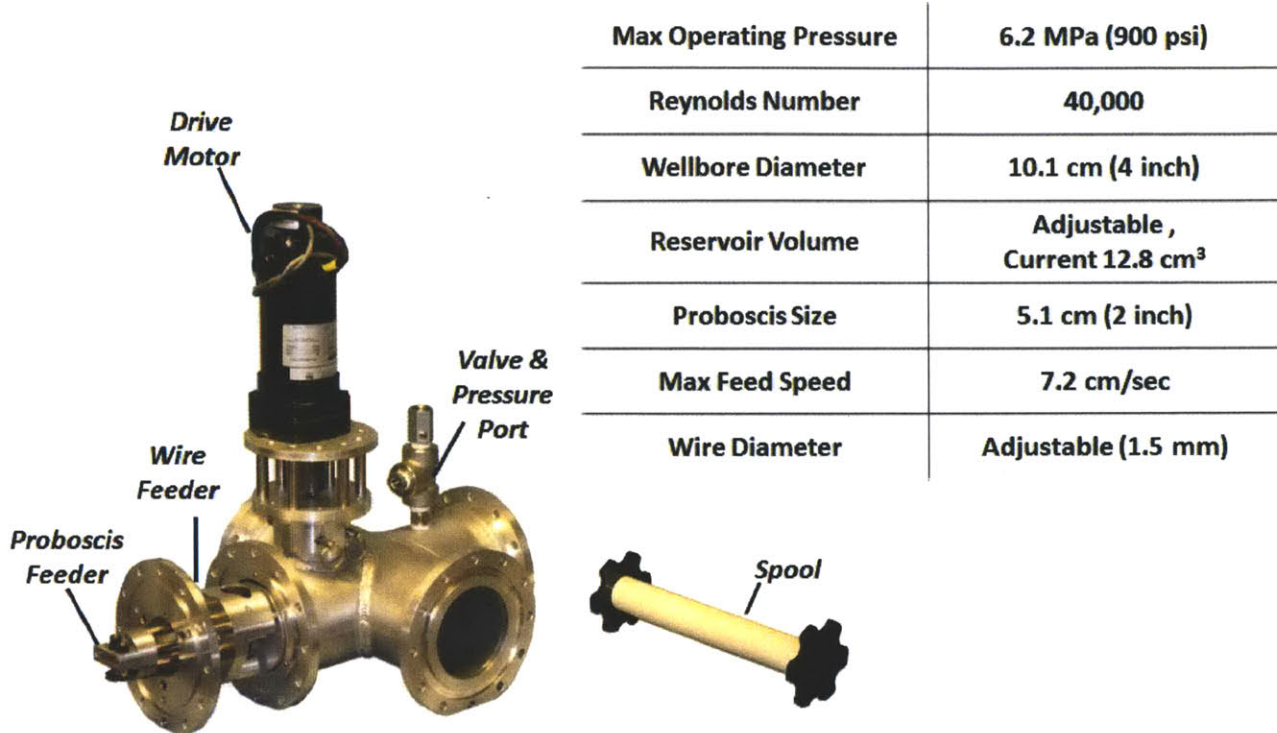


Figure 6-2: Integrated prototype experimental setup

6.1.1. Power & Controls

Due to the testing environment, the power interface and controls unit need to be versatile to allow for testing in remote areas such as lakes, rivers, or in a flow loop. The only power source for the components is fixed to 120 AC from a fire truck generator or wall outlet. There are three things that will require power from the single AC source: 1) drive motor, 2) pressure excitation, and 3) flow meter excitation. The controls box for operating the feeder prototype needs a watertight enclosure in the event of an unforeseen leakage.

6.1.2. Machine Design

From the machine design stand point; all of the components need to be designed for manufacturing which will reduce the overall cost of the unit. The components of the feeder machine should be modular to be able to independently test each module. Alignment features should be included as allowed by geometric constraints. The design should, whenever possible, error on the side of consolidating parts together. To limit the cost a dynamic seal is used to separate the pressurized region from the motor drive system.

6.2. Design and Analysis

The following section contains the detailed design and engineering analysis for each module of the test prototype: 1) housing, 2) spool, 3) feeder, and 4) drive. As shown in Figure 6-4, each module is broken down into the fundamental analysis required for that module. The prototype connects to the existing chamber used in the high-pressure flow experiment.

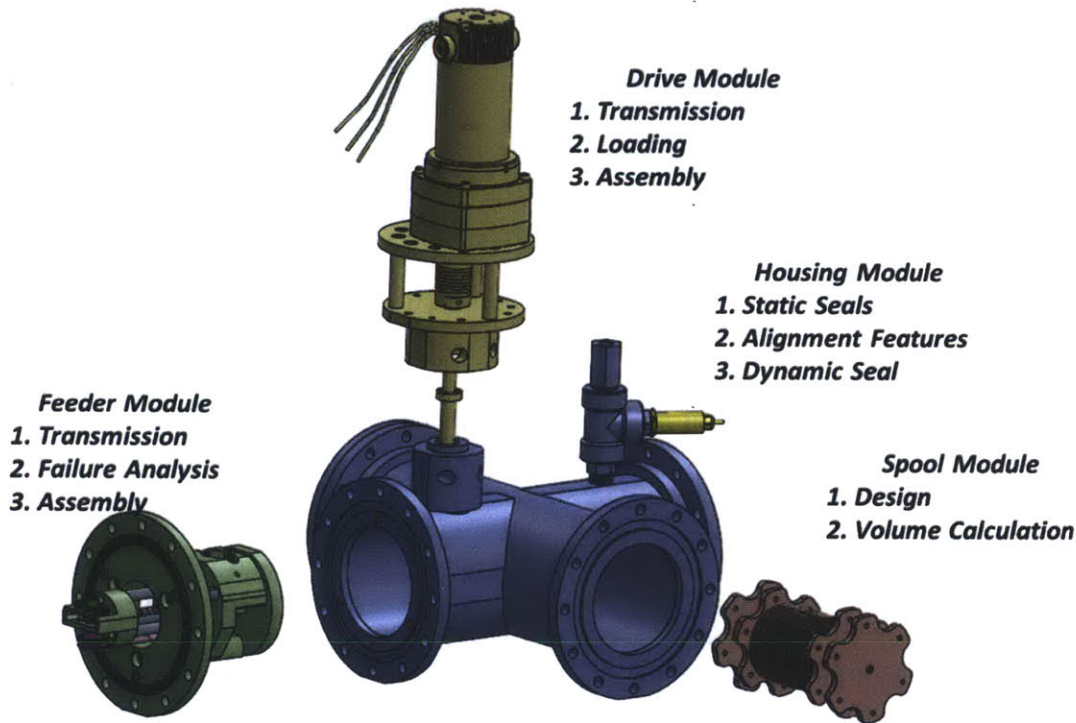


Figure 6-3: Module break down and analysis for each module

6.2.1. Housing Module

The primary purpose of the housing is to hold at least an internal pressure of 3.4 MPa (500 psi) and to secure all of the wire feeding components. There are several possible configurations for the housing; however, a cross “t” configuration with four ports was chosen for ease in manufacturing, scaling, and availability of components. The flanges that are welded to the wall structure are the same size as that for the flow chamber. To maintain consistency the structure of the housing was made with 10.2 cm (4 inch) pipe with a 12.7 mm (½ inch) wall thickness, as shown in Figure 6-3. The primary port is where the wire feeder module interfaces. The two longer mirrored ports are for inserting the wire spool. There is also an auxiliary port in the system that can be used for assembly or to test an axial spool.

The housing detailed design is separated into four sections: dynamic seal analysis, dynamic seal torque, thrust loading, and quasi-kinematic interface. Since the drive motor is external to the pressurized chamber, a hydrodynamic seal is used, details found in section 6.2.1.1. As the pressure increases, the O-ring is pressed against the rotating shaft inducing friction losses. The thrust loading analysis includes the sizing of the thrust bearing to hold the axial loading. The primary port has three spheres that protrude from face to be used as an alignment feature for the wire feeder module as shown in Figure 6-4.

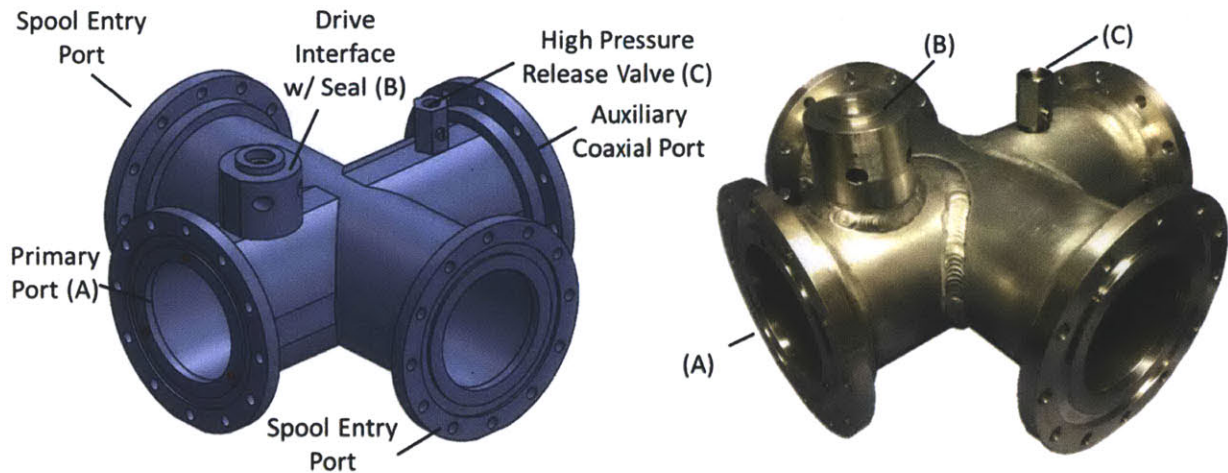


Figure 6-4: Housing module in detail

6.2.1.1. Dynamic Seal Analysis

The dynamic O-ring seal required was designed using Machinery's Handbook to find the diametrical clearance needed to prevent extrusion. As shown in Figure 6-5, the seal must also work to allow an open configuration during assembly and an engaged configuration during the duration of the experiment. The diametrical clearance for 3.4 MPa (500 psi) of back pressure varies with the durometer of the O-ring, with lower durometers having a higher potential to extrude with increasing pressure. The diametrical clearance at 3.4 MPa 500 psi for O-ring durometers 70, 80, and 90 are 430 μm , 610 μm , and 710 μm (~ 0.017 inch, ~ 0.024 inch, and ~ 0.028 inch) respectively. The higher durometer also makes it more challenging to insert and remove the O-ring in the case of failure; therefore, the design uses a diametrical clearance of 430 μm (~ 0.017 inch) corresponding to using an O-ring whose durometer is 70. The cross sectional diameter of the o-ring was chosen based between five and ten diametrical clearances applying Saint Venant's principle of characteristic dimensions. The groove is placed in the interface in the interests of using a precision ground rod instead of machining a rod to a given diameter. A dynamic seal requires a surface roughness between 8 to 16 $\mu\text{in. rms}$, which is more challenging to achieve than purchasing a ground rod and inserting the groove into the drive interface. However, a surface roughness below 5 μin is detrimental for dynamic seals because the drive shaft can go without lubrication, thus overheat, and kill the seal [157]. A 12.7 mm (half inch) diameter ground shaft from a commercial supplier (e.g. McMaster) has around a 2.3×10^{-7} $\mu\text{m rms}$ (9 $\mu\text{in rms}$). Given the requirements, a standard 3.2 mm ($1/8$ inch) (actual cross section is 0.139 inch) diameter o-ring was chosen, which is ANSI 206.

The design was modified to accommodate manufacturing processes. Instead of boring out the drive interface to a diameter of 13.1 mm (0.516 inch), a standard 13 mm (0.5118 inch) reamer is used to finish the hole thereby reducing the diametrical clearance to 300 μm (0.012) inch and increasing the rating of the seal to 6.2 MPa (900 psi). Since this seal interface is a component that is welded to the housing, it is in the interest of the design to increase the pressure rating of the seal. The primary O-ring groove is placed near the bearing at the top in order to not over constrain the shaft. A secondary groove was manufactured in the event that additional support is required at higher speeds.

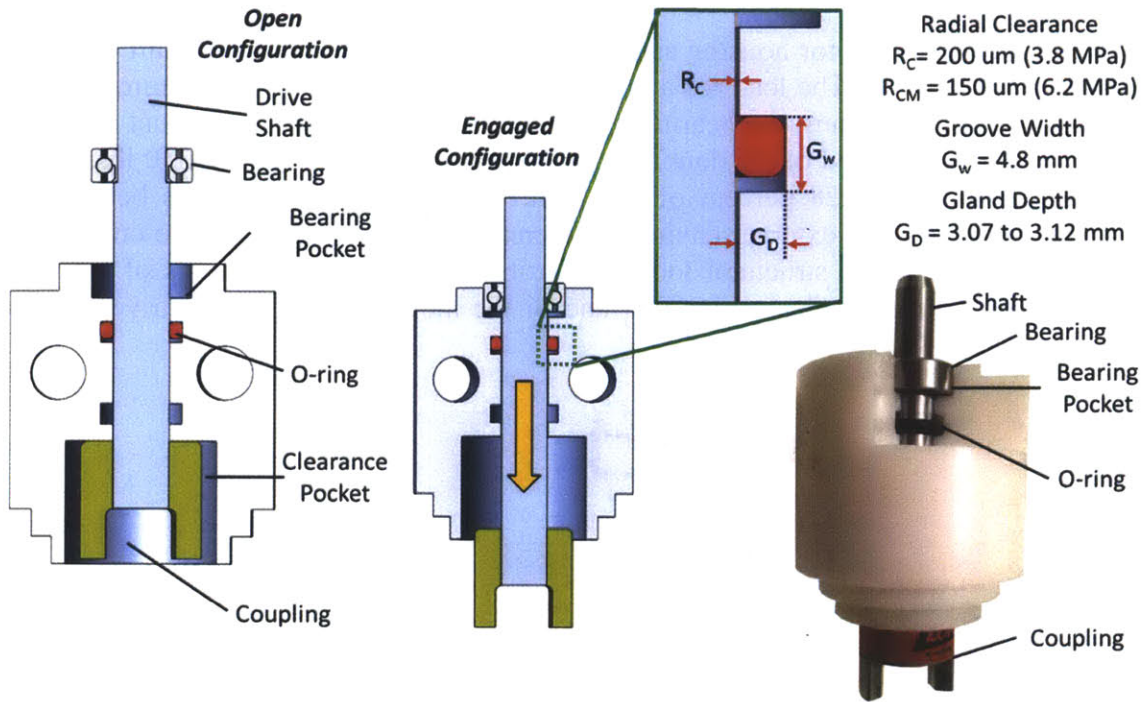


Figure 6-5: Dynamic bearing configurations and o-ring specifications

6.2.1.2. Dynamic Seal Torque

As the dynamic seal is loaded with a differential pressure a torque is applied on the drive shaft that reduces the amount useful torque delivered to the device. The torque lost can be calculated using Equation 6.1 as described in Figure 6-6. The calculated loss in torque for the given geometry with a 206 O-ring with a diametrical clearance of 150 um is 3.9 N*m, which is less than 4 percent of the max torque of the chosen motor.

$T_{seal} = 2\pi \cdot R_{oring} \cdot D_{oring} \cdot r_{shaft} \cdot P \cdot \mu_f$	Equation 6.1
---	--------------

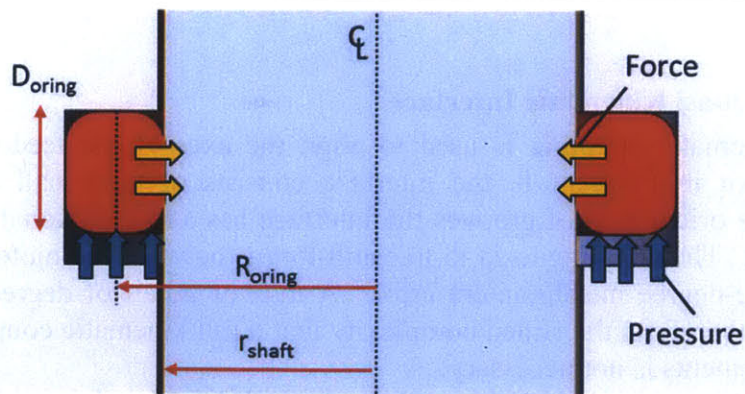


Figure 6-6: Dynamic seal with a known back pressure pushing against the O-ring seal, which imparts a force on the shaft that reduces the torque potential

6.2.1.3. Structural Loop

The drive interface in the motor housing supports thrust load imparted on the shaft due to the differential pressure in the system. The load for a 3.4 MP (500 psi) pressure on a 12.7 mm (½ inch) diameter shaft is 436 N (98 lbs.). Thus, the bearing between the drive interface and mount cap has to withstand the load. The dynamic load of the double shielded bearing used is 1556 N (350 lbs.), hence the maximum operating load is at 28 percent of the limit. The differential pressure between the internal region of the drive unit and external environment creates an axial pushing force on the drive shaft. As shown in Figure 6-7, the structural loop supporting the axial force consists of the thrust bearing, mount cap, and two quick release pins that anchor the mounting cap to the drive interface section of the housing.

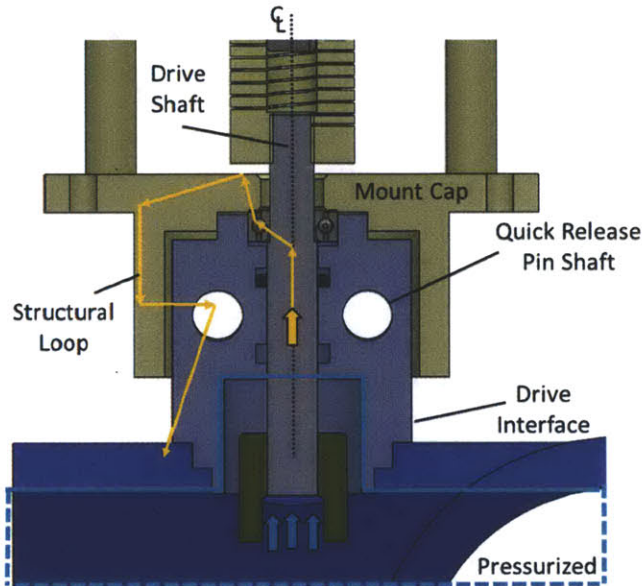


Figure 6-7: Thrust load structural loop going through shaft, bearing, mount cap, and drive interface port

The failure analysis performed on this section includes determining the maximum pressure of the unit limited by the dynamic seal that is designed for 6.2 MPa (900 psi) which will result in leakage of water.

6.2.1.4. Quasi Kinematic Interface

A quasi-kinematic coupling is used to align the axes of the feeder interface plate and the housing. As shown in Figure 6-8, the interface consists of three ball and groove connections; however, due to the orientation of grooves the interface has a low torsional rigidity and is not a true kinematic coupling. The coupling used to transmit torque between the motor and the wire feeder can accommodate a one-degree misalignment error. A max of a half of degree error is assigned to the interface coupling; therefore, the added complexity that a full kinematic coupling would require based on the space requirements is not necessary.

The assembly of the interface requires press fitting the three spheres into corresponding pockets in the feeder port (part of the housing module). The housing module is placed in an arbor press with feeder interface plate used to close the gap and permanently securing the spheres in the feeder port, as shown in Figure 6-9.

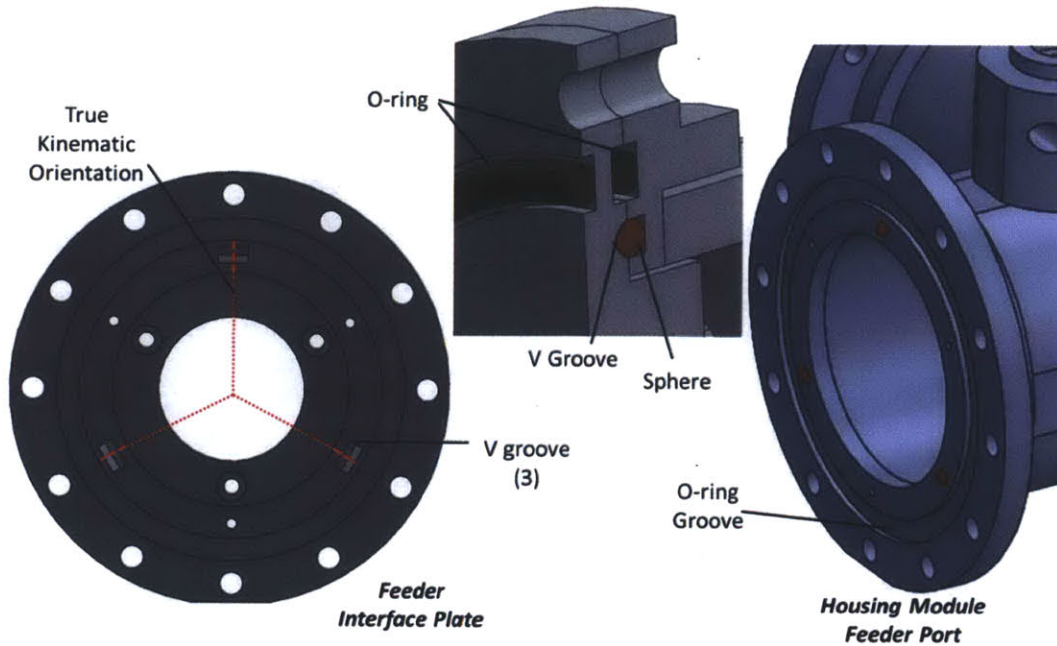


Figure 6-8: Soft kinematic interface between feeder interface plate and housing module showing ball and groove interfaces. For a true kinematic orientation the orientation of the grooves need to be rotated by ninety degrees.

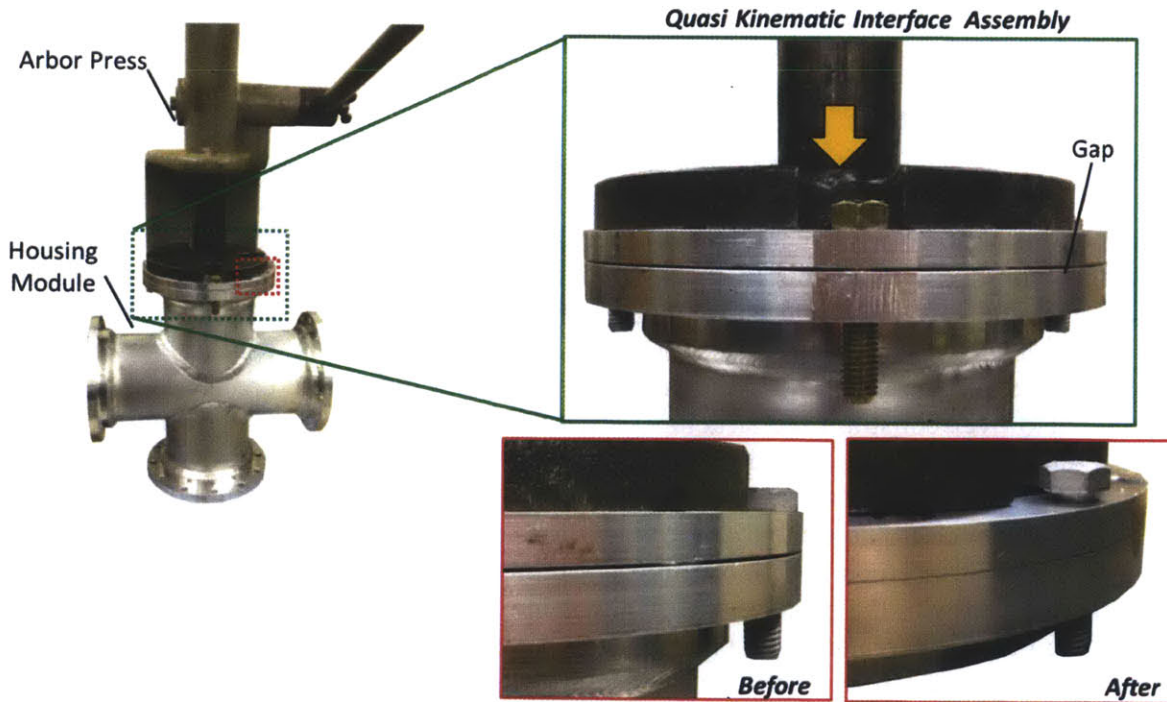


Figure 6-9: Quasi-kinematic interface assembly in arbor press used to close the gap and press fit the spheres into the feeder port

6.2.2. Feeder Module

The purpose of the feeder module is to pull wire from the spool and to push it into wellbore. As shown in Figure 6-10, the wire feeder is separated into three sub modules: 1) mount, 2) main body, and 3) proboscis.

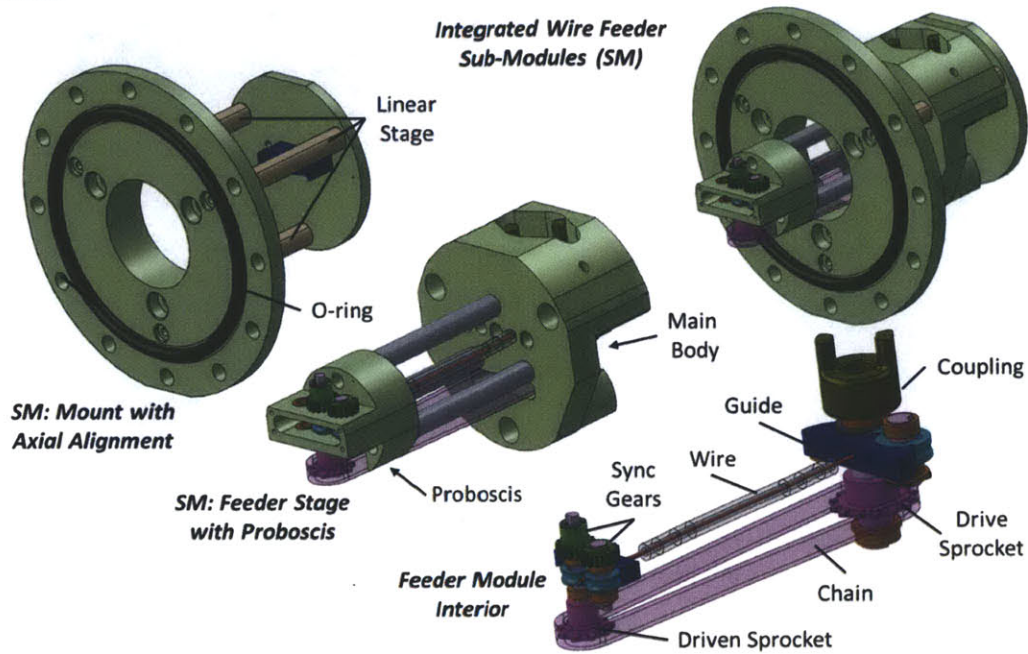


Figure 6-10: Wire feeder sub modules

6.2.2.1. Guide Rail

The mount was designed with a linear stage that allows the main body to slide into alignment with the motor drive interface in the housing. While this feature adds complexity to the structure, it also adds flexibility. From the manufacturing perspective, the linear stage reduces the need to keep tight tolerances on six components (3 in the housing, 3 in the feeder). The tight tolerance is then moved to one single part, the guide rail mounting plate. There were several options for designing the bearing; however, given the space and stiffness requirements a three-rod bearing was chosen. Using three rods to create a linear stage will inherently overly constrain the structure. In fact having two rods alone would also over-constrain the structure. Therefore, during the manufacturing of the guide rail mount the holes were undersized and reamed to a tight sliding interface with a 100 μm (0.001 inch) clearance between the rod and the mounting holes. The depth of the mounting holes for the rods was set to 12.7 mm (0.5 inch) to hold the rods by at least one characteristic dimension.

For assembly, the rods are placed into the mounting holes and tightened loosely. The main body fully assembled with the proboscis, then slides into the three rods of the linear stage. Two posts of the stage are flat in an area to allow brass tip set screws to lock. The tips of the stage rods allow for ease of assembly by contacting at different times during the insertion process as shown in Figure 6-11.

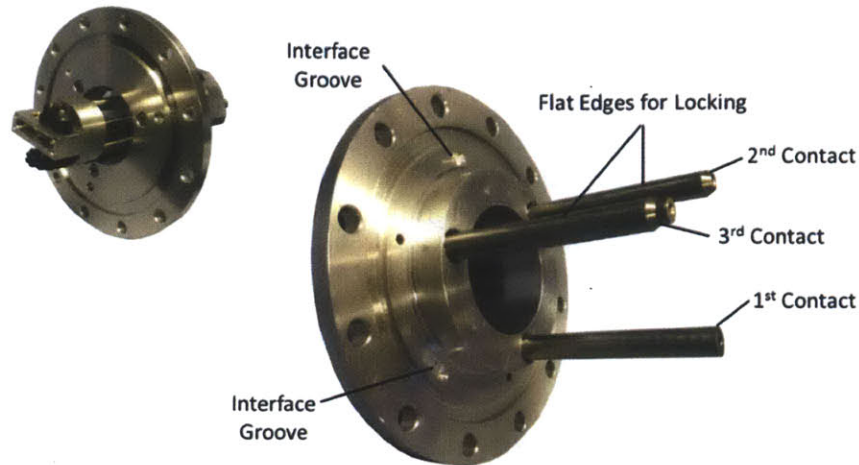


Figure 6-11: Assembly of wire feeder main body to linear stage

6.2.2.2. Main Body

The main feeder module is mirrored to allow the same unit to feed through different ports by reversing the direction of the motor. After initial alignment of the feeder unit to the drive module, the body is anchored using a set of 8-32 brass tip set screws that eliminate the sliding motion. The purpose of the main body is to hold the pull wheels and to connect that unit to the proboscis via a chain drive system. Three rods, 10 mm (0.395 inch) in diameter, extend from the body to hold the proboscis. A 6.4 mm (1/4 inch) stainless steel wire guide is used to transfer the wire from the body to the proboscis without entangling in the process.

The body was designed to manufacture all of the key components (bearings and guides) to setups in order to minimize errors, as shown in Figure 6-12. The first setup provides all of the alignment features to the structure, while the second setup gets the bearing channels. All of the other port details are not crucial and can be made on a standard drill press.

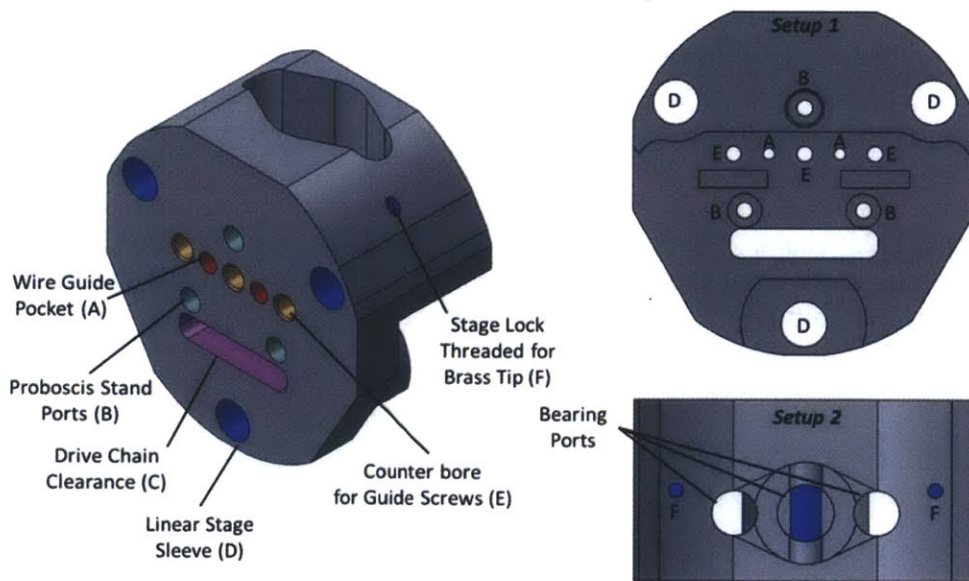
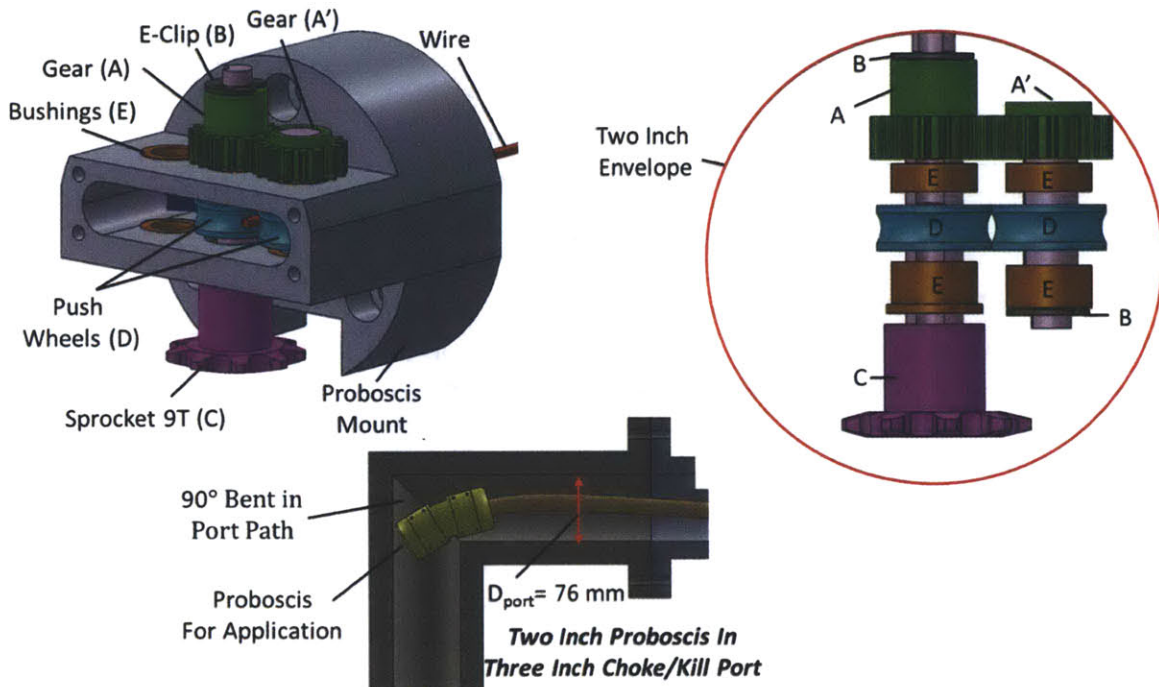


Figure 6-12: Feeder main body mount plate with all key ports labeled. Also includes the two setups used to manufacture the units.

6.2.2.3. Proboscis head

The proboscis extends to the face of the flow chamber and pushes the wire the flow stream. As illustrated in Figure 6-13, one key functional requirement of the proboscis is that it all has to fit in a 50.8 mm (2 inch) diameter circle. This requirement originates from the need of the full proboscis to travel in right angle bends in the choke/kill port, which is 76.2 mm (3 inches) in diameter. While this proboscis prototype is static, it is desirable to design the system such that it could be easily retrofitted and scaled for the application.



6.2.2.4. Transmission Feeding System

The feeding speeds between the pulling in the body and the pushing in the proboscis has to be equal in order to prevent buckling or tensioning of the wire within the machine. The only parameter that could be changed to feed at the same speed is the diameter of the pull system in the body. The transmission ratio was fixed to 1.55 (in/out), due to a geometric constraint of standard sprocket components for a M25 chain. The sprocket at the proboscis that met the geometric functional requirements is a nine-tooth sprocket. The largest sprocket at the body is the fourteen-tooth sprocket that keeps the chain from hitting the edges in the 50 mm (2 inch) port region.

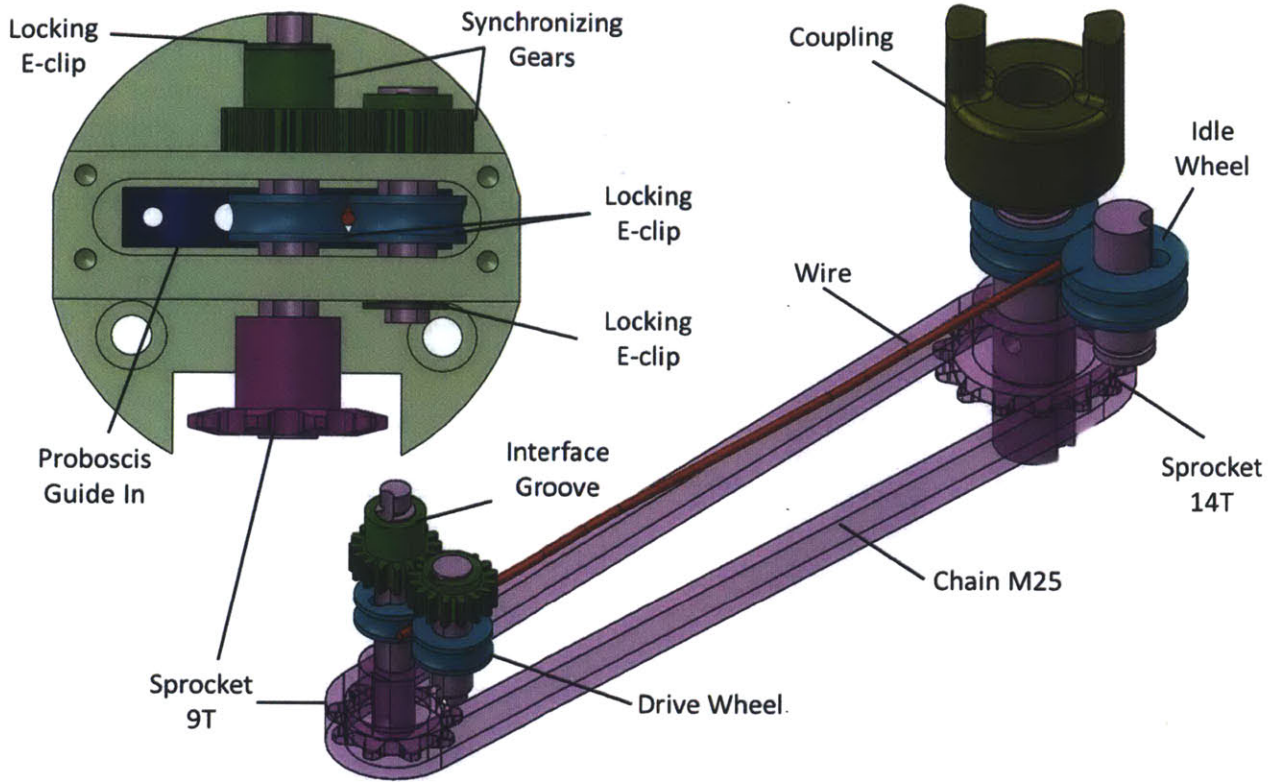


Figure 6-14: Proboscis transmission system

6.2.3. Drive Module

The drive module needed to be disassembled quickly to allow the wire feeder unit to be separated from the housing effortlessly.

6.2.3.1. Sizing the motor

The motor must have enough torque to deform the wire thus reducing the amount of energy required to buckle. The motor must also feed the wire at a rate of at least 20 percent of the flow velocity for the turbulent conditions, based on the bench level experimental data. One of the available motors that met the functional requirements was a Bison PMDC motor (Model 011-175-0025) with a maximum torque of 112 N*m (84 ft*lb) and max rpm of 71 revolutions per minute. Based on our earlier calculation of the transmission system, the diameter of the pull wheel is 19.6 mm (0.77 inches) resulting in a maximum feed velocity of 73 cm/sec. At a Reynolds number of ~38,500, for a 10.2 cm (4 inch) wellbore with water at 3.2 lpm (50 gpm), the average flow velocity is calculated to 0.39 m/sec. Assuming that the velocity ratio of 0.2 is accurate for large diameter wellbore then the required feed velocity is 0.078 m/sec. Therefore, the motor chosen could feed wire at a max speed of 7.2 cm/sec, fast enough to generate an entanglement in the flow. The dependence on velocity and entanglement for varying wire stiffness still has to be studied further.

6.2.3.2. Drive Module Assembly

The drive module can be separated as an independent unit, as illustrated in Figure 6-15 (A). The motor is mounted to a top plate that is raised from the mounting cap by six stainless steel pillars that serve to transfer the loads onto the housing structure to close the loop. A flex coupling can be used to connect the motor to the drive shaft. The drive module works like a cohesive unit that can be added or removed to the assembly via two stainless steel quick release pins $3/8$ inch in diameter that go through the housing interface as shown in Figure 6-15 (B).

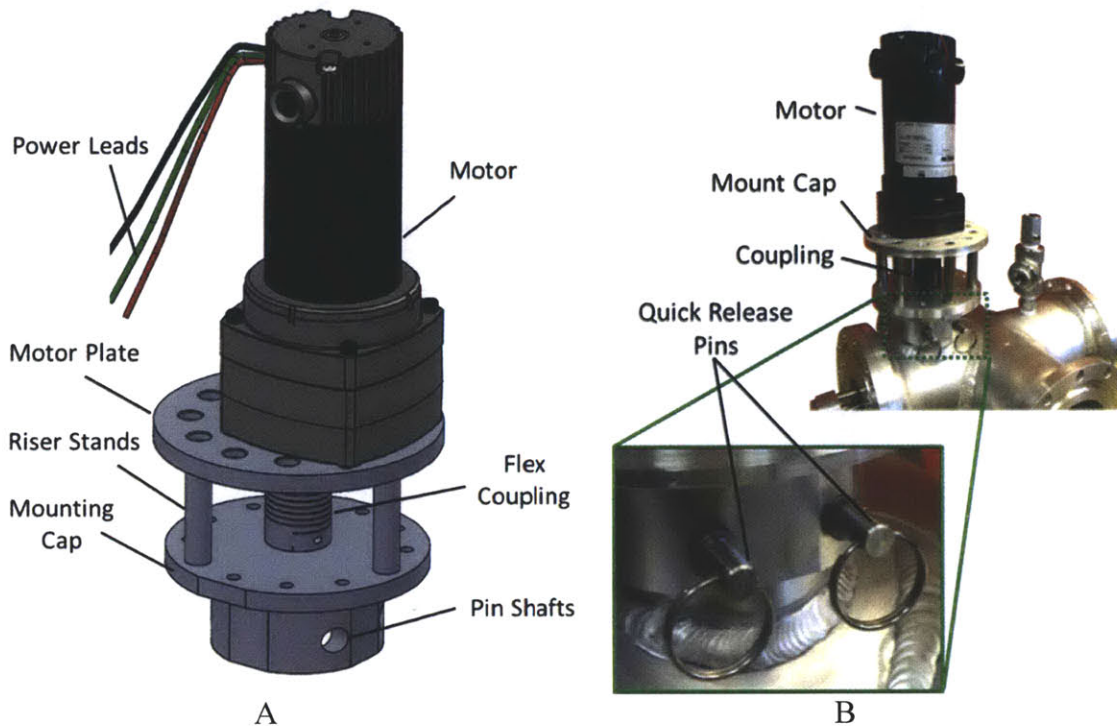


Figure 6-15: On the left is the drive module assembly showing mounting cap, flex couplings, motor plate, and motor. On the right is the mounting structure for the drive module to the housing via two 9.5 mm quick release pins.

The pins that mount the drive module to the housing support the torque provided by the motor. The maximum motor torque is 112 N*m (83 ft*lb) which is the maximum reaction torque that the pins must hold across the four contact locations. The radius of application is at 4.12 cm from the center; therefore, the maximum shear force per contact is approximately 680 N. Since the 9.5 mm ($3/8$ inch) pins are made from stainless 18-8 the maximum shear load of 9.5 MPa is only 2.7 percent of the total load before shearing. In practice the motor will not be providing the full torque required to feed the wire.

6.2.4. Spool Module

While the operation of the spool module seems simple at first it is one of the most important components next to the wire feeder. If there is nesting inside the machine, then the wire feeder will not operate properly.

6.2.4.1. Alignment to Housing

The housing module can accommodate two different spool configurations, axial and radial. The radial module is used for its reliability but need to account for bearing travel length. As shown in Figure 6-16, version 1 of the spool needed additional spacers to ensure the spool behaving as a bearing as illustrated by version 2. One disadvantage is the loss of operational volume; however, it is at the expense of functionality.

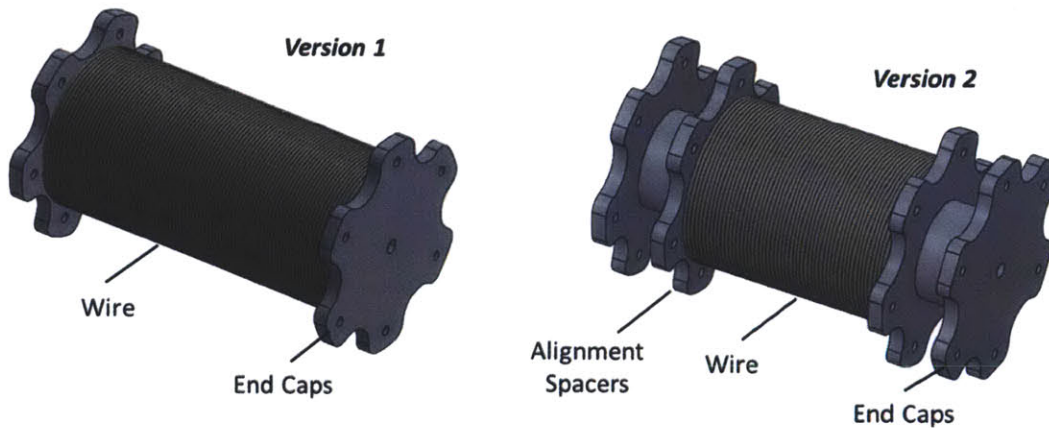


Figure 6-16: Radial spool module first and second iteration

6.2.4.2. Volume calculation

Volume of wire in the spool can be calculated using Equation 6.2, where L_s is the spool effective length, R_o is the outer radius, R_i is the inner radius, and η_p is the packing efficiency.

$$V_{Spool} = L_s \cdot \pi \cdot (R_o^2 - R_i^2) \cdot \eta_p$$

Equation 6.2

6.3. Measurement and Instrumentation

The wiring layout of all of the components is shown in Figure 6-17. The assembled control box, Figure 6-18, shows the user interface to the electronics inside the enclosure. One of the initial challenges of the system was the noise caused while the motor operates, even after isolation units, i.e. bypass capacitors, were used to reduce noise in the signals. The data storage device was created using a National Instruments 6211 DAQ board that interfaces with a computer to record the pressure measurements. One option for upgrade is to replace the DAQ board with a compact cRIO.

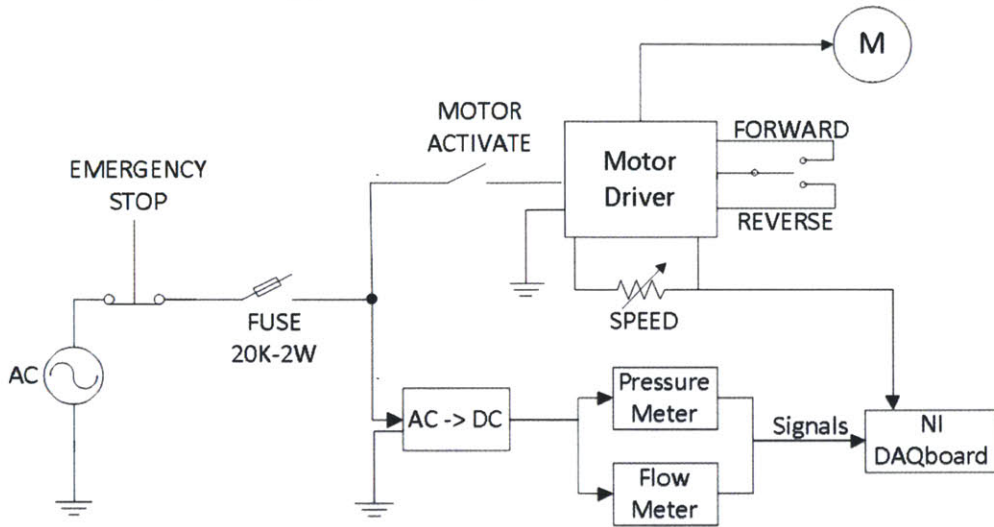


Figure 6-17: Wiring diagram of the controls module. The power supply (Model No FSP018-DEDA2) converts the AC signal to a 12 V DC with 1.5 Amps.

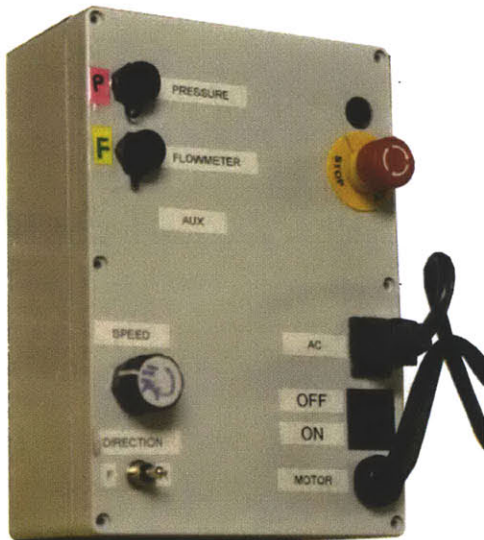


Figure 6-18: Images of control box showing the AC inlet, emergency stop, motor control, and instrument sensors.

6.3.1. Pressure meter

The pressure meter chosen for this application was an Omega PX309-500G-5V (Max pressure 3.4 MPa (500 psi)) 0-5 Volts signal. The range was based on the maximum expected operating pressure for the unit. In order to minimize the number of ports in the housing or the cap a T junction was added to the valve port on the auxiliary housing port, as shown in Figure 6-19.

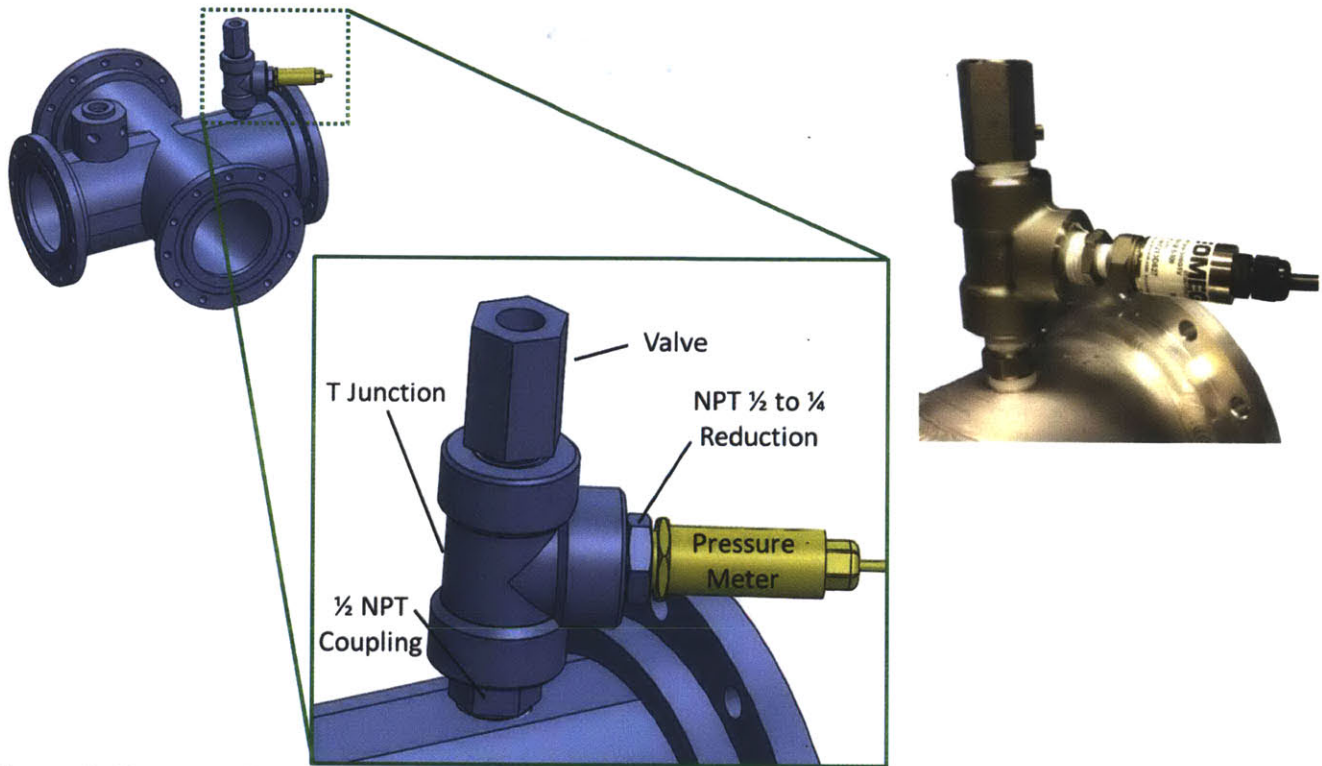


Figure 6-19: T configuration for Omega pressure sensor (PX309-500G-5V) that is incorporate to the valve in the flow chamber. The valve (McMaster Part : 4912K99) is a miniature chrome- plated brass vall valve with half an inch NPT female and male connection rated to 450 psi at 100 F.

6.3.2. Flow Meter Configuration

The flow meter used is a high-pressure turbine flow meter (CPT32-NP-C-M25) from Badger Meter Inc. The flow meter working range is from 95 to 1136 lpm (25 to 300 gpm), with an accuracy of 0.25 percent of the reading. To avoid entrance effects, it is recommended to have at least ten diameters upstream and downstream from the sensor; therefore the standard connection currently to the flow chamber was increased to accommodate the flow meter, as shown in Figure 6-20. The two inch NPT pipe schedule 80 has a maximum working pressure of 17.2 MPa (2500 psi). The 2.5 NH swivel connection can be changed for any two inch NPT tapered pipe thread unit to interface to the female receiver. For the flow loop test that connection is actually done with a Dixon cam lock brass fitting.

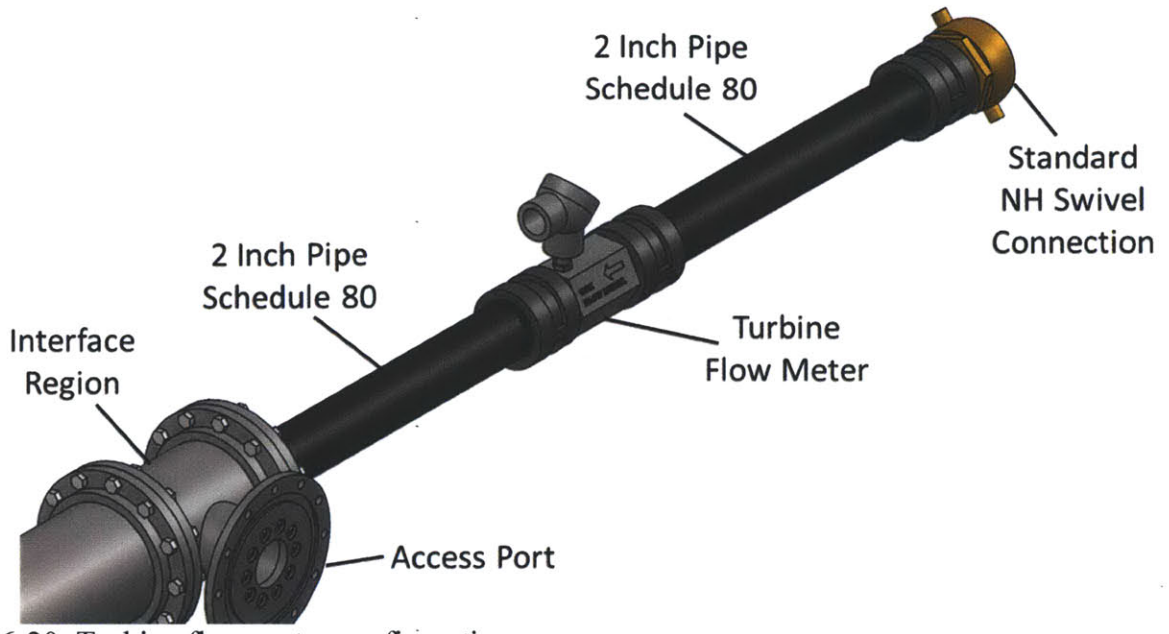


Figure 6-20: Turbine flow meter configuration

6.4. Wire Sizing

The wire used for the anchoring region needs to have a significantly low stiffness so that it can buckle and plastically deform inside of the region, yet also remain be flexible such that it interacts with the flow. The wire is sized based on the non-dimensional stiffness that generates a known entanglement form. For the desired non-dimensional stiffness between 1,000 and 5,000, at a Reynolds Number of 30,000 the calculated wire diameter required using a galvanized steel wire is between ~0.2 to 0.5 mm. However, since the wire required for the full application must be significantly larger (1.5 to 3 mm see next section), it was decided to demonstrate the ability to feed wire that is close in size to commercially available galvanize wire. A 16 gauge galvanized steel wire diameter is 1.29 mm.

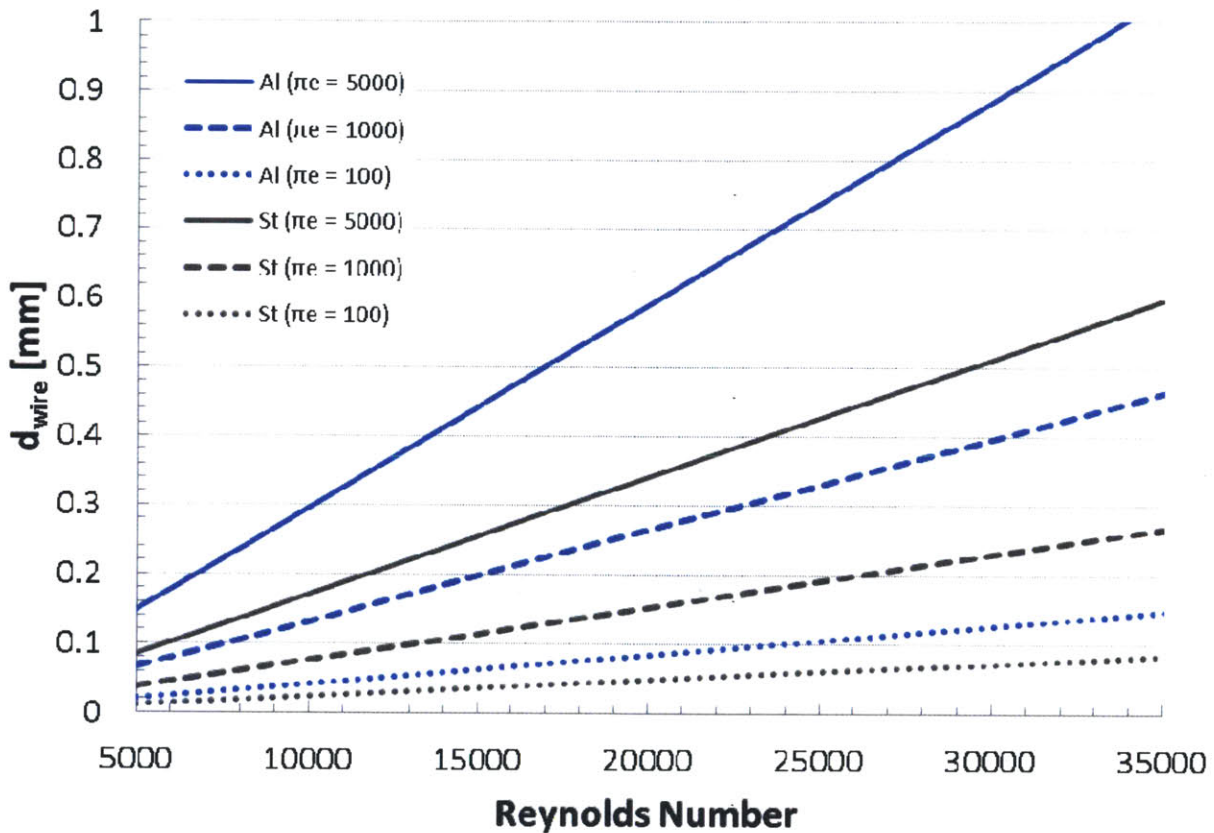


Figure 6-21: Wire size requirement for experimental setup based on the non-dimensional stiffness. The value circle in red corresponds the value used for the scaled prototype which is a 0.7 mm radius wire of galvanized steel. The calculation is made for assuming a 10.2 cm (4 inch) wellbore diameter, water viscosity 1×10^{-3} Pa*sec and Young's Modulus of 210 GPa.

6.4.1. Wire Size for Industry

The projected radius of the anchoring wire required to generate an entanglement for production well in a standard 47.6 cm (18.75 inch) diameter wellbore is shown for varying Reynolds number. At a turbulent flow of 30,000 Reynolds number the mean flow velocity ($\mu = 0.01 \text{ Pa}\cdot\text{sec}$, $\rho = 850 \text{ kg/m}^3$) in the wellbore is 74 cm/sec.

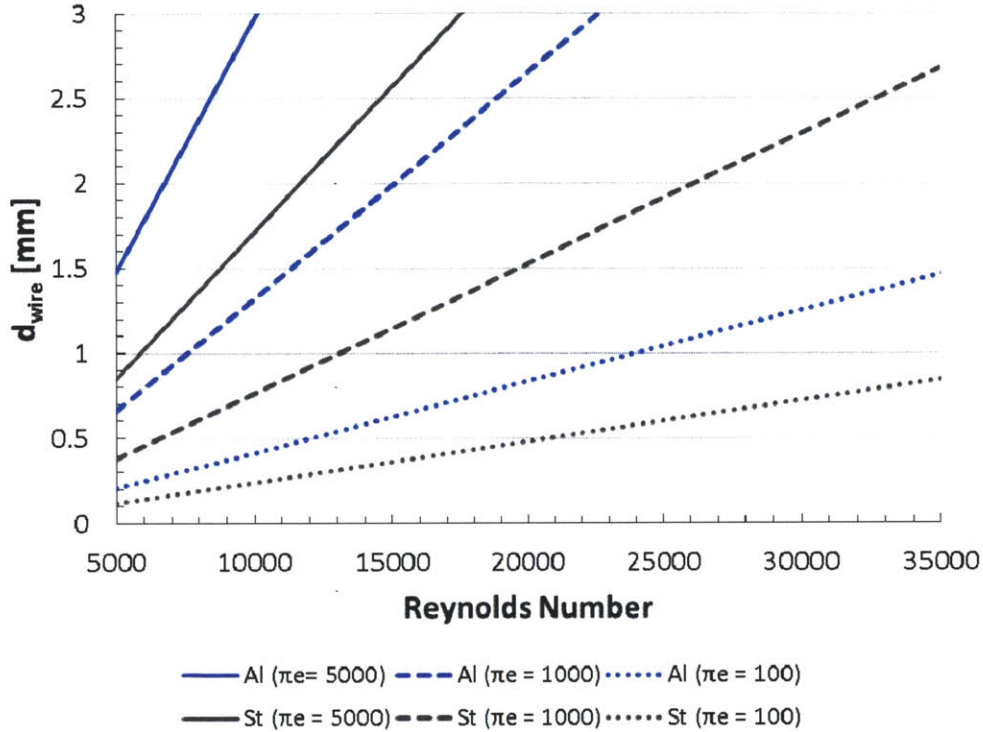


Figure 6-22: Wire size requirement for offshore industry for an 47.6 cm (18.75 inch) wellbore with an oil viscosity of 0.01 Pa*sec, and density of 839 kg/m³, for varying non-dimensional stiffness values.

6.5. Preliminary Testing

The preliminary run for the prototype consisted of connecting the entire assembly to a fire truck to provide an uncontrolled fluid flow loop. The objective of the preliminary run was to determine system failures in the machine, seals, flow chamber components, operations, etc. prior to testing in an integrated flow loop. The test plan was to first test the properties of the mechanical plug under higher pressures loads and second to determine functionality of the wire feeder prototype components.

6.5.1. Experimental Setup

The experiment was setup in Somerville Massachusetts with the assistance and support of the Somerville Fire Department.^{†††} As shown in Figure 6-23, the full assembly was placed on a granite slab and anchored with straps. A 2.5 inch NH hose was used to deliver water from the fire truck to the experimental setup. The first part of the experiment consisted of inserting unconsolidated sealing material and a pre-manufactured entanglement into the bore. The flow was activated and the material allowed to move along the length of the flow chamber until it caught on an obstruction and anchored. The extension region was used to remove the compressed mechanical plug as a whole for measuring lengths used to calculate permeability. For the second part, the flow was activated and the drive motor powered to feed wire into the interface region of the flow chamber.

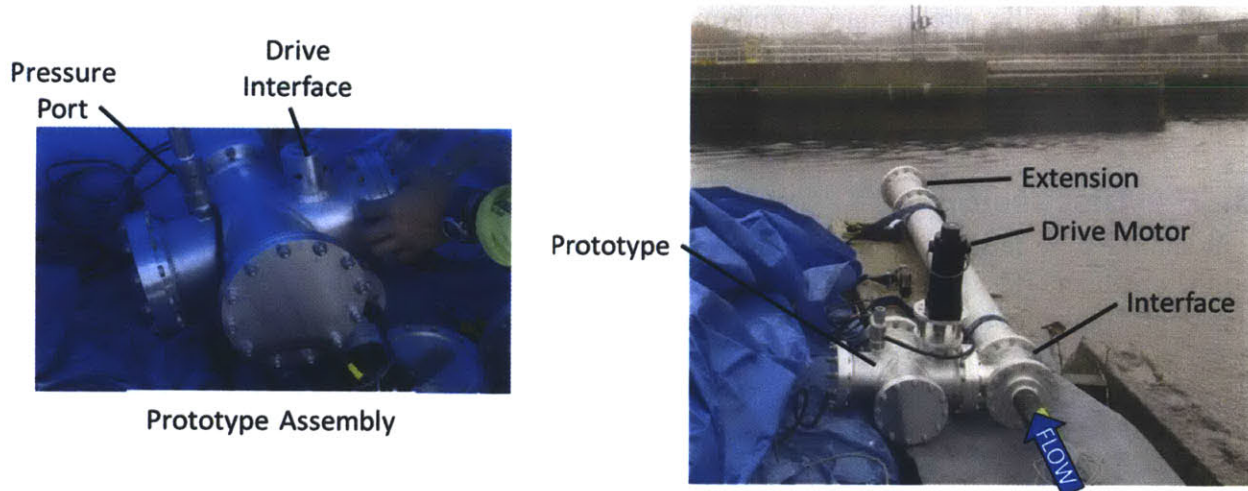


Figure 6-23: Somerville Massachusetts preliminary experimental run on the banks of the Mystic river

^{†††} This test would not have been possible without the help from the Somerville Fire Department: Deputy Chief Patrick Sullivan, Deputy Chief Charlie Breen, Captain Matt Wall, Lieutenant Greg French, Master Mechanic Paul Dickie, Firefighter Jack Beckwith, Firefighter Antonio Cicolini, Firefighter Andrew Patriquin, Firefighter Jim Piwinski. And John Freidah with the MIT Meche Department.

6.5.2. Results

The data from testing the preformed mechanical plug inside the chamber (see Figure 6-24) shows that a mechanical plug consisting of an entanglement backed by a more compressible material can achieve sealing greater than 90% for pressures as high as 2.4 MPa (350 psi).

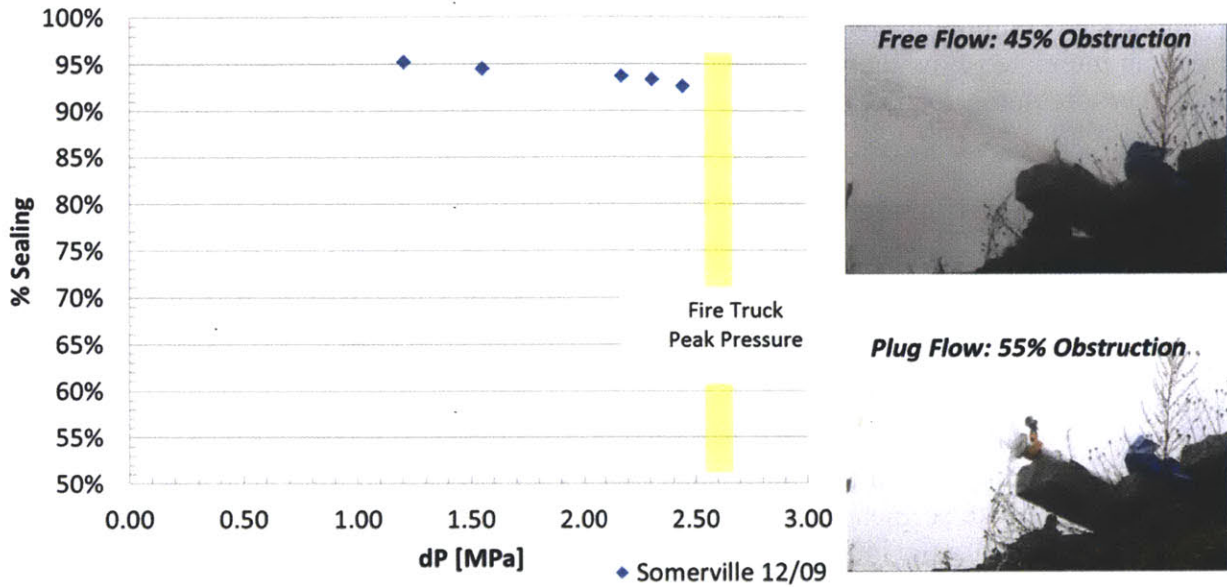


Figure 6-24: Somerville preliminary experimental run sealing as a function of pressure for a mechanical plug introduced into the flow chamber. Galvanized Steel Wire $D_{wire} = 1.55$ mm (0.061 inch), $D_{bore} = 10.2$ cm (4 inches), Anchor Mass $m_e = 0.510$ kg (1.1 lb), Mass Plug Material $M_p = 0.875$ kg (1.9 lb), Obstruction 45 %, Anchor Compaction Measured 22%, Plug Permeability 16-22 Darcy

6.5.3. Discussion

When the wire feeder unit was tested one component inside the feeder slipped, as the wire was fed into the chamber. The source of the problem was too much friction, caused by the wedging of the spool inside the housing, hence the need a second version of the spool design.

6.6. Full Flow Loop Test Setup

The objective of the flow loop tests was to scale the entanglement experiments. The experiments were established in two sections: wire entanglement and anchoring/sealing. The first setup sought to demonstrate entanglement in a 10.2 cm borehole at Reynolds numbers exceeding 100,000 (124 gpm), but with non-dimensional stiffness parameters equivalent to those performed at the 2.5 cm (1 inch) scale. The second setup subjected the entanglement and sealing material to a significant pressure load using drill mud inside the flow chamber.

6.6.1. Wire Entanglement

The flow was powered by 14.9 kWatt (20 hp) pump capable of delivering city water at a rate of 1,136 L/min (300 gpm) at a maximum pressure of 6.7 kPa (100 psi). The wire entanglement experiment was setup as shown in Figure 6-25. The flow chamber was held at a thirty-degree incline using a mounting frame. The exit of the chamber is aimed at the deeper end of the pit to minimize splash. For balance the wire feeder was mounted facing down. Flow to the chamber was provided through a 2-inch brass Dixon valve connection to a flexible flow loop. As shown in Figure 6-26 and Figure 6-27 the entire setup was free standing. The chamber was anchored to the ground using high strength straps.

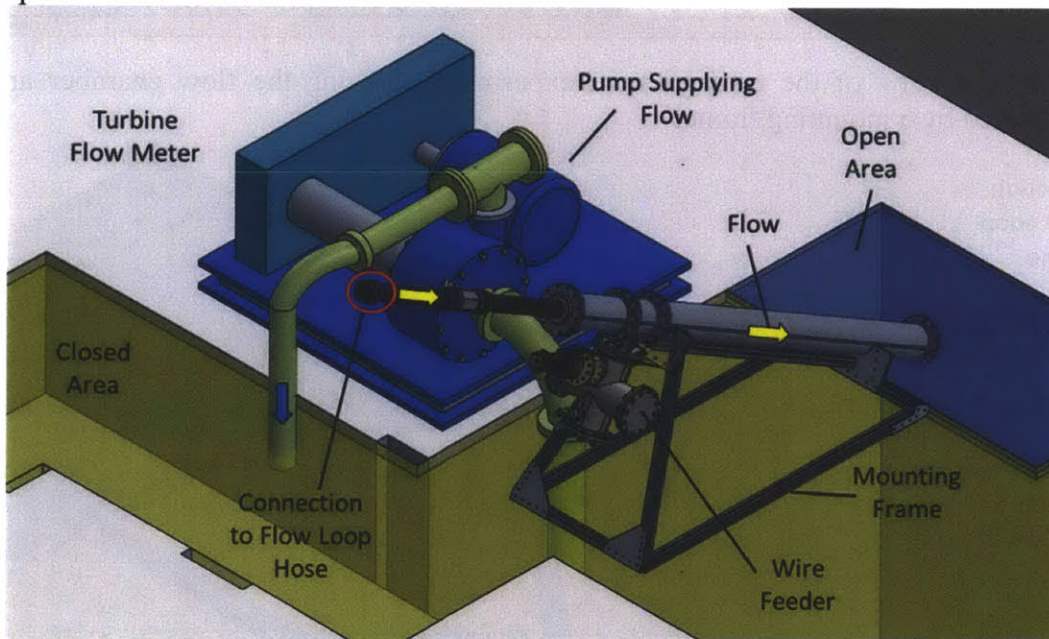


Figure 6-25: Isometric view showing the location of the entanglement experiment with respect to the pit and the pump supplying the flow

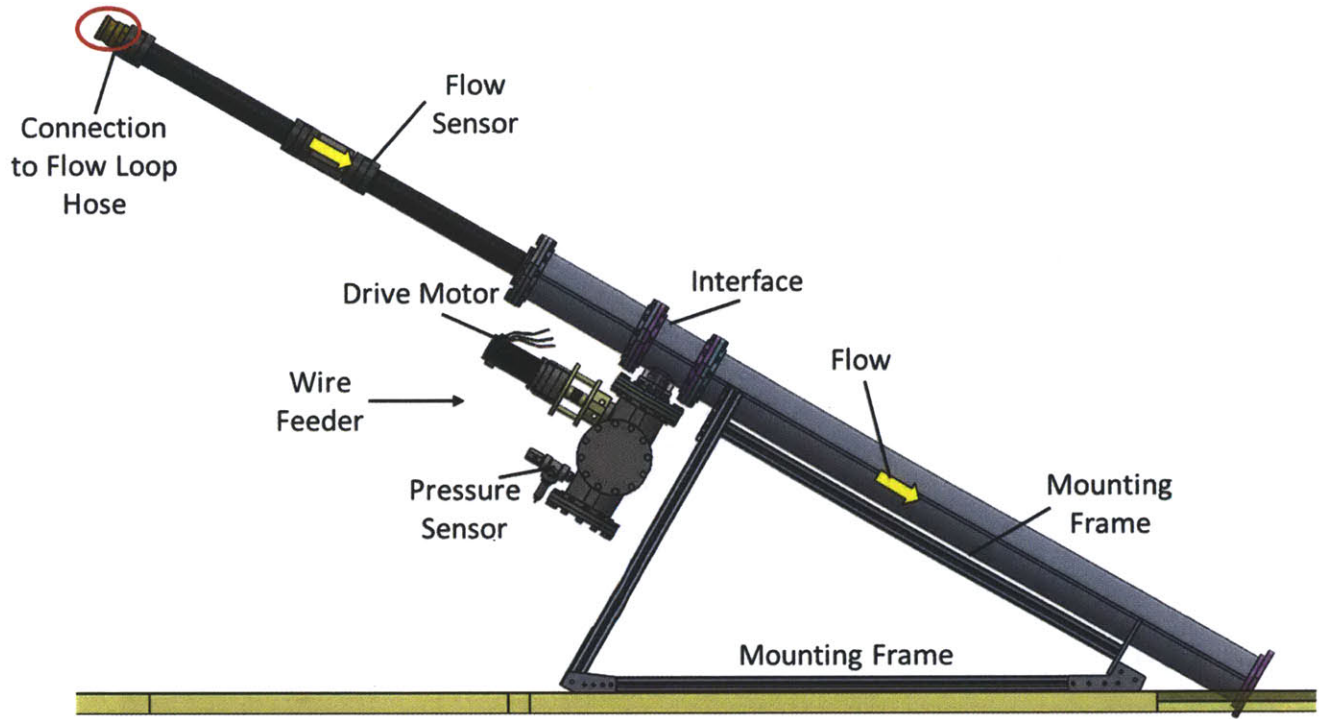


Figure 6-26: Side view of the entanglement experiment showing the flow chamber angled at 30 degrees supported by a mounting frame.

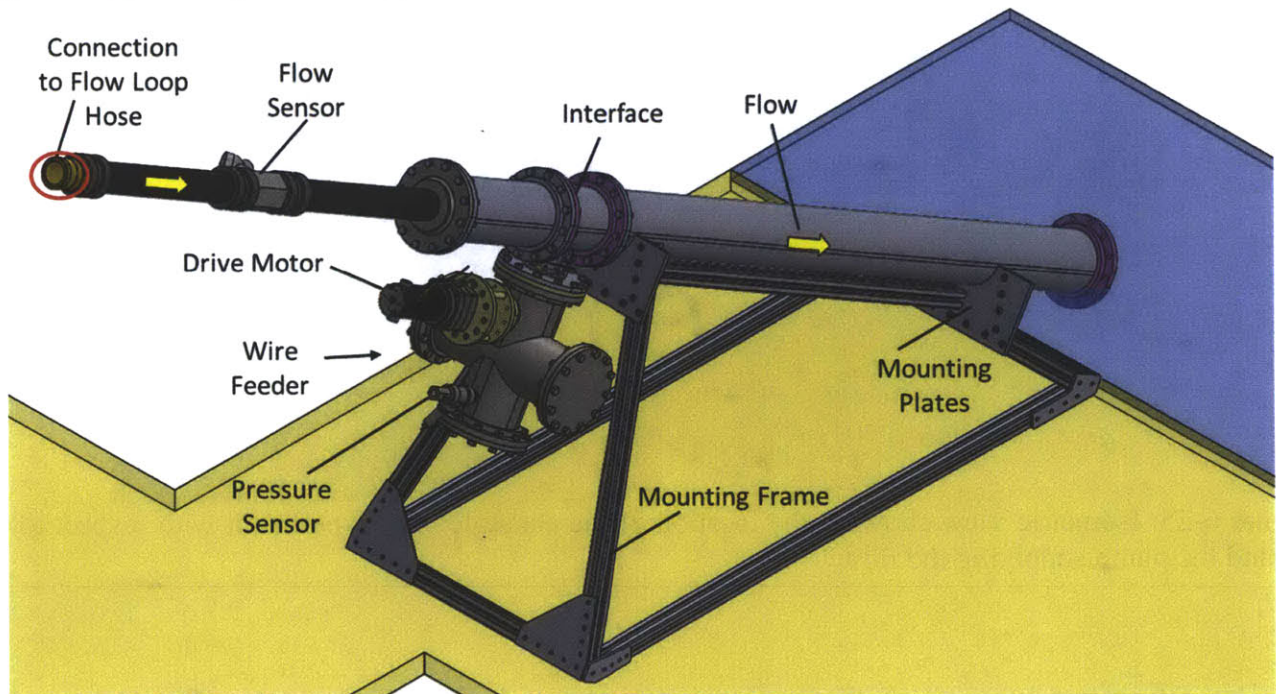


Figure 6-27: Isometric view showing the entanglement experiment with the flow chamber mounted on the frame. The chamber is going to be strapped down to the frame and the frame to the foundation.

6.6.2. Pressure Loading

The flow chamber assembly connects to the drill mud supply line via a Dixon 3-inch hammer union (1002). The interface to the mud loop was achieved with a 3-inch 1002 Dixon hammer union (max pressure 10,000 psi). A custom coupling was been created to join the 3-inch female NPT port to the flow chamber. The pressure loading was provided using drill mud with a density of 9.2 ppg. As shown in Figure 6-28, the extension interface was placed towards the exit of the chamber to allow for measurement of the compression of the mechanical plug. During operation the maximum pressure loaded on this unit was intended to be 13.8 MPa (2.0 ksi) keeping a 3.4 MPa (500 psi) safety margin.

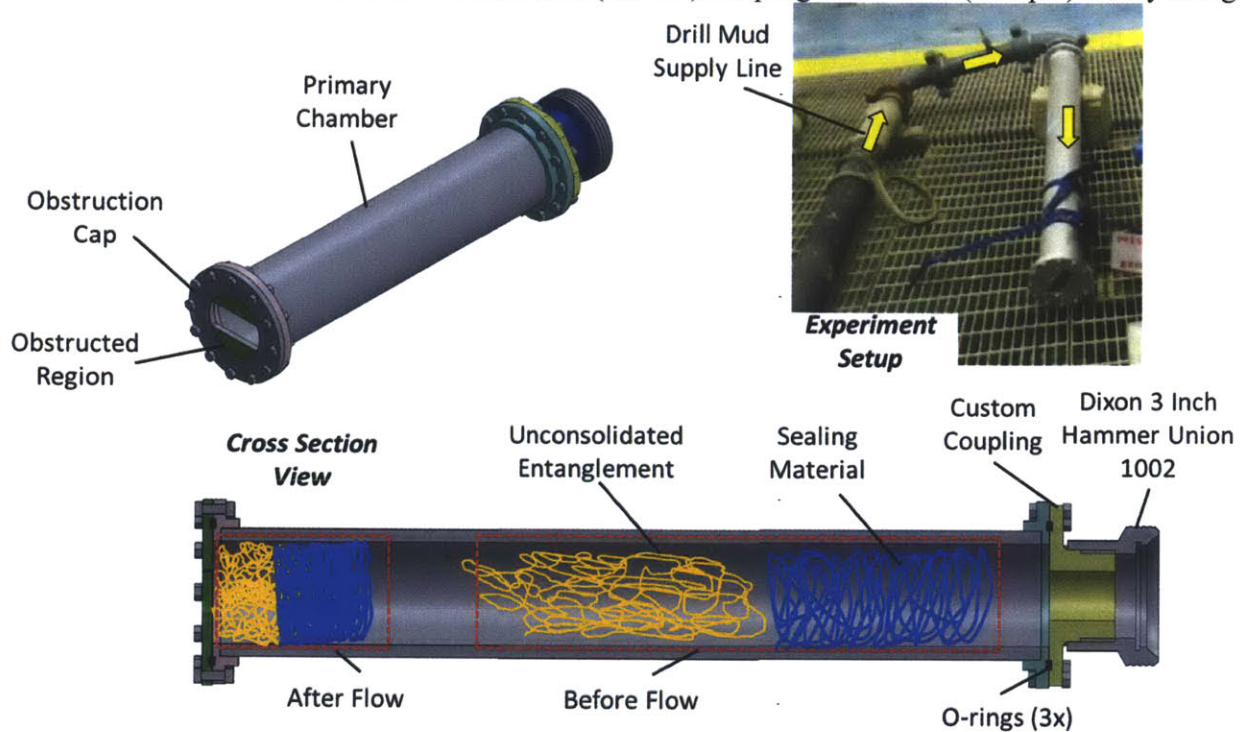


Figure 6-28: Overview of pressure test showing the setup and how the mechanical plug is going to compress

As shown in Table 6-1, each interface in the assembly is analyzed to make sure it can withstand the load (see the detailed Excel spreadsheet document can be found in the Appendix Section under: High Pressure Loads in Flow loop). The limiting agent of the maximum operating pressure was the weld between the flanges and the chamber components. The process of welding inherently decreases the material properties of the material; therefore, the yield stress of the weld is no longer that of the Al 6061-T6 but rather significantly lower. The calculations at these interfaces were performed assuming that the material was locally annealed during the welding process and has a lower yield and tensile strength. The annealed yield strength is 95 MPa, assuming that the material was annealed to a T0, which results in a shear strength of 54.8 MPa. At an operating pressure of 13.8 MPa (2,000 psi), the weld is expected to be operating at sixty percent of the allowable stress which includes a 1.5 safety factor.

Table 6-1: Chamber and interface failure modes and maximum pressure ratings (* Assumes that load is at full bolt diameter which is a highly conservative estimate)

Component/ Interface	Failure Mode	Factor of Safety	Maximum Pressure rating	Operating to Yield % (2,000 psi)
Hammer Union	Leakage	NA	68.9 MPa (10.0 ksi)	20.0%
3 Inch NPT Hammer Union & Mounting Flange	Shear	1.5	15.6 MPa (9.3 ksi)	21.7 %
Mounting Flange	Tension Section	2.0	>68.9 MPa (10.0 ksi)	7.7%
	Shear Near O-ring Region	1.5	41.4 MPa (6.0 ksi)	33.3%
12x 3/8-16 Bolts Grade 9 (Tensile Strength 180,000)	Head shearing	1.5	>68.9 MPa (10.0 ksi)	11.4%
	Tension	1.5	37.2 MPa (5.4 ksi)	37.2 %
		1.5*	14.1 MPa (2.0 ksi)*	98.3%
Chamber Flange Interface	Shear	1.5	28.3 MPa (4.1 ksi)	49.0
Weld between Flange and Chamber	Yield	1.5	22.8 MPa (3.3 ksi)	60.3%
Pressure Chamber	Yield	1.5	31.7 MPa (4.6 ksi)	43.1%

6.7. Data

6.7.1. Wire Entanglement

As shown in Figure 6-29, the first experiment consisted of feeding the galvanized steel wire at a 15 degree tilt and 30 degree rotation against the flow whose Reynolds number is approximately 150,000; whereas in the second configuration, the wire was fed orthogonal to the flow with zero tilt to a flow whose Reynolds number is approximately 240,000. These two experiments demonstrate that entanglements can be generated both against the flow and within the flow as well.

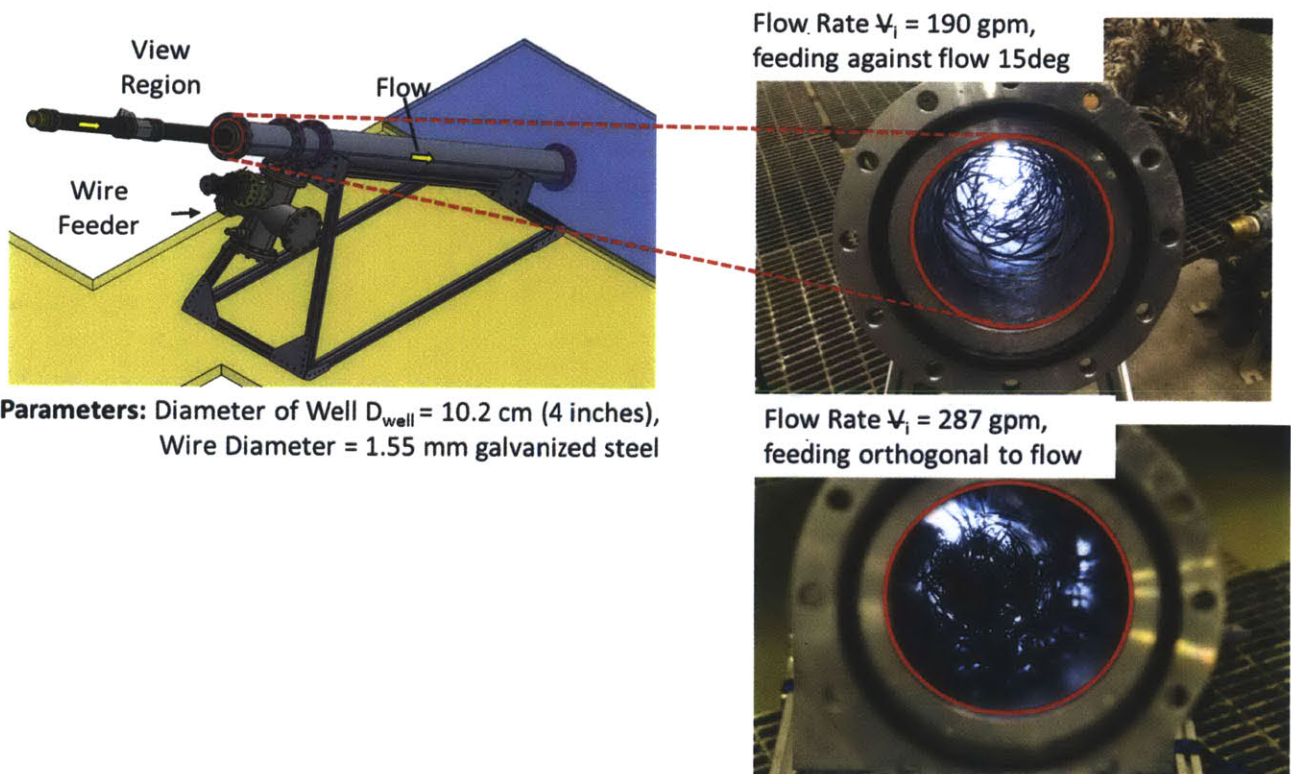


Figure 6-29: Wire entanglement generated by feeding against the flow and orthogonal to the flow. The non-dimensional stiffness at 720 lpm (190 gpm) is $\pi_e = 1830$ and at 1098 lpm (290 gpm) is $\pi_e = 785$.

Sealing material was introduced into the flow chamber with the entanglement generated by orthogonal feeding. The introduction of the sealing material demonstrated that significant sealing can be achieved with 0.68 MPa (100 psi) of back pressure as shown in Figure 6-30.

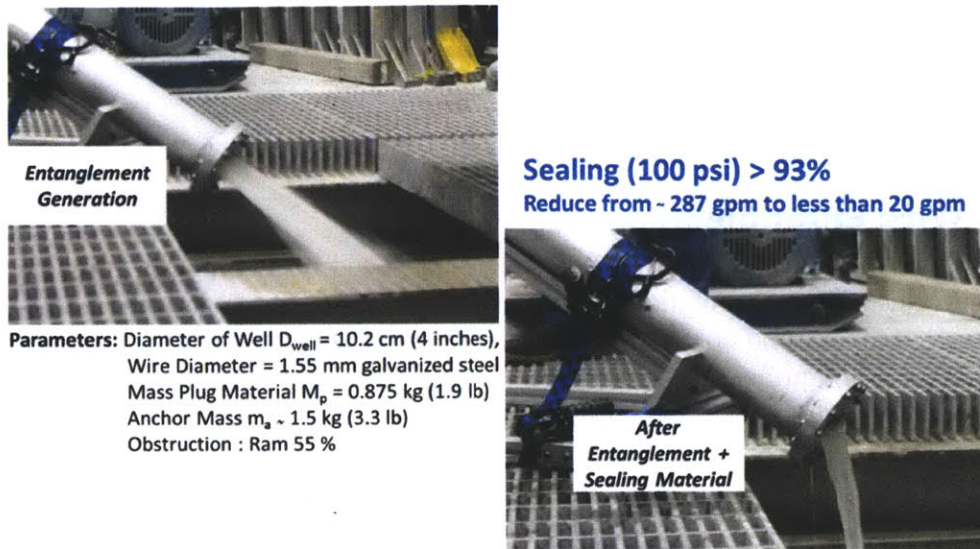


Figure 6-30: Wire entanglement sealing at low pressures

Comparing the non-dimensional entanglement stiffness values shows that the entanglements generated are in the same range as those within the 2.5 cm bore experimental setup.

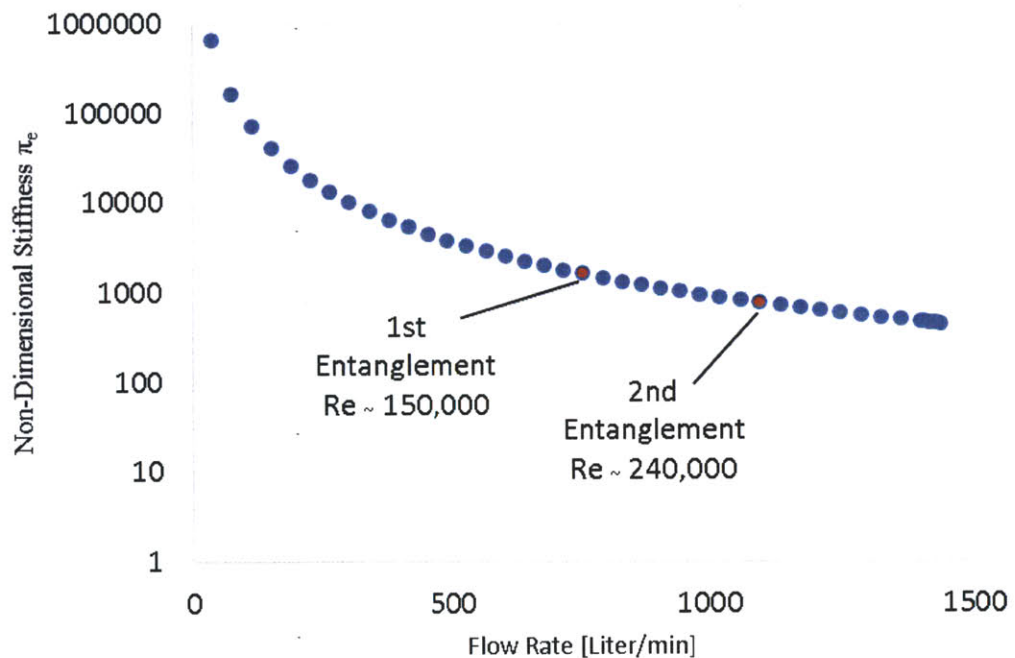


Figure 6-31: Flow rate versus non-dimensional entanglement stiffness showing that the test points for entanglement are in the same range of the smaller scale experiments

The entanglements generated were created at Reynolds numbers significantly higher than those expected. The Reynolds number of a fully open well whose bore diameter is 47.6 cm (18 3/4 inch) diameter bore, flowing at 184 liters/sec (100,000 bbl./day extreme max) is 50,000. Therefore, the entanglement tests performed were at least a factor three higher than the maximum expected under operating to demonstrate the feasibility of entanglement generation with high flow rates.

6.7.2. Pressure Loading

The system in Figure 6-28 demonstrated that a significant amount of load could be withstood while sealing was achieved. As shown in Figure 6-32 the unit was tested to a maximum pressure of 15.9 MPa (2300 psi), which is 2.1 MPa (300 psi) greater than the intended objective. The applied pressure is twelve percent of the maximum expected under operating conditions, but only at 1/5 the scale (based on wellbore diameter 4/18.75). After 10.3 MPa (1,500 psi) the pressure in the chamber increased at a drastic rate that could not be controlled using the available pumps. At 15.9 MPa (2,300 psi), the weld between the flange and chamber failed due to limited weld penetration depth.

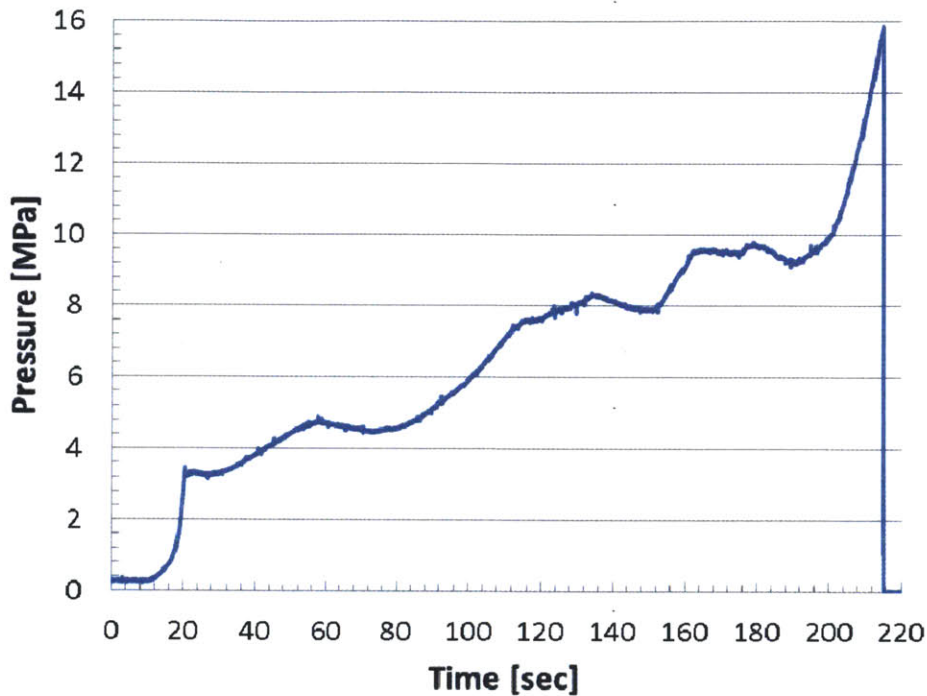


Figure 6-32: Pressure experiment using drill mud (9.2 pounds per gallon) with a generated entanglement and added ribbon sealing material (heat shrink) $m_p = 0.875$ kg (1.9 lb) and approximately anchoring mass of $m_e = 1.5$ kg (3.3 lb).

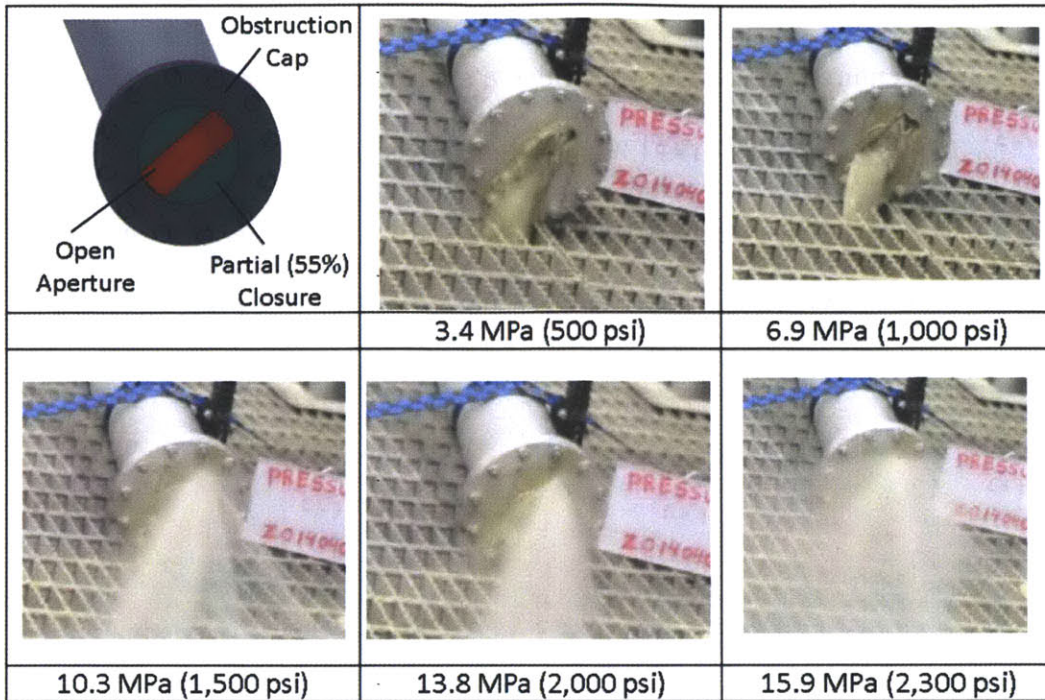
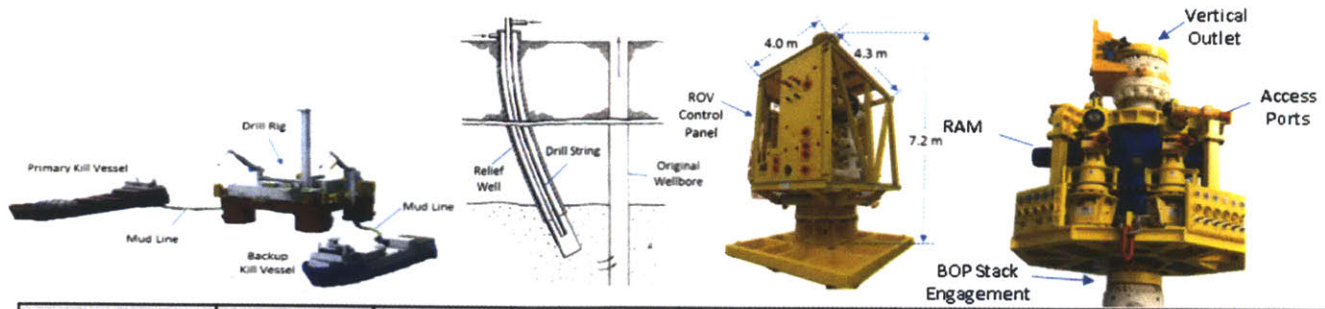


Figure 6-33: Pressure loading images throughout the loading process

6.8. Technology Comparison

This work has shown that a mechanical plug can be used to create a significant reduction in a high-pressure flow. The size of HAWK allows for rapid deployment and interface with existing BOPs requiring minimal alterations to the existing infrastructure. As shown in Figure 6-34, the greatest technological advantage of HAWK is low implementation cost and the rapid response time for deployment. The machine has the added advantage of minimal risk to existing formations since the closure of the well is gradual.



	Response Time	Cost	Support Equipment	Weight & Transportation	Reliability	Applicability	Risk
HAWK	< 1 week	Low	VOF	<2/3 T Airplane/Ship	Medium	Medium	Low
Junk Shot	2 – 4 weeks	High (\$1M/d)	Ship w/ Drill Mud	N/A Ship	Low	Medium	Med
Relief Well	4 – 10 weeks	High	VOF	N/A Drill Rig	High	High	Low
Capping	2 – 4 weeks	High	VOF	40/100 T Ship	Medium	High	Med
Containment	4 – 6 weeks	High	VOF	500 T Ship	High	High	Med

Figure 6-34: Technology comparison

6.9. Conclusion

The manner in which the pressure increased during the pressurized experiments demonstrates the need for pressure feedback control when feeding the sealing material. If the sealing material is introduced into the borehole too quickly, then an unfavorable pressure spike may be generated. Overall, the tests have demonstrated that a mechanical plug consisting of an anchoring region followed by a more compressible sealing material can be used to effectively close a free flowing well. Further work will focus on closing the well to the point of zero leakage.

[Left Blank]

Chp 7.

Discussion

The existing feasibility study has demonstrated that introducing a mechanical plug can significantly reduce an uncontrolled flow.

7.1. Future Work

While this work focused on identifying some of the key parameters of the wire entanglement, a great deal of additional work is required to develop a more complete understanding of the phenomena. Future work on this project can be separated into two sections: academic, and industry. From the academic standpoint, there is now an opportunity to explore the high plastic deformation of wire entanglement in a free flowing medium. From the industry perspective, there are at least three different of offshore oil industry tools that could benefit from use of wire entanglement to bring a well under control: ROV, incorporated, and tool. Another option is to create an integrated tool that gets placed inside of the well to achieve the same effect. These are now engineering opportunities to optimize and scale. It is crucial to look at both the production oil barrels and cubic feet of gas produced as the phase envelope may influence the behavior of the entangling process.

7.2. Closing Remarks

The next steps following this work would be the development of a commercial product that could be used to bring an offshore well under control. It is the author's hope to have this technology accepted as a blowout preventer backup safety tool used by the oil industry as a means to mitigate blowouts before more permanent solutions are implemented.

[Left Blank]

Bibliography

- [1] "Macondo Well - Deepwater Horizon Blowout: Lessons for Improving Offshore Drilling Safety," National Academy of Engineering and National Research Council, Washington DC2011.
- [2] G. A. Hill, "Down Hole, Hydrodynamic Well Control, Blowout Prevention," US Patent 6,357,566 B1, Apr. 9, 2002.
- [3] E. R. Hemphill, M. W. Berckenhoff, and W. L. Carbaugh, "Mounts for Blowout Preventer Bonnets and Methods of Use," US Patent 7,802,626 B2, Sept. 28, 2010.
- [4] C. S. Isaacks, H. P. Hiebeler, N. T. Cordova, J. Livingston, and R. Gilleylen, "Shear/Seal Ram Assembly For a Ram-Type Blowout Prevention System," US Patent 2006/0113501 A1, Jun. 1, 2006.
- [5] R. M. Mackowsky, C. B. Kende, R. C. Bennett, and J. A. Ziemplanski, "The Deepwater Horizon Catastrophe: A Factual Overview and Preliminary First-Party Analysis," Cozen O'Connor 2010.
- [6] F. B. Springett and J. D. Brugman, "Blowout Preventers and Methods of Use," US Patent 7,814,979, Oct. 19, 2010.
- [7] "Forensic Examination of Deepwater Horizon Blowout Preventer," United States Department of the Interior EP030842, March 20, 2011.
- [8] H. Fountain, "'Junk Shot' Is Next Step for Leaking Gulf of Mexico Well," in *The New York Times*, ed. Houston, 2010.
- [9] L. Greenemeier, "BP Plans Kill Shot for Leaking Deepwater Well," *Scientific American*, May 11, 2010.
- [10] K. Wells, "BP Technical Briefing," May 25, 2010.
- [11] "Capping & Containment: Global Industry Response Group Recommendations," International Association of Oil & Gas Producers May 2011.
- [12] (2012), Offshore Outlook, Infield: The Energy Analyst Available: <http://www.infield.com/articles/offshore-outlook-2012.pdf>
- [13] David Izon, E. P. Danenberger, and M. Mayes, "Absence of fatalities in blowouts encouraging in MMS study of OCS incidents 1992-2006," *Drilling Contractor*, 2007.
- [14] (2010). *Black Tides: The Worst Oil Spills in History*. Available: <http://earth.tryse.net/oilspill.html>
- [15] D. Schmidt-Etkin, *Oil Spill Science and Technology - Prevention, Response, and Cleanup*: Gulf Professional Publishing, 2011.
- [16] T. J. Crone and M. Tolstoy, "Magnitude of the 2010 Gulf of Mexico Oil Leak," *Science Magazine*, vol. 330.
- [17] S. d. S. Croix, "New Chevron Oil Leak in Brazil: Daily," in *The Rio Times*, ed, 2012.

- [18] M. Stigset. (2010), Sevan Slumps on Blowout Malfunction on Drilling Rig. *Bloomberg*. Available: <http://www.bloomberg.com/news/2010-11-05/sevan-marine-plunges-on-blow-out-malfunction-on-drilling-rig.html>
- [19] (2012, Sevan Brasil Experiences Problems with BOP Control Systems. *Subsea World News*.
- [20] C. Nelson and H. Austin, "Fire Subsides After Gulf Rig Partially Collapsis," in *NBC News*, ed.
- [21] (2013). *Marine Well Containment Company*. Available: <http://www.marinewellcontainment.com/index.php>
- [22] (2013). *Oil & Gas UK*. Available: <http://www.oilandgasuk.co.uk/index.cfm>
- [23] (2013). *Deepstar - Technology Development for Deepwater Research*. Available: <http://www.deepstar.org/>
- [24] F. J. Schempf, "Top, Bottom Kill Prospects Leave Macondo Just a Nasty Memory," *Offshore*, pp. 50-53, Oct. 2010.
- [25] A. Fontevecchia. (Feb 5, 2013). BP Fighting a Two Front War As Macondo Continues to Bite and Production Drops. *Forbes*.
- [26] "Civil Penalty Policy for Section 311(b)(3) and Section 311(j) of the Clean Water Act," ed: Office of Enforcement and Compliance Assurance.
- [27] "Financial Statements BP Annual Report," ed, 2012, pp. 177-288.
- [28] J. Lenker and K. D. Crockett, "Wire Frame Partial Flow Obstruction for Aneurysm Treatment," US Patent 6,183,495 B1, Feb. 6, 2001.
- [29] F. H. Bartlit, S. N. Sankar, and S. C. Grimsley, "Macondo The Gulf Oil Disaster - Chief Counsel's Report " 2011.
- [30] W. P. Orr, "Emergency Blowout Preventer Closing System," US Patent 4,317,557, Mar. 2, 1982.
- [31] Transocean, "Macondo Well Incident Transocean Investigation Report Vol 1,2," ed, 2011.
- [32] P. P. L. Couren and H. P. Hopper, "Blow Out Preventer Testing Apparatus," US Patent 7,062,960 B2, 2006.
- [33] W. J. Winters and R. B. Livesay, "Blowout Preventer Testing System and Method," US Patent 7,706,980 B2, Apr. 27, 2010.
- [34] P. A. Huff and K. Prudent, "High Pressure-Rated RAM Blowout Preventer and Method of Manufacture," 2008/0078081 A1, Apr. 3, 2008.
- [35] P. A. Huff and S. Khandoker, "Reinforcement of Irregular Pressure Vessels," US Patent 7,721,401 B2, May 25, 2010.
- [36] M. F. Whitby and J. E. Kotrla, "More Than The Sum of its Parts: How 20,000 psi Subsea BOP Stack was Designed and Developed," *Drilling Contractor*, June 1, 2013.
- [37] M. W. Berckenhoff and E. R. Hemphill, "Quick Release Blowout Preventer Bonnet," US Patent 6,554,247 B2, Apr. 29, 2003.
- [38] J. VanDelden, "Magnetorheological Blowout Preventer," US Patent 2011/0297394 A1, Dec. 8, 2011.
- [39] S. Khandoker, "Method of Designing Blowout Preventer Seal Using Finite Element Analysis," US Patent US 2008/0027693 A1, Jan. 31.
- [40] S. Butuc, "BOP Packing Units Selectively Treated with Electron Beam Radiation and Related Methods," US Patent 2010/0140516 A1, Jun. 10, 2010.
- [41] R. W. Walker, "Blowout Preventer," US Patent 3,323,773, Jun. 6, 1967.
- [42] M. Y. Huang, "Fluorinated Elastomeric Blowout Preventer Packers and Method," US Patent 2012/0000644 A1, Jan. 5, 2012.

- [43] K. M. Nicolson, "Shearing Device And Method for Use in Well Drilling," US Patent 2,919,111, Dec. 29, 1959.
- [44] M. R. Jone, "Shear Ram Blowout Preventer," US Patent 4,347,898, Sep. 7, 1982.
- [45] S. Harrison, "Cutting Apparatus," US Patent 4,549,349, Oct. 29, 1985.
- [46] E. J. Scharinger, "Blade for Cutting Cylindrical Structures," US Patent 5,237,899, Aug. 24, 1993.
- [47] S. Yadav and L. Melendez, "Shear Blade Geometry and Method," 2012/0193556, Aug. 2, 2012.
- [48] E. Koutsolelos, "Numerical Analysis of a Shear Ram and Experimental Determination of Fracture Parameters," Doctoral, Mechanical Engineering, Massachusetts Institute of Technology, 2012.
- [49] *Guide to Blowout Prevention*. Harvey, Louisiana: Well Control School, 2000.
- [50] R. E. Sweatman, "Method of Plugging a Well," US Patent 4,275,788, Jun. 30, 1981.
- [51] J. U. Messenger, "Well Control Method Using Low-Melting Alloy Metals," US Patent 4,489,784, Dec. 25, 1984.
- [52] P. Beiersdorfer, D. Layne, E. W. Magee, and J. I. Katz, "Viscoelastic Suppression of Gravity-Driven Counterflow Instability," *Physical Review Letters*, vol. 106, 2010.
- [53] C. L. Hamburger, Y.-h. Tsao, B. Morrison, and E. N. Drake, "A Shear-Thickening Fluid for Stopping Unwanted Flows While Drilling," *Society of Petroleum Engineers*, 1985.
- [54] E. N. Drake and P. Calcavecchio, "Plugging Wellbores," US Patent 4,475,594, Oct. 9, 1984.
- [55] D. W. Osmun, C. W. Johnson, and R. A. Plummer, "Method for Controlling Offshore Petroleum Wells During Blowout Conditions," US Patent 3,738,424, June 12, 1973.
- [56] W. E. Holland, C. B. Corley, and W. C. Lindsey, "Method of Plugging a Well Bore with a Thermosetting Resin," US Patent 3,170,516, Feb. 23, 1965.
- [57] J. W. Ely, "Terminating the Flow of Fluids from Uncontrolled Wells " US Patent 4,133,383, Jan. 9.
- [58] L. Winerman, "Relief Wells Will Work, Experts Say, but Will Take Time, Trial and Error," *PBS News*, June 2, 2010.
- [59] R. E. Hermes, "Reducing or Stopping the Uncontrolled Flow of Fluid Such as Oil From a Well," US Patent 2012/0285683 A1, Nov. 15, 2012.
- [60] R. R. Vann and F. R. George, "Method for Controlling Subsurface Blowout," US Patent 4,436,154, Mar. 13, 1984.
- [61] E. M. Blount, "Method of Dynamically Killing a Well Blowout," US Patent 4,224,989, Sep. 30, 1980, 1980.
- [62] D. M. Tumlin, G. K. Fugatt, D. Hosie, and M. Luke, "Method and Apparatus for Plugging a Wellbore," US Patent 6,595,289 B2, Jul. 22, 2003.
- [63] C. C. Brown, "Method of Cementing Wells," US Patent 2,743,779, May 1, 1956.
- [64] E. B. Naess and N. Lauritssons, "Method and Apparatus for Collecting Oil and Gas from an Underwater Blow-Out," 4,447,247, May 8, 1984.
- [65] H. Y. A. M. Mothaffar, "Deep-Water Oil Well Spill Controller and Container," US Patent 2012/0285704 A1, Nov. 15.
- [66] M. A. Ba-abbad, "Method and Apparatus for Plugging Leaking Oil and Gas Wells," US Patent 8,371,373 B2, Feb. 12, 2013.
- [67] M. R. Lugo, "Diverter System for a Subsea Well," US Patent 2012/0318520, Dec. 20, 2012.
- [68] J. L. Renfrow, "Collapsible Oil Spillage Recovery System," US Patent 4,790,936, Dec. 13, 1988.

- [69] D. S. Hammett, "Subsea Blowout Containment Method and Apparatus," US Patent 4,324,505, Apr. 13, 1982.
- [70] W. M. Caldwell and J. P. Payne, "Apparatus and Method for Isolating and Securing an Underwater Oil Wellhead and Blowout Preventer," US Patent 2012/0160509, Jun. 28, 2012.
- [71] J. Spacek, "Oil Well Improvement System," US Patent 2012/0241160 A1, Sep. 27, 2012.
- [72] S. Wolinsky, "Contained Top Kill Method and Apparatus for Entombing a Defective Blowout Preventer Stack to Stop an Oil and/or Gas Spill," US Patent 8,025,103 B1, Sep. 27, 2011.
- [73] A. Kagi, "Method for Fighting an Oilspill in the Aftermath of an Underwater Oil Well Blowout and Installation for Carrying out the Method," ep Patent 2013/0126178 A1, May 23, 2013.
- [74] M. C. O'Malley, "System and Method for Channeling Fluids Underwater to the Surface," US Patent 2012/0152560, Jun. 21, 2012.
- [75] (Jun. 17, 2013). *UKCS Well Capping Device* Available: <http://www.oilspillresponse.com/services-landing/well-incident-intervention/ukcs-well-capping-device>
- [76] (June 23, 2013), *The OSPRAG Well Capping Device*. Available: http://www.oilandgasuk.co.uk/knowledgecentre/OSPRAG_Capping_Device.cfm
- [77] J. P. Pavlich and J. L. Elbel, "Method of Plugging Wellbore Casing Perforations," US Patent 3,384,175, May 21, 1968.
- [78] K. G. Rowley and R. H. Barron, "Method for Controlling Well Blowouts," US Patent 3,647,000, Mar. 7, 1972.
- [79] R. H. McCall, "Methods and Apparatuses for Controlling and Preventing Blow-outs in Wells," US Patent 3,926,256, Dec. 16, 1975.
- [80] J. F. Carrascal, "Method to Shut Down a High Pressure Oil/Gas Well That is Leaking Under Blowout Conditions," US Patent 8,215,405, Jul. 10, 2012.
- [81] S. Salkin, "System and Method for Controlling Underwater Oil-Well Leak," US Patent 8,205,677 B1, Jun. 26, 2012.
- [82] J. C. Bowersock, R. D. Bennett, J. R. Korte, and E. D. Griffith, "Plug-Inducing Matter and Method of Plugging a Wellbore," US Patent 2012/0168161 A1, Jul. 5, 2012.
- [83] R. Meinke, M. Senti, and G. Stelzer, "Closing of Underwater Oil Spills with the Help of Magnetic Powders," WO Patent WO2011153245 A1, Dec 8, 2011, 2011.
- [84] E. K. Taylor, J. V. Boyd, and J. H. Williams, "Wire Moving Apparatus," US Patent 3,901,425, Aug. 26, 1975.
- [85] M. R. Christopher and N. A. Matiash, "Welding Wire Feeder with Improved Wire Guide," US Patent 2013/0048621 A1, Feb. 28, 2013.
- [86] J. E. Miller, "Device for Pushing or Pulling Using Gripping," US Patent 5,934,537, Aug. 10, 1999.
- [87] L. E. Seuffer, "Wire Feeding Apparatus," US Patent 5,816,466, Oct. 6, 1998.
- [88] F. V. Collins, "Feed Apparatus for Tubes," US Patent 2,525,590, Dec. 7, 1950.
- [89] J. C. Jeannette, "Wire Feed Apparatus," US Patent 3,447,730, Jun. 3, 1969.
- [90] J. W. Heijnis and C. Engels, "Ribbon Guide," US Patent 2,786,674, Mar. 26, 1957.
- [91] B. J. Belfiore, E. A. Enyedy, and B. Nelson, "Wire Gripper for a Drive Unit of a Wire Feeder " US Patent 7,026,574 B2, Apr. 11, 2006.
- [92] A. G. Olivieri, "Wire Feed Assembly," US Patent 3,331,545, Nov. 10, 1967.
- [93] L. W. Blank, D. C. Griffin, and D. T. Wiersema, "Electrode Wire Feeder for an ARC Welding System," US Patent 6,427,894 B1, Aug. 6, 2002.
- [94] W. R. Babbitt and S. C. Sabo, "Hose Feeder," US Patent 3,946,918, Mar. 30, 1976.

- [95] R. A. Lyons and J. B. Mascheck, "Apparatus for Inserting and Withdrawing Coiled Tubing with Respect to a Well," US Patent 4,585,061, Apr. 29, 1986.
- [96] G. H. Calhoun and H. Allen, "Equipment for Inserting Small Flexible Tubing Into High Pressure Wells," US Patent 2,567,009, Sept. 4, 1951.
- [97] W. P. Bridges and A. Crosby, "Skate Roller Bearing For Coiled Tubing," US Patent 5,918,671, Jul. 6, 1999.
- [98] A. C. Ugural and S. K. Fenster, *Advanced Strength and Applied Elasticity*, 4th ed.: Prentice Hall, 2003.
- [99] E. K. Bassett, A. H. Slocum, P. T. Masiakos, H. I. Pryor, O. C. Farlkhzad, and J. M. Karp, "Design of Mechanical Clutch-Based Needle-Insertion Device," *PNAS*, vol. 106, 2009.
- [100] H. Y. Bae, "Device for Preventing Entanglement of Welding Wire," US Patent US 2012/0006802 A1, Jan. 12, 2012.
- [101] R. Bender, D. Barton, and H. Matthews, "Welding Wire Guide Ring," US Patent 2009/0014579 A1, Jan. 15, 2009.
- [102] H. A. Bernat, "Downhole Coiled Tubing Recovery Apparatus," US Patent 6,550,536 B2, Apr. 22, 2003.
- [103] M. J. Shelley and J. Zhang, "Flapping and Bending Bodies Interacting with Fluid Flows," *Annual Reveiw of Fluid Mechanics*, vol. 43, pp. 449-465.
- [104] S. Hornung, S. A. Cassidy, P. Yennadhiou, and M. H. Reeve, "The Blown Fiber Cable," *Journal on Selected Areas in Communications*, vol. SAC-4 No. 5, Aug. 1986.
- [105] P. Cochrane and M. Brain, "Future Optical Fiber Transmission Technology and Networks," *IEEE Communications Magazine*, 1988.
- [106] J. C. Guerrero, "Fiber Optics Insertion into Coiled Stainless Steel Tubing (Analysis)," *Wire Journal International*, pp. 78-85, 2001.
- [107] J. C. Guerrero, "Fiber Optics Insertion into Coiled Stainless Steel Tubing: Part II Experiment," *Wire Journal International*, pp. 86-89, 2001.
- [108] G. F. Carrier, "The Spaghetti Problem," *The American Mathematical Monthly*, vol. 56, pp. 669-672.
- [109] H. Sugiyama, N. Kobayashi, and Y. Komaki, "Modeling and Experimental Methods for Dynamic Analysis of the Spaghetti Problem," *Journal of Vibration and Acoustics*, vol. 127, pp. 44-51.
- [110] N. Kobayashi and M. Watanabe, "Dynamics and Stability of Spaghetti and Reverse Spaghetti Problems Coupled with Fluid Force," *Multibody System Dynamics*, vol. 11, pp. 111-125.
- [111] K. Behdinan, M. C. Stylianou, and B. Tabarrok, "Dynamics of Flexible Sliding Beams - NonLinear Analysis Part I: Formulation," *Journal of Sound and Vibration*, pp. 517-539.
- [112] L. Mansfield and J. G. Simmonds, "The Reverse Spaghetti Problem: Drooping Motion of an Elastica Issuing from a Horizontal Guide," *Journal of Applied Mechanics*, vol. 54, pp. 147-150.
- [113] B. Drury, *Control Techniques Drives and Controls Handbook*, 2nd ed., 2009.
- [114] R. W. Medeiros, T. Y. Tam, and S. A. Abdalla, "Entangled Polyamide Yarn," US Patent 5,434,003, Jul. 18, 1995.
- [115] D. M. Raymer and D. E. Smith, "Spontaneous Knotting of an Agitated String," *Proceedings of the National Academy of Sciences*, vol. 104, pp. 16432-16437, Oct. 16, 2007 2007.
- [116] J. S. Andrade, U. M. S. Costa, M. P. Almeida, H. A. Makse, and H. E. Stanley, "Inertial Effects on Fluid Flow Through Disordered Porous Media," *The American Physical Society*, vol. 82, June 28, 1999.

- [117] U. M. S. Costa, J. S. Andrade, H. A. Makse, and H. E. Stanley, "The Role of Inertia of Fluid Flow Through Disordered Porous Media," *Physica*, pp. 420-424, 1999.
- [118] H. E. Stanley and J. S. Andrade, "Physics of the Cigarette Filter: Fluid Flow Through Structures with Randomly-Placed Obstacles," *Physica*, pp. 17-30, 2001.
- [119] H. Darcy, *Les Fontaines Publiques de la ville de Dijon*. Paris: Distribution D'EAU, 1856.
- [120] C. T. Simmons, "Henry Darcy (1803-1858): Immortalised by His Scientific Legacy," *Hydrogeology Journal*, pp. 1023-1038, 2008.
- [121] G. O. Brown, "Henry Darcy and the Making of a Law," *Water Resources Research*, vol. 38, 2002.
- [122] R. Larson, "Derivation of Generalized Darcy Equations for Creeping Flow in Porous Media," pp. 132-137, 1981.
- [123] F. A. L. Dullien, *Porous Media Fluid Transport and Pore Structure*. New York: Academic Press, 1992.
- [124] F. M. Tiller, "The Role of Porosity in Filtration Part 3: Variable-pressure - Variable-rate Filtration," *AIChE*, 1958.
- [125] F. M. Tiller and H. R. Cooper, "The Role of Porosity in Filtration Part 4: Constant Pressure Filtration," *AIChE*, vol. 6, pp. 595-601, 1960.
- [126] F. M. Tiller and M. Shirato, "The Role of Porosity in Filtration: VI. New Definition of Filtration Resistance," *AIChE*, vol. 10, pp. 61-67, 1964.
- [127] P. A. Domenico and F. W. Schwartz, *Physical and Chemical Hydrogeology*. New York: John Wiley & Sons, 1990.
- [128] R. A. Freeze and J. A. Cherry, *Groundwater*. New Jersey: Prentice-Hall, Inc, 1979.
- [129] J. H. Kirby, "Junk Shot," US Patent 3,016,830, Jan. 16,, 1962.
- [130] (May 14, 2014)). *Offshore Petroleum History*. Available: <http://aoghs.org/offshore-technology-history/offshore-oil-history/>
- [131] *Handbook of Offshore Engineering* vol. 1-2: Elsevier, 2005.
- [132] "Deepwater Drilling System," ed: Hydril Pressure Control, 2008.
- [133] P. Holand and H. Awan, "Reliability of Deepwater Subsea BOP systems and Well Kicks," Exprosoft. Aug. 2012.
- [134] (2012, Worldwide Progression of Water Depth Capabilities for Offshore Drilling and Production. Available: <http://www.mustangeng.com/AboutMustang/Publications/Publications/Deepwater%20Poster%20Final.pdf>
- [135] M. Tomczak. (2002). *An Introduction to Physical Oceanography*. Available: <http://www.es.flinders.edu.au/~mattom/IntroOc/lecture05.html>
- [136] (2006, Jun. 28, 2013). *National Weather Service Climate Prediction Center*. Available: <http://www.cpc.ncep.noaa.gov/products/GODAS/climatology.shtml>
- [137] R. D. Grace, B. Cudd, R. S. Carden, and J. L. Shursen, *Blowout and Well Control Handbook*: Elsevier, Inc, 2003.
- [138] (July 15, 2013). *Ocean Water: Salinity*. Available: <http://www.onr.navy.mil/focus/ocean/water/salinity1.htm>
- [139] (2009, Analysis: Offshore BOP Companies Play It Safe. *Rigzone*. Available: http://www.rigzone.com/news/article.asp?a_id=82682
- [140] H. Cholet, *Well Production Practical Handbook*. Paris, France: Technip, 2008.
- [141] A. Callus, "Offshore Oil Rigs Drilling Deeper than Ever," in *The Globe and Mail*, ed. London, 2012.

- [142] D. o. Energy, "Annual Energy Review 2011," U.S Energy Information Administration. 2012.
- [143] "Federal Offshore - Gulf of Mexico Field Production of Crude Oil," U. S. E. I. Administration, Ed., ed, 2013.
- [144] I. MacDonald, "Deepwater Disaster: How the Oil Spill Estimates Got it Wrong," *Significance*, 2010.
- [145] T. Ahmed, *Reservoir Engineering Handbook*, 4th ed.: Gulf Professional Publishing, 1946.
- [146] M. F. Whitby, "Design Evolution of a Subsea BOP," *Drilling Contractor*, May/June 2007.
- [147] F. M. White, *Fluid Mechanics*, 5th ed.: McGraw-Hill, 2003.
- [148] S. T. Smith, *Flexure Elements of Elastic Mechanisms*: CRC Press LLC, 2000.
- [149] M. L. Culpepper, "Design of Quasi-Kinematic Couplings," *Precision Engineering*, vol. 28, pp. 338-357, 2004.
- [150] S. Kalpakjian and S. R. Schmid, *Manufacturing Engineering and Technology*, 5th ed.: Pearson Prentice Hall, 2006.
- [151] Aluminum 6061-T651 Properties [Online]. Available: <http://matweb.com/search/DataSheet.aspx?MatGUID=1b8c06d0ca7c456694c7777d9e10be5b>
- [152] E. Oberg, F. D. Jones, H. L. Horton, and H. H. Ryffel, *Machinery's Handbook 29th Edition*. New York: Industrial Press, 2012.
- [153] J. E. Shigley and L. D. Mitchell, *Mechanical Engineering Design*, 4th ed. New York: McGraw-Hill Book Compar, 1983.
- [154] R. Levien, "The elastica: a Mathematical History," Aug. 23, 2008
- [155] J. Stolte and R. C. Benson, "Dynamic Deflection of Paper Emerging from a Channel," *Journal of Vibration and Acoustics*, vol. 114 pp. 187-193, 1992.
- [156] S.-K. Hong, J.-G. Jee, Y. H. Jang, N.-C. Park, and Y.-P. Park, "Dynamic Analysis of Flexible Media by Dynamic Elastica Theory with Aerodynamic Effect," *Microsystems Technology*, 2007
- [157] *Parker O-ring Handbook (ORD 5700)*: Parker Hannifin Corporation, 2007.
- [158] M. H. Greenstone, "Meteorological Determinants of Spider Ballooning: the Roles of Thermals vs. The Vertical Windspeed Gradient in Becoming Airborne," *Oecologia*, vol. 84, pp. 164-168, 1990.
- [159] J. A. C. Humphrey, "Fluid Mechanic Constraints of Spider Ballooning," *Oecologia*, pp. 469-477, 1987.
- [160] J. M. Gosline, M. W. Denny, and M. E. DeMont, "Spider Silk as Rubber," *Nature*, vol. 309.
- [161] Y. Termonia, "Molecular Modeling of Spider Silk Elasticity," *American Chemical Society*, 1994.
- [162] J. V. B. Dries Bonte, Luc Lens, Jean-Pierre Maelfait, "Geographical variation in Wolf Spider Dispersal Behaviour is Related to Landscape Structure," *The Association for the Study of Animal Behaviour*, pp. 655-662.

[Left Blank]

Appendix

Calculations

Reynolds Number of Free Flowing Oil Well

Find: Reynolds number of free flowing oil well

Given:

- 1 oil barrel = 42 gallons
- Flow Rate (FR) = 65,000 bbl/day
- 1 gal = 3.785 L
- 1 L = 0.001 m³
- Viscosity = 0.008 Pa·sec
- D_{bore} = 18.75 inch
- Density = 839 kg/m³

$$Re = \frac{4 \cdot FR \left\{ \frac{bbl}{day} \right\} \cdot 42 \left\{ \frac{gal}{bbl} \right\} \cdot \frac{1}{1440} \left\{ \frac{day}{min} \right\} \cdot \frac{1}{60} \left\{ \frac{min}{sec} \right\} \cdot 3.785 \left\{ \frac{L}{gal} \right\} \cdot 0.001 \left\{ \frac{m^3}{L} \right\} \cdot \rho \left\{ \frac{m^3}{kg} \right\}}{\pi \cdot \mu \left\{ \frac{kg}{m \cdot sec} \right\} \cdot D_{bore} \{m\}}$$

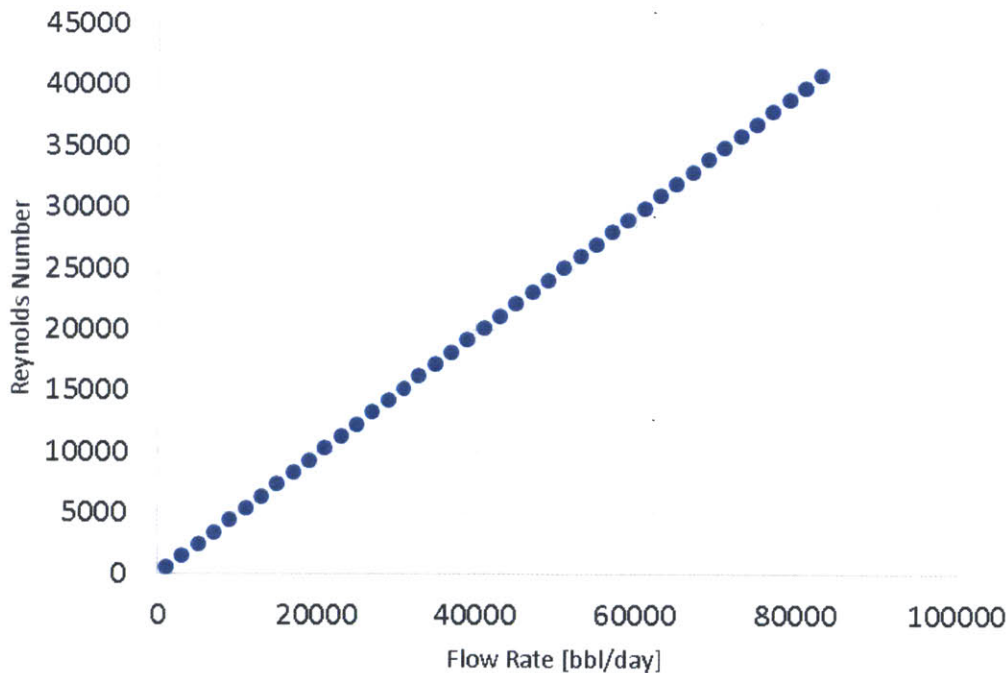


Figure 0-1: Flow rate versus Reynolds Number showing that at roughly 60,000 bbl./day the Reynolds number is around 30,000 thus the flow is turbulent.

Fluid Dynamics of a Wire Inside a Guide

This section looks at the fluid dynamics of the wire inside the guide. The objective is to find the axial velocity of the fluid cylinder as a function of radius. Figure 0-2 is a schematic diagram of a fluid section.

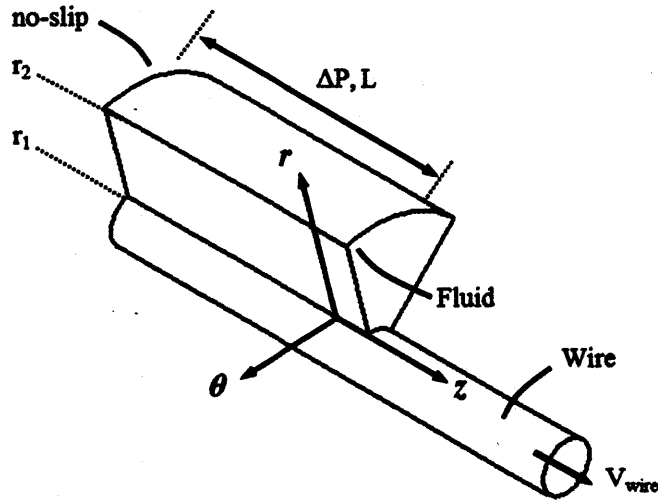


Figure 0-2: Fluid schematic in wire guide

Assumptions shown in Table 0-1 are made to simply the full Navier-Stokes equation, Equation 0.1, in polar form. The result from the simplification is shown in Equation 0.2.

$\rho \cdot \left(\frac{\partial V_r}{\partial t} + V_r \frac{\partial V_r}{\partial r} + \frac{V_\theta}{r} \frac{\partial V_r}{\partial \theta} - \frac{V_\theta^2}{r} + V_z \frac{\partial V_r}{\partial z} \right)$ $= \frac{-\partial P}{\partial r} + \rho \cdot g_r + \mu \cdot \left[\frac{\partial}{\partial r} \left(\frac{1}{r} \frac{\partial}{\partial r} (r \cdot V_r) \right) + \frac{1}{r^2} \frac{\partial^2 V_r}{\partial \theta^2} - \frac{2}{r^2} \frac{\partial V_\theta}{\partial \theta} + \frac{\partial^2 V_r}{\partial z^2} \right]$ $\rho \cdot \left(\frac{\partial V_\theta}{\partial t} + V_r \frac{\partial V_\theta}{\partial r} + \frac{V_\theta}{r} \frac{\partial V_\theta}{\partial \theta} - \frac{V_r V_\theta}{r} + V_z \frac{\partial V_\theta}{\partial z} \right)$ $= \frac{1}{r} \frac{\partial P}{\partial \theta} + \rho \cdot g_\theta + \mu \cdot \left[\frac{\partial}{\partial r} \left(\frac{1}{r} \frac{\partial}{\partial r} (r \cdot V_\theta) \right) + \frac{1}{r^2} \frac{\partial^2 V_\theta}{\partial \theta^2} - \frac{2}{r^2} \frac{\partial V_r}{\partial \theta} + \frac{\partial^2 V_\theta}{\partial z^2} \right]$ $\rho \cdot \left(\frac{\partial V_z}{\partial t} + V_r \frac{\partial V_z}{\partial r} + \frac{V_\theta}{r} \frac{\partial V_z}{\partial \theta} - \frac{V_\theta^2}{r} + V_z \frac{\partial V_z}{\partial z} \right)$ $= \frac{-\partial P}{\partial z} + \rho \cdot g_z + \mu \cdot \left[\frac{1}{r} \frac{\partial}{\partial r} \left(r \frac{\partial V_z}{\partial r} \right) + \frac{1}{r^2} \frac{\partial^2 V_z}{\partial \theta^2} + \frac{\partial^2 V_z}{\partial z^2} \right]$	Equation 0.1
--	--------------

Table 0-1: Navier Stokes Assumptions

Assumption	Validity	Terms
Steady State	Assume no time dependence	$\frac{\partial V_r}{\partial t} = \frac{\partial V_\theta}{\partial t} = \frac{\partial V_z}{\partial t} = 0$
Ignore gravity	Small enough that gravitational effects don't play a critical role.	$g_r = g_\theta = g_z = 0$
Only Axial Pressure Gradient	Any pressure gradient in the r or theta direction are much smaller than z direction	$\frac{\partial P}{\partial r} = \frac{\partial P}{\partial \theta} = 0$
Velocity	Velocity in the r and theta direction are much smaller than z direction	$V_\theta = V_r = 0$
Concentric Symmetry		$\frac{\partial V_z}{\partial \theta} = 0$
Fully Developed	Velocity in the z direction only depends on r and not at location along z	$\frac{\partial V_z}{\partial z} = 0$

$-\frac{\partial P}{\partial z} + \mu \cdot \left[\frac{1}{r} \cdot \frac{\partial}{\partial r} \left(r \cdot \frac{\partial V_z}{\partial r} \right) \right] = 0$	Equation 0.2
--	--------------

The solution takes the form of Equation 0.3 with two integration coefficients C_1 , and C_2 which are solved for using the boundary conditions. The complete solution including

$V_z = \frac{r^2}{4\mu} \left(\frac{\partial P}{\partial z} \right) + C_1 \cdot \ln(r) + C_2$ <p>B.C. $V_z _{r=r_1} = V_{wire} \quad \& \quad V_z _{r=r_2} = 0$</p> $C_2 = \frac{\left\{ \ln(r_2) \left(V_{wire} - \frac{r_1^2}{4\mu} \frac{\partial P}{\partial z} \right) + \ln(r_1) \left(\frac{r_2^2}{4\mu} \frac{\partial P}{\partial z} \right) \right\}}{\ln(r_2/r_1)}$ $C_1 = \frac{\left(V_{wire} - \left(\frac{r_1^2}{4\mu} \frac{\partial P}{\partial z} \right) - C_2 \right)}{\ln(r_1)}$	Equation 0.3
---	--------------

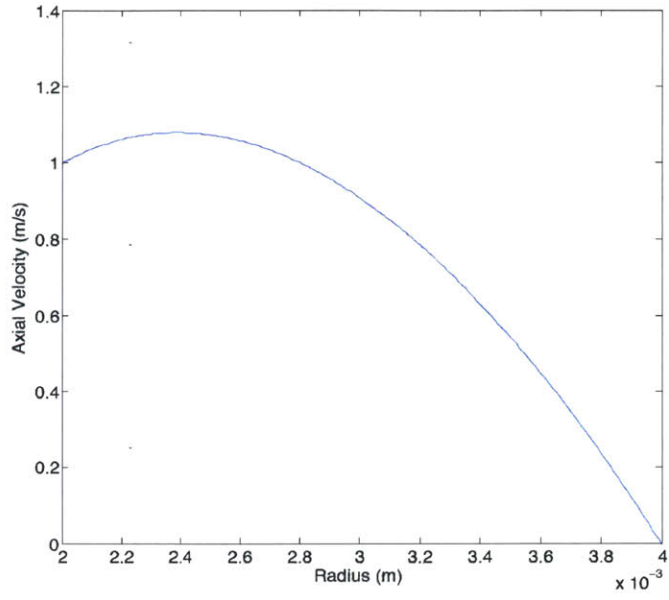


Figure 0-3: Flow axial velocity as a function of radius

Access Port Interface for Analysis

Components Design: Access Port Oring Cap

Flow Channel : Assuming thin walled pressure veseel			
Parameter	Symbos	Unit	Value
--- Add Thick Walled: Assuming thin Walled pressure veseel			
1	Pinterior	P1	Pa psi
	Pexterior	P2	Pa
	Axial Load	Faxial	N
		Length	inch
		width	inch
		Area	
	ADDED AXIAL	Paxial	
O-ring Design			
	Interior Diameter	ID	m
	Exterior Diameter	OD	m
	Center Diameter	MID	m
	Thickness	t	m
	Machinery Guide Gland Depth		
	Machinery Guide Gland Width		
Flange at caps			
	Radius Bolt Circle	rb	m
	Number of Bolts	Nb	-
	Diameter of Bolt	db	m
	Angle between bolts	Ab	degrees
	Distance between bolts	dbb	m
	Number of Bolt Diameter	Nbd	-
	Effective Flange thickness		
	Yield strength of Bolt	σ_y	Pa
	Young's Modulus of Bolt	Ebolt	Pa
	Yield strength of Cap	σ_y	Pa
	Yield Strength of Flange	σ_y	Pa
	Young's Modulus of Flange&Cap	Eflange	Pa
	Flange Safety Factor	-	-
	Cap Safety Factor	-	-
	Max Shear of Flange	tshear Max	Pa
	Flange Weld Shear Stress		
	Flange Operating to Yield Percentage		

Bolt Preload Parameters				
3/8 diameter 16 thread	Bolt Yield Strength	Syb	Pa	2.76E+08
	Nut Thickness (Effective)	tnut	m	0.00635
	Bolt thickness of head	thead	m	0.005953125
	Loadfactor	nlf	-	1.1
	Total Clamping Force Adjusted	Fclamp	N	1.42E+05
	Force Clamp Per Bolt	Fcbolt	N	1.42E+04
	Lead Angle Gamma	Gamma	Deg	3.00E+00
	lead length	Llead	m	9.10E-04
	bolt pitch diameter	dpitch	m	5.52E-03
	Friction Coeff between nut and bou t		-	0.45
	Nominal diameter of bolt			0.00635
	Diameter of bolt surface			0.009525
	Friction Coeff between surfaces	uf	-	0.45
	thread angle	Alpha	Deg	30
	Machinery's handbook Equation			
	Torque Preload	Tpreload	N*m	47.91
Shigley's Equation				
		tan(gamma)		0.052407779
		sec(alpha)		1.154700538
	Torque Preload	Tpreload		48.54
Bolt Shear Failure Modes				
All safety factors 2	Total Load Force on Bolt with Pres Ftp		m	2.59E+04
	Shear Stress of head			2.18E+08
	Shear head Percentage of Yield			273.49%
	Shear Stress of threads			2.35E+08
	Shear Threads Percentange			294.71%
Bolt Tensile Failure Modes				
	Bolt Tensile Strength		Pa	1.08E+09
	Bolt percentage of system		%	586.72%

NPT Interface shear loading				
	Axial Force			1.42E+05
	Diameter Effective			0.05715
	Yield Stress		MPA	2.76E+08
	Thickness			0.0127
	Shear Stress			62419295.44
	Percentage of operating to shear yield			97.93%

Component Analysis of Prototype Design

Components Design: Final Prototype

Main Drive : Transmission system to Front

Objective: find distance Length in to avoid using idler

Parameter	Symbols	Unit	Value	Comments
Chain Pitch	C	inch	0.25	this is for a #2
Teeth in large Sprocket	Dn	value	14	this is primaril
Number of links	NL		56	KEEP EVEN
Length of Chain	Lchain	inches	14.00	
Teent in small sprocket	Rn	inches	9	Number teeth
Center to Center Distance	ctc	inch	5.559	This is the cen
Transmission Ratio	TR	IN/OUT	1.5556	Transmission F

Machiner Handbook
Pg 2552

Probosis Drive : Transmission Ratio

Objective: Determine the size of the primary wheel to maintain the same speed in the rollers at contact.

Motor Driving system	Rpm in	rev per min	40
	R1	inch	0.387
	D1	inch	0.774
Calculated R1 Based	R1 Calc	inch	0.389
	Vfeed 1	inch/sec	1.621
	Vfeed 1 Metric	m/sec	0.041
Probosis rpm	Rpm out	rev per min	62.22
Probosis outport	R2	inch	0.25
	Vfeed 2 Out	inch/sec	1.629

Guides: Max wire Dimension Needed for Stiffness

Objective: Find the Maximum wire diameter needed for withstanding the flow.

Parameter	Symbols	Unit	Value	Comments
Uncontrolled flow Rate	Fgpm	gal per min	100.00	
Back Pressure	Bpsi	Psi	50.00	
Diameter of Chamber	Dc	m	0.1016	
Viscosity of water u	uw	Pa*sec	1.00E-03	
Density of Water	rouw	kg/m3	1000.00	
Mass Flow Rate	mdotm	kg/sec	6.31	
Reynolds Number from mass flow	rem	-	78897.10	
Velocity of flow	vflow	m/s	0.78	
Vfeed/Vflow Ratio	Vr	-	0.2000	
Vfeed Min		m/sec	0.1556	
Non dim Stiffness of Wire	Pstiff		200.0000	
Young's Modulus	Ey	Pa	7.00E+10	
Rwire	Rwcalc	m	0.00132	
		inch	0.05204	

Find the Stiffness of the Test Setup Configuration

Calculated Stiffness for test Entanglement			153.30
Etest		Pa	7.00E+10
r wire		m	4.00E-04
Re test		-	30000
d test		m	0.0254
velocity flow		m/s	1.18
Imoment		m^4	2.01E-14

$$\pi_s = \left(\frac{EI}{r_w \rho u_{flow}^2 D_{bore}^3} \right)$$

Guides: Torque Calculation System

Objective: Transmit torques through out the system

Parameter	Symbols	Unit	Value	Comments
Shaft Diameter	Ds	in	0.5000	
Groove Width	Gw	in	0.1680	For Size 014 C
Diametrical Clearance	Dc	inch	0.0140	to withstand r
Diameter Bore	Dbore	inch	0.5140	
Gland Depth	hgland	inch	0.121	
Gland Diameter	Dgland	inch	0.7420	

Dynamic Seal Torque

Objective: What is the torque that is wasted on the seal

Parameter	Symbols	Unit	Value	Comments
Radius of Oring diameter	Rring	m	0.0079375	
Diameter of Oring	Dring	m	0.0035306	
Rshaft	Rshaft	m	0.00635	
Pressure	Press	Pa	3447000	
Torque	T	N*m	3.854136859	
Motor Max Torque		N*m	112.5423729	
$Torque = 2 \pi * Rring * Dring * rshaft * P$			0.034246096	

Thrust Load

Objective: What is the torque that is wasted on the seal

Parameter	Symbols	Unit	Value	Comments
Pressure	Rring	m	3447000	
Area Cross section	Dring	m	0.000126677	
			436.6551701	
		lbs convert	98.16008224	
		Bearing Max	350	
		% Usage	0.280457378	

Guides: Pins on drive module failure

Objective: What are the Oring Dimensions and clearance values

maximum torque		N-m	112	
radius of application		m	0.041275	
Force Shearing		Newtons of sh	2713.506965	
Number of Locations supports			4	
Shear force per contact		Newtons of sh	678.3767414	
Yield stress of pins		Pa	6.21E+08	
Shear of material		Pa	3.59E+08	
Area of pin		m2	7.13E-05	
			9.52E+06	
Percent shearing of operating			2.66%	
Radius outside		meter	0.2	
radius inside			0.1905	
Area cross section		m2	0.011654523	
Yield strength		P110	7.58E+08	
Shear strength of casing			4.38E+08	
		Newtons	5.10E+06	

High Pressure Loads in Flow loop

Pressure Testing
Analysis

ENGINEERING VALUES

	Parameter	Value	Unit	Description
Thread of Connection for Pressure Testing	Diameter thread	0.0848	m	Maximum Interior Pressure
	Yield Strength	2.76E+08	Pa	AL 6061 T6
	Shear Strength	1.59E+08	Pa	
	Operating Pressure	2000	psi	
		1.38E+07	Mpa	
	Safety Factor	1.5		
	Pressure with Safety	3.00E+03	psi	
		20682000	Pa	
	Load	116907.61	Newtons	
	Height of Thread	0.0127	m	
	Shear Load	3.454E+07	Pascal	
	VERIFY Thread Strength	Thread Interface Ok		
Operating Thread Strength	21.7%	%		
Tension of custom coupling	Interior Diameter	4.45E-02	m	
	Exterior Diameter	7.62E-02	m	
	Axial Load	3.21E+04	N	
	Area of Loading	3.01E-03	m^2	
	Axial Stress	1.07E+07	Pa	
	Safety Factor	2.0		
	Max Axial Load with Safety	1.38E+08	Pa	
	VERIFY Interface Tension	Interface Ok		
	Operating Thread Strength	7.7%	%	
	Check Thickness of Coupling Interface	Flange thickness	0.0127	m
Depth of Oring		0.002794	m	
True Flange Thickness		0.009906	m	
Diameter Flange		0.1016	m	
Load on Flange		1.68E+05	Newtons	
Shear Load on Flange		5.30E+07	Pa	
VERIFY Flange Strength		Flange Int. Coup. Ok		
Operating Flange Strength		33.3%	%	
Check Thickness of Flange	Flange thickness	0.009525	m	
	Depth of Oring	0.002794	m	
	True Flange Thickness	0.006731	m	
	Diameter Flange	0.1016	m	
	Load on Flange	1.68E+05	Newtons	
	Shear Load on Flange	7.80E+07	Pa	
	VERIFY Flange Strength	Flange Interface Mount Ok		
	Operating Flange Strength	49.0%	%	
Check Bolts	Diameter of Bolt Circle	1.65E-01	m	
	Effective Diameter	1.02E-01		
	Number of Bolts	12	Pa	Part 90201A321
	Tensile Strength	180000	psi	Tensile Strength from McMaster
		1.24E+09	Pa	Verified and correct that is insane
	Shear Strength of Bolt	7.16E+08	Pa	
	Safety Factor	1.5	-	
	Root Diameter of Bolts	0.0076	m	
	Total Axial Load	1.68E+05	N	
	All bolts cross sectional area	0.000544329	m^2	
	Tensile Stress	4.62E+08	Pa	
	VERIFY Bolts Strength	Bolts Tension Test Ok		
	Operating Flange Strength	37.2%	%	
	Bolt Head Thickness	0.00714375	m	
	Total Area of Shearing	0.002046693	m^2	
	Shear Load on Bolt Heads	8.19E+07	Pa	
VERIFY Bolts Strength	Bolts Heads Ok			
Operating Flange Strength	11.4%	%		

Check Weld between Flange and Chamber	Internal Pressure	2.07E+07	Pa	
	Yield Strength	9.50E+07	Pa	If T0 then it will fail (55.2 MPa)
	Shear Strength	5.48E+07	Pa	
	Shear Safety Factor	1.5		
	Adjusted Shear Strength	3.66E+07	Pa	
	thickness of weld	0.0127	m	
	Diameter of Weld	0.127	m	
	Adjusted Load	1.68E+05	Newtons	
	Shear Stress on Weld	3.31E+07	Pa	
	VERIFY Flange Strength	Weld Ok		
	Operating Flange Strngth	60.3%	%	
Pressure Chamber Calculation	Safety Factor	1.5	Preset	
	Temperated Diff (ΔT)		C	
	Thermal Expansion	1.60E-05	m/m	
	Poisson Value	0.3	-	
	Pinterior	2.07E+07	Pa	Interior Pressure above exterior
		3.00E+03	psi	
	Pexterior	1.00E+05	Pa	
	Interior radius	0.0508	m	Interior Radius
	Exterior radius	0.0635	m	Exterior Radius
	Center Diameter of O-ring	0.136525	m	
	Radial Stress (σ_{rr})	-2.07E+07	Pa	Without Temperature Effect
	Location radius for σ_{rr}	0.0508	m	For interior radius of the chamber
	Hoop Stress $\sigma_{\theta\theta}$	9.37E+07	Pa	Without Temperature Effect
	Axial Load	3.01E+05	N	Use the center diameter of the Oring
	Axial Stress σ_{zz}	1.03E+08	Pa	
	Von Misses Principal σ_v	1.19E+08	Pa	
	VERIFY Flange Strength	Chamber will Hold Ok	-	
Operating Flange Strngth	43.1%	%		

Natural Phenomena

Spiders are flightless arthropods, that disperse through the process ballooning where a silk strand is ejected from the spider into the air cross flow [158, 159]. The objective of this section is to determine the non-dimensional entanglement stiffness for the spider ballooning process using **Error! Reference source not found.**

$\pi_{se} = \frac{E \cdot \pi \cdot r_w^2}{8 \cdot C_d \cdot \rho_f \cdot L_{strand}^2 \cdot V_{flow}^2}$	Equation 0.4
---	--------------

The Young's modulus of spider silk Young's modulus is 8.5 ± 1.6 MPa with a with an approximate diameter of 0.1 mm [160]. Another paper that looked at modeling the Spider silk elasticity obtained a similar number of around 7 MPa [161]. The lower speeds of the ballooning process is approximately 1 - 1.2 m/s [162]. The range in wind speeds is between 2 m/s to 5 m/s.

As shown in the figure below the stiffness coefficient for entanglement is so low that the silk strand gets taken by the flow.

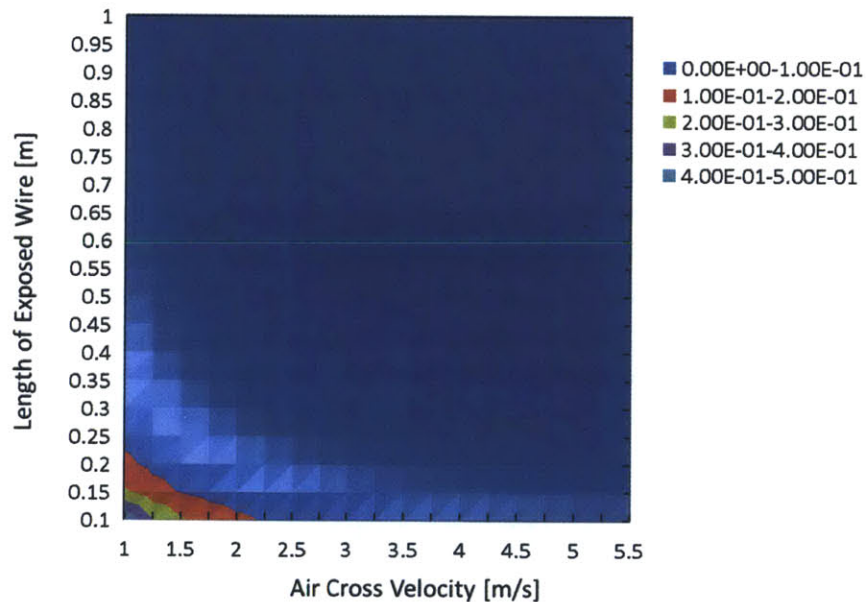


Figure 0-4: Entanglement stiffness for the spider silk strand ballooning process

PUPs Problems

The idea behind the PUP problems is to relate college level research to simple problems that can be done by a high school student.

Chp1:

1. The Deepwater Horizon was flowing at 60,000 barrels per day. Given the fines per barrel established by the Clean Water Act Section 311, what is the fine costs per second assuming no negligence? What is the flow rate in gallons per second? (See Appendix Calculations for Help)
2. What is the hydrostatic pressure at a water depth of 1.5 km? How many times greater than sea level pressure of 1 atm is at 1.5 km below the sea level?
3. Find the Reynolds number of the flow through a blowout preventer whose diameter is 18 ¾ inch (0.47 m), flowing oil with no gas with a density of 950 kg/m³, and a viscosity of 10cp. Is this reasonable?

Chp2:

1. One recent patent, U.S. Pat. No. 2012/0285683 A1 (*Hermes*), proposes to introduce of 2-cyanoacrylate ester monomer into the uncontrolled fluid to close the well. As you are reading the patent you want to know if it will work in an accident like Macondo. Assuming a fluid flow velocity of 0.7 m/s, how fast does this reaction have to take place?
2. Another patent also considered (U.S. Pat. No. 8,205,677 B1) proposes to insert metal javelins inside of the flow in order to obstruct the flow. It proposes the insertion vertically against the flow. As the Jr. Engineer you are tasked with doing the back of the envelope calculation to determine the force balance on the first javelin to determine how fast it has to be pushed down in order to enter the bore.
3. Transmission system are often used in wire feeders since a motor cannot always be placed in line with the wheels. Design a wire feed system with a transmission system with a transmission ratio of 10:1.
4. What is the friction and compression needed between the wire and the rollers in order to provide enough force to buckle the wire?
5. What are the advantages of a discrete, continuous, hybrid feeder designs.
6. A flag pole 10 m tall is made from plastic whose diameter is 10cm. On a windy day the wind speed is 10 m/s. What is the tip deflection of the top of the flag if we ignore ground effects? (State assumptions and list sources)
7. Consider now inserting a wire structure into the BOP orthogonal to the flow as shown below. What is the expected tip deflection of the structure inserted if we assume that drag is proportional to the mean velocity only?

8. The flow rate of a household garden hose is 2 gal/min. If we insert a straw that is made from polypropylene into the flow what is the estimated deflection placing the straw orthogonal to the flow.
9. Calculate the wire radius required for aluminum and steel to minimize the tip deflection to ten percent of the bore diameter.
10. In 1856, Darcy's law was discovered using a flow meter apparatus. You decide to build your own apparatus at home using duct tape, several 2 Liter bottles of soda, and sand to see if you can come to the same conclusion. Your only measurement tool are a watch and a coffee mug. One liter of water can fill approximately 5.7 coffee mugs. Now perform Darcy's column experiment with sand.